SURFACE ACTIVE LANTHANIDE COMPLEXES FOR SENSING APPLICATIONS ON SILICA AND GOLD SURFACES

By

Suleman Manawar Khan

A thesis submitted to

The University of Birmingham

For the degree of

DOCTOR OF PHILOSOPHY

School of Chemistry

College of Engineering and Physical Sciences

The University of Birmingham

September 2014

Abstract

The work presented in this thesis investigates the use of new luminescent lanthanide bis-amide DTPA complexes, both in solution and bound to gold and silica surfaces. The bis-amide arms have been modified with surface attachment groups consisting of disulphides, thioacetates and silyl ethers. Both sensitising and non-sensitising bisamides arms were attached to DTPA in order to develop the best lanthanide based sensor. When these visible and NIR emitting lanthanide complexes are bound to the surface they can be used to detect various small analytesm including benzoic acid, phthalic acid, isophthalic acid, picolinic acid, dipicolinic acid, quinaldic acid, dibenzoyl methane and curcumin. The detection of analytes was performed on surfaces and in solution allowing for comparisons between the two techniques to be made. Lanthanide complexes were attached to silica microparticles and they were used for detection of analytes under flow conditions; these studies were compared to surface and solution analyte detection. The lanthanide-based silica microparticles were developed further to show the advantages of bimodal luminescent silica microparticles. The development of self-assembled monolayers of the lanthanide complexes on gold were studied using surface plasmon resonance and ellipsometry.

Acknowledgments

I would firstly like to thank my supervisers Zoe Pikramenou and Jon Preece for the all their support, motivation and the opportunity to carry out my Ph.D, without which I wouldn't be who I am today. My thanks also goes to past and present members of both research groups for all the good times and the bad: Dave L, Sam, Alison, Sunil, Kimmy, Nicola, Richard, Shiva, Parvez, Alex and Zarrar, good luck to you all. I have made many friends and the list is too long to mention you all, so I will say you know who you are and thank you. A special mention to Amrit my partner in crime for the last seven years, cheers bud and see you at graduation. I would also like to thank my parents and brother for the love and support to make it through to where I am now. Last but no means least I would like to thank my gorgeous girlfriend, Naz, who truly has been my pillar of support and encouragement for my time here, especially when there was no one else and I really could not have done it without her, so thank you honey and thank you all.

Table of Contents

Table of Figures

1 - Background

We have been interested in developing a cheap and easy method to create sensing platforms for the coordination of simple aromatic acids with the formation of self-assembled monolayers (SAMs) of lanthanide complexes coordinated on gold and silica surfaces. In this thesis we explore the synthesis of four new luminescent lanthanide complexes attached to silica and gold surfaces (*figure 1*), and their ability to be used as molecular sensors. The aim of the research is not to compete with commercial methods but to scope for the development of a cheap, effective early detection system for potential dangerous chemicals at the molecular level.

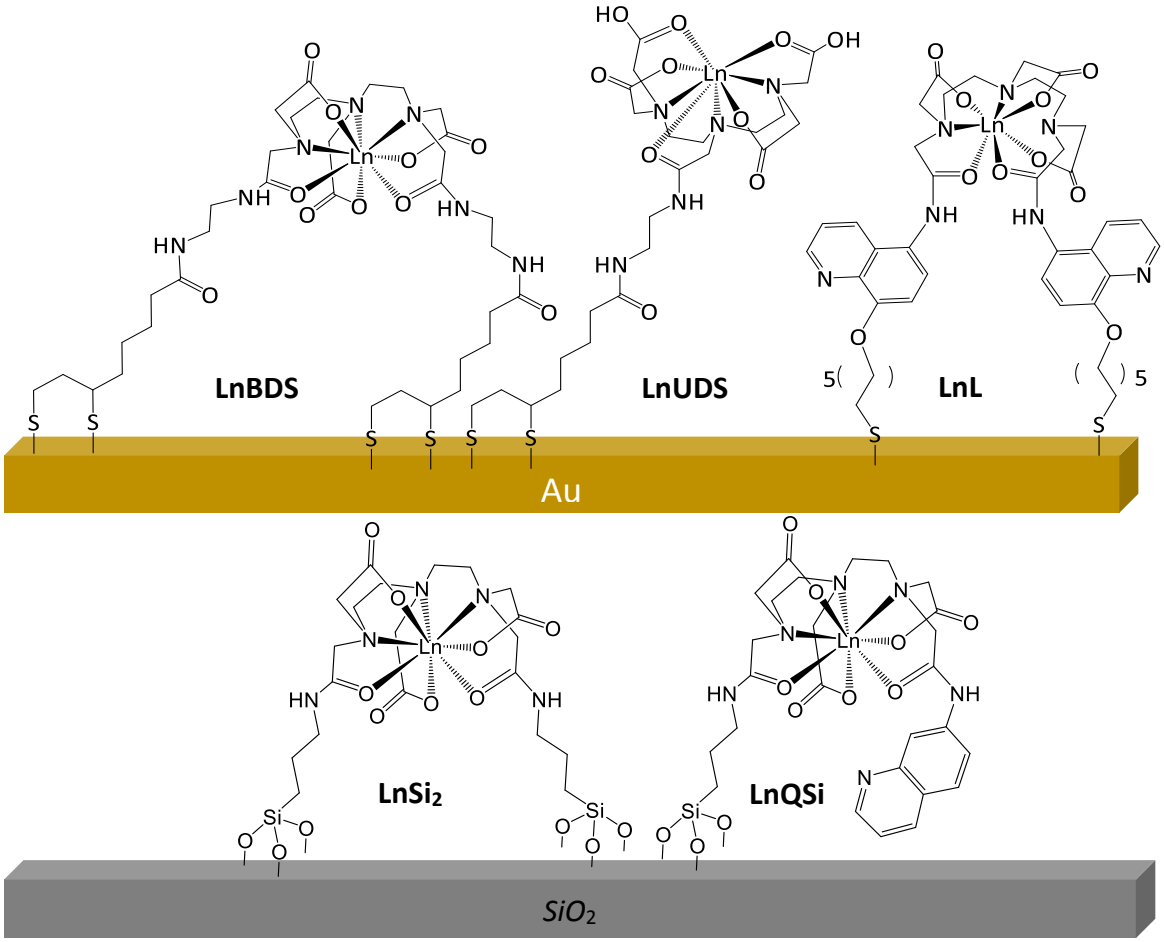

Figure 1.0- The chemical structure of from Top left to Top right, LnBDS, LnUDS, LnL, and $LnSi_2$, and LnQSi on the bottom respectively

Recent research has made great advances in sensing at the nanoscale level, from Lab-on-Chip devices to microfluidic devices.[1] These systems are becoming increasingly more sophisticated and expensive to manufacture; thus finding alternative ways to develop effective and efficient systems would save money, time and potentially lives, depending on the system's application.

1.1 - Self-Assembled Monolayers (SAMs) – Effective building blocks for device fabrication

Self-assembled monolayers (SAMs) are relatively cheap to produce and an established technique for covering surfaces and various substrates, ranging from gold, silver, copper, palladium and nickel for thiol based SAMs or silanes to cover silica or titanium.[2-16] These functionalised substrates have led to a huge host of research areas and applications, such as micro-patterning,[10,17-19] cell patterning,[20,21] electrochemistry,[19] controlling the growth of nanoparticles and nanorods,[22] and more recently as molecular sensors.[18,23,24]

Gold surfaces and gold nanoparticles have played a big role in the past few decades in the development of nanosensors.[25-27] Gold surfaces allow for a highly organised SAMs to form on the surface of well-defined thickness, composition and structure.[28] One of the most favoured approaches in the formation of SAM's on gold surfaces is the use of sulphur-gold interactions, as thiols, which are able to form strong bonds with gold, typically 188 kJ mol^{-1}.[29] Organic based SAMs use the sulphur group in conjunction with a long alkyl chain which helps promote hydrophobic interactions along the surface, lowering surface energy and increasing self-

assembly, creating more dense monolayers. The most common form of gold surface binding groups include thiols, thiol acetate and disulphides.[4,30]

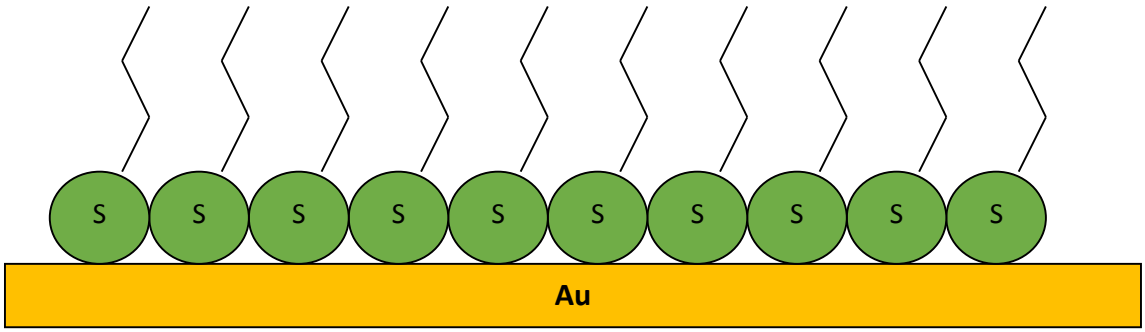

Figure 1.1 - An example of a SAM, Gold surface with propyl-thiol attached to the surface in a structured and ordered manner.[6]

Organic SAMs have been used to create molecular printboards in order to create read-write-erase functionality on the surface which could lead to the development of a memory storage devices. Bassini et *al.*[19] used post-SAM modification techniques as an alternative to molecular stamping techniques.

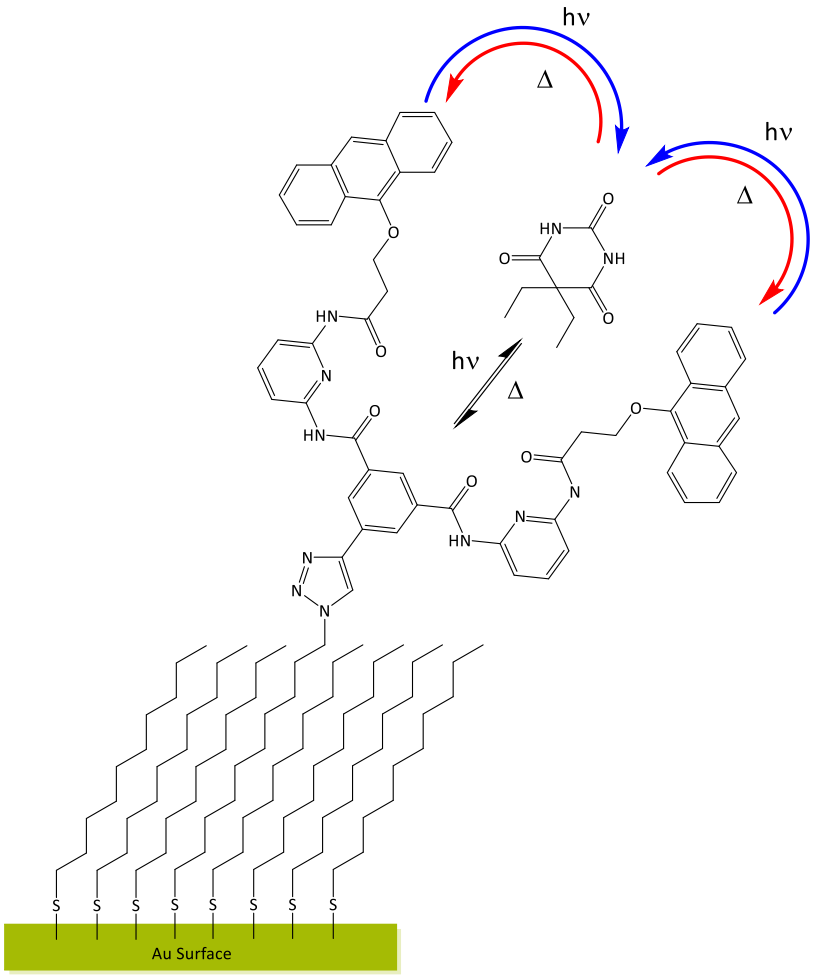

Figure 1.2- Schematic representation of the molecular printboard using read-write-erase approach on the surface of gold.[19]

They demonstrated that by forming a densely packed monolayer of decanethiol and mixing the SAM surface with azide terminated thiols, they could perform click chemistry on the SAM allowing the attachment of the receptor directly to the surface (*figure 1.2*). The group had previously established that the receptor is capable of binding barbiturate derivatives in solution,[31] and separately form SAMs with anthracene graphed onto silicon oxide surfaces.[32] They showed that using hydrogen bonding motifs they could bind barbital when the SAM receptor was open and then remove the barbital when the SAM was irradiated with UV light. The UV radiation caused the anthracene molecules to dimerise and the receptor site to form

a pseudo macrocycle, restricting competitive binding from guest molecules and decreasing the cavity size and change in hydrogen bond orientation. This in turn limits the barbital binding potential. Whilst if the SAM was heated, the dimerization effect of the anthracene was reversed and receptor site opened up, breaking the pseudo macrocycle. This again allows barbital into the receptor site which regenerates the receptors original binding potential, hence the process being termed read-write-erase. The group compared the SAM receptor capabilities to the solution counterpart indicating that the process is more effective in solution than on the surface. The group attributes this to the fact that it is difficult to form densely packed SAMs on surface whilst avoiding any intermolecular interactions such as dimerization between two receptors.

1.2 - Molecular Sensors

Molecular sensors,[25,33,34] host-guest chemistry,[10,17,35] and molecular recognition[20,36,37] all rely on chemical recognition and the interaction of the functional groups involved. The most common reaction from a chemical recognition is a photophysical response. The photodynamics of a system that has undergone a binding event normally differs significantly from the parental systems, thus the information can be used for detection and thus provide molecular sensors. Depending on the application, sensors typically retain their individual intrinsic properties in order to differentiate the output signal from that of the detecting species. Other sensors may vary in design and take the approach that the sensor itself changes upon recognition. The design of molecular receptors is developing to suit the needs of the user, particularly in the fields of molecular biology,[38,39] gas detection[40] and anion sensing[41]. Early sensor design particularly involved the use of organic fluorophores, one example of this sensors has been developed to detect the change in pH using the fluorescence emitted from the dye as a detection method.[42,43]

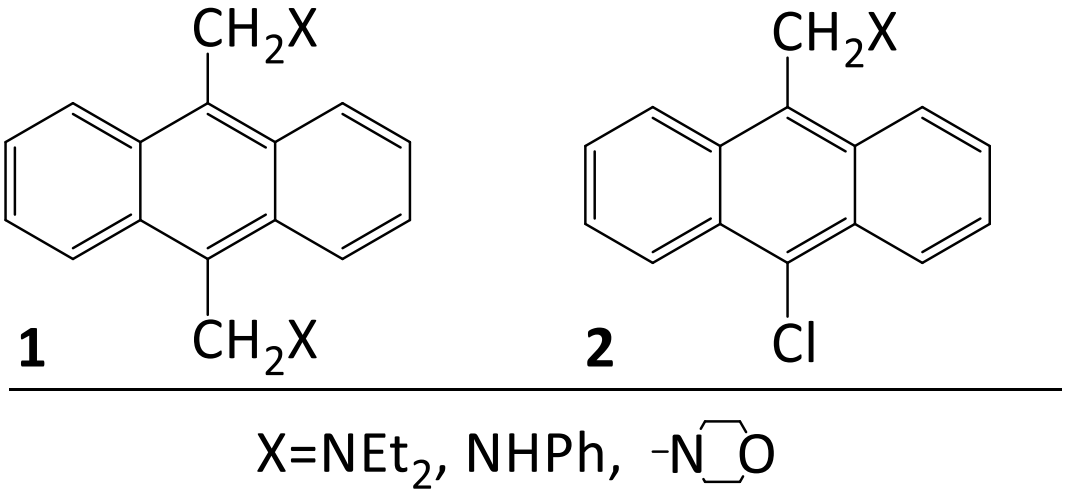

Figure 1.3- ***pH sensor designed be A.P de Silvia.***[43]

De Silva *et al*.[42] used the photo-induced electron transfer principle with anthracene derivatives as a pH indicator (*figure 1.3*). The anthracene derivatives had almost identical absorption and emission properties independent of the sensors pH, the only spectral property that differed was the quantum yield. Due to the molecular design of the fluorophores, the sensor was able to accurately determine the pH at which the amine becomes protonated and the fluorescent signal from the anthracene is no longer quenched. Using the anthracene derivative was an improvement over existing pH fluorophores. Previous indicators had to have an isosbestic point, where the excitation wavelength had to be the same for protonated and deprotonated species and secondly the pKa of the excited state differed from the ground state.

Many molecular systems and sensors are designed to contain organic dyes which absorb light, typically ultra-violet light. This can prove to be problematic in biological applications due to the autofluorescence associated with biological tissue coinciding with the emission of organic dyes. Utilising dyes that absorb alongside tissue can cause limitations on the detection limits of the device or even data interpretation. One method of circumventing this issue is by using lanthanides in the sensor design.

1.3 - The Unique Properties of Lanthanides

The use of lanthanides allows for three main core advantages, firstly lanthanides have long luminescent lifetimes typically in the order of hundreds of microseconds to milliseconds, large stokes shifts and sharp line like emission bands (*Schematic 1.0)*. These long lifetimes in practice can be utilised to implement a time gated approach that excludes the autofluorescence observed from organic dyes or analyte emission, leaving only lanthanide emission.[44]

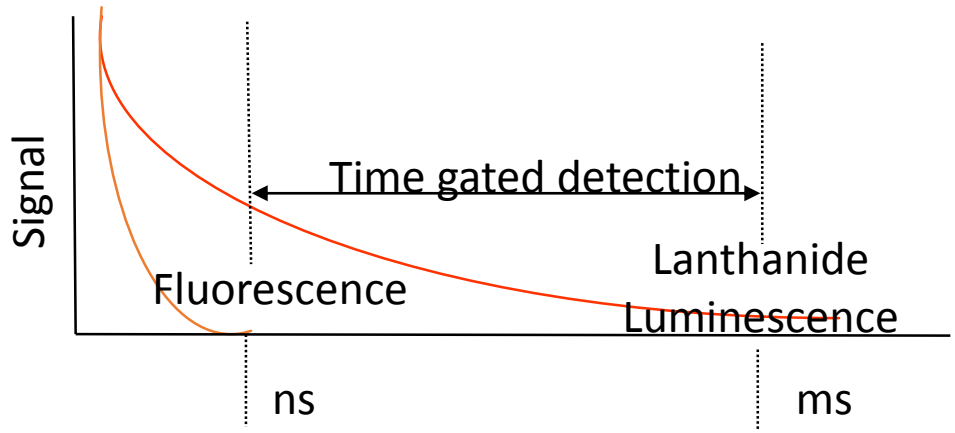

Schematic 1.0 - Showing the potential detection window applicable to lanthanide lifetimes than can minimise autofluorescene.

Lanthanide systems' long lifetime is due to a combination of the energy transfer process, excited states and forbidden relaxation pathways.[45] Lanthanides aren't without flaws in their capacity to be used as sensors. The lanthanides *f – f* transitions are forbidden by a number of rules; the Laporté (parity, $\Delta L \neq 0$) selection rule prohibits the redistribution of electrons in the 4*f* subshell and the orbital angular momentum selection rule ($\Delta l = \pm 1$) also forbids *f – f* transitions. Additionally some transitions are also forbidden by the spin conservation selection

rule ($\Delta S = 0$).[46] These transitions can be broken to a certain extent, and thus these transitions may become allowed due to weak vibronic coupling; in this process a molecular vibration temporarily lowers the symmetry of the lanthanide ion, bending Laporte's rule. As the rules are broken then the transitions grow in intensity as symmetry and orbital angular momentum are changed. With these rules in place it means that lanthanides have very weak extinction coefficients of the order of only 0.5–3 $dm^3\ mol^{-1}\ cm^{-1}$.[47] This renders direct excitation of the lanthanide ion very inefficient and only practical with lasers. One solution to circumvent this problem is to incorporate a sensitising chromophore (often termed an 'antenna') into the ligand design. This allows the system to make use of the large absorption coefficients of chromophores allowing the energy to be transferred via for a new relaxation pathway to the lanthanide ion, usually via intramolecular energy transfer.[48] This is often termed the "antenna effect". [47-51]

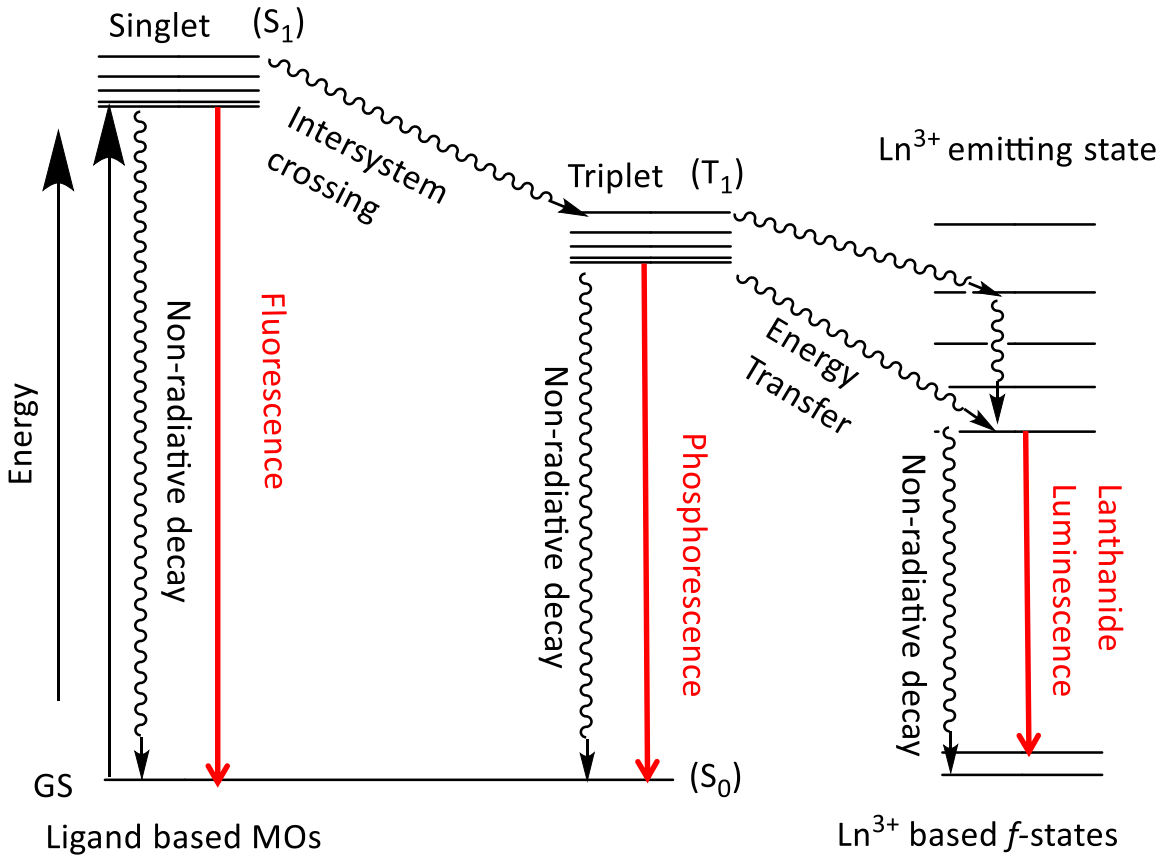

Schematic 1.2 - A schematic representation of an energy flow diagram representing the relaxation routes

Lanthanide ions display three types of electronic transitions, the first is the forbidden, weak *f-f* transition mentioned above. These corresponding transitions are typically quite narrow and the ligand field theory's barycentre split bands aren't influenced greatly from the chemical environment of the ion.[33] The resulting effect allows these transitions to be easy recognisable, aiding in characterisation for use in optical probes for example. The second kind of interaction involves a promotion from the 4*f* orbital into the 5*d* subshell, an *f-d* transition. These transitions are allowed unlike *f-f* transitions, are broader in nature and the barycentre is affected by the external chemical environment. The final type of electronic transfer, although more commonly associated with transition metals, is Ligand to Metal Charge Transfer (LMCT) and Metal to Ligand Charge Transfer (MLCT).

Schematic 1.2 shows the energy pathway of a photoelectron taken from a sensitised lanthanide complex to *f-f* transition. Light is absorbed in the first instance promoting an electron into a singlet excited state, from this point the system can either relax back down to its ground state through non-radiative pathways, or through radiative pathways i.e. fluorescence. Alternatively it can undergo a spin change via intersystem crossing to triplet excited state. Again the electron can relax through non-radiative or radiative pathways (phosphorescence) or undergo an energy transfer process to the lanthanide ion's excited states, these long pathways lead to longer lifetimes and a larger stoke shift. The overall process has been directly observed by Nocera and co-workers.[52]

Lanthanide luminescence is an umbrella term that is associated with lanthanides because it incorporates both fluorescence and phosphorescence.[53] The umbrella term is needed because lanthanides have long lifetimes that encroach into the time scale realm of fluorescence (1 ps-10 μs) and the realm of phosphorescence (100 μs-1 s). Lanthanides that normally undergo fluorescence include Pr^{3+}, Nd^{3+}, Ho^{3+}, Er^{3+} and Yb^{3+}.[25] Remaining lanthanides that undergo phosphorescence include Sm^{3+}, Eu^{3+}, Gd^{3+}, Tb^{3+}, and Tm^{3+}.[25] With all the lanthanides excluding La^{3+} and Lu^{3+} (empty and full *f*-orbitals respectively), they cover the whole visible spectrum and stretching into the near-infrared.

There is a long energy pathway from excitation of bound chromophores to the lanthanides emissive states. This gives rise to many non-radiative pathways, such energy lost through vibrational, or translational molecular movements with energy lost as heat. However whilst

energy is being lost across electronic states and down vibrational levels it gives rise to another benefit of using lanthanides, the large stokes shift (*see schematic 1.3*).

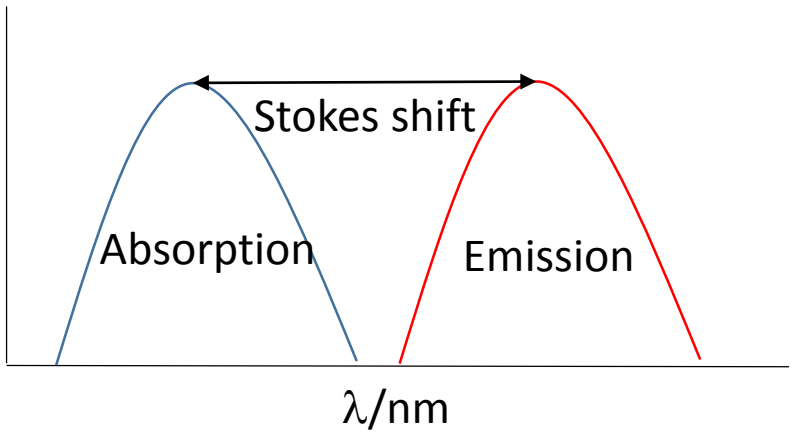

Schematic 1.3- Showing what a Stokes shift is.

Having a large stokes shift is beneficial because it prevents any issue within a photoactive system in which the emission could potentially be reabsorbed by the system, (self-quenching). Thus a large stokes shift separates the absorption bands of a systems from the emission bands, and by isolation of the two bands the results will be more accurate and reliable. Having a large stokes shift also separates the signals from the excitation source allowing for clear distinction between emission arising from excitation source and that which arises from the sample being studied.

1.4 - Lanthanide Ion Coordination

A multitude of different ligands bearing aromatic sensitising chromophores have been devised (*figure 1.4*) including bipyridines,[54] terpyridines,[42] substituted phenyl[55], naphthyl groups[56] and has led to a wide array of lanthanide chelating ligands; such as cryptands,[51] crown ethers,[57] calixarenes,[25] and other polydentate chelating ligands.[58-65]

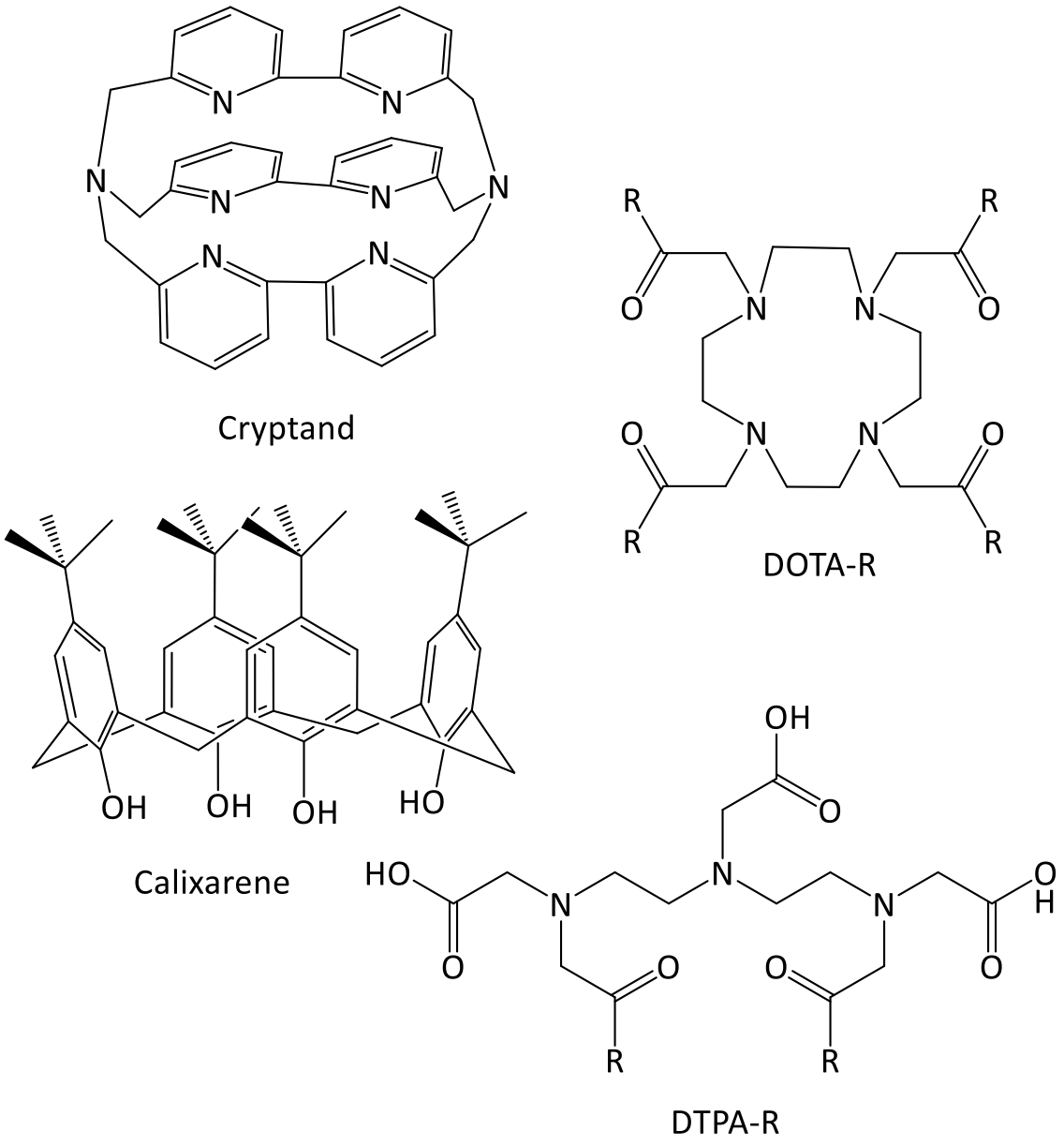

Figure 1.4 - Examples of lanthanide chelating ligands with modifiable 'R' groups.

Many variations of sensors have been designed to meet the demand for molecular recognition to improve selectivity or sensitivity. With the understanding of metal-ligand interactions, the detection of metals and incorporation of metals into the sensor design has been researched. Ln^{3+} are classified as hard acids[66] and coordinate hard donors such as oxygen and nitrogen atoms. In addition to the displacement of water molecules, hard donors are used for lanthanide coordination because of the non-directionality and disperse nature of the *f*-orbitals, thus hard donors have better binding affinity for lanthanide ions. Appropriate ligands have been designed and typically take advantage of lanthanides most common oxidation state of +3, forming an overall neutral complex. This increases the stability of the complex, which is particularly sort after in biological studies as lanthanide ions will have a toxicological effect if they are leached out from the chelate via transmetallation with existing metal cations.[67]

Whilst forming neutral complexes is advantageous, ligand design has tried to address another important factor whilst addressing lanthanide luminescence and lifetimes; the quenching of high vibrational oscillators such as O-H, N-H and to a lesser extent C-H vibrations, which is classed as non-radiative decay. [56] This can be achieved by ensuring these are never adjacent to lanthanide coordination atoms. Europium is particular susceptible to quenching by OH vibrations through water molecules. This is because europium's emissive states overlap with the vibrational over tones of O-H vibrational energy levels, thus providing a competitive energy pathway for the energy in the lanthanide excited state to relax down back to the ground state.[56]

1.5 - Sensing with Lanthanide Encapsulated Systems

He and co-workers[68] have used the lanthanide cerium (III) in a metal-organic framework (MOF) which was achieved by placing the cerium at the corners of the tetrahedron in the MOF and linear shaped ligands to bridge between the cerium atoms to create two different self-assembled MOF, TE1 and TE2 (*figure 1.5*). These two MOF contain different binding sites for selective detection of natural saccharides; mannose, glucose, xylose, ribose, trehalose, sucrose and maltose. TE1 being more selective for mannose, glucose, xylose, and ribose and TE2 being more selective for trehalose, sucrose and maltose.

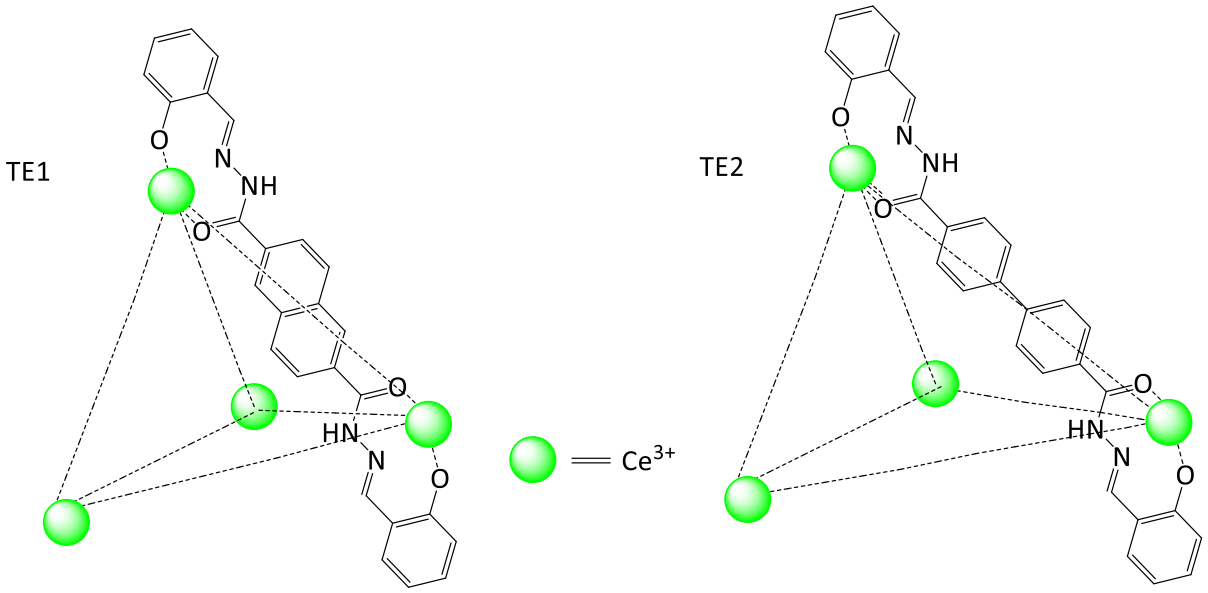

Figure 1.5 - TE1 and TE2 is displayed in the Cerium tetrahedron.[69]

The emission profile for each saccharide was of different intensity and so individual saccharides were distinguishable from each other. The cavity size was calculated to be 550 Å^3

and taking into consideration the size of the current saccharides it was theorised that the cavity has potential to hold larger saccharides as well.

Lanthanides have also emerged in the area of chemical warfare detection methods. The detection of chemical warfare agents is of increasing importance in the modern age, and has also driven development of lanthanide based molecular sensors.

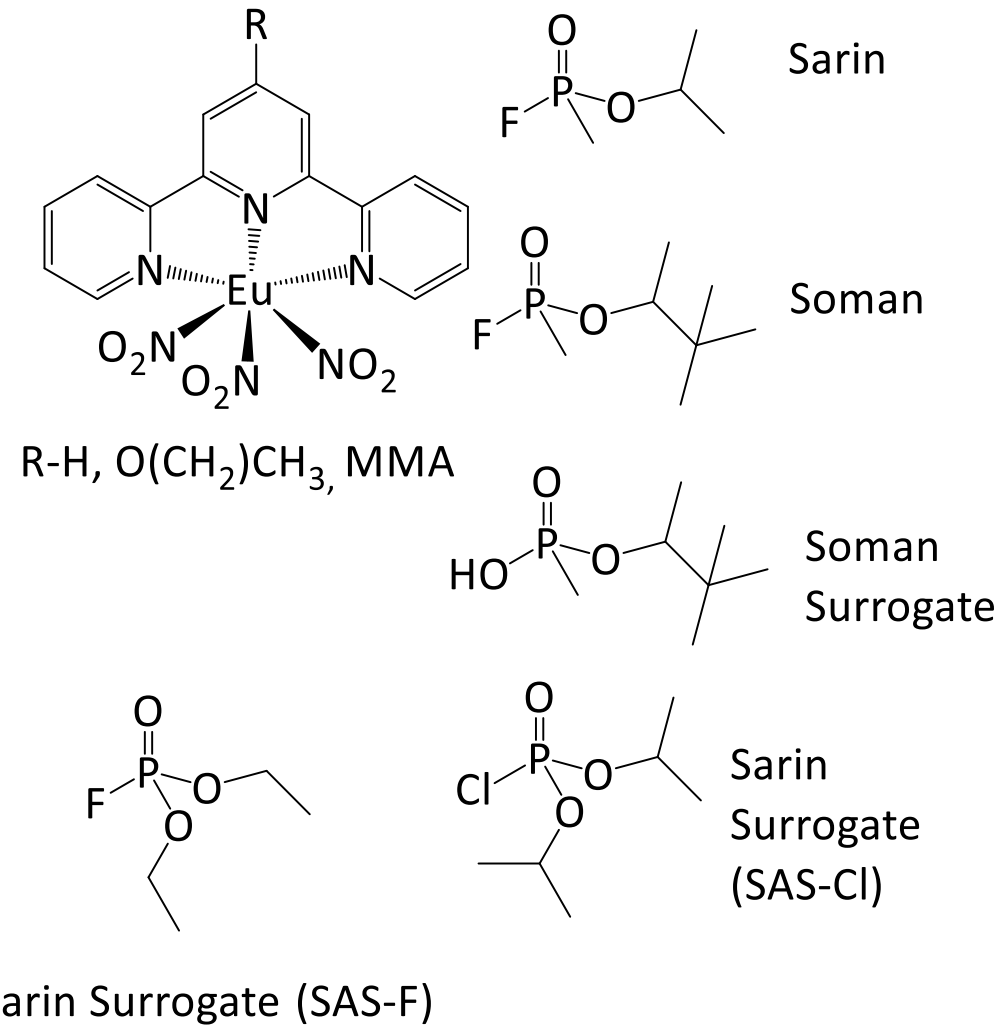

Figure 1.6- The lanthanide system developed by Tew et al. for sensing Sarin agents in the fight to detect chemical warfare agents.[70]

The detection of nerve gas agent surrogates has been reported by Tew *et al*. (*figure 1.6*).[70,71] They have designed a lanthanide complex with terpyridine to detect V-type and G-Type agents, which can be distinguished from other common organophosphates found in pesticides. Another biological warfare agent sensor has been produced by Ai *et al.*[72] A lanthanide complex to detect the presence of calcium dipicolinate. Calcium dipicolinate is present in the anthrax bacterium, *B.anthracis.* The project was to design a new europium based sensor, which would improve its luminescence characteristics upon binding to calcium dipicolinate. Terbium based sensors have already been produced and are used in current detection methods.[73-76] However using the europium lanthanide shows greater potential in detection due to a larger Stokes shift in emission spectra, exclusion of second-order scattering interference at the maximum fluorescence intensity and reduced false positive results arising from the use of aromatic groups with Tb. With the advantages of europium in place, the detection limits of lanthanide based sensors can be improved, detecting lower quantities of analytes like calcium dipicolinate.

The use of lanthanides for the detection of cations[77] or anions has not only been limited to mononuclear complexes. Dinuclear complexes have been studied and shown to improve the stability of the probe, but also provide different photophysical properties when compared to their mononuclear analogs. Morrow *et al*.[78] developed a heterodinuclear macrocycle complex to show luminescence with different biologically relevant anions. The luminescence was observed by the displacement of water molecules coordinated to the lanthanide ion, which upon removal of the high vibrational molecules allowed luminescence to facilitate a

measurable outcome. Luminescent Resonance Energy Transfer (LRET) was used to characterise the type of anion binding.

LRET which is analogues to Fluorescent Resonance Energy Transfer (FRET) has been used in many systems depicted by Foster in 1959[79] that involves both an acceptor molecule and a donor molecule, in which the donor molecules transfers energy to the acceptor molecule through a non-radiative dipole-dipole interaction through, in which the emission band of the donor overlaps with absorbance band of the acceptor. This will only occur if molecules are within nanometres of one another. This can work to both enhance luminescence and quench luminescence, depending on the system involved.

Lanthanide luminescence has been studied in solution and on the surface of materials, another approach commonly used is to incorporate lanthanides into sol-gels for the use of their optical properties. The sol-gel is a composite that starts as a solution and a precursor for the formation of an integrated network. Sol-gels have very defined parameters and are very sensitive to surrounding conditions. Armelao *et al.*[80,81] incorporated europium, terbium and carbazole derivatives into a silica layer with an acid. They found that by varying the concentrations of the sol-gel components and the excitation wavelength they could fine tune the emission wavelength and even produce white light, showing great promise for optical application. Minoofar *et al.*[82] found that it was possible to localise two different lanthanides in the sol-gel, although limited by concentration of the dopant, they showed that it was possible to use lathanides to produce thin films of variable emissive properties. Variations of complexed lanthanides in sol-gels have been tried and it has been shown that ligands like

dibenzoylmethane (DBM) and 1,10-phenanthroline are more desirable sensitisers in silica than polyvinyl butyral (PVB).[83] Other approaches have varied the concentration of the luminescent dopant and the exciting radiation wavelength to affect the colour of the sol-gel glass, and thus control emission properties.[84]

Turel *et al.*[85] developed a new optical luminescent-lifetime pH sensor based on a sol–gel doped with europium (III) chelate. Eu^{3+} complex and bromothymol blue (BTB) - were co-immobilized within a sol–gel layer under acidic conditions on a glass support, providing a pH-sensitive layer with decay times in the microsecond range. Eu^{3+} complex was entrapped in a sol–gel, preventing any leaching from occurring. The sensor also showed reproducible results and had high photostability. The sol–gel polymer showed good mechanical stability for the sensor layer, adequate ion permeability and excellent optical transparency. The sensor was developed from previous work which demonstrated that by varying the pH, the pH indicator (BTB) in a sol–gel membrane effects the emission from Eu^{3+}.[86]

Since many published luminescent sensors require high UV excitation frequencies and as a consequence more expensive light sources, the utilization of a blue LED reported in Turel's paper[85] places the pH sensor among cheaper devices. The Eu^{3+} sol–gel has an advantage in its long lifetimes (0.57 μs), wider working range (linearity spans between pH 4 and 9.5) and a neutral p*K*a value. However, the main negative aspect of the presented sensor is that it shows high dependence on the ionic strength where the sensitivity and pH of the sol-gel layer decreases with an increase of ionic strength interference from other species present in the sol-gel layer. This might possibly limit its utilization in complex media, like cell media or in

buffered solutions. Other disadvantages of using sol-gels is that the production is extremely sensitive to alcohol vapour, water humidity and acidic concentrations, all of which limit the amount of useful outcomes.

1.6 - Lanthanide Complexes on Gold Surfaces

Organic based SAMs have been studies for decades [4,6,21,87] ranging the application from molecular sensors[87] to microcontact printing[21] and various others applications discussed earlier in the introduction. It is only until recently, and more precisely since 2009 when this research had stated that the first lanthanide based self-assembled monolayer on gold had been reported.[23] Gunnlaugsson *et al.* showed that it was possible to form a SAM of thiolated lanthanide DOTA complexes on gold surfaces and used these SAM as reversible sensing platforms.

Transitions metals have been reported in the past on gold surfaces to form SAMs,[88-91] however these are typically in the field of electrochemistry[90] and solar cells,[92] studying thermodynamics[88] and redox potentials.[89] Few have been studied for the photophysical properties[91] and even less so for the potential of molecular sensors. Binnemans *et al*. did form SAMs of lanthanide based metallomesogens on the surface.[93] These metallomesogens are metal containing liquid crystals and self-assembled, aligning the liquid crystals on the surface of gold. However these SAMs were not anchored onto the surface through a covalent bond (Chemisorbed). For the purpose of this thesis SAMs are defined as chemisorbed species on the surface.

Lanthanide based SAMs do exist, Huskens *et al.* has developed a molecular printboard on silica, which shows a decrease in luminescence in the presence of dipicolinate,[18] and lanthanide based microfluidic device sensing for phosphate anions.[10] Davis *et al.* [24] has formed an organic fluorescent SAM, which does chelate a binuclear lanthanide complex, to give a pseudo lanthanide SAM which exhibit typical lanthanide emissive properties. The research that has been carried out in this thesis demonstrates the potential of anchored lanthanide complexes on gold and silica surfaces, and their potential to be used as stand- alone molecular sensors.

Although research on sensing capable lanthanide complexes on planar silica and gold surfaces is limited, the work done with gold[94-96] and silica[97-99] nanoparticles is more substantial. Gunnglasson *et al.* has developed DOTA chelating ligand with a thiol functional group and twelve carbon long linker. The complex showed self-assembly around nanoparticle through bright europium emission while in the presence of compound 2 (*figure 1.7*), and then luminescence switching off upon displacement of compound 2 by biologically relevant phosphate anion flavin monophosphate, compound 3.[20]

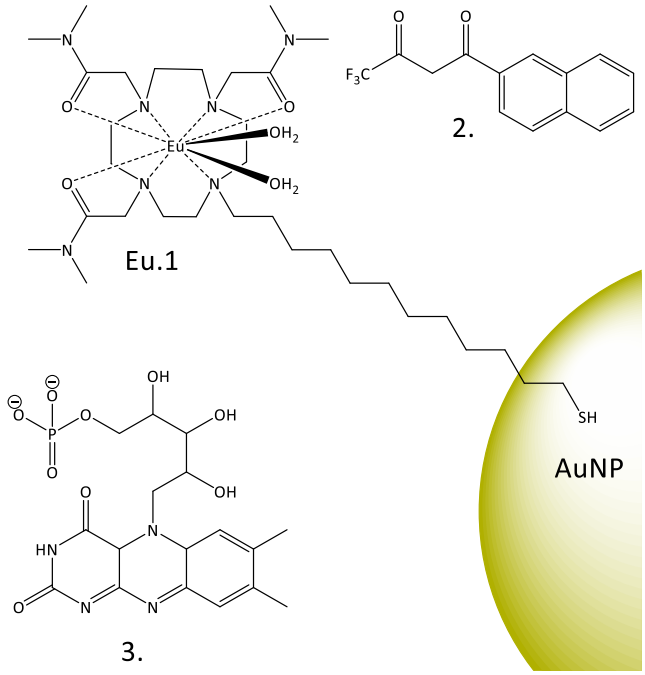

Figure 1.7- Phosphate anion sensor using europium complex functionalised on gold nanoparticles

Pikramenou *et al.* has taken DTPA-Bisamide derivatives and attached them to nanoparticles (*figure 1.8*).

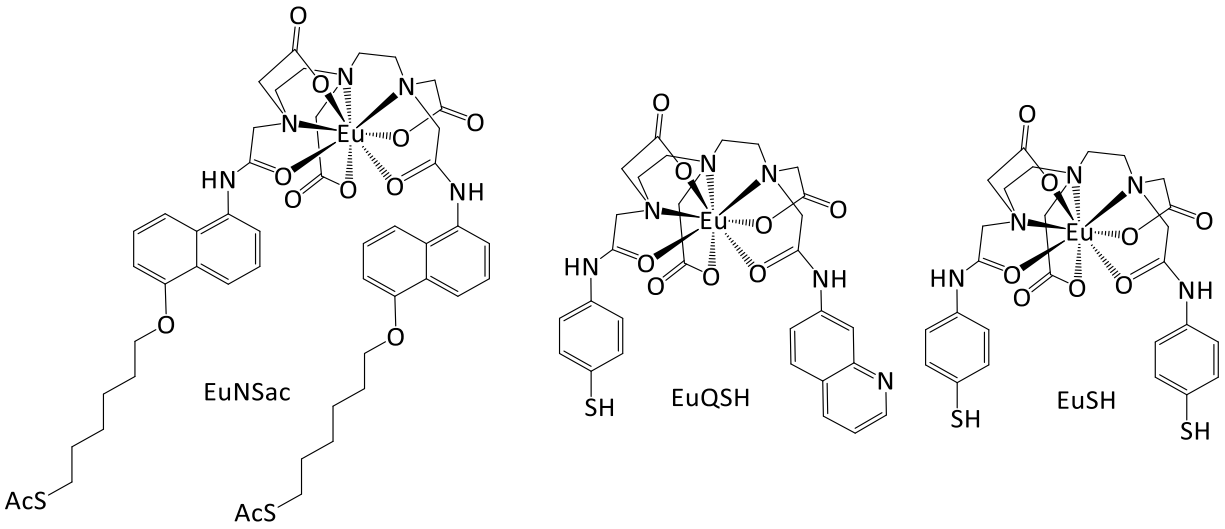

Figure 1.8 - Previous Eu DTPA-Bisamide complex developed by Pikramenou et al. for gold nanoparticle attachement.

Through thiol and thioacetyl functionalization of these europium complexes the group was able to attach these compounds on gold nanoparticles of various sizes and observe luminescence. A. Savage *et al*. coated gold nanoparticles with cell targeting peptides showing that they could bind to lanthanides and observe lanthanide luminescence.[100] S. Hammond *et al*. used EuNSac and attached the complex to nanoparticles and studied the compound in flow environments.[101] A.Davis *et al* used EuL (*figure 1*) attached to nanoparticles, co-coated with pH low insertion peptide (pHLIP). pHLIP is a peptide that transgresses across cellular membranes at low pH (pH 6.5 rather than physiological pH 7.4). With the dual coated nanoparticle, both pHILP and EuL they observed that with the pHLIP present the nanoparticle was able penetrate the cell membrane of the human platelets and observe luminescence. [102]

1.7 - Thesis Outline

There is great potential to use SAMs formed of photoactive lanthanide complexes on both silica and gold surfaces. This thesis aims to produce highly sensitive SAMs composed of lanthanide complexes and to test the viability of these SAMs to sense with simple aromatic acids, both in visible and near infra-red spectrum. In Chapter 2 we aim to synthesise a non-absorbing lanthanide complex and test it for its binding potential in solution and on the surface, demonstrating an off-on approach to molecular sensing on a SAM surface consisting lanthanide formed SAMs. In Chapter 2 we also aim to produce a negatively charged non-absorbing complex, and test its capabilities for simple aromatics in solution and on the surface and also test for its sensing capacity for positively charged species. In Chapter 3 we aim to synthesise an absorbing lanthanide complex in order to increase the amount of water exclusion, and aim to increase the luminescence with analyte binding increase light harvesting potential of SAMs, and thus the luminescence. In Chapter 4 we aim to show how SAM formation on silica differs from gold, how optical transparency of the substrate can hinder the lanthanide system and enhance it, as well contrast the surfaces behaviour with a nanoparticle system, in which we show that it is possible to sense in *situ* under flow conditions, using lanthanide silica nanoparticles. The silica nanoparticles was also developed further to show the benefits of lanthanide-transition metal bimodal nanoparticles. In the final Chapter 5 we aim to analyse SAM formation of these compounds on gold through analysis of ellipsometry and SPR we can observe and compare various europium complex binding to the surface over time.

2 - Lanthanide complexes without absorbing chromophores on gold

2.1 - Introduction

There are many stimuli that can be monitored by observing the change in luminescence, such as light[103], ions[104], analytes[105], and acidity[42]. Many life processes and biological functions rely on signals that are essentially a yes or no answer, or an "on- off" state. Research has led us to mimic these natural events through the creation of luminescent switches[106], sensors[107] and logic gates.[108-110] Lanthanide luminescent switches have been particularly useful when dealing with dipicolinic acid (DPA), a unique biomarker for the detection of anthrax spores. DPA accounts for about 10-15% of the dry weight of the anthrax spores, and isn't present in other common spores like pollen or mold spores.[72] Lu *et al*[72] reports a europium based system that was able to achieve rapid and extremely low LOD of 0.2 nM in 2 minutes, which is six orders of magnitude lower than the infectious dose of anthrax spores.

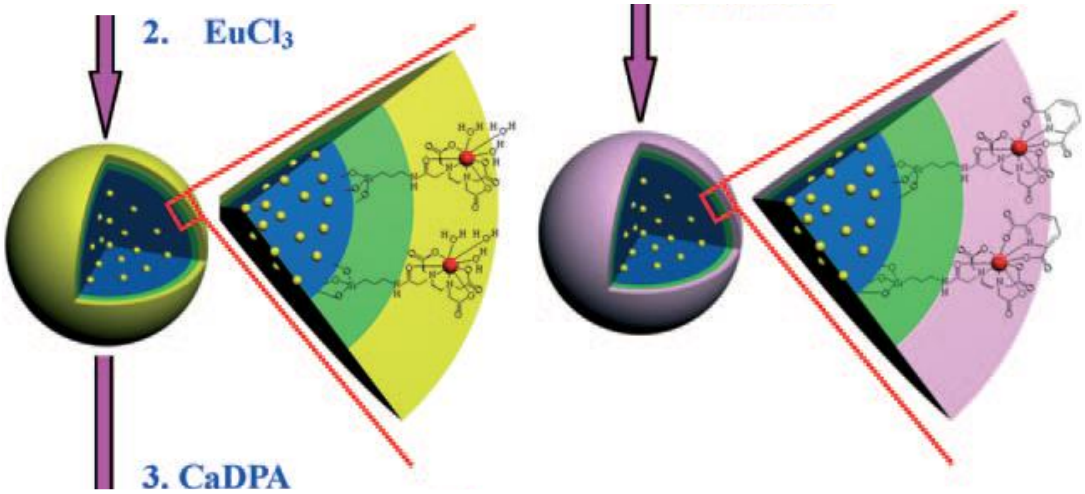

Schematic 2.0 -Here is the formation of the silica nanoparticles coated by europium NAL.[72]

The EuNAL produced by Lu *et al*. was attached to FITC doped silica nanoparticles through an APTES (aminopropyltriethoxysilane) linker protruding to the outside of the nanoparticle, and when exposed to a solution of EDTA dianhydride, the outer shell formed a chelating ligand for europium. Thus when exposed to a europium salt, the nanoparticles formed EuNAL. Without the presence of DPA the system showed luminescent activity only from the FITC dye, evident by a clear green solution, but when DPA was present the dominant luminescent signal came from the europium. The group compared the EuNAL on SiNP in the presence of DPA against free europium and DPA. The finding was that the intensity of the EuNAL in SiNP was 33-fold more intense than just europium and DPA. Thus having a scaffold from the EDTA and a SiNP showed luminescent enhancement and a more sensitive LOD. They also compared the sensitivity of the system with other simple aromatics acids such as benzoic, ortho-phthalic and meta-phthalic acid, resulting in very high selectivity for DPA.

Lanthanide complexes as SAMs on gold were first reported by Gunnlaugsson *et al*.[23] The group reported the formation of a luminescent self-assembled monolayer, with the ability to have a reversible europium emission "off-on" state. They demonstrated the ability to bind europium complexes to a gold surface using long alkyl thiol, forming a SAM at the gold interface, and upon binding of sensitizer the lanthanide luminescence was "switched on". Gunnlaugsson *et al*. uses a DOTA derivative to chelate the lanthanide, and whilst in the presence of a methyl-flurоinated β-diketonate naphthalene derivative the luminescence of the europium is switched on. The "switched off" state occurs when the sensitiser is displaced through competitive binding, by flavin, which lacks the ability to efficiently sensitise the europium. It

has been reported that gold quenches lanthanide luminescence[111], and that the amount of quenching is distance dependant, thus a long alkyl chain in the linker unit binding with the gold surface was chosen in their design (*figure 2.0*).

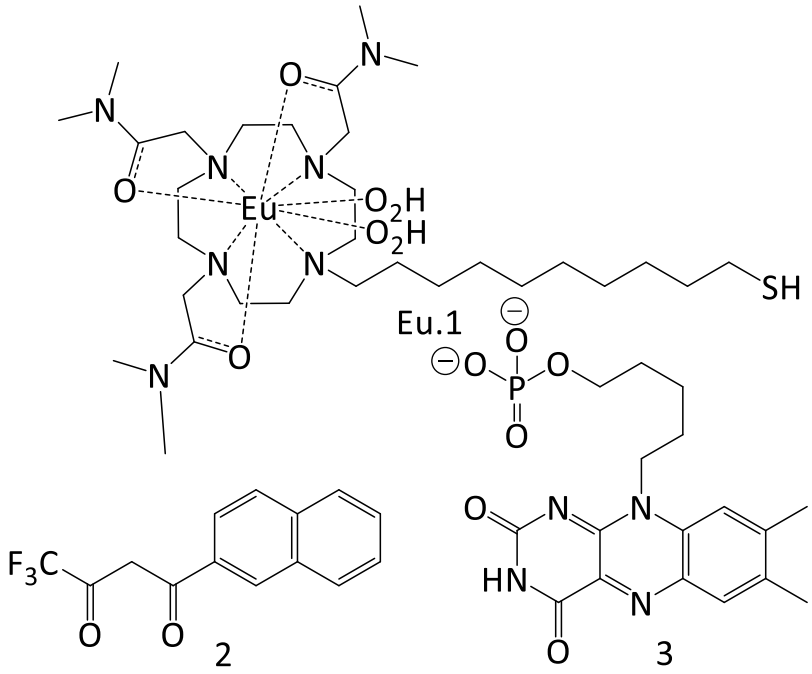

Figure 2.0 – Eu.1-Europium DOTA complex, 2-sensitizer(on sensitiser), 3-anion (competitive inhibitor).[111]

Using emission spectroscopy, the group showed that the europium complex on its own had no emission upon excitation of UV radiation at 280 nm. With the sensitizer present the europium complex showed intense emission bands, indicating successful population of the $^5D_0$, Eu^{+3} excited state. To investigate the sensitisation of the "on-state" further, the excitation wavelength was varied and displayed predicted emission lines with the addition of a line corresponding to second order scattering.

To confirm the presence of SAM's "off-state", the surface emission was investigated and showed only a small amount of emission intensity from the surface, thus indicating that the anion was coordinated to the Eu^{3+} ion but lacked the ability to absorb and transfer energy to the europium's excited state. If the anion wasn't bound then there would be no emission detected. The evolution of europium emission was then monitored by two methods. The first was by forming a SAM of the europium complex in solution of the sensitizers over set periods of time and recording the SAM emission. Results showed that the SAM was fully formed and "switched on" within 1 hour.

The stability of the europium complex and the "on-state" was also examined. The "on-state" was stored in a solution containing no sensitizer for 24 hrs and showed that the emission intensity was reduced by almost 85%; the intensity was almost completely recoverable once re-immersed in a solution of sensitizer **2**. The group theorised that the SAM undergoes reorganisation in the absence of sensitizer **2**, facilitating quenching by the gold surface. Dehydration of the SAM with air also showed significant quenching, but the luminescence could also be switched back on upon submersion in sensitizer solution. Exposing a sample of the "on-state" SAM to the anion **3**, showed that the europium signal was rapidly quenched, and indicating that the anion binds more strongly than the sensitizer, turning the SAM into the "off-state".

2.1.1 - Diethylenetriaminetetraacetic Acid Bisamides as Non-Absorbing Ligands

Previous research in the Pikramenou group had isolated modified DTPA ligands without the presence of a chromophore, and thus forming non-absorbing ligands (NAL).[64] The NAL ligands synthesised showed octadentate binding to lanthanides. When binding these NAL to lanthanides, the chelating nature of the eight coordinate ligand results in the exclusion of eight pre-existing coordinating ligands. In an aqueous environment these are usually water molecules. Water molecules quench europium emission due to similar energy levels in the emissive states of europium and the vibrational overtones of O-H bonds. The vibrational overtones are close enough in energy to provide a preferred relaxation pathway for the molecule to relax back to the ground state, thus no radiative energy is evident as emission.

The purpose of using eight coordinate ligands is to form strong binding interactions between the lanthanide and the NAL, (log K = ~10^{20}),[60] and as lanthanides can accommodate up to 12 coordination sites, it leaves up to two sites available for further binding opportunities or solvation. In addition to having a strong binding affinity for lanthanides, the NALs have a hydrophobic design, promoting the exclusion of water and thus reducing any additional quenching from the water. When binding LnNAL with analytes containing a chromophore, the resultant effect shows a dramatic enhancement of lanthanide luminescence, acting as a “light-switch” for detection. Using Chromophores to absorb light and channel it’s energy to lanthanide ions is known as the “antenna effect”.

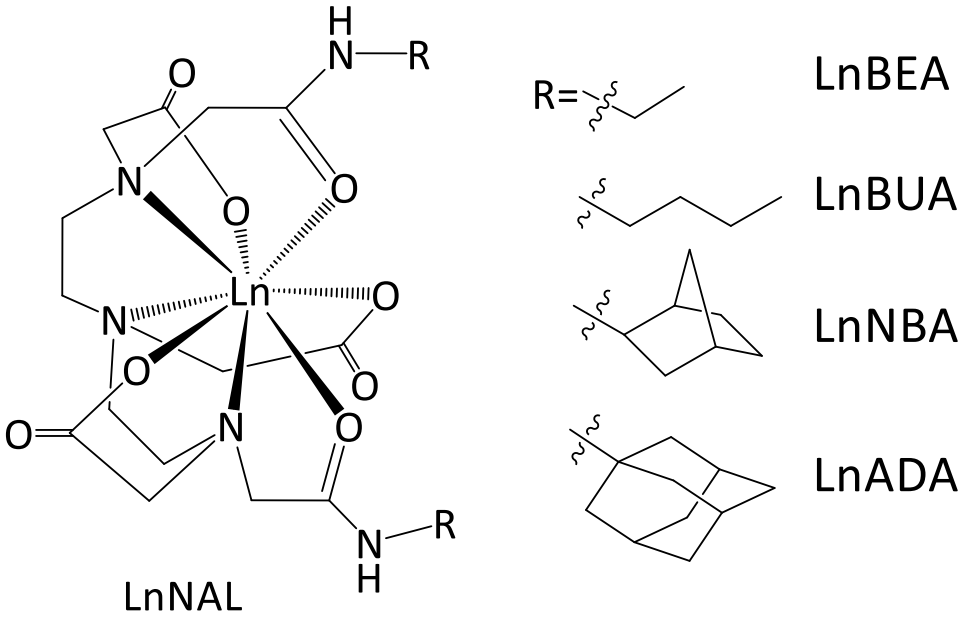

Figure 2.1-Chemical structure of NALs explore in Ruston et al research.[64]

The research further developed through the modification of NAL compounds by modifying the two amide arms to incorporate sterically hindering groups varying in their capacity to exclude water coordination, to limit quenching by water molecules (*figure 2.1*). We compared how the modified NALs improved detection with an assortment of small aromatic acids; Benzoic acid, phthalic, iosphthalic, picolinic acid and dipicolinic acid. The hydrophobic nature of the bisamides arms was increased by changing chain length and arm bulkiness. All arms were aliphatic in nature. Results showed that there was a clear relationship between the hydrophobicity of the LnNAL and the luminescence intensity produced from LnNAL with coordinated aromatic acids. The research was confirmed by using modified simple aromatic acids and investigating the difference in luminescent intensity caused by modification of hydrophobicity in the analyte. These analytes were simple aromatic acids that were varied to incorporate the same changes as the NAL ligands themselves evaluating the hydrophobicity,

sterics interactions and coordinative nature of the ternary system. The results agreed with previous results indicating that ligands which contained the most sterically hindering bisamide arms, provided the most enhanced lanthanide emission whilst in the presence of a simple aromatic acid. Similarly analytes which contained a sterically hindering group and a hydrophobic tail lead to the most enhanced lanthanide emission whilst bound to LnNAL. This was mainly attributed to the exclusion of water provided by the additional hydrophobicity and sterics of the system preventing the water molecules from entering the inner core coordination sphere of the complex and quenching the lanthanide emission.

Whilst simple aromatics are good absorbers of UV light, moving into molecules which can absorb further into the visible spectrum is advantageous in both biological work and device fabrication. Where in biology cells are more readily damaged using UV light, in device fabrication glass optics deliver an absorption barrier of anything below 350 nm. Ternary complex formation is formed between the LnNAL and the analyte, with the analyte binding between the two bis-amide arms because this is sterically the most favourable.

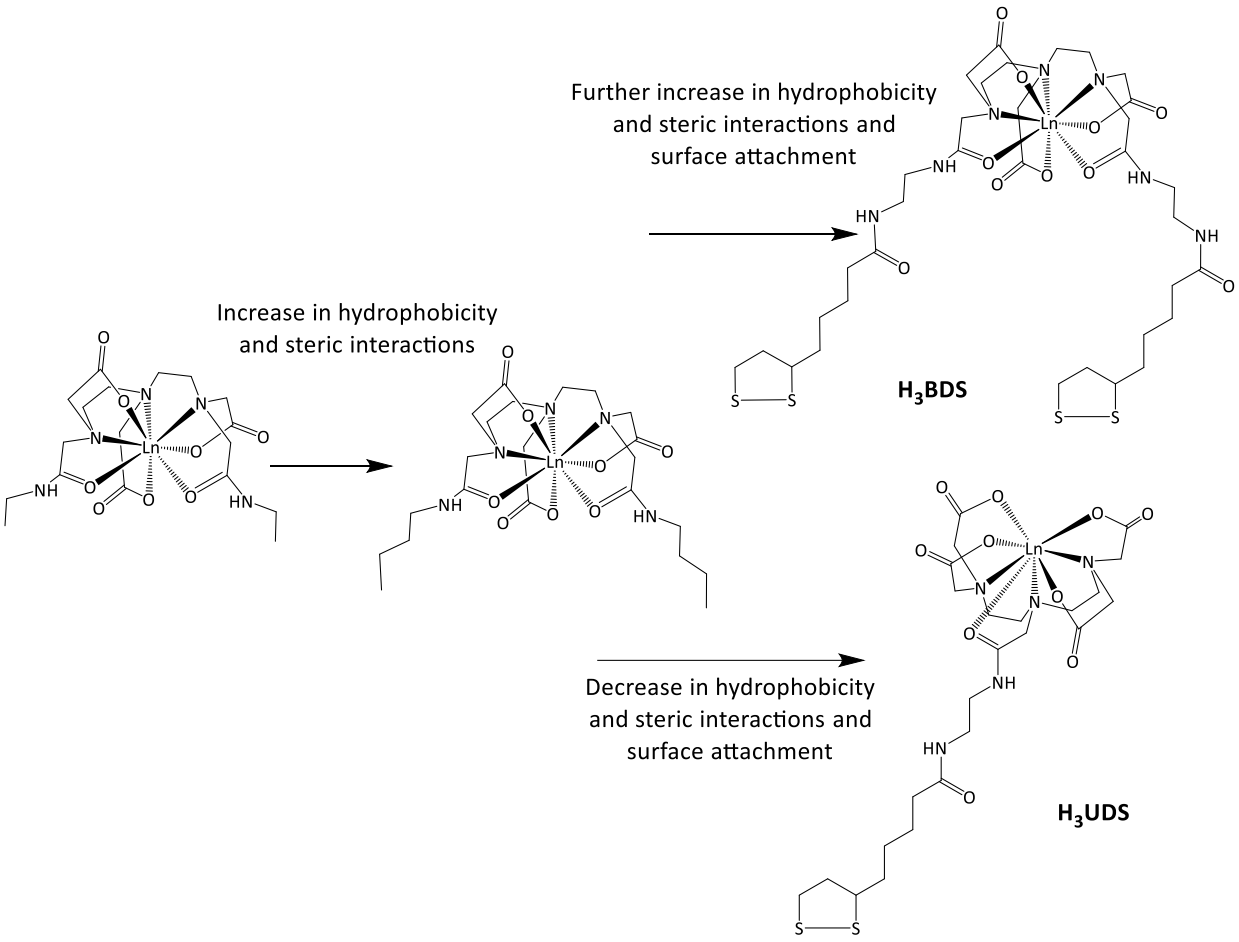

Schematic 2.0- Showing the development DTPA-Bisamide lanthanide complexes to surface active DTPA-Bisamide lanthanide complexes, H_3BDS (top-right) and H_3UDS (bottom-right).

The design of surface binding compounds was largely based on previous research in the group (*Schematic 2.0*), enabling a functionalised surface to be developed and novel screening platforms to be produced; the idea being that screening on a surface can be very different than screening in solution. Having a planar surface and surface attachment allows for the development of devices similar to lab-on chip systems and gives advantages such as regenerative possibilities of the device, saving in costs. Making a device regenerative allows for an easier use for a mobile user, e.g. field operatives in the military, having one chip and

using it repeatedly is more efficient than carrying a one use vial of solution of the sensing system. In contrast, complexes could be used to attach to the surface of nanoparticles allowing a local point scaffold of high concentration, and multiple coatings for multiple combinatorial effects, allowing more data to be extracted. However this removes the ability to be effectively regenerated, providing more waste material and greater expense.

2.1.2 - Ligand Design of H_3BDS and H_3UBS

We have utilised the unique photophysical properties of the lanthanides to aid in the detection of various molecules by incorporating lanthanides into our ligand design. Here we have synthesised **H_3BDS** and **H_3UBS** as NALs for lanthanides chelation without incorporating the aid of chromophores in the ligand design. The NAL choice here allows lanthanide luminescence to be "switched on" in the presence of analyte binding. With the ligand architecture designed to accommodate lanthanides and with octadentate chelation from the ligands, it leaves two potential binding sites available for analyte recognition. The analytes must contain a chromophore for lanthanides to luminesce; in effect a "light-switch" to indicate detection. These chromophores are typically aromatics and are generally good absorbers of UV and visible light.

Chromophoric analyte detection narrows the selectivity of potential analytes down. Each lanthanide has a definitive emissive state. These emissive states are Laporte forbidden, making transition to a lower laying state through a photonic pathway inefficient. Thus we utilise the energy harvested from the chromophore's triplet state to increase the population

of the emissive states. However not every chromophore will activate the lanthanides luminescence. The chromophore will need to have a greater triplet state than the lanthanides emissive state, but not too great to induce phosphorescence of the chromophore as the dominant pathway.

By designing surface bound compounds and attaching them onto the surface, we can use the SAM as devices and directly excite the surface for analyte presence. When the lanthanide system and the analyte bind it is known as a ternary complex and it is to be noted that on surfaces, ternary complex formation can be very different than that in solution. The most obvious point of binding for the analyte is the major site; between the two bis-amide arms, because this is the most sterically favourable location to bind. The major binding site is less freely available on the surface than it is in solution, due to the pseudo macrocycle formed on the surface, which would prevent the coordination of larger molecules.

There are two significant ligand design differences between **H_3UDS** and **H_3BDS.** The first is the modification of the surface attachment. **H_3UDS** has one disulphide functional group for attachment to gold and **H_3BDS** has two disulphides. Secondly is the ligand architecture: **H_3UDS** has a single 10 carbon alkyl chain between the surface attachment and the lanthanide binding site, attaching directly to DTPA backbone, causing the lanthanide ion to face outwards, facilitating greater lanthanide exposure and binding potential. **H_3BDS** has two 10 alky chains between the surface and the lanthanide binding site creating greater structural rigidity and a pseudo macrocycle between **H_3BDS** and the gold surface. The pseudo macrocycle between

the surface and **EuBDS** is still going to cause a restriction on the size of the binding analyte. This restriction makes the system more specific, removing any competitive binding occurring from larger undesirable analytes in a screening process. The long chain between the surface and lanthanide binding site would also remove any possible quenching effects the might occur from the gold surface.

2.2 - Results and discussion

2.2.1 - Characterisation of H_3BDS

H_3BDS was synthesised from a 3 step protocol, starting with the peptide bond formation between thiotic acid and excess ethylene diamine (*figure 2.2*). Excess ethylene diamine was used to reduce the potential of by-product formation; a bis-amide dithioctic acid compound forming.

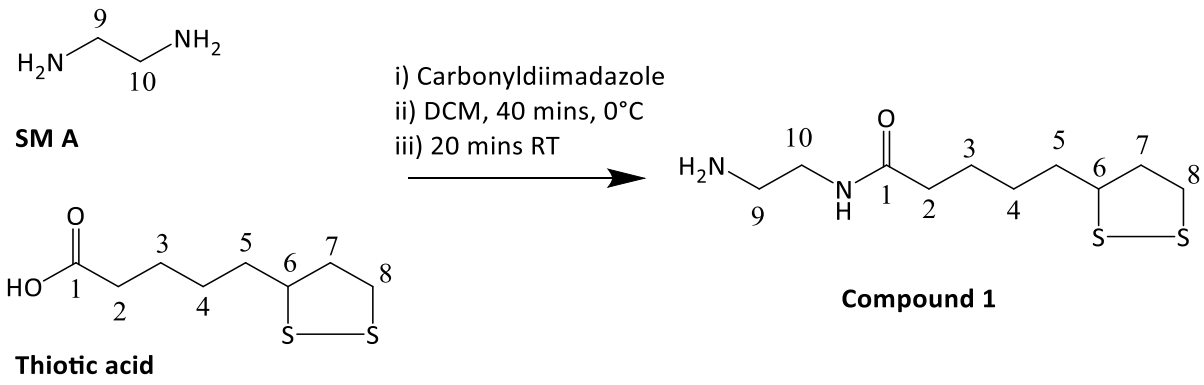

Figure 2.2 - Synthesis of Compound 1.

The ^{1}H-NMR spectrum of thioctic acid showed characteristic peaks in the aliphatic region, which translated into the ^{1}H-NMR spectrum of N-(2-aminoethyl)-5-(1,2-dithiolan-3-

yl)pentanamide here by referred as **Compound 1** (*figure 2.3*). The disappearance of the hydroxyl peak from thioctic acid (11 ppm) and the shift of the amine hydride peak (1.1 ppm) to amide peak (7.8 ppm), in conjunction with the movement of the alpha hydrogens on the diamine (H-10) from 2.6 ppm to 3.2 ppm when peptide coupled to the thioctic acid, indicates the formation of aminoethylene lipoamide.

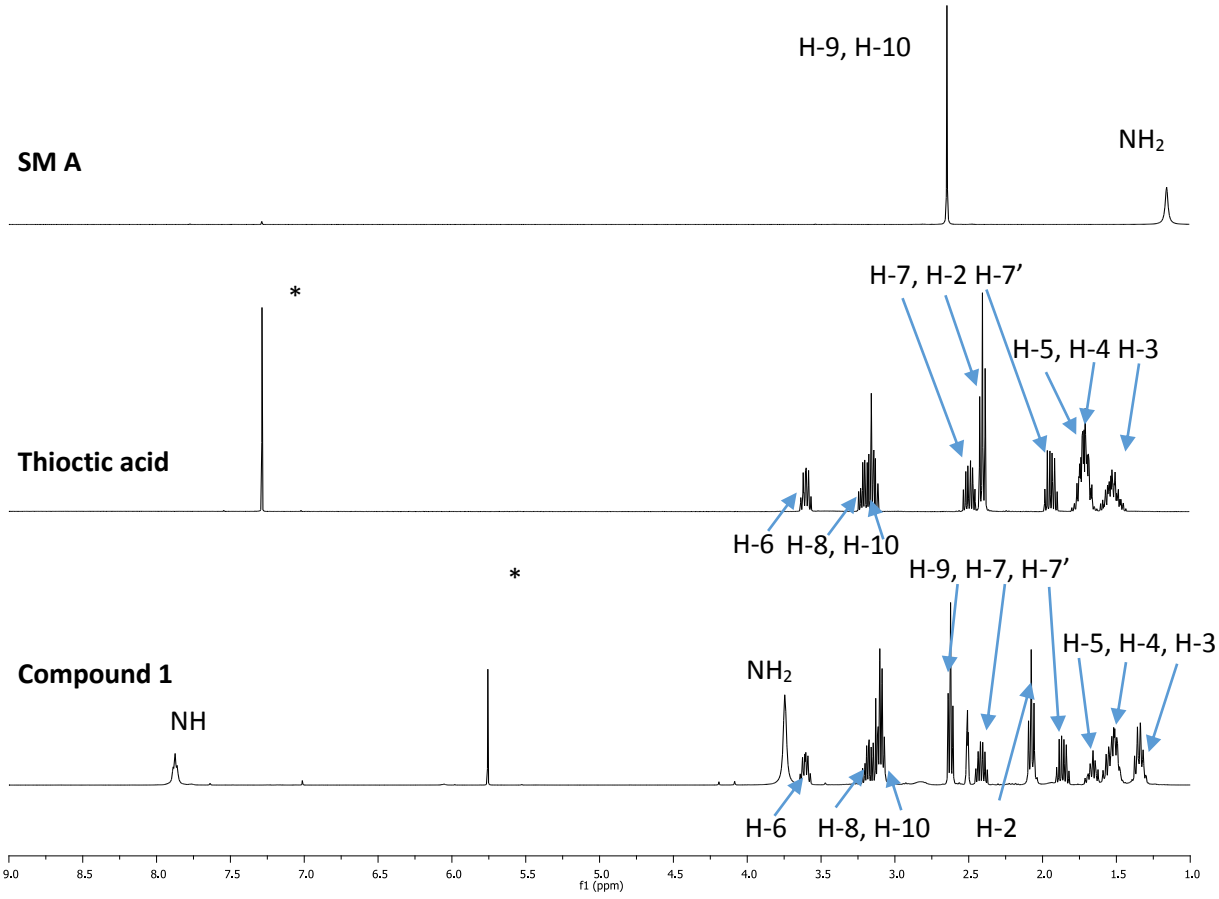

Figure 2.3- ^{1}H-NMR of SM A (Top), Thiotic acid (middle) and Compound 1 (bottom)

Furthermore the movement of H-2 in thiotic acid from 2.4 ppm to 2.1 in **Compound 1,** shows a change in proton environment due to the change in electronegativity. Being adjacent to a carboxylic acid is more electronegative than being adjacent to an amide, thus H-2 is shift up

field. The stereocentre attached to H-6 and the distereotopic hydrogens H-7, and H-8 are present in **Compound 1**.

H_3BDS has been characterised by ^{1}H-NMR spectroscopy, ^{13}C-NMR spectroscopy, mass spectrometry and elemental analysis. The aliphatic region of the ^{1}H-NMR spectrum showed the distinct resonance peaks associated with the thioctic acid, particularly the presence of the enantiomeric peaks (*figure 2.5*).

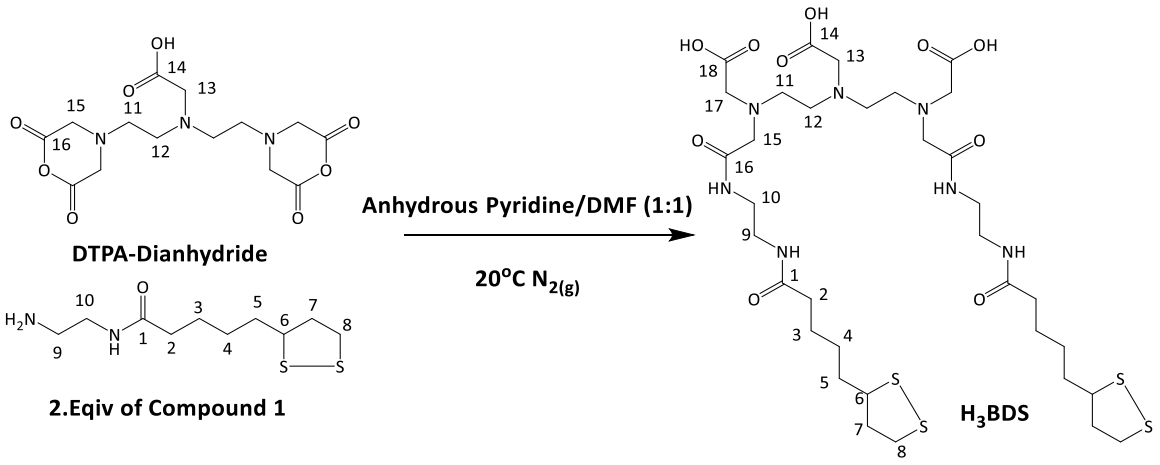

Figure 2.4- The synthesis of H_3BDS

Three additional key features in the proton NMR (*figure 2.5*) indicated that the product had been formed. The protonic environment corresponding to the primary amine, had shifted down field due an amide bond formation, now integrating for just two rather than integration of protons from the free amines. The addition of the electronegative carbonyl, de-shielding the proton, causing a greater chemical shift explaining the down field shift in the spectrum.

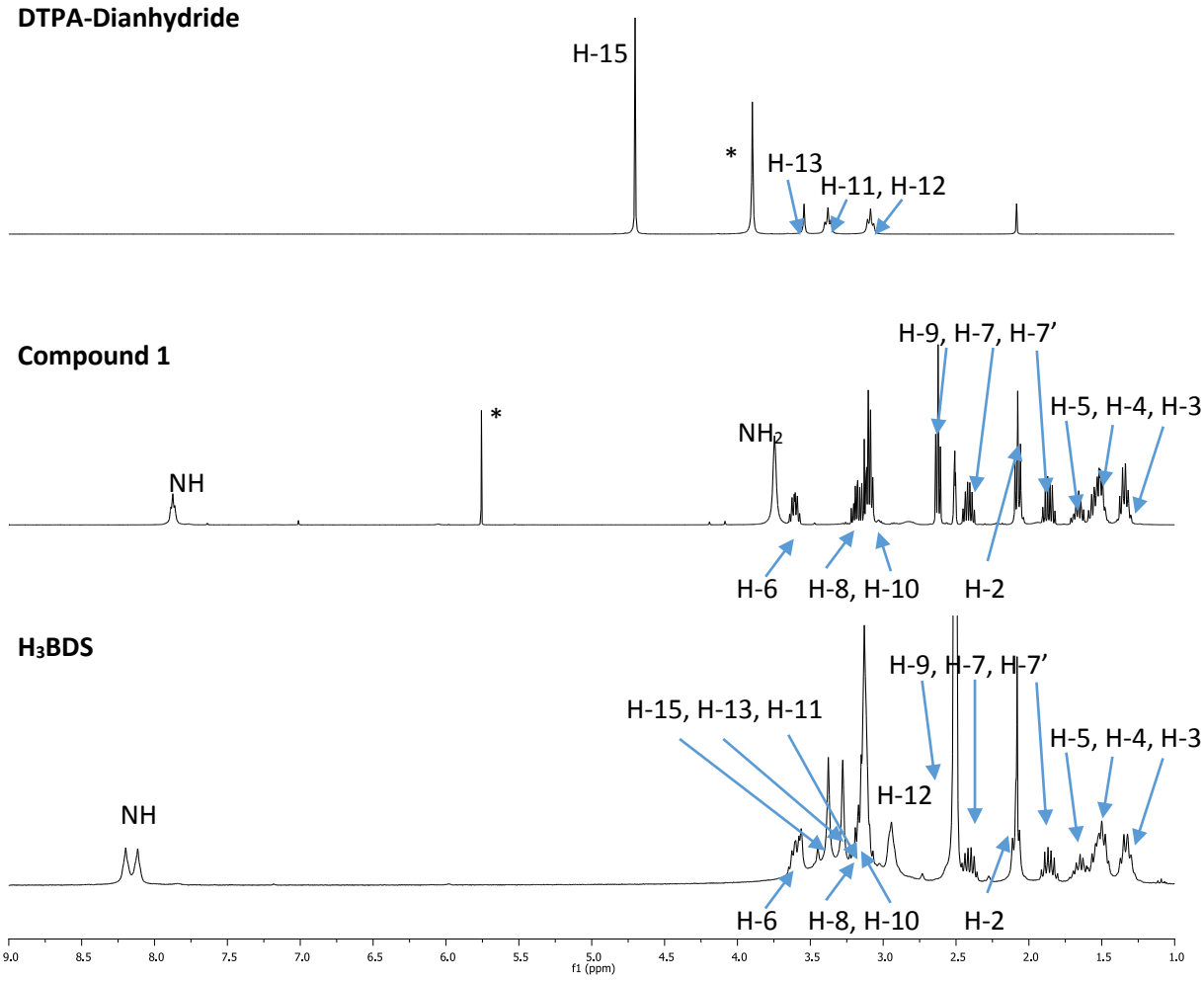

Figure 2.5-^{1}H-NMR of DTPA-Dianhydride (D_2O, Top), Compound 1($CDCl_3$, middle) and H_3BDS (bottom d_6- DMSO)

The second key attribute is the removal of the DTPA-dianhydride's symmetrical environments, creating an additional environment to represent H-15, whilst the H-13 now integrates for six protons including H-17. The final attribute is the shift of H-10 from 2.6 ppm to 3.1 ppm, due to the amide bond formation. ^{13}C-NMR spectrum shows an expected 18 resonances peaks. Mass spectrometry shows the parent peak at 854.3 m/z corresponding to the protonated product, as well as two smaller peaks at 855.3 m/z and 856.3 m/z corresponding to the thiolated derivative of **H_3BDS**.

2.2.2 - Characterisation of H_3UDS

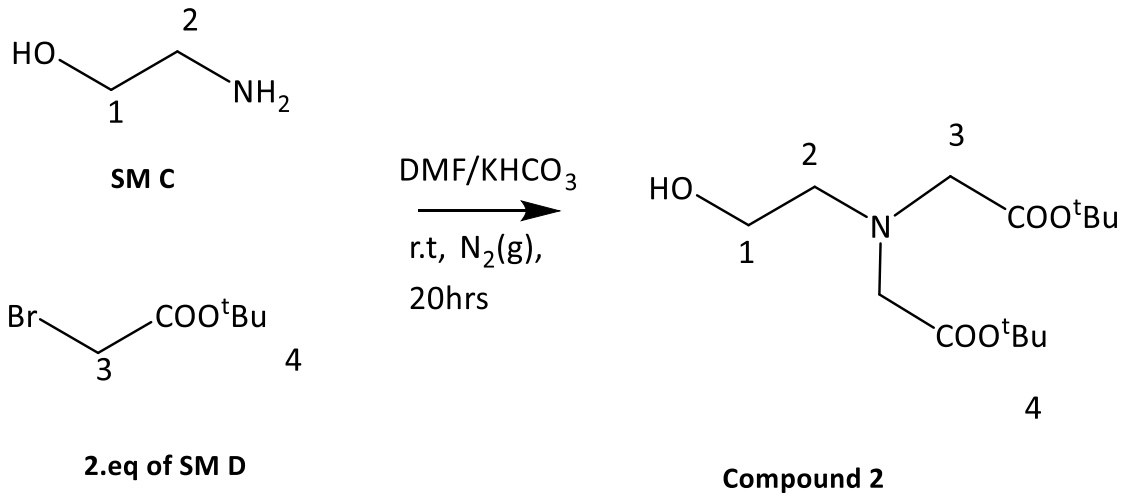

Figure 2.6 - Reaction scheme for the synthesis of Compound 2

H_3UDS was synthesised over a five step synthetic process. The synthesis of N,N-Bis[(tert-butoxycarbonyl)methyl]-2-ethanolamine (**Compound 2)** has been characterised by ^{1}H-NMR spectroscopy, ^{13}C-NMR spectroscopy and mass spectrometry and synthesised via *figure 2.6*. The ^{1}H-NMR shows the formation of **Compound 2** from starting material ethanolamine and *tert*-butyl bromoacetate (**SM C** and **SM D** resepectively)**.**

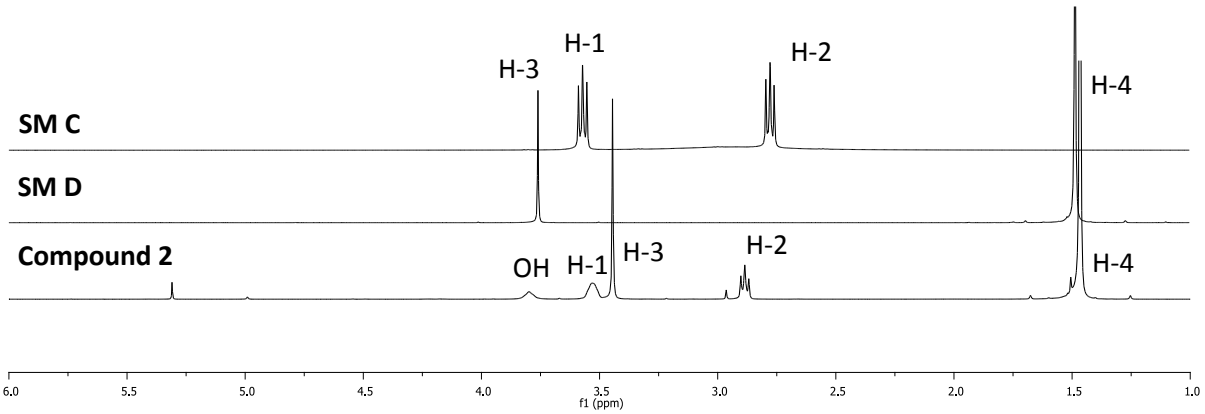

Figure 2.7- ^{1}H-NMR of SM C (top), SM D (middle) and Compound 2 (bottom)

The ^{1}H-NMRs shown by *figure 2.7* indicates the formation of **Compound 2**. The major peaks are shown by the presence of the tertiary butyl groups in **Compound 2** at 1.5 ppm from **SM D** and the triplet of H-2 is translated from **SM C** to **Compound 2** with a downfield field shift from 2.6 ppm to 2.8 ppm. H-3 has shifted up-field from 3.7 ppm to 3.4 ppm due to the reduced electronegative environment in **Compound 2** going from being adjacent to bromine to a tertiary amine.

The next reaction in the formation of **H_3UDS** was the bromination of **Compound 2** by reacting it with *N*-bromosuccinimide (NBS) and triphenylphosphine (PPh_3) in DCM.

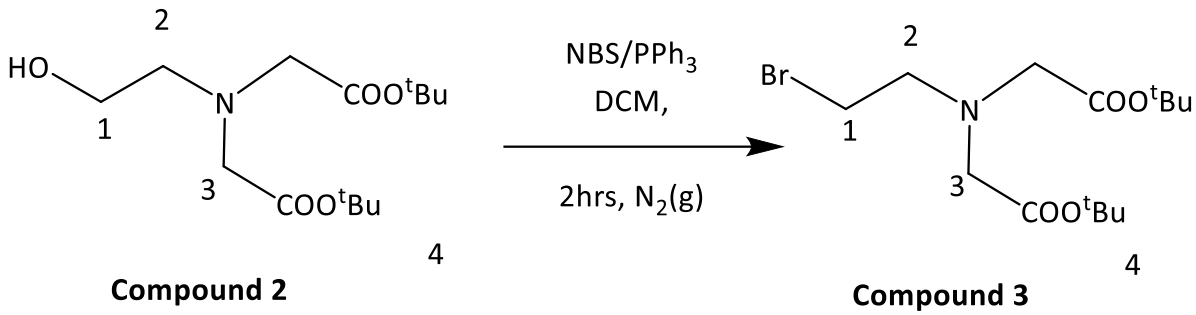

Figure 2.8- The bromination of Compound 2

The bromination of **Compound 2** has been characterised by ^{1}H-NMR spectroscopy, ^{13}C-NMR spectroscopy and mass spectrometry and synthesised via *figure 2.8*. The ^{1}H-NMR shows the formation of N,N-Bis[(tert-butoxycarbonyl)methyl]-2-bromoethylamine, **Compound 3** (*see figure 2.9*).

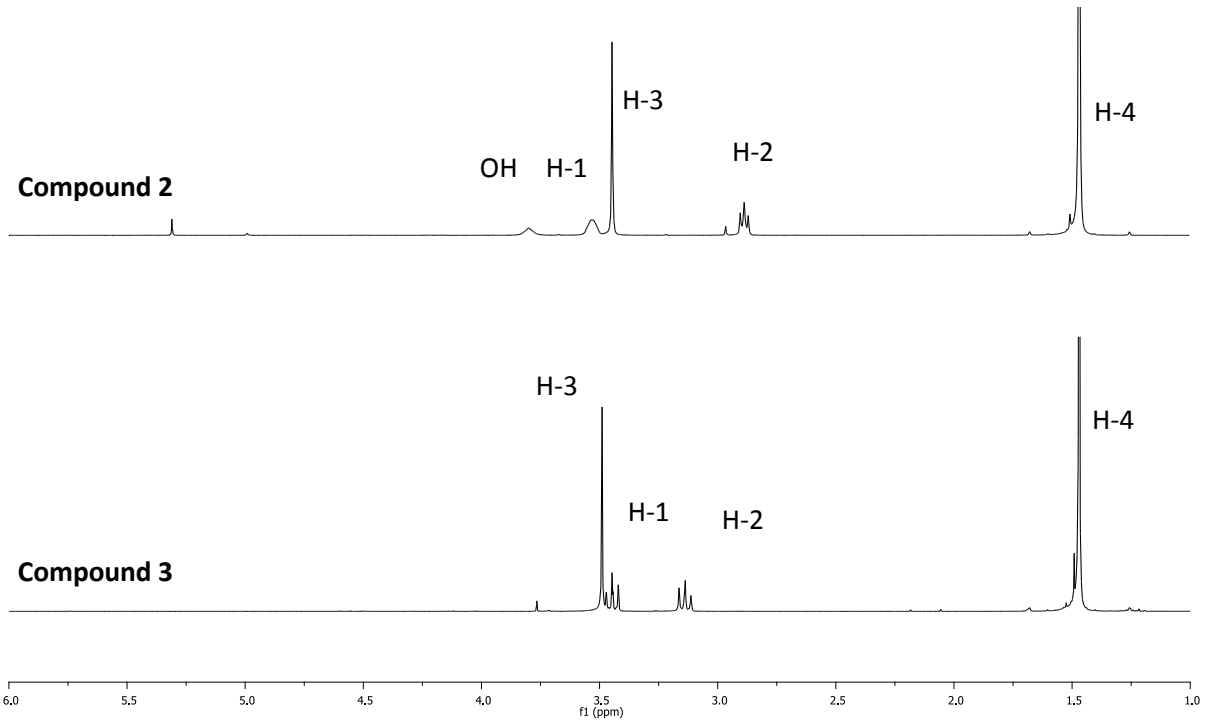

Figure 2.9- ^{1}H-NMR of Compound 2 (top) and Compound 3 (bottom)

The ^{1}H-NMR of **Compound 3** (*figure 2.9*) shows disappearance of the hydroxyl group present at 3.7 ppm in **Compound 2**. There is also an up field shift of H-1 due to the reduction of electronegativity in the hydrogen environment due to changing the adjacent atom from hydroxyl group to a bromide. The singlets from H-4 and H-3 remain relatively unchanged and present in **Compound 3**.

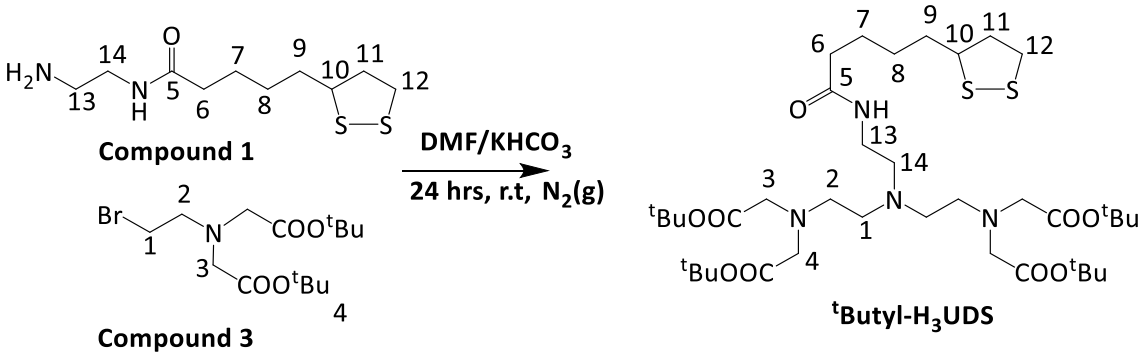

Figure *2.10*- Reaction scheme for the synthesis of ^{t}Butyl-H$_3$UDS

The formation of **^{t}Butyl-H$_3$UDS** is shown by *figure 2.11*. **Compound 1** used in the synthesis of **H$_3$BDS** was also used here as the surface attachment component of the ligand. **^{t}Butyl-H$_3$UDS** was synthesised by reacting two molecular equivalents of **Compound 3** with one molecular equivalent of **Compound 1.**

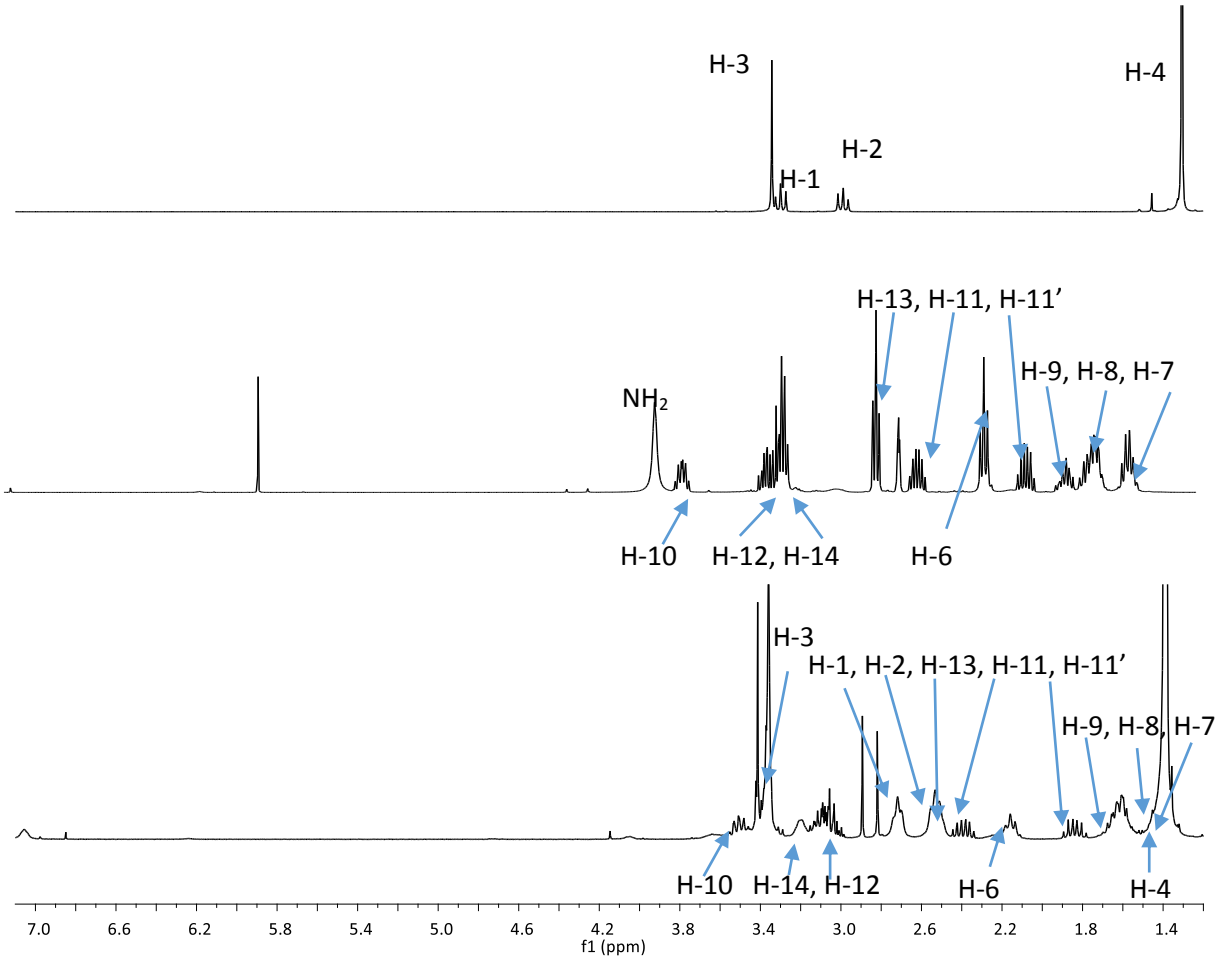

Figure 2.11 - ^{1}H-NMR of Compound 3 (top), Compound 1 (middle) and ^{t}Butyl-H$_3$UDS (bottom).

The ^{1}H-NMRs in *figure 2.11* shows the formation of **^{t}Butyl-H$_3$UDS**. The significant protonic shifts that indicate the formation of **^{t}Butyl-H$_3$UDS** is the disappearance of NH_2 peak and the

shift of protons H-1, H-2 up field due to the loss of bromine in **Compound 3** in the reaction, displaced by a nucleophilic attack from **Compound 1's** amine. Also with correct proton integration of all peaks, especially the 36:1, H-4 to H-11 ratio, and the presence of the disterotopic protons H-11 and H-11'.

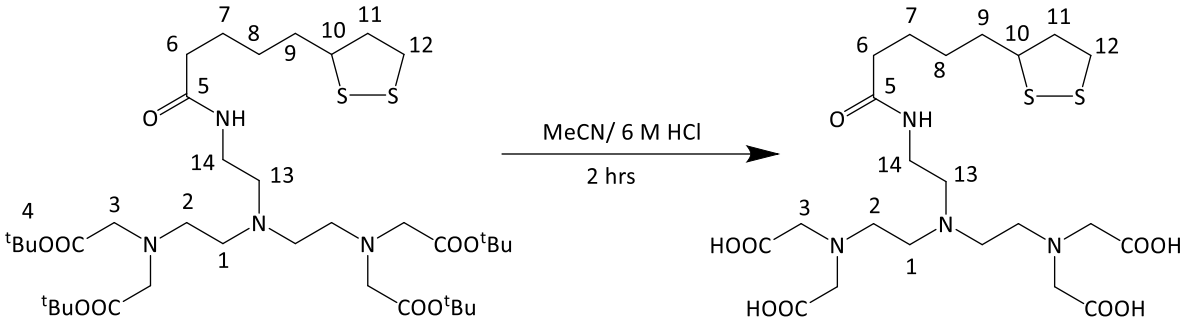

Figure 2.12 - Show the deprotection of ^{t}Butyl-H_3UDS to form H_3UDS

The removal of **^{t}Butyl-H_3UDS** carboxylic acid protecting groups was removed by treatment with 6 M hydrochloric acid in acetonitrile (*figure 2.12*). Treatment of **^{t}Butyl-H_3UDS** with trifluoric acid (TFA) in DCM for 2.5 hrs was attempted, however those conditions didn't remove the ^{t}butyl group, thus much harsher conditions were necessary. After two hours, the organic and aqueous layers were separated and organic layers was treated with saturated potassium bicarbonate and then washed with brine.

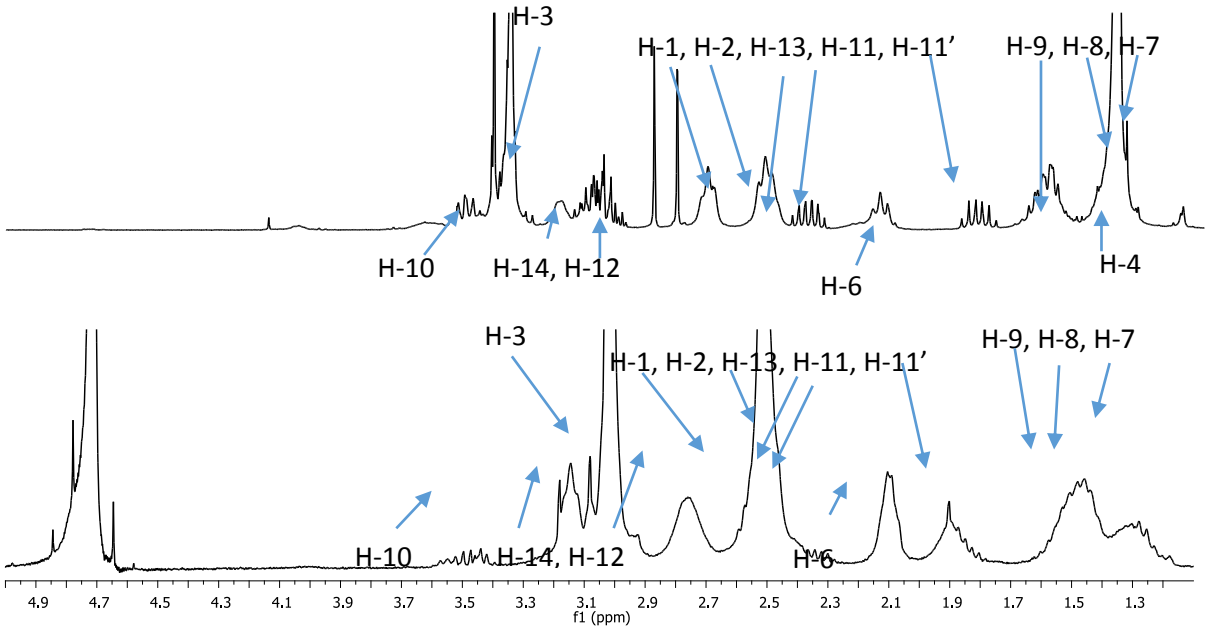

Figure 2.13 - ^{1}H-NMR of ^{t}Butyl-H$_3$UHDS (top) and H$_3$UDS (bottom)

The deprotection of **^{t}Butyl-H$_3$UDS** is shown by ^{1}H-NMR in *figure 2.13*. The **^{t}Butyl** functional group's deprotection is shown by the disappearance of H-4 in figure 13 and 14, to synthesis **H$_3$UDS.** The resultant compound left a highly charged compound, and soluble only in water, caused considerable broadening of peaks. H-1 and H-2 shift from 2.7 ppm and 2.5 ppm respectively to form one peak at 2.5 ppm. In attempts to resolve peaks, the deutrated NaOD was used and provided no distinct NMR improvement. **H$_3$UDS** was confirmed by IR, ^{13}C-NMR and HR-MS.

H_3UDS to **H_3BQUDS**

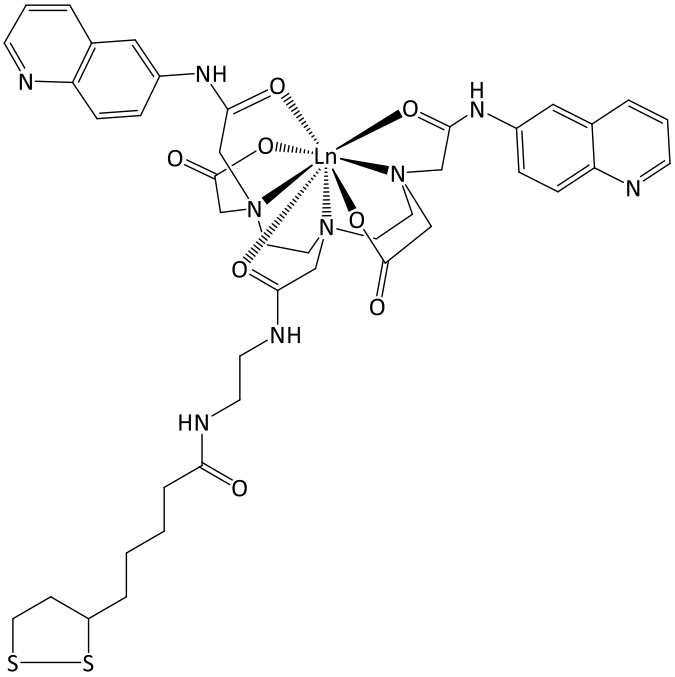

Figure 2.14- The chemical structure of H_3BQUDS

H_3UDS was also used in an attempt to synthesise a light absorbing ligand, **H_3BQUDS** (*figure 2.14*) similar to **H_3L** synthesis in Chapter 3. However the only ligands that was synthesised were NAL, which are reported here. The first route used to synthesis **H_3UDS** was attempted through the synthesis of **Compound 4**. **Compound 4** has been characterised by ^{1}H-NMR spectroscopy, ^{13}C-NMR spectroscopy and mass spectrometry and synthesised via reaction shown in *figure 2.12*.

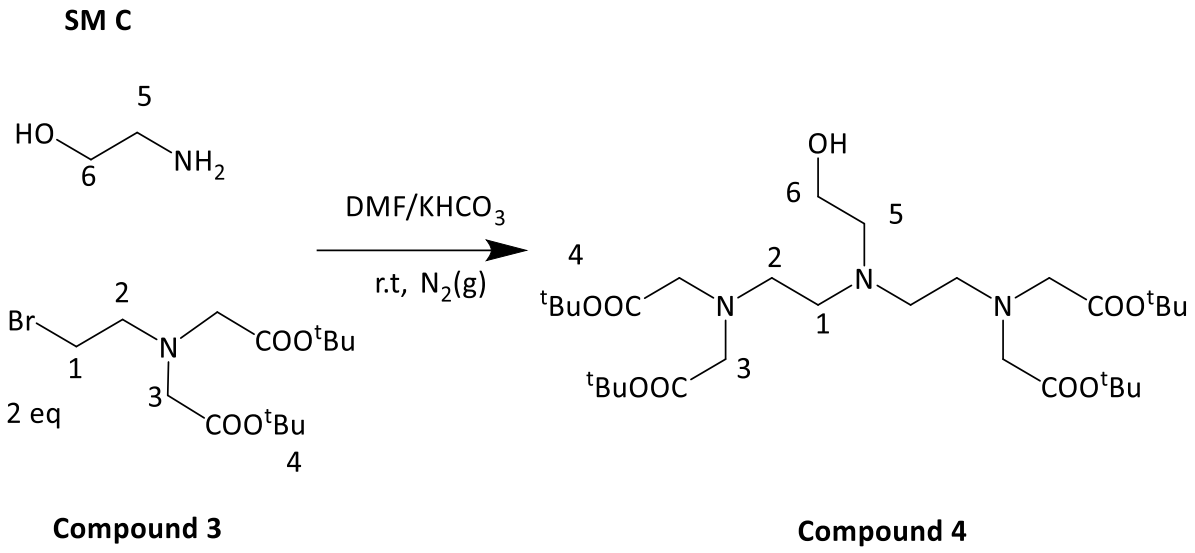

Figure 2.15 - Reaction scheme for the synthesis of Compound 4

Compound 4 was synthesised by reacting two equivalents of **Compound 3** with **SM C** (*figure 2.15)***.*** The ^{1}H-NMR shows the formation of **Compound 4. Compound 4** has been characterised by ^{1}H-NMR spectroscopy, ^{13}C-NMR spectroscopy and mass spectrometry and synthesised via *figure 2.15*.

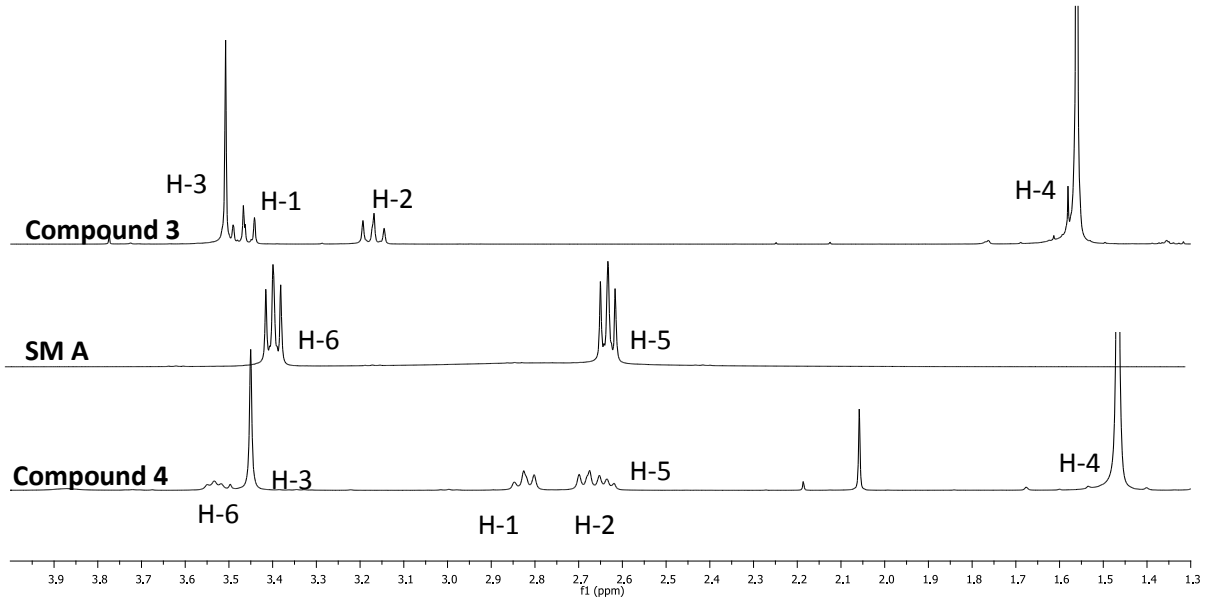

Figure 2.16- ^{1}H-NMR of Compound 3 (top), SM C (middle) and Compound 4 (bottom)

The ^{1}H-NMRs in *figure 2.16* shows the formation of **Compound 4**. The key characteristic are the 36:2 hydrogen integration of H-4 to H-5 present in **Compound 4**, indicating the presence of both reactants. The formation is indicate by the downfield shift of H-1 and H-2 from 3.4 ppm, and 3.1 ppm to 2.8 ppm and 2.7 ppm respectively.

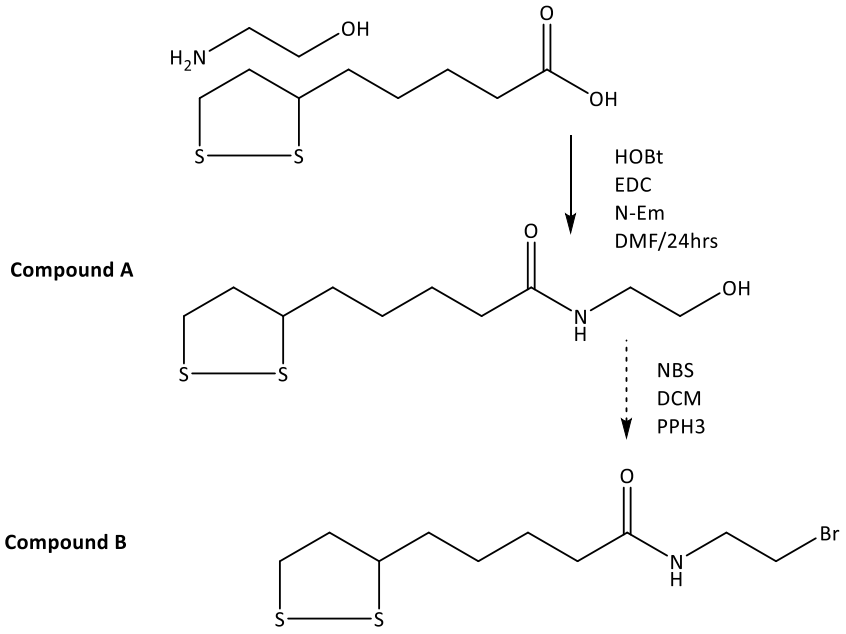

Figure 2.17- Reaction scheme of attempt 1 to make H_3BQUDS

In the first attempt to make **H_3BQUDS**, **Compound 4** was reacted further, but first a surface attachment linker was needed. *Figure 2.17* shows the surface linker being developed. Whilst **Compound A** was successfully synthesised, the bromination of the primary alcohol proved difficult and **Compound B** was not synthesised. Alternate methods were attempted to create a better leaving group than the hydroxyl in **Compound A** (*figure 2.17*), such as traditional chlorination or tosylation reaction conditions.

Whilst synthesising Compound B (*figure 2.17*), several attempts of cyclising **Compound 5** were attempted (*figure 2.18*).[62,112] **Compound 5** was synthesised under the same conditions as **H_3UDS** (*figure 2.13*). Cyclisation of **Compound 5** was necessary in order to incorporate two 6-aminoquinoline molecules on separate sides of **Compound 5**. The formation of a dianhydride creates a greater nucleophilic site for 6-aminoquinoline to attack on separate sides reducing bi-product formation. However after trying various conditions, cyclisation was not achieved. Products were analysed with ^{1}H-NMR, Electrospray Mass spectrometry, MALDI and IR spectrometry.

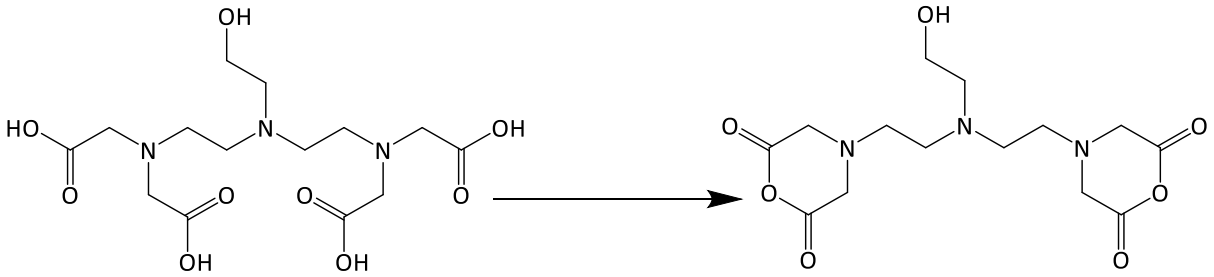

Compound 5

i) Acetic Anhydride/ Pyridine, 80^{o}C, 6 hrs, $N_{2(g)}$
ii) Acetic Anhydride/ Pyridine, 80^{o}C, 24 hrs, $N_{2(g)}$
iii) Acetic Anhydride/ Pyridine, 120^{o}C, reflux, 24 hrs, $N_{2(g)}$
iv) Acetic Anhydride/ Pyridine, 250^{o}C, 5 minutes, $N_{2(g)}$

Figure 2.18- Reaction scheme of cyclisation attempts.

After **Compound 5** could not be cyclised and **Compound B** could not be synthesised, attempts at cyclising **H_3UDS** were made demonstrating difficultly in cyclisation. As a result **H_3BQUDS** was not synthesised, and alternative methods would need to be used to achieve cyclisation or through an alternative synthetic route. Thus **H_3UDS** was used only as a non-absorbing ligand (NAL) to chelate lanthanides.

2.2.3 - Ternary Complex Formation of EuBDS with Small Aromatic Acids in Solution

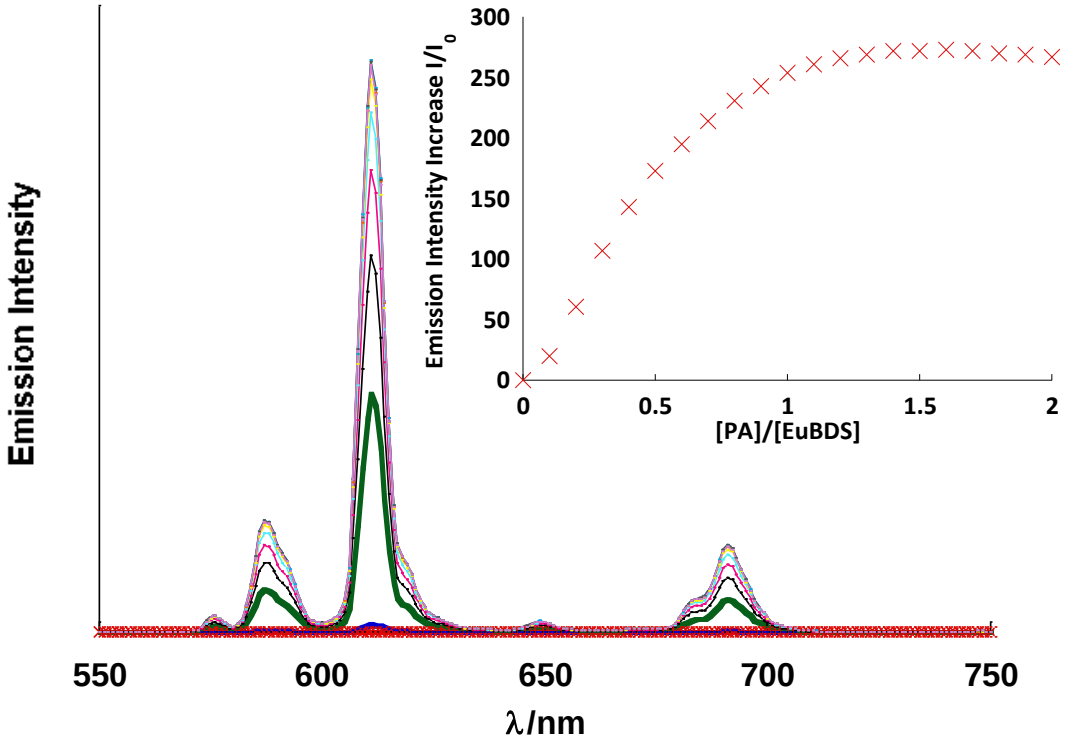

Figure 2.19 - Corrected emission spectra (λ_{ex} =280 nm) for titration of picolinate (0-100 μL, 9 mM, 3 eq of NEt_3) into an ethanolic solution of EuBDS (0.12 mM), (inset) integrated emission intensity plot against the molar equivalents of titrant added.

The ternary complex formed between **EuBDS** and picolinate demonstrated its bidentate nature with two different functional groups. Picolinate has a heteroatom in the pyridine ring and contains a carboxylic acid functional group. Picolinate is capable of bidentate coordination to **EuBDS** and demonstrated the strongest sensitisation of **EuBDS**. The **EuBDS** is designed to accommodate potential analytes between the bis-amide legs, leading to a 1:1 stiochiometric ratio between picolinate and **EuBDS** (*figure 2.19)*. The excitation scan shows intramolecular energy transfer from the picolinate to europium further indicating that picolinate is

coordinated to europium. The integration plot shows a major increase in europium signal and saturates around one equivalent of picolinate to **EuBDS**, thus further indicating a 1:1 binding, and formation of a luminescent ternary complex. The graph saturates at one equivalent, however there is a negligible increase after one equivalent of PA has been added this is due to slow coordination of the picolinate to **EuBDS** in solution competing for the remaining free coordination sites.

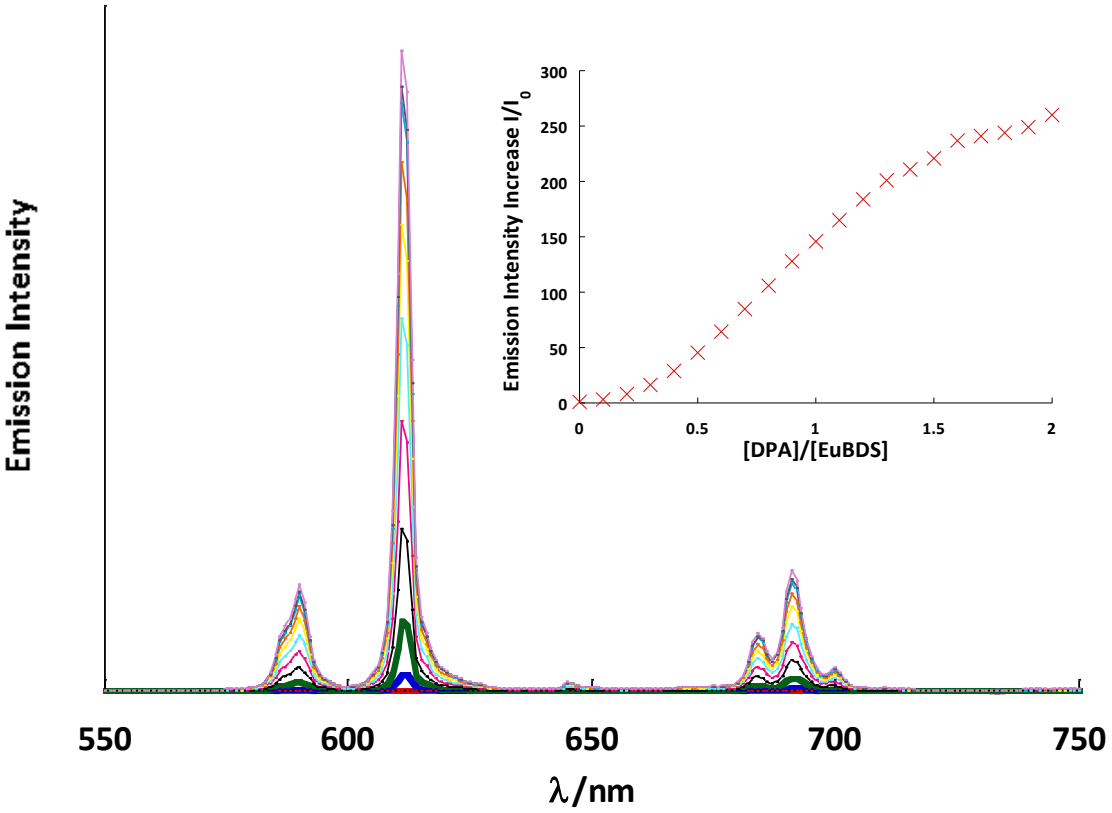

Figure 2.20 - (Left) Corrected emission spectra (λ_{ex} =280 nm) for titration of dipicolinate (0-100 μL, 9 mM, 3 eq of NEt_3) into an ethanolic solution of EuBDS (0.12 mM), (inset) integrated emission intensity plot against the molar equivalents of titrant added.

Dipicolinate gave another example of lanthanide sensitisation through energy transfer from the chromophore to the europium emissive states (*figure 2.20*). Dipicolinate like picolinate has both a heteroatom in the benzene ring and carboxylic acid groups with an additional carboxylic acid group in the *meta*-position. Having two carboxylic acid groups and a pyridyl group, would suggest a sensitiser that would have tridentate binding nature. As mentioned previously lanthanides prefer a coordination number of 8-10, eight of which would be a bis-amide DTPA ligand. Thus when dipicolinate binds to the **EuBDS** it should only bind in a bidentate or monodentate motif.

Analysis of the photophysical data suggests there is almost a linear increase in the emission intensity increase from zero equivalents of dipicolinate to 1.5 equivalents, and thus saturating out at two equivalents. It is not possible that two dipicolinate molecules are coordinated to the europium complex in a tridentate or bidentate motif, thus it would suggest that dipicolinate in this case is binding through a monodentate motif to **EuBDS**, and stabilised through a π–π stacking of the two molecules. The DPA molecule could also be binding through other minor binding sites around the **EuBDS** molecules. Alternatively the molecule is competing for the europium ion or there is some molecular rearrangement within the **EuBDS** complex, and releases partial coordination from the europium, to allow dipicolinate to coordinate in a bidentate or less likely a tridentate moiety.

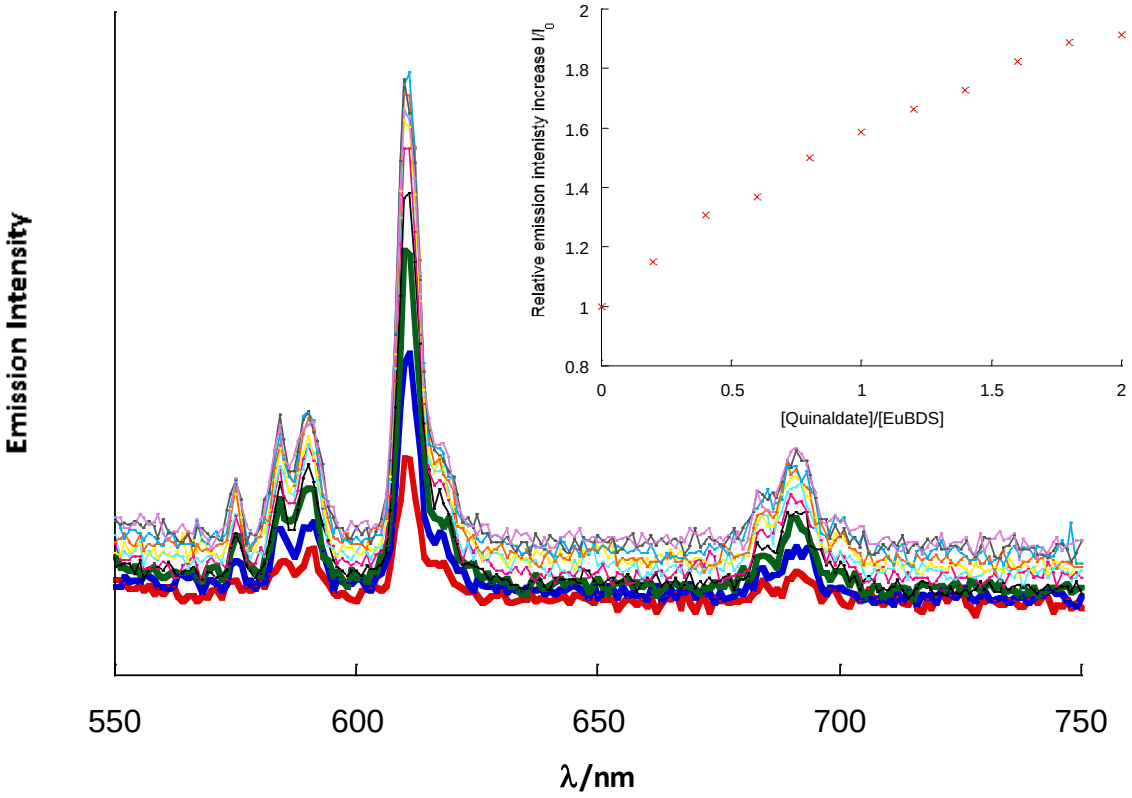

Figure 2.21- (Left) Corrected emission spectra (λ_{ex} =280 nm) for titration of quinaldate (0-100 μL, 9 mM, 3 eq of NEt3) into an ethanolic solution of EuBDS (0.12 mM), (inset) integrated emission intensity plot against the molar equivalents of titrant added.

Quinaldate, much like picolinate, has the same functional group; one carboxylic acid group in the *meta*-position and heteroatom in the pyridine ring. The only variation is that quinaldate is a fused ring systems, the combine nature of a benzene ring and picolinate. The variation of the acid introduces a more conjugated π- system and exhibits greater steric interactions than picolinate as the molecule is larger. However in this scenario the quinaldate does shows very limited sensitisation of the europium (*figure 2.21*), meaning that there is coordination to the europium of **EuBDS**. With poor sensistisation it shows some selectivity in the system dependant on emission intensity and the ability of **EuBDS** to accommodate slightly larger

aromatic acids. The weak sensitisation could be attributed to weak binding, causing fewer quinaldate to be bound to **EuBDS**, thus making the energy transfer process inefficient, and reducing the amount of energy transferred to the lanthanide emissive states.

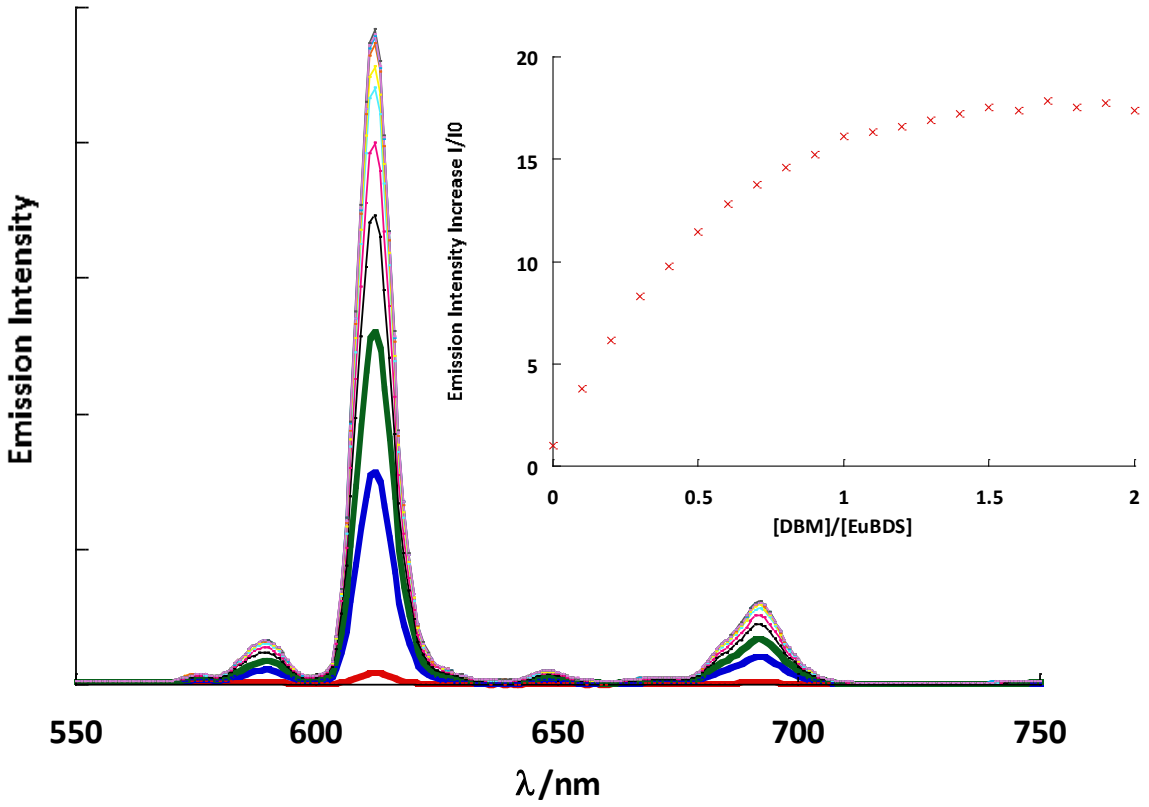

Figure 2.22 - (Left) Corrected emission spectra (λ_{ex} =280 nm) for titration of DBM (0-100 μL, 9 mM, 3 eq of NEt_3) into an ethanolic solution of EuBDS (0.12 mM), (Right) integrated emission intensity plot against the molar equivalents of titrant added.

DBM is another well-known sensitiser of europium, and in the case of **EuBDS** sensitisation is also observed. The β–diketonate DBM is a bidentate molecule which coordinates through two ketone functional groups, potentially forming a six membered with the europium ion, in the

same way as isophthlate. DBM also has two chromophores of benzyl nature, but has a significantly higher molar absorption coefficient than all of the previous mentioned aromatic acids. DBM here shows greater sensitisation than that of isophthalate, and that of quinaldate (*figure 2.22*). This shows that **EuBDS** can accommodate larger molecules than that of quinaldate. Through analysis of the binding curve, it shows that only one molecule of DBM can bind to **EuBDS** at any one time, there is no $\pi-\pi$ stacking involved or major rearrangement of the **EuBDS** molecule.

Simple aromatic acids appear to have coordinated to **EuBDS** successfully but have varying amounts of sensitisation, with picolinate giving just under 250 fold increase in the luminescent intensity and benzoate barely giving a 2 fold increase. With a system like **EuBDS** it is possible to differentiate between these aromatic acids, with limited selectivity in a mixed solution.

2.2.4 - Detection of DPA Using EuBDS SAM

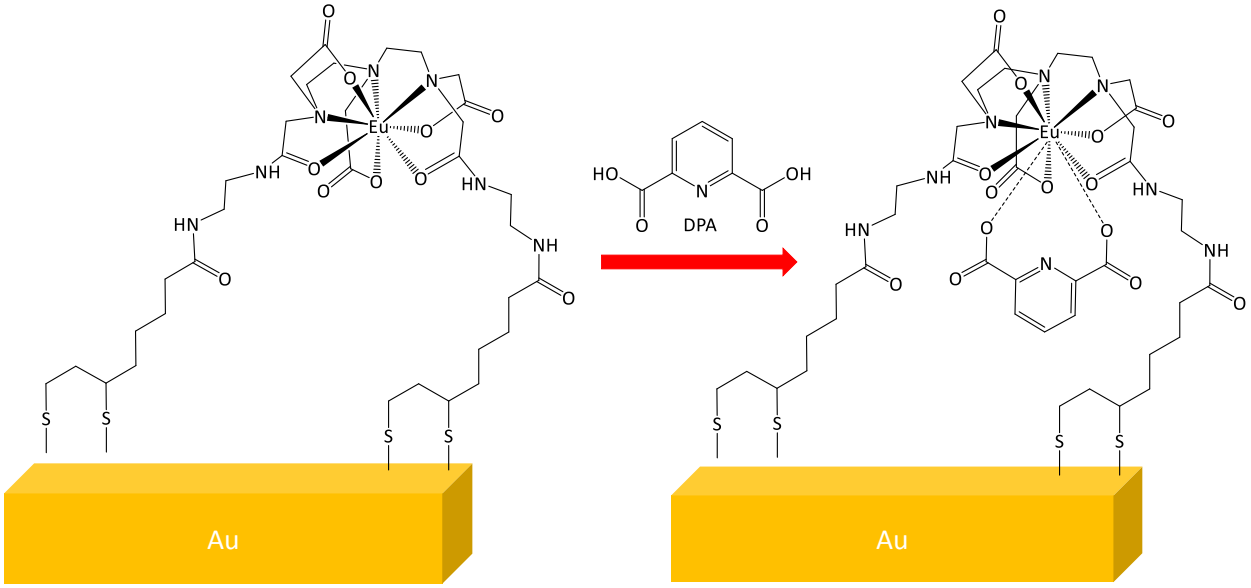

Figure 2.23 - Representing the detection of DPA on a EuBDS SAM.

A **EuBDS** SAM was formed as described in Chapter 6 and tested for its sensing properties of Dipicolinic Acid (DPA) and Picolinic Acid (PA). The emission spectrum of the europium signal is weaker than the solution of **EuBDS,** but detection of DPA and PA is possible down to nanomolar concentrations with a SAM of **EuBDS**. Firstly, we demonstrate the ability to coordinate DPA to europium within the self-assembled monolayer of **EuBDS** on gold, to switch on the surface luminescence and how this technique can be used to screen for small analytes.

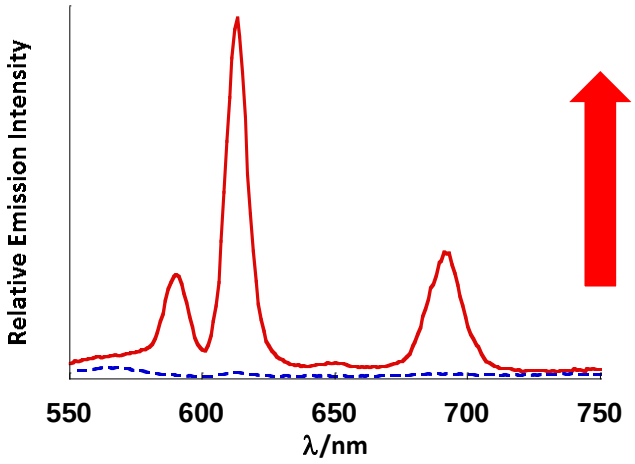

Figure 2.24- Emission spectra demonstrating the increase in luminescent intensity when a SAM of EuBDS is submerged in a 1 mM ethanolic solution of Dipicolinate. (- - -) EuBDS and EuBDS-DPA (—).λ_{exc} = 280 nm

The surface emission was tested by exciting the surface with a 280 nm laser (represented by (- - -) in *figure 2.24*). The lack of emission represents the "off-state" of the **EuBDS** SAM. The SAM was then submerged in a 1 mM ethanolic solution of dipicolinic acid pre-treated with three molar equivalents of triethylamine for 24 hrs. After which the SAM was rinsed with copious amounts of ethanol, and dried under a nitrogen stream. Upon exciting the SAM pre-exposed to DPA, the luminescent intensity at the surface increased by 800 % indicating the presence, and coordination of DPA to **EuBDS** on the surface, the "on-state". The emission shows sharp band structure, which is typical of europium, and indicative of europium being sensitised by DPA at the surface.

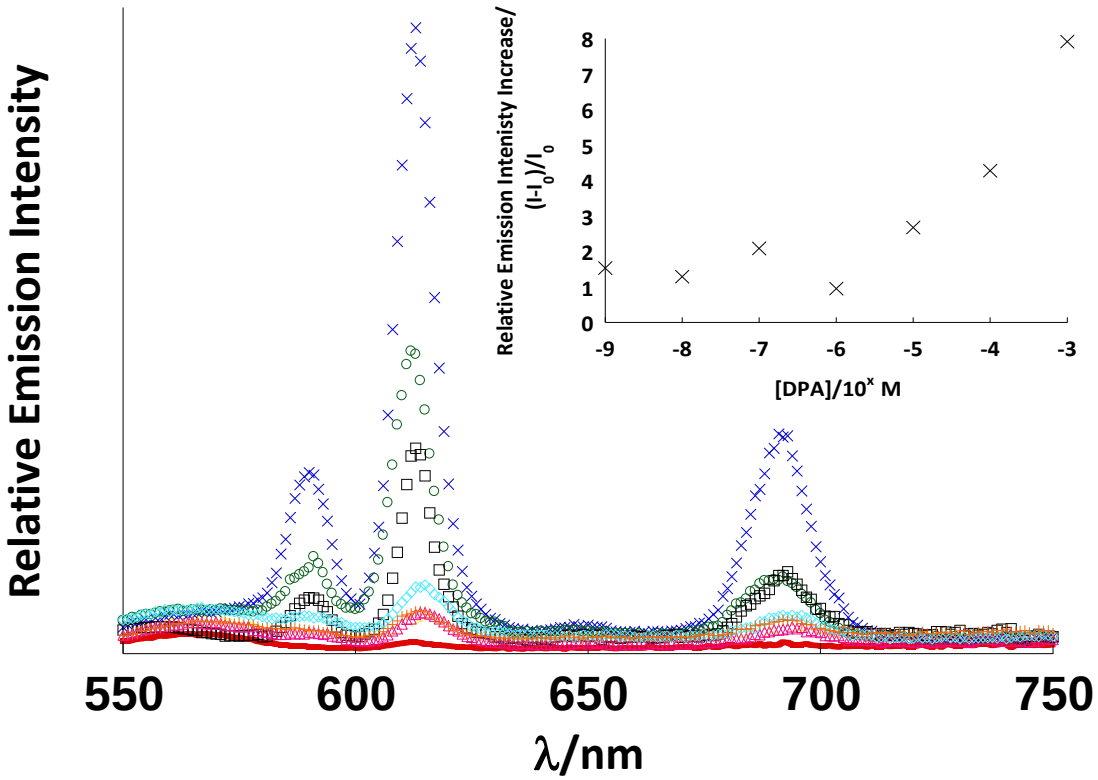

Figure 2.25- (Left) shows the europium emission from a SAM formed from EuBDS, after submersion of the SAM into increasing concentrations of dipicolinate. (inset) shows the integrated europium emission from a EuBDS SAM, after submersion of the SAM into increasing concentrations of dipicolinate. λ_{exc} = 280 nm

The limit of detection of **EuBDS** was then determined by subjecting the SAM surface to a gradual decrease in analyte solution concentration (*figure 2.25*). **EuBDS** was able to sense solutions of DPA down to a concentration of 1 nM showing a 150 % increasing in surface luminescence. However the correlation of analyte concentration and surface luminescence is limited to 1 μM, at which the surface luminescence increase by 100 % and below which the surface luminescence is slightly greater with a 230 % with an analyte concentration of 0.1 μM.

2.2.5 - Detection of DPA Using EuBDS SAM

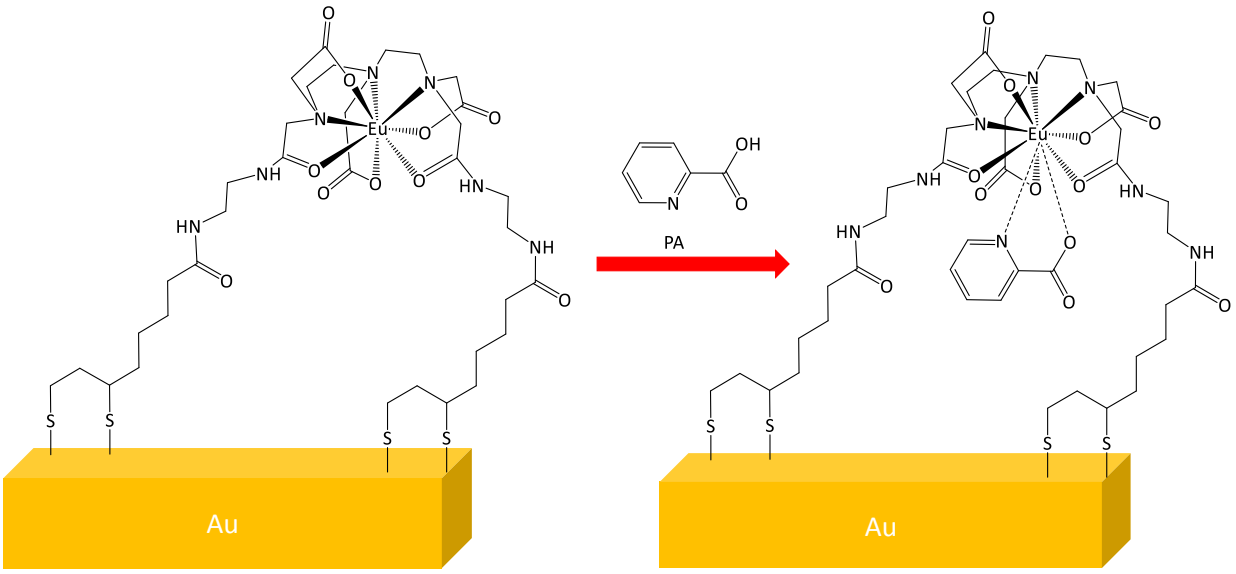

Figure 2.26 - Representing the detection of PA on a EuBDS SAM.

The **EuBDS** was also used to sense for picolinate. Similarly to DPA the surface was first excited in the absence of DPA ((- - -) in *figure 2.26*) and then exposed to increasing concentrations of pretreated picolinic acid. The concentration was increased from nanomolar to millimolar concentrations increasing by factors of 10. Picolinic acid was pretreated with 3 molar equivalents of triethylamine. The **EuBDS** was also used to sense for picolinic acid. Similarly to DPA the surface was first excited in the absence of DPA ((- - -) in *figure 2.24*) and then exposed to increasing concentrations of pretreated picolinic acid.

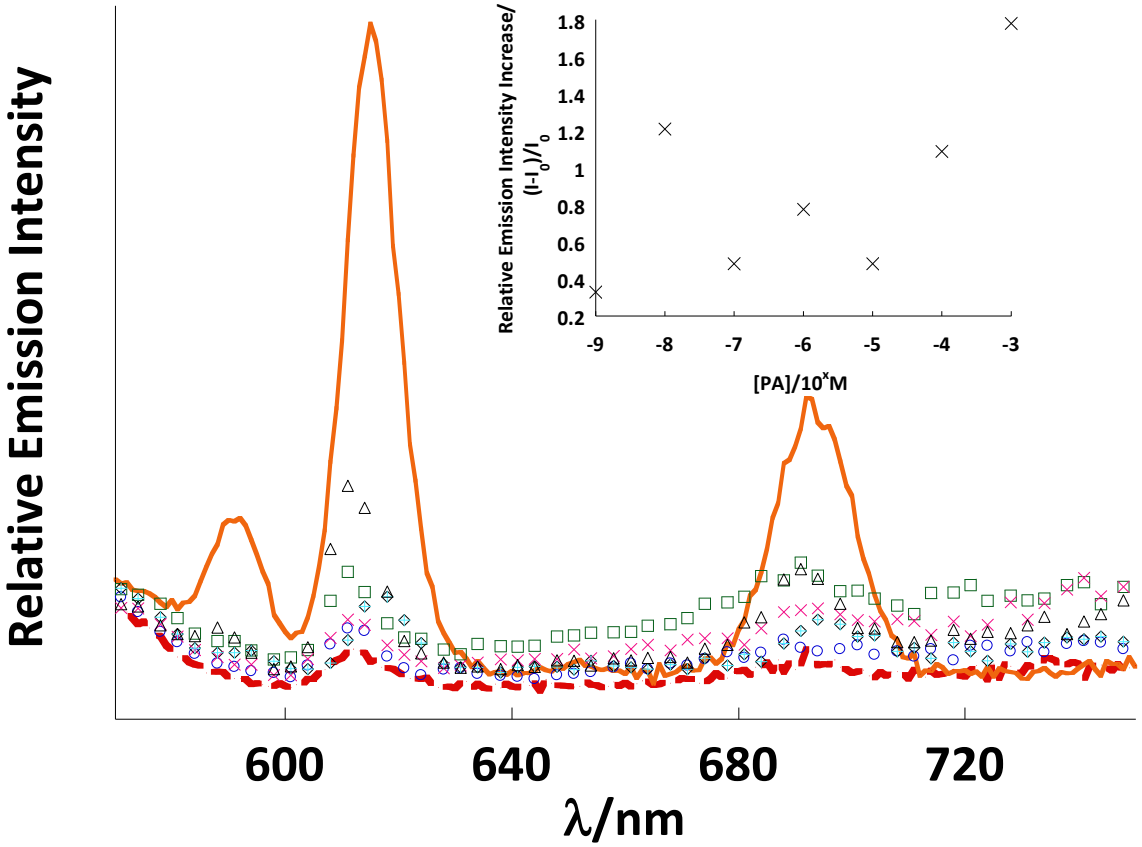

Figure 2.27 - (Left) shows the europium emission from a SAM formed from EuBDS, after submersion of the SAM into increasing concentrations of picolinate. (Inset) shows the integrated europium emission from a EuBDS SAM, after submersion of the SAM into increasing concentrations of picolinate. λ_{exc} = 280 nm.

The concentration was increased from nanomolar to millimolar concentrations increasing by factors of 10 (*figure 2.27*). Picolinic acid was pretreated with 3 molar equivalents of triethylamine. The results showed that picolinic acid can be sensed, as the surface luminescence was increased by 180 % at millimolar concentrations. Although the surface showed an increase in luminescene for all concentrations down to nanomolar concentrations, the increase was only minor, and there is no clear relationship between surface luminescent intensity and concentration. The increase in luminescent intensity is similar to that found in

solution, where at one molar equivalent of picolinate the luminescence from the solution increased by 60%, containing 0.12 mM of picolinate in solution, and at the surface at 0.1 mM, the surface luminescence increased by 100%, both methods show that picolinate weakly sensitises **EuBDS**.

As mentioned before, these analytes have met certain criteria in order to sensitise europium in solution; small enough for cavity size, coordination sites and containing a chromophore, with appropriate triplet energy levels. However when we are screening for analytes and using SAMs, the surface cavity size becomes more restricted as the **EuBDS** and the gold surface forms a pseudo macrocycle through covalent bonds between complex's two terminal disulphide legs and the gold surface forming Leg-S-$(Au)_x$-S-Leg. The pseudo macrocycle acts as steric barrier for larger analytes that could bind to the free complex. Forming the pseudo macrocycle makes the system more selective as the access to the coordination site is more restricted whilst **EuBDS** is anchored to the surface. The aforementioned emission caused by the coordination of DPA and PA to **EuBDS**, and ellipsometric studies (see chapter 5) we show evidence that there is space in the pseudo macrocycle cavity for analyte binding.

2.3 - Experimental

2.3.1 - Compound 1

Ethylene diamine (2 mL, 29.57 mmol) was dissolved in anhydrous DCM at 0 ^{o}C. Thioctic acid (784 mg, 3.80 mmol) and carbonyldiimidazole (812mg, 5.01 mmol) was dissolved together in anhydrous DCM (25 mL). The solution of Thiotic acid and carbonyldiimidazole was then added drop wise under nitrogen for 20 minutes, then left stirring for 40 minutes whilst maintaining the temperature at 0^{o}C. The Reaction was then allowed to warm to room temperature for 30 minutes. The reaction was then stopped, and the organic layer was then washed with brine (3 x 20 mL). Then the reaction was dried over sodium sulphate, filtered and the solvent was removed in vacuo, leaving a thick yellow oil (900 mg, 95%). ^{1}H-NMR (300 MHz, d_6-DMSO) δ_H ppm: 1.2-1.4 (2H, m, H-4), 1.4 -1.6 (3H, m, H-3, H-5), 1.8-1.6 (1H, m, H-5'), 1.8-1.9 (1H, dddd, *J*=, 6.9, 7.0, 10.0, 13.1, H-7), 2.0-2.1 (2H, t, H-2, *J*= 7.4, 8.4), 2.3-2.5 (1H, dddd, *J*= 6.3, 6.9, 9.7, 13.1 H-7'), 2.6-2.7 (2H, t, *J*= 6.4, 7.1, H-10), 3.0-3.2 (4H, m, H-8, H-8', H-9), 3.5-3.7 (1H, m, H-6), 3.7-3.8 (2H, s br, N*H*$_2$), 7.8-8.0 (1H, t, *J* = 5.7, N*H*). ^{13}C-NMR (400 MHz, d_6-DMSO) δ_c ppm:24.9, 28.3, 34.1, 35.2, 38.1, 38.3, 40.6, 56.1, 172.2. M/z (ES+): 249.1 $[M+H]^+$.

2.3.2 - DTPA Dianhydride

Was prepared by Dr. Alison Savage and ^{1}H-NMR characterisation coincided with her results. Acetic anhydride (220 ml, 2.33 mol) was added slowly via a dropping funnel to a stirring suspension of DTPA (160.6 g, 0.41 mol) in pyridine (150 ml) at 65^{o}C. The solution was stirred for 5 hrs and the solid was isolated by suction filtration and washed with acetic anhydride (2

x 50 ml). Acetonitrile (250 ml) was added to the solid and the solution refluxed for 1 h. Once the solution had cooled, the white solid was isolated by suction filtration and washed with acetonitrile (2 x 50 ml) and diethyl ether (2 x 50 ml). The final solid was dried *in vacuo*. (134.69 g, 92 %) 1H NMR (300 MHz, D_2O) δ (ppm) 3.98 (8H, s, NCH_2CO), 3.63 (2H, s, NCH_2COOH), 3.48 (4H, t,NCH_2CH_2N), 3.18 (4H, t, NCH_2CH_2N).

2.3.3 - H_3BDS

Compound 1 (0.82 g, 3.29 mmol) was dissolved in a stirring solution of compound DTPA-Dianhydride (0.53 g, 1.48 mmol) in anhydrous pyridine (35 mL) and anhydrous DMF (30 mL). The mixture was stirred at ambient temperature under nitrogen for 24 hours, and then filtered and the filterate was reduced under vacuum at 60°C, leaving a yellow oil. Water (30 mL) was added to give a yellow solution. The pH of the solution was adjusted to 3, where a gummy precipitate was formed. The water was decanted from the flask. The gummy precipitate was triturated in acetone (50 mL) for 24 hours, after which a light yellow powder had formed, after which it was filtered and the cake was washed with acetone (2 x 10 mL) yield = 35% (0.46 g, 0.53 mmol). ^{1}H-NMR (300 MHz, d_6-DMSO) δ_H ppm: 1.2-1.4 (2H, m, H-4), 1.4 -1.6 (4H, m, H-3, H-5), 1.8-1.9 (1H, dddd, *J*=, 6.9, 7.1, 10.6, 13.9, H-7), 2.0-2.1 (2H, t, *J*= 7.1, 8.6, H-2), 2.3-2.4 (1H, dddd, *J*= 6.2, 6.3, 9.6, 13.0, H-7'), 2.6-4.0 (26H, br s, H9-,H-10, H-12, H-13, H-15, H-16, H-17), 7.7-8.3 (4H, t, *J* = 5.7, N*H*). ^{13}C-NMR (400 MHz, $CDCl_3$) δ_C ppm: 25.0, 28.3, 34.1, 35.0, 38.1, 38.5, 50.1, 52.6, 54.2, 54.7, 55.3, 55.7, 56.1, 161.3, 168.4, 170.2, 172.2, 172.7. M/z (ES+) MS: 854 $[M+H]^+$.

2.3.4 - EuBDS

H_3BDS (327 mg, 0.38 mol) dissolved in water 30 ml, pH adjusted to 6, then DMF (20 mL) was added, and stirred for 2hrs. Then $EuCl_3.H_2O$ (130 mg, 0.38 mmol) in water (5 mL) was added and the pH adjusted to 6, and stirred for 16 hrs. The mixture was reduced in *vacuo.* The reaction was then cooled to 0^{o}C and acetonitrile (30 mL) was added to induce precipitation. The compound was then filtered and the residue was washed with acetonitrile (20 mL x 2) and ether (10 mL). The compound was then dried under high vacuum, leaving a white powder (130 mg). HR-MS (ES +): 1002.23 m/z

2.3.5 - Compound 2

^{t}Butyl-bromo-acetate (13.5 g, 69.2 mmol) was dissolved in DMF (25 mL) potassium bicarbonate (7.68 g, 76.8 mmol) was added. The suspension was then cooled to 0 °C, then ethanolamine (1.89 g, 30.9 mmol) was added over a 5-min period, and the reaction mixture was stirred at 0 °C for 30 min and then for 22 hrs at rt. After that the solution was partitioned between ether (150 mL) and saturated $NaHCO_3$ (100 mL), the organic phase was washed again with saturated $NaHCO_3$ (100 mL). The combined aqueous washes were extracted with ether (100 mL), and the combined ether extracts were washed with brine (100 mL), dried using sodium sulphate, filtered and evaporated to give the crude product (3.7 g) as an oil. The crude oil was then purified by silica gel chromatography, R_f = 0.35 (40/60 ethyl acetate/hexane) to give a colourless oil (3.0 g, 46%).^{1}H-NMR (300 MHz, $CDCl_3$) δ_H ppm: 3.7 (br s, O*H*), 3.6 (s, 4 H,), 3.4 (t, 2 H, J = 7.4), 2.8 (t, 2 H, J= 7.4), 1.5 (s, 18H). [113]

2.3.6 - Compound 3

The crude **Compound 2** (7.50 g, 25.95 mmol) was dissolved in CH_2Cl (50 mL), Ph_3P (6.82 g, 25.95 mmol) was added, the solution was cooled to 0 °C, and solid NBS (4.65 g, 25.95 mmol) was added portion wise over 5 min. After the solution was stirred at 0 °C for 1.5 h, evaporation of the solvent gave a semisolid residue which was triturated with ether (200 mL) and the resulting solid was separated. Evaporation of the ether gave a pale yellow oil which was purified by silica gel chromatography to afford the bromide (6.56 g, 72% yield) as a light yellow oil: R_f : 0.29 (5/1 hexanes/ether); ^{1}H-NMR (300 MHz, $CDCl_3$) δ_H ppm: 3.7 (s, 4 H,), 3.42 (t, 2 H, J = 7.4), 3.2 (t, 2 H, J= 7.4), 1.5 (s, 18H); ^{13}C-NMR (400 MHz, $CDCl_3$) δ_C ppm: 55.1, 56.2, 66.1, 128.0, 128.2, 135.2, 170.5. [113]

2.3.7 - ^{t}Butyl-H_3UDS

Compound 1 (100 mg, 0.4 mmol) was dissolved in DMF (10 mL), DCM (10mL) and potassium bicarbonate (122 mg, 1.2 mmol) was added. Di-t-butyl-carboxyl-ethanolamine was dissolved in DMF (5 mL) and added to the reaction vessel the suspension was left stirring at room temperature for 22 hrs. After that the solution was filtered, washed with DMF:DCM (1:1, 5 mL) and the filterate was concentrated in *vacou* leaving a yellow oil. The oil was then titurated in diethyl ether (100 mL), and filtered. The ether was then removed under high vacuum to leave the crude yellow oil. The oil was then purified with silica chromatography. R_f = 0.3 (95:5, $CHCl_3$: MeOH), to leave a yellow oil. (32 %, 100mg). ^{1}H-NMR (300 MHz, $CDCl_3$) δ_H ppm: 1.3-1.5 (40H, m, H-8, H-7, H-4), 1.5 -1.7 (2H, m, H-9), 1.7-1.8 (1H, dddd, *J*=, 6.9, 7.1, 10.6, 13.9, H-11'), 2.1-2.2 (1H, m, H-6), 2.3-2.4 (1H, dddd, *J*=, 6.9, 7.1, 10.6, 13.9, H-11'), 2.5 -2.6 (6H , m, H-2, H-

13), 2.6-2.7 (4H, m, H-1), 2.9-3.3 (4H, m, H-12, H-14), 3.3-3.4 (8H, s, H-3), 3.4-3.6 (2H, m, H-10), 7.1-7.2 (2H, br s,N*H*). ^{13}C-NMR (400 MHz, $CDCl_3$) δ_C ppm: 25.6, 28.1, 28.2, 29.1, 34.7, 36.1, 38.1, 40.2, 51.5, 52.2, 55.8, 56.5, 81.1, 170.6, 173.0

2.3.8 - H_3UBS

^{t}Butyl-H_3UDS (430mg, 0.54 mmol) was dissolved in 3 ml of acetonitrile and sonicated for ten minutes. Then hydrochloric acid (6 M, 10 mL) was added and stirred at ambient temperature for two hours. The solvent was then reduced to a minimum in *vacuo,* and then water (5 mL) was added and the pH was adjusted to 3 inducing precipitation and left in the fridge overnight. The compound was then filter and dried, (yield = 99 %, 308 mg). ^{1}H-NMR (300 MHz, $CDCl_3$) δ_H ppm: 1.3-1.7 (6H, m, H-8, H-7, H-9), 1.7-1.9 (1H, H-11'), 2.1-2.2 (1H, m, H-6), 2.3-2.4 (1H, m, H-11'), 2.4 -2.6 (10H , m, H-10, H-2, H-13), 2.6-2.9 (4H, m, H-1), 2.9-3.3 (12H, m, H-12, H-14, H-3), 3.4-3.6 (2H, m, H-10), ^{13}C-NMR (400 MHz, $CDCl_3$) δ_C ppm: 24.9, 27.8, 35.5, 35.9, 36.0, 50.6, 51.7, 58.9, 59.1, 159.2, 176.5, 179.3, 179.8, 191.1. HR-MS: 567.2158 $[M+H]^+$.

2.3.9 - Compound 4

Compound 3 (6.42 g, 18.4 mmol) was dissolved in DMF (25 mL) potassium bicarbonate (1.85 g, 36.8 mmol) was added. The suspension was then cooled to 0 °C, then ethanolamine (0.56 g, 18.4 mmol) was added over a 5-min period, and the reaction mixture was stirred at 0 °C for 30 min and then for 22 hrs at rt. After that the solution was partitioned between ether (150 mL) and saturated $NaHCO_3$ (100 mL), the organic phase was washed again with saturated $NaHCO_3$ (100 mL). The combined aqueous washes were extracted with ether (100 mL), and the combined ether extracts were washed with brine (100 mL), dried using sodium sulphate, filtered and evaporated to give the crude product (3.7 g) as an oil. The crude oil was then purified by silica gel chromatography, R_f = 0.35 (60/40 ethyl acetate/hexane) to give a colourless oil (3.0 g, 46%).^{1}H-NMR (300 MHz, $CDCl_3$) δ_H ppm: 3.9 (br s, O*H*), 3.7 (m, 2 H,), 3.4 (s, 8 H), 2.8 (t, 4 H, J= 7.4), 2.7 (t, 4 H, J= 7.4), 1.5 (s, 36H). MS: 606 $[M+H]^+$,626 $M+Na]^+$

3 - Sensing with Silyl Active Lanthanide Complexes on Surfaces and Nanoparticles

3.1 - Introduction

Glass has been used since 4000BC in Ancient Egypt to glaze beads, making these beads was aesthetically pleasing and desirable. It wasn't until 1500BC that the first receptacle was made of glass, using a sand core and pouring molten glass over the top of the core, making the first hollow container[114]. Since then the history of glass has changed dramatically. We know that glass consists of silicon dioxide, commonly known as silica, and advances in science and technology have made use of the unique properties of silica; such as its optical transparency and its biocompatibility within the human body. In particular, the last two decades silica research has had a huge impact and a range of applications within science to create silica nanoparticles[65,97-99,106,115-133], molecular devices[10,17-19,106], metal organic frameworks[99] and various quartz materials. Two of the most promising areas that we have been looking at are silica nanoparticles and molecular devices in which research is specifically flourishing and lead to the advances in the areas of biomedical applications for imaging and diagnostics,[124] biosensing,[129] bone repair,[134] scaffold engineering,[119,135] and drug delivery.[126,127,130]

Silica is particularly useful in the area of biosensing which incorporates many aspects of recognition such as molecular switches,[7,123] chemical warfare detection, antibodies,[44,136] and chemical recognition.[87,136-139] Biosensing can benefit from the advantageous properties of silica when used in conjunction with each other; such as its optical transparency and its biocompatibility being beneficial to bio-imaging of fluorescent silica nanoparticle dyes within the body, or for use in Lab-on-Chip devices. The Pikramenou group used highly luminescent

transition metal complexes and incorporated them into silica nanoparticles, and used tracking techniques such as Particle Imaging Velocimetry (PIV) and Particle Tracking Velocimetry (PTV) to monitor their silica nanoparticles in a flow system.[65]

Microfluidic devices are lab-on-chip devices in the field of micro-analytics and detection. Over the last two decades they have assumed a major role within micro-total analysis systems,[140] aiding micro-analysis through the fields of biology, chemistry and medicine.[105,106,136,141-143] Device complexity has increased from valve and pump systems[144] to entire lab-on-chip systems that have assaying routines of significant complexity[145] resulting in saving time and money for analytical diagnostics. These functionalities have made microfluidic systems a big player in biomedical diagnosis applications. The devices are normally categorised into three main areas due to the detection method used: optical, electrochemical and mass spectrometric. Optical methods of detection use light to thoroughly investigate and analyse the sample, and are the most common form of microfluidic devices. Optical detection methods are used frequently because they offer relatively low limits of detection, and label-free analyte recognition.[146,147]

Recognition is best described as the 'lock and key' method where two complimentary components interact together forming a new component. For us to monitor this, the system would need to have a measurable outcome upon the binding event of the two components. The most common technique of identifying chemical recognition is through the use of photoluminescence which can be carried out in solution, on surfaces and on nanoparticles,

each having their own advantages and disadvantages. Through the use of a photoluminescent system, we are able to track the change in photophysical dynamics of the system, whether it is an increase or decrease in luminescent intensity, or change in colour or a change in shape of the emission spectrum. With a change in luminescent intensity being the most advantageous as it can provide the greatest difference in signal, i.e from a non-luminescent state to a highly luminescent state can be seen by eye in some cases.[75]

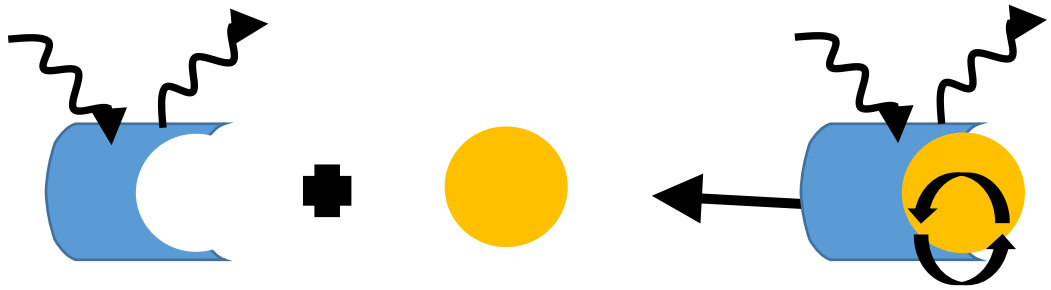

Figure 3.0 - A Representation of a very basic photophysical system for chemical recognition. ET denotes energy transfer processes, either from or to the analyte. x- Initial wavelength, and Δy-is a change in wavelength or a change in intensity from the original wavelength.

Chemical recognition involves the use of a photoactive compound *(figure 3.0)*. These include organic dyes, transition metals, quantum dots and lanthanides. Each type of photoactive compound has its own advantages and disadvantages. Having a photophysical system that incorporates the use of organic chromophores and/or transition metals leads to broad spectral peaks in the emission spectrum, due to the presence of vibrational energy levels.[148] Monitoring changes in these emission bands can lead to complex data analyses, particularly if

the system involves multiple chromophores that are independent of the analyte being detected. The difficulty arises when deconvoluting the resulting emission spectrum to be an effect of binding or just an amalgamation of two non-binding molecules. Many organic dyes have emissive properties in the short wavelength range in the visible region of the electromagnetic spectrum, and due to the rotational and vibrational bands, theses emissive bands are broad in nature and could overlap with that of the photophysical system's existing chromophores or transition metals emission bands. One way of circumventing this problem is to use lanthanides. Lanthanides have three unique properties mentioned in the introduction chapter which give advantages over organic dyes, transition metals and quantum dots. They have a larger Stokes shift when compared to organic dyes (200 nm vs 50 nm), making it easier to deconvolute emissive properties arising from the lanthanides and the analyte. They have sharp band structure in the emission spectrum, giving the lanthanides distinguishable characteristics in emission spectroscopy. The lanthanides also have considerably longer lifetimes compared to organic dyes, comparing milliseconds as opposed to nanosecond timescales which allows for time-gated emission spectra to be obtained. This allows the excited states of the analyte to relax quickly before measuring the luminescence of only the lanthanides.

3.1.2 - Surface Active Silica Lanthanide Complexes as Sensing Platforms

Two of the leading researchers on self-assembled monolayers, Huskens and Reinhoult have utilised their knowledge and managed to create functionalised printboards on silica.[10,17,18,149] Their printboards were developed for the indirect detection of anthrax. The printboard didn't detect for anthrax spores or the bacterium, but used their printboards to detect dipicolinic acid with accounts for 5-15% dry weight constituent of an anthrax spore shell.[18] Through the coordination of surface bound lanthanide complexes with dipicolinic acid they were able to create luminescent sensing platforms on silica.

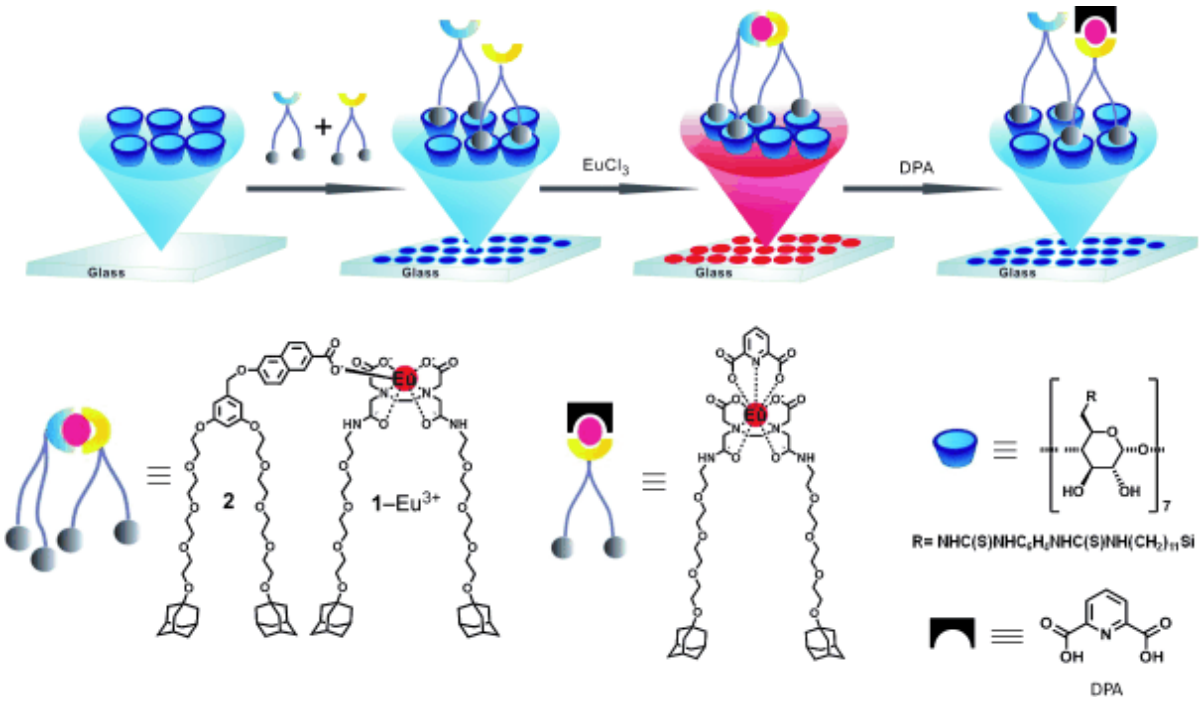

Figure 3.1 -Figure reproduced from Huskens' Printboard on silica for the detection of anthrax.[18]

The printboard consisted of a self-assembled monolayer of β-cyclodextrins represented by the six cones on *figure 3.1A*, previously characterised on gold by AFM, electrochemistry and XPS ensuring dense coverage of the β-cyclodextrins.[35] These were bound to the silica through hydroxyl terminus. The use of β-cyclodextrins allows for the utilisation of its cavity. The cavity itself has specific dimensions, enabling the occupation by adamantyl functional groups, which anchor themselves into the SAM a bilayer *figure 3.1B*.[150] This approach allows for controlled and uniform bilayers to be fabricated. Firstly the β-cyclodextrins are bound directly to the silica ensuring that the surface is covered in cavities ready to accommodate the next layer containing the guest, the adamantyl groups, to create a dense molecular layer. The interaction between the adamantyl and the β-cyclodextrins is purely hydrophobic and not covalent. Forming the adamantyl-β-cyclodextrins compounds pre-SAM formation would not ensure that all adamantyl groups have occupied β-cyclodextrins cavities, which would reduce the overall surface coverage of the silica and make a less ordered surface for SAM developement. Thus by using the layer by layer approach the group maximised coverage and in turn functionality of the device. The adamantyl groups are linked to the receptors by ethylene glycol chain creating 'adamantyl legs'. There are two different ligands bound to the β-cyclodextrins cavity, each utilising two adamantyl legs to anchor itself into the printboard (*figure 3.1C*). One is a europium chelated by a by ethylenediaminetetraacetic acid (EDTA). The second component is a naphthalene moiety with a carboxylic acid functional group, again containing two adamantyl legs. Each ligand is bound in two different β-cyclodextrins sites and it the naphthalene group that sensitises europium to give strong luminescence. The device mechanics then allowed selective displacement of the naphthalene moiety by dipicolinic acid. This is due to its stronger binding potential, being tridentate over the naphthalene moiety's

monodentate nature. Whilst displacing the naphthalene moiety the europium luminescence was reduced in intensity by 60 %. It is also important to note that any DPA excitation at 270nm is cut off through the use of narrow band filters at 350 nm.

Gulino *et al.,*[103] used a silyl functional groups to form a europium phenanthroline-trisdibenzoylmethane derivative SAM on silica (*figure 3.2*). This was achieved by first forming a monolayer of the chlorobenzylsilyl methane (4-$ClCH_2C_6H_4SiO_3$), followed by cleaning the surface using copious amounts of pentane to remove any unbound material prior to submerging the SAM in a basic solution of the trisdibenzoylmethane mono (5-amino-1,10 phenanthroline) europium (III). The amine undergoes nucleophilic substitution reaction at the SAM's methylene chloride's carbon.

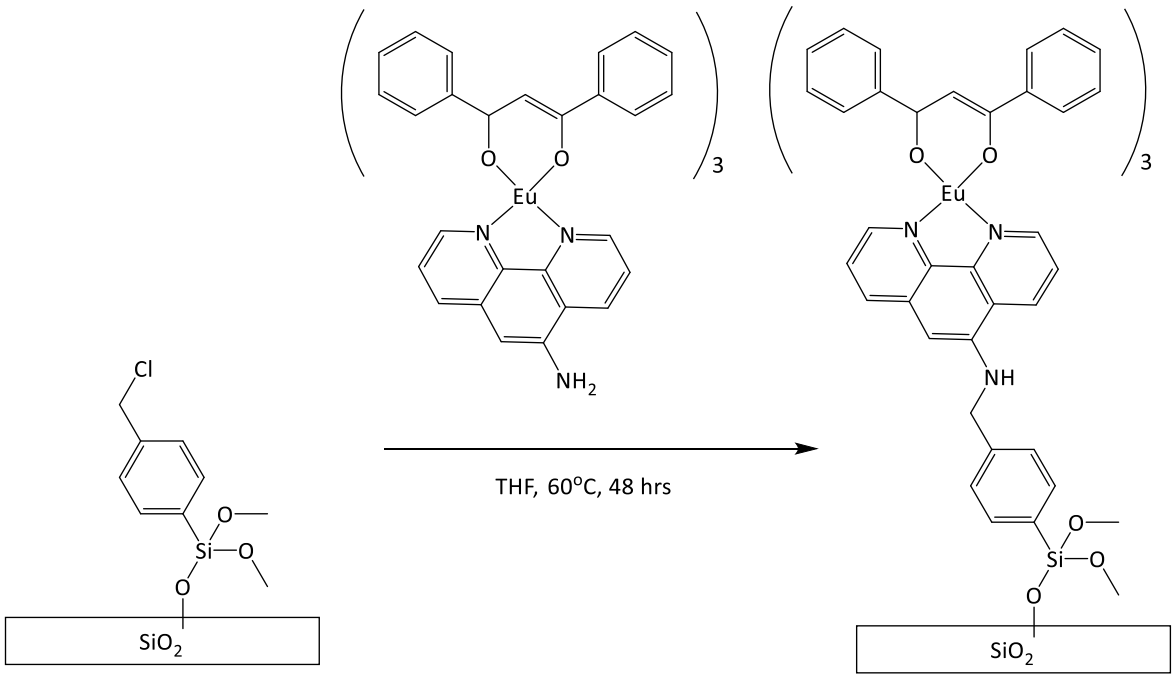

Figure 3.2-The chemical structure and reaction scheme to develop Gulino's et al SAM.[103]

They studied the optical properties of these monolayer system through means of both UV-Vis spectroscopy and photoluminescence measurements, as well as x-ray photoelectron spectroscopy (XPS). This system shows interest in both the scientific and industrial sectors due to the unique nature of europium compounds as efficient light-conversion molecular devices, phosphors in full colour flat-panel displays and for sensing applications and memory devices.[54]

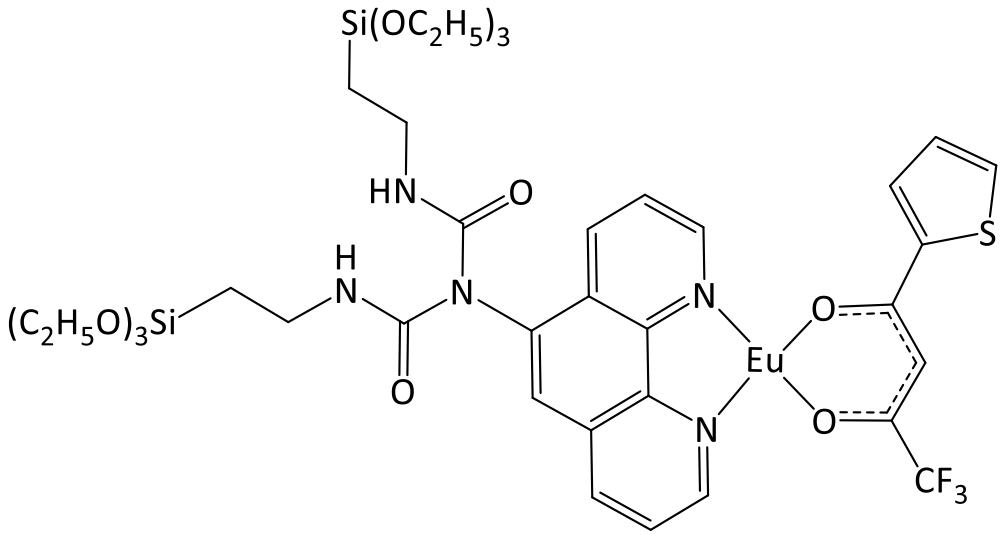

Figure 3.3-The chemical structure of the Euphen derivative used by Binnemans et al. to make a Sol-Gel.[151]

Europium complexes have also been incorporated into sol-gels.[151] Binnemans et al. used one of the most well-known types of lanthanide sensitiser, a β-diketonate complex; tris(2-thenoyltrifluoroacetonato) and 1,10-phenanthroline (*figure 3.3*) to coordinate europium ions and incorporate into sol-gels. The sol-gel consisted of 5-(N, N-bis-3-(triethoxysilyl)propyl) ureyl-1,10-phenanthroline), preformed tris(2-thenoyltrifluoroacetonato) dihydrate complex with polymerisation linkers; tetramethoxy-silane and diethoxy-dimethylsilane in the presence of water (pH 7) to induced hydrolysis and condensation reactions of the siloxanes and form

the sol-gel. Sol-gels are difficult to reproduce uniformly, and general require harsh conditions to synthesise. Here Binnemans reports difficulty with reproducibility for several reported literature methods and the only successful attempts require hydrazine as a reducing agent and palladium on carbon reductions (5% Pd/C and not 10% Pd/C), which is generally not desirable for industry due to costs implications.

3.1.3 - Surface Functionalised Silica Nanoparticles as Luminescent Probes

Researchers choose to use silica nanoparticles in addition to the properties of using silica because they have high surface area both internally and externally and they exhibit great colloidal stability. Internally silica particles have a large cavity size which is tuneable whilst externally the surface can be functionalised with relative ease. Silica nanoparticles was first reported in 1956 by G. Kolbe,[152] and later optimised by Stöber.[153] Stöber claimed that they had developed a system of chemical reactions that allowed controlled growth of spherical particles of uniform size. The size of the nanoparticles was tuned by varying the alcoholic solutions used, producing a controllable particle size range of 50 nm to 2000 nm. The nanoparticles were formed used hydrolysis/condensation of alkyl silicates and ammonia as a catalyst.

Caruso *et al*. a few years later established another approach for hollow silica particles through a polymer template(*figure 3.4*).[117] This allowed the formation of a self-assembled multilayer around a colloidal nanoparticle, and by either a thermal treatment process called calcination or a change in solvent exposure they produced hollow silica nanoparticles or inorganic hollow

nanoparticles. From the preliminary results, they demonstrated that they could make titanium dioxide nanoparticles and hollow shells from templated biological specimens. They used their template method to produce mesoporous silica particles (MSNs) and then allowed for a drug-polymer capsule to form around the MSNs, and investigated the capsules ability in anticancer drug delivery.[154,109]

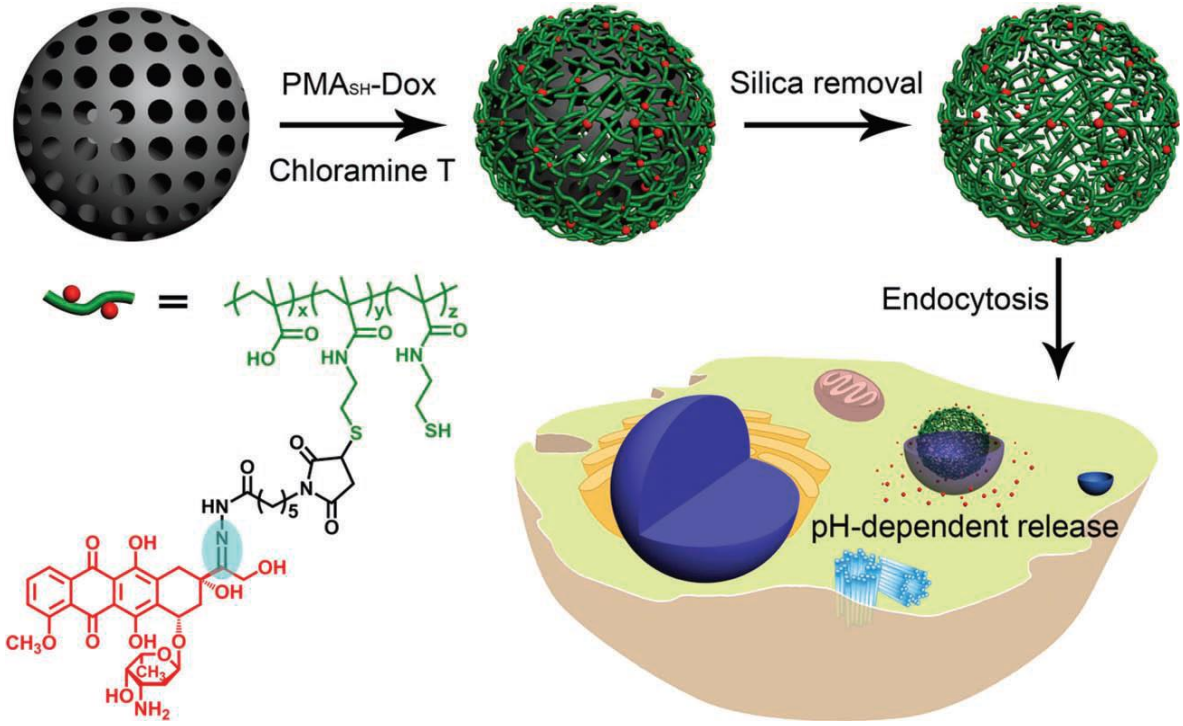

Figure 3.4 - A reproduced schematic diagram representing the Caruso et al. work on using silica nanoparticles as a template for biopolymer vesicle formation and drug delivery. [109]

Caruso found that drug-loaded particles were stable at physiological conditions, and were able to release the drug at a low pH through the cleavage of the hydrazone bonds between the polymer and the drug. After uptake of the drug-loaded particles into colorectal cancer cells and the drug was released, the results showed significant cell apoptosis.

The synthetic method of producing MSNs is based on the hydrolysis and condensation of organosilanes precursors, using base as a catalyst; very similar to a sol-gel approach. Common organosilanes precursors include tetramethylorthosilicate (TMOS) and tetraethylorthosilicate (TEOS) and can be used in conjunction with other organosilanes for additional properties.[99]

The base catalysed sol-gel process is as follows:

Hydrolysis: $OH^- + Si(OR)_4 \rightleftharpoons Si(OR)_3OH + RO^-$ (1)

Condensation: $SiO^- + Si(OH)_4 \rightleftharpoons Si–O–Si(OH)_3 + OH^-$ (2)

This leads to the formation of a new phase (sol). The small colloidal particles within the sol then condense into the gel phase. Simple variation of the organosilane allows for easy modification of the MSNs not just through covalent bonding but through electrostatic binding. The MSNs can be coated with surfactants stabilised through electrostatic interactions between the surfactant and the negatively charged terminal silicate groups. This allows for a wide range of diverse mechanical and functional MSNs to be produced. Covalent modification is usually incorporated into the co-condensation method above but can also be achieved through post formation of the MSNs.

The co-condensation method allows the hydrolysis of the functional organosilanes during the formation of the MSNs, resulting in the functional organosilanes being part of the silica framework. Having a functional organosilane framework usually infers a much higher loading of drugs, dyes or other functional materials. This is advantageous for luminescent probes and

MRI agents,[116] as the potential for loading is much higher. In contrast to incorporating the functional material into the silica framework, post-synthetic grafting of the exposed terminal silica groups can be performed before or after any stabilising surfactants have been removed.[130]

MSNs have also been used as carriers for drug delivery. They have the ability to encapsulate drugs within the pores of the nanoparticle and carry the drug to its vector. This is advantageous in drug delivery because as the drug is encapsulated with the silica nanoparticle, it is essentially shielded from any potential enzyme interaction and degradation. One method of encapsulating drugs or dyes, is to soak the MSN in a solution of the drug, and this will allow the MSN to uptake the drug through adsorption. This obviously facilitates an aspect of leaking, which occurs when the solvent is changed or the MSNs are placed into a new environment i.e. the drugs target environment. These drugs are normally suspended within the MSN through means of electrostatic interactions or H-bonding. The amount of possible loading is correlated to the surface area of the materials. Through correct modifications of the MSNs the loading and controlled release can be achieved, thus reducing any possible side effects that could be resultant of premature drug release and also controlling the effective dose of the MSN drug carriers.

Pikramenou *et al.*[65] demonstrated dye encapsulation, both post nanoparticle formation and during nanoparticle formation (*figure 3.5)*. Although encapsulation of transition metal complexes within silica nanoparticles is well studied,[106,155-160] here they demonstrated that the **Ir-4** dye encapsulated silica nanoparticle can be monitored in flow and through the addition

of fluoro-surfactant Zonyl 7950 the emissive properties of the nanoparticles increase, allowing for more effective particle tracking capabilities.

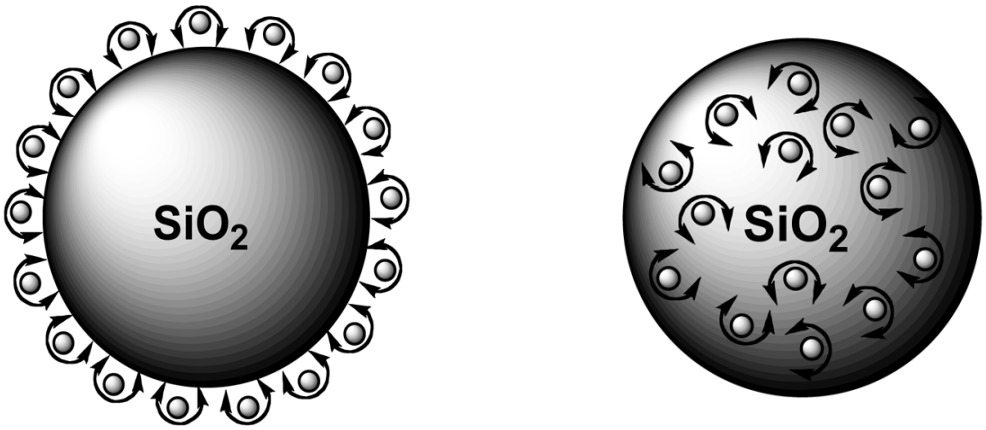

Figure 3.5- A schematic diagram showing silica nanoparticles surfaced bound iridium complexes (left: [Ir-4]@Si500) and the encapsulated iridium based dyes (right: [Ir-4]CSi500) prepared in the Pikramenou group.[65]

MSNs have also been used to incorporate gadolinium ions using a diethylenetriaminetetraacetic acid (DTPA) derivates and aminopropyltriethoxy silane (APTES) to covalently bind to the gadolinium complex to the MSNs.[99,116] Taylor-Pashow et al. produced several MSNs containing contrast agents that have been synthesised using a co-condensation method to incorporate two different Gd^{3+} complexes within the MSNs. The gadolinium coated MSNs were investigated and compared for their MRI contrast capabilities.

Organosilanes are well-known coupling agents for its ability to hydrolyse to silica and silicon surfaces, and are typically used in the formation of MSNs.[161] They can also be amine terminated allowing for bifunctional capability and further functionalisation of silanes are also possible which in turn can be incorporated with other organosilanes to make multifunctional MSNs. Organosilanes, particularly APTES have been used to form MSNs in conjunction with tetraethylorthosilicate (TEOS),[82,98,99,154,162-164] but not just to form MSNs but also to form self-assembled monolayers (SAMs).[165]

Near-infrared emitters have certain key benefits over shorter wavelength emitters in the field of bioanalytical and bio-imaging. Common areas of biological detection are typically in the visible region of the electromagnetic (EM) spectrum, partially due to the fact we can see colour change or intensity variations by eye. Shorter wavelengths than blue light leads us to the ultraviolet part of the EM spectrum and this is where most organic matter absorbs due to naturally occurring fluorophores and chromophores. These have radiative transitions in UV and visible areas of the EM spectrum this is known as autofluorescence. The well-known example of chlorophyll in green plants absorb UV light in photosynthesis. In this case plants actually absorb most of the UV-Vis spectrum, except green light and thus green light is reflected. Similarly in bio-imaging the most useful wavelength for detection is red and near infrared, as these are the most transmissive wavelengths of light that can pass through the body and that we can safely detect for without causing damage to the biomaterial. Probes that luminesce in the visible region on the EM spectrum normally require UV excitation, in vivo or in vitro this can cause tissue or cell damage, and in devices this can require the use of

quartz material to bypass the adsorption edge of silica, making devices more expensive to manufacture.

The auto-fluorescence associated with endogenous fluorophores and chromophores can overwhelm the signal to noise ratio and cause intense scattering profiles, and in bio-imaging this cause loss of signal intensity and spatial resolution. Dealing with autofluorescence can be difficult, however with lanthanides we can use time gated approach which cuts out the short lived signal from autofluorescence, leaving just the long-lived lanthanide luminescence. We can reduce effects of autofluorescence by working at longer wavelengths. This in turn could provide stronger signals and more accurate results when using NIR probes, assuming that NIR probes are as luminescent and equally effective in the environment as UV probes. Lanthanides that emit in the visible area of the EM spectrum, such as europium and terbium, require excitation in the UV region. This has high costs associated with the excitation sources and are usually bulky and require quartz optics. This can be reduced by the use of NIR lanthanides as these are normally excited in the visible region, and these excitation sources are relatively cheaper and can be less bulky.

3.2 - Project Aims

In this chapter we report the attachment of silyl functionalised Non-Absorbing Lanthanide (NAL) complexes to silica microparticles for sensing application. Based on my previous results in Chapter 2 we take our knowledge of gold functionalised Non-Absorbing lanthanide complexes discussed in Chapter 2 and use it make silica functionalised Non-absorbing lanthanide complexes and compare the **$EuSi_2$** SAMs surfaces for DBM analytes detection. In the beginning of this chapter we discuss the system design and synthesis of the **$EuSi_2$** (*figure 3.6*). Then we demonstrate attaching **$EuSi_2$** to the surface of silica microparticles, and how they can be used to visualise the dynamic event that indicates the mixing of two fluids under flow. We then show the development of bimodal silica microparticles, including the development of **EuQuinSi** (*figure 3.6)*, displaying the advantages of combining lanthanides and transition metals together. In contrast to this we introduce forming a SAM of **$EuSi_2$** on silica and demonstrate the switching on of luminescence through sensing DBM using luminescent microscopy and emission spectrometry, and how silica based SAMs can be used to screen small analytes. Towards the end of this chapter we screen and compare the limit of detection with small analytes in solution.

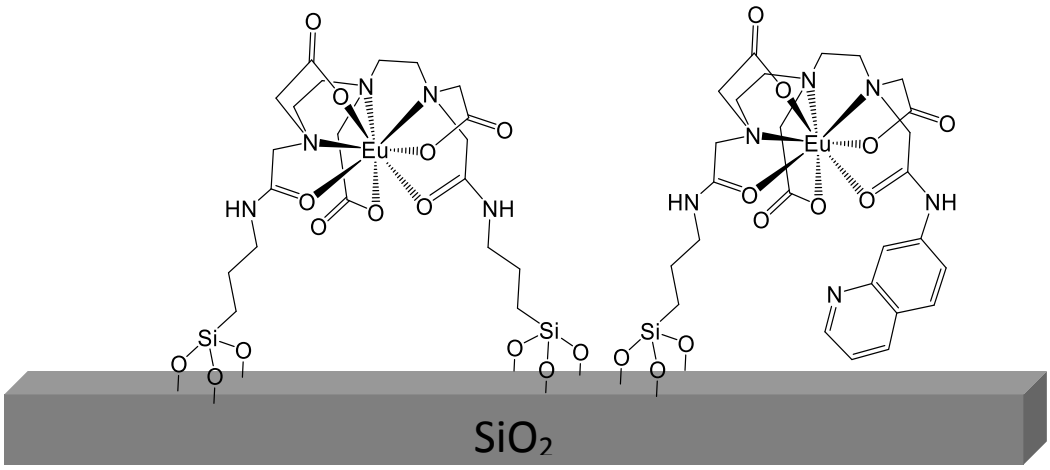

Figure 3.6 - Chemical structure of $EuSi_2$ (left) and EuQuinSi (right) bound to silica

3.3 - Surface Active DTPA - Bisamides as Non-Absorbing Ligands

3.3.1 - System Design of $EuSi_2$

The system which has been developed here use lanthanide sensitisation as recognition and is composed of three major components. The first component is that the **$EuSi_2$** which has no chromophore in its ligand architecture and thus lacks the capacity to effectively absorb UV-Vis radiation, and has very weak *f-f* luminescence without the presence of a chromophore. This allows it to be categorised as a lanthanide complex of a non-absorbing ligand (LnNAL), resulting in a relatively non-luminescent lanthanide complex. The second component of the system is the analyte, the component in which the system is designed to detect for. In this system, it has been designed to only detect analytes which have chromophoric units which have the correct excited state energy gap to undergo intersystem crossing to the lanthanide emissive state. The analytes have a size criteria, to be small enough to fit into the cavity of **$EuSi_2$** and have a coordinating functional group to directly bind to the lanthanide. The third component is a surface-active functional group. In the case of **$EuSi_2$**, it contains two silyl ether groups which can hydrolyse onto silica or silicon surfaces.

Placing complexes on a surface forms a scaffold allowing for a more controlled system to be created. Having a planar surface and surface attachment allows for the development of devices similar to lab-on-chip systems and gives advantages such as the ability to make the device regenerative, saving in costs. SAMs can be made with regenerative capabilities allowing the SAM to reused multiple of times, this allows for easier use to mobile user. An example of this would be in the case of field operatives in the military, where having one chip and using

it repeatedly is more efficient then carrying a one use vial of solution of the sensing system. Attaching complexes to microparticles surfaces allows a local point scaffold of high concentration, and multiple coatings for multiple combinatorial effects from the same nanoparticle. When **$EuSi_2$** is bound to a surface there is a pseudo macrocycle between the surface and **$EuSi_2$**. Whilst the ligand does contain a 3 carbon chain adjacent to the silicon atom, this will only allow relatively small molecules to bind into the cavity, preventing larger molecules from entering and binding. This restriction makes the system more selective for binding smaller and less sterically hindering analytes.

3.4 - Results and Discussion

3.4.1 - The Formation of H_3LSi_2

Here we show the synthesis of **H_3LSi_2** prepared over 3.5 hrs, as opposed to 24 hrs proposed in the literature,[99] sped up by the addition of sterically hindered bases; Dimethylamino pyridine (DMAP) and Diisopropylethyl amine (DIPEA). The procedure was carried out under nitrogen using standard Schlenk line techniques and under nitrogen atmosphere.

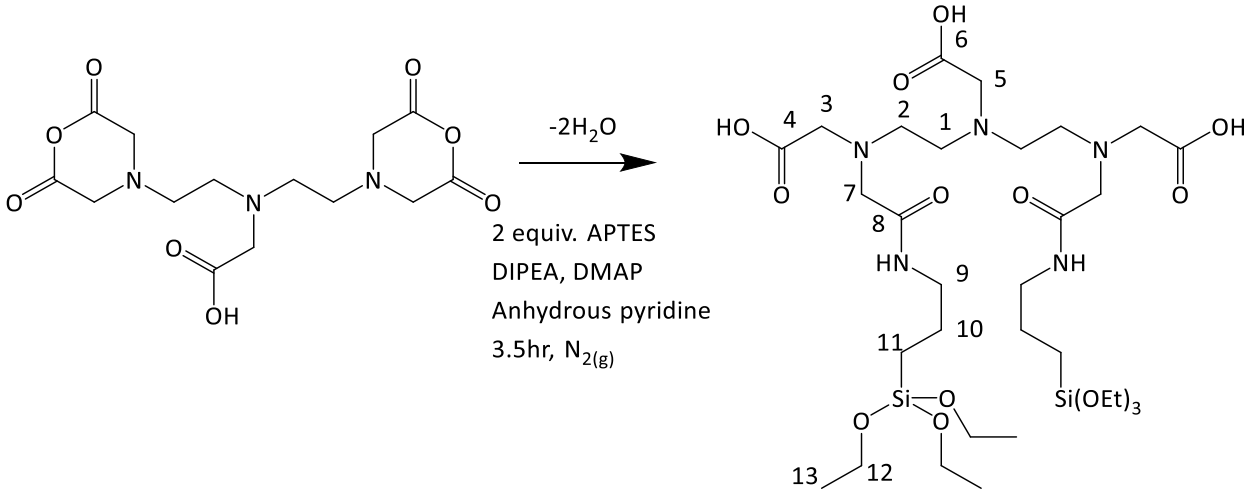

Figure 3.7-Reaction scheme for synthesis of H_3LSi_2

The 300 MHz ^{1}H-NMR spectrum of **H_3LSi_2** in d_6-DMSO is shown in *figure 3.7*. H-9 has shifted from 2.50 ppm to 3.05 ppm, integrating for 4H. This is indicative of the formation of an amide bond. The proton signals adjacent to the amide shows a downfield shift in the aliphatic region of the NMR spectrum. The amide bond formation N*H*CO appears as a new signal in the aromatic region on the NMR spectrum at 8.10 ppm represented by triplet and integrates for 2H. H-7 and H-5 has changed from a singlet into two new singlets, with H-7 moving downfield

to 3.34 ppm integrating for 4H and H-5 now appearing next to a carboxylic acid as opposed to an anhydride joining H-3 integrating for 6H. This is due to the change in symmetry about the molecule and the formation of a greater electron withdrawing amide bond. The ethylene backbone of H-1 and H-2 are indicated as separate triplets at 2.94 ppm and 2.81 ppm respectively. The silyl ether H-12 and 13 groups are shown at 1.18 ppm and 3.91 ppm and the propyl spacer environments are shown at 3.05 ppm and 1.49 ppm.

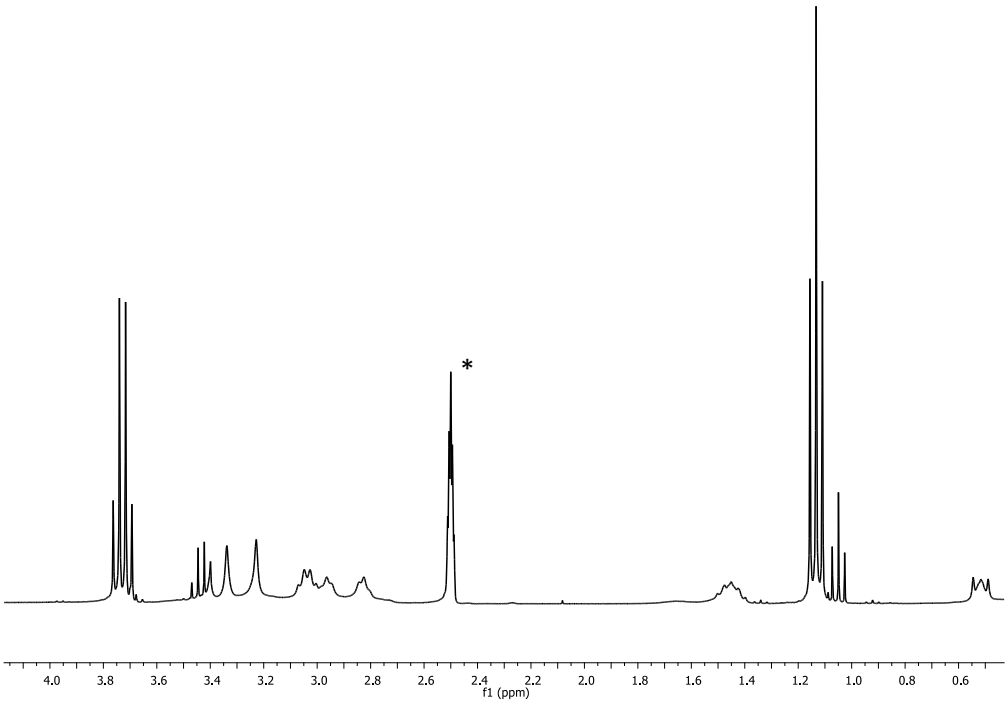

Figure 3.8- 400 MHz ^{1}H NMR spectrum of H_3LSi_2 in d_6-DMSO (*=solvent peaks).

The 100 MHz ^{13}C { PENDANT NMR spectrum of **H_3LSi_2** in *D_6*-DMSO is shown in *figure 3.8*. It contains 13 resonance peaks as expected. Positive-mode electrospray mass spectrometry confirmed the mass of the protonated ligand species at m/z 823 for the sodium adduct. The

methylated species at m/z 631 in negative mode electrospray mass spectrometry similar to what has been reported in the literature.[99]

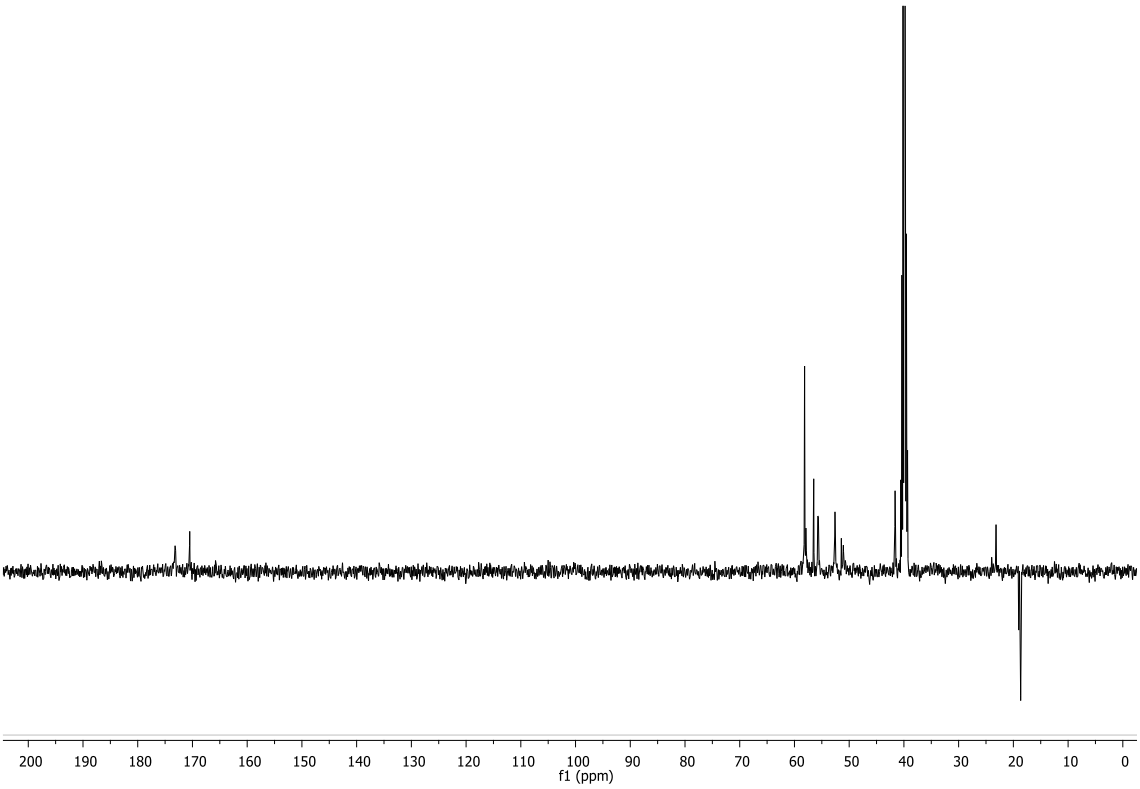

Figure 3.9- 100 MHz $^{13}C\{^{1}H$ PENDANT NMR spectrum of H_3LSi_2 in D_6-DMSO

3.4.2 - The Formation of H_3LQuinSi

H_3LQuinSi was synthesis via *figure 3.10* and characterised by ^{1}H-NMR and ^{13}C-NMR and ES^{+} mass spectrometry.

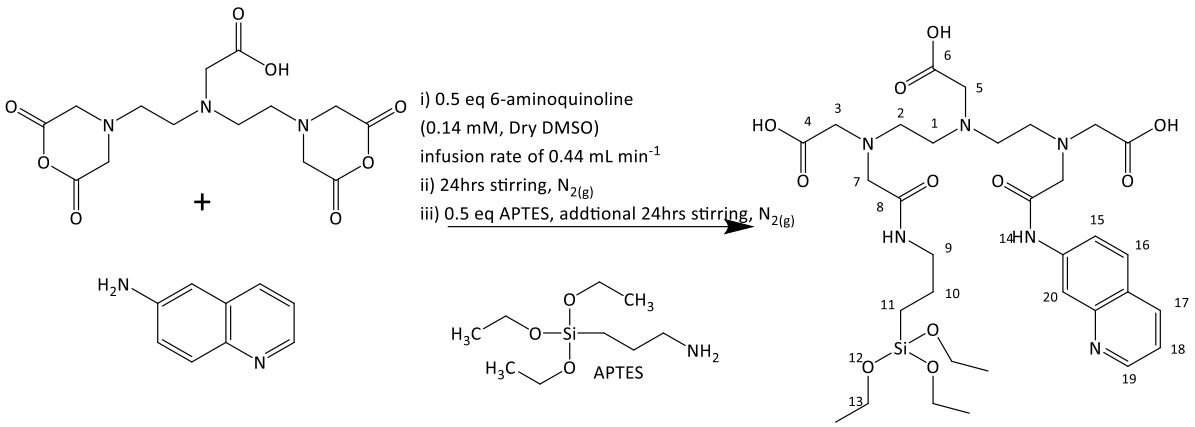

Figure 3.10 - Reaction scheme for the synthesis of H_3LQuinSi

The asymmetric ligand, **H_3LQuinSi** has similar changes in the proton NMR when compared to **H_3LSi_2**. The attachment of ATPES to the DTPA-dianhydride can be seen with the addition of the H-12 and H-13 groups which appear at 1.18 ppm and 3.91 ppm, whilst the propyl spacer environments are shown at 3.05 ppm and 1.49 ppm. The quinoline peaks are shown in the correct ratio of protonic environments 1:1 with respect to the APTES arm as expected. The opening of the anhydrides are shown by proton H-7 to moving downfield to 3.34 ppm for 4H due to amide bond formation and H-3 now appears next to a carboxylic acid as opposed to an anhydride joining H-5 to integrate for 6H. All the expected quinoline resonances have shifted downfield from the starting material. There are remnants of biproduct formation with no silica surface functional activity, NMR integration shows 40% bi-product formation which was

purified out during the nanoparticle purification phase. The major bi-product here is the H_3LQuin_2 complex with two quinolones, and no silyl functional group (*figure 3.11*).

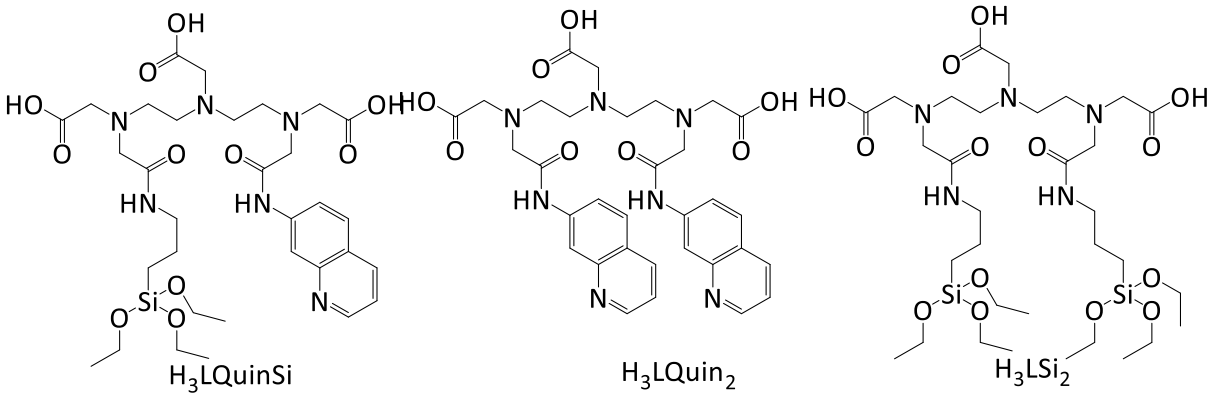

Figure 3.11- Chemical structures of the three products as of result of $H_3LQuinSi$ reaction.

After varying the synthesis, confirmation of the ligand being made was given by the ^1H NMR spectrum in D_2O. Despite the presence of the undesired H_3LQuin_2 ligand, the reaction was continued to attach the ligand to the microparticles, as the non-surface active ligand would be discarded during the purification process of the silica microparticles with water and ethanol and centrifiguation, leaving only the desired ligand active on the surface.

3.4.3 - The Formation of $EuSi_2$

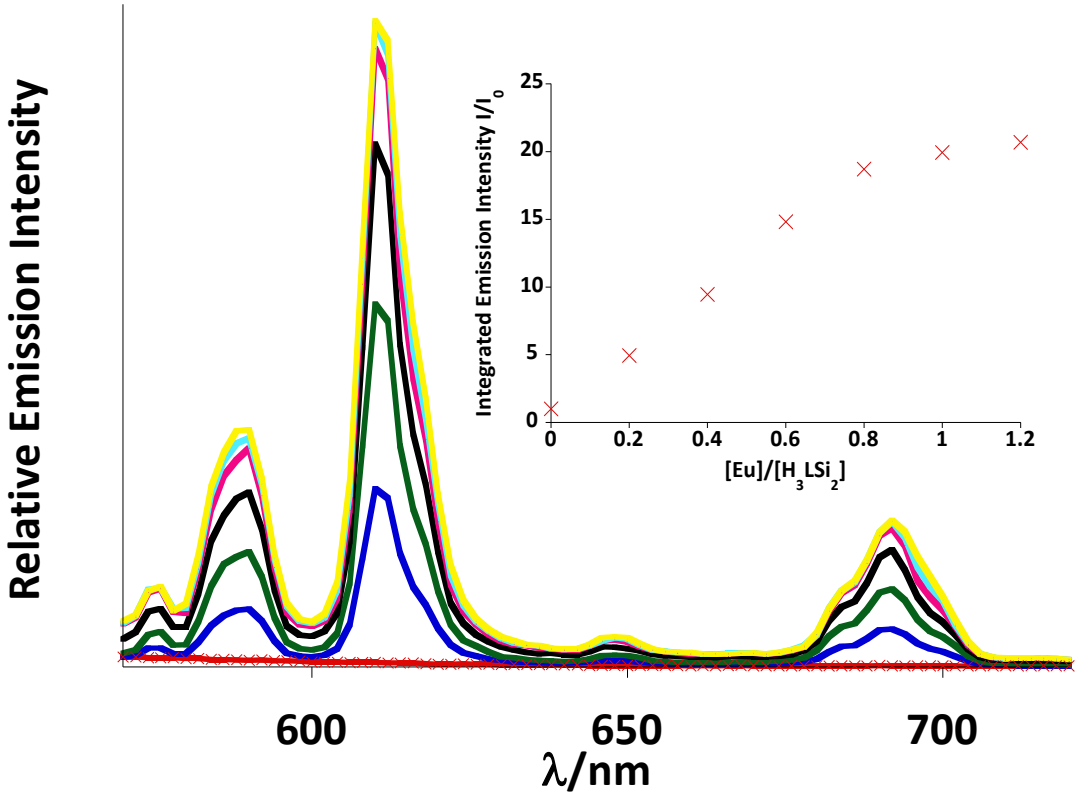

Figure 3.12- Left is the emission increase of $EuSi_2$ as an aqueous solution of $EuCl_3{\cdot}6H_2O$ (0-50 μL, in 10 μL additions, 9 mM) is titrated into an ethanolic solution of H_3LSi_2 (3 mL 0.15 mM), Right- integrated emission intensity plot against the molar equivalents of titrant added. λ_{exc}=395 nm

To confirm the formation of **H_3LSi_2**, the chelation of $EuCl_3{\cdot}6H_2O$ and **H_3LSi_2** to form **$EuSi_2$** was monitored *in situ* by emission spectroscopy (*figure 3.12*). $EuCl_3{\cdot}6H_2O$ (9 mM) was added incrementally (10 μL) to a stirring solution of **H_3LSi_2**. The lanthanide ion was excited directly at 395 nm ($^7F_0$-$^5L_6$) and the evolution of the luminescent profile of europium was monitored until a saturation point was observed. The titration showed the saturation peak occurring at 1.0 molar equivalents of $EuCl_3{\cdot}6H_2O$, followed by no significant increase in the next titration. The ligand is expected to be in a one to one ratio with the metal. MALDI showed the parent Ion

peak at 869 m/z. The emission spectrum (*figure 3.12*) clearly shows defined, sharp emission bands at 579, 594, 615, 652, and 696 nm in the red region of the visible spectrum, attributed to europium emissive states $^5D_0 \rightarrow {}^7F_J$ (J=4-0). The complex was then used as prepared in *situ* for analyte binding experiments, as isolation of the compound led to insolubility.

3.4.4 - Sensing for Dibenzoylmethane (DBM) with $EuSi_2$

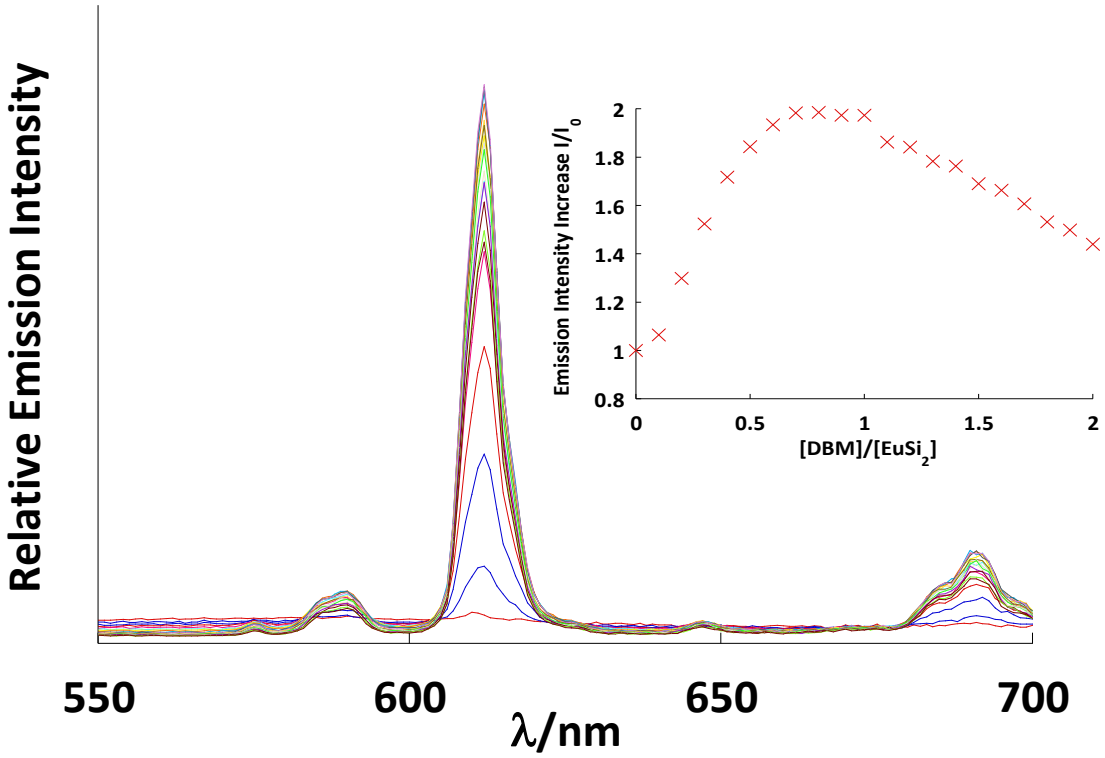

Figure 3.13 - (Left) Corrected emission spectra (λ_{ex}=370 nm) for titration of DBM (9 mM, 3 eq of NEt_3) into an ethanolic solution of $EuSi_2$ (0.12 mM), (inset) integrated emission intensity plot against the molar equivalents of titrant added.

Here we use an ethanolic solution of **$EuSi_2$** to sense DBM, a well-known sensitiser of europium, and in the case of **$EuSi_2$** sensitisation is observed in *figure 3.13*. The β–diketonate DBM is a bidentate molecule which coordinates through two ketone functional groups, potentially

forming a six membered with the europium ion. DBM also has a larger conjugated chromophoric system thus has a high molar absorption coefficient of 12400 cm^{-1} at 370 nm. **$EuSi_2$** and DBM are theoretically supposed to bind 1 to 1 molar equivalents as shown in *figure* 3.13 (right). After one equivalent of DBM has bound to **$EuSi_2$** the emission intensity starts to decrease due to the high molar absorption coefficient of DBM. With more unbound DBM present due to all the **$EuSi_2$** binding sites being occupied, the unbound DBM absorbs energy from the excitation source and as it's not bound to **$EuSi_2$** no energy is transferred to the europium, and thus resulting in a decrease in europium emission at the detector.

$EuSi_2$ was then attached to the surface of **Si_{800}** (*figure 3.14)* to produce microparticles with the surface coated in lanthanide complexes. The europium complexes were formed in situ and added to a collidial suspension of preformed **Si_{800}** microparticles. The **Si_{800}** are 800 nm sized silica particles that were synthesised by Dr. Lewis.[65,166]

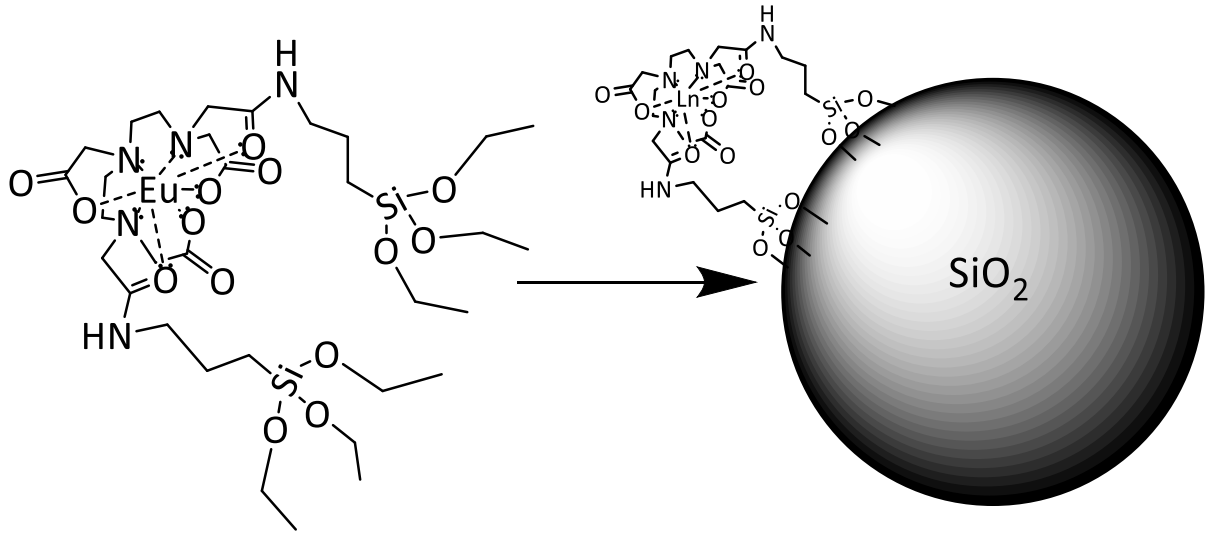

Figure 3.14 - Schematic diagram showing the attachment of $EuSi_2$ to the surface of Si_{800} silica microparticle.

These complexes attach to surface of the silica microparticles to give **$EuSi_2@Si_{800}$** and following purification, gave silica microparticles surface coated with europium complexes. **$EuSi_2@Si_{800}$** was used to investigate sensing under flow conditions and to visualise the mixing dynamics of two fluids.

3.4.5 - $EuSi_2$ on Silica Microparticles: Sensing in Flow with $EuSi_2$ Silica Microparticles

Here we present a flow system to monitor the sensing event occurring between **$EuSi_2$** on silica microparticles and the formation of a ternary complex with DBM in solution using luminescent microscopy (*figure 3.15*). The flow system utilises a custom made micro-channel device, pump and the luminescent microscope setup described in Chapter 6.

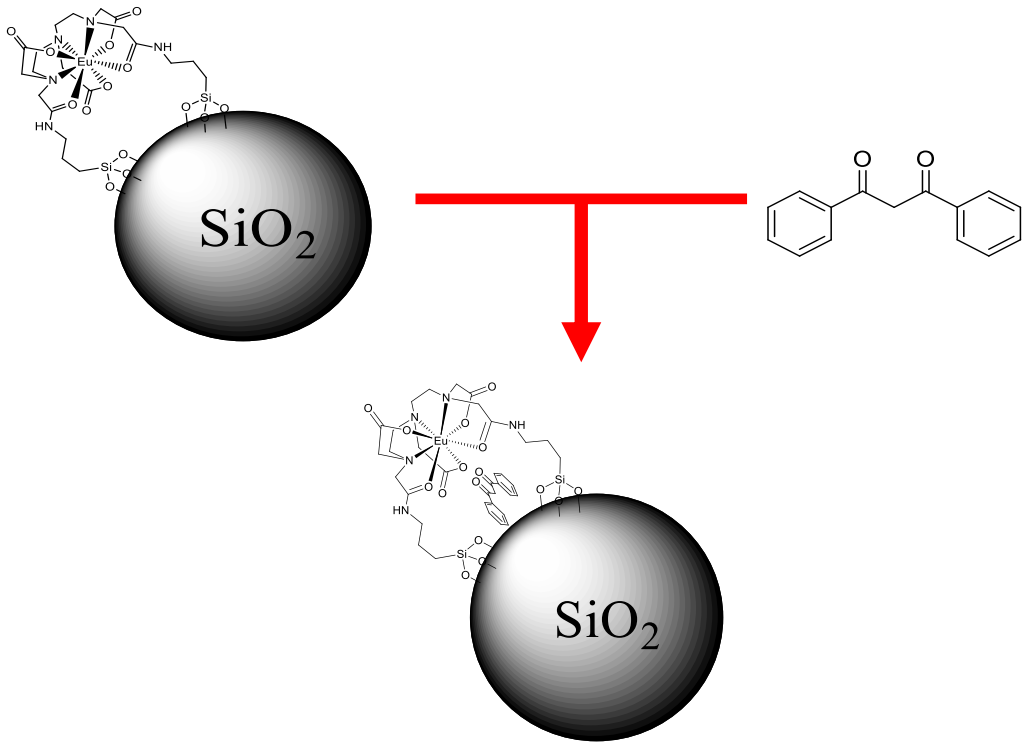

Figure 3.15- Shows the mixing of DBM analyte to $EuSi_2$ on a silica microparticles.

The custom made micro-channel were placed on the microscope stage and the **$EuSi_2$** coated silica microparticles and DBM analyte solutions were pumped into the micro-channel using a syringe pump, at a flow rate of 200 μL per minute. The flow rate was regulated by the syringe pump and visualised using the microscope in both the bright field and photoluminescence modes.

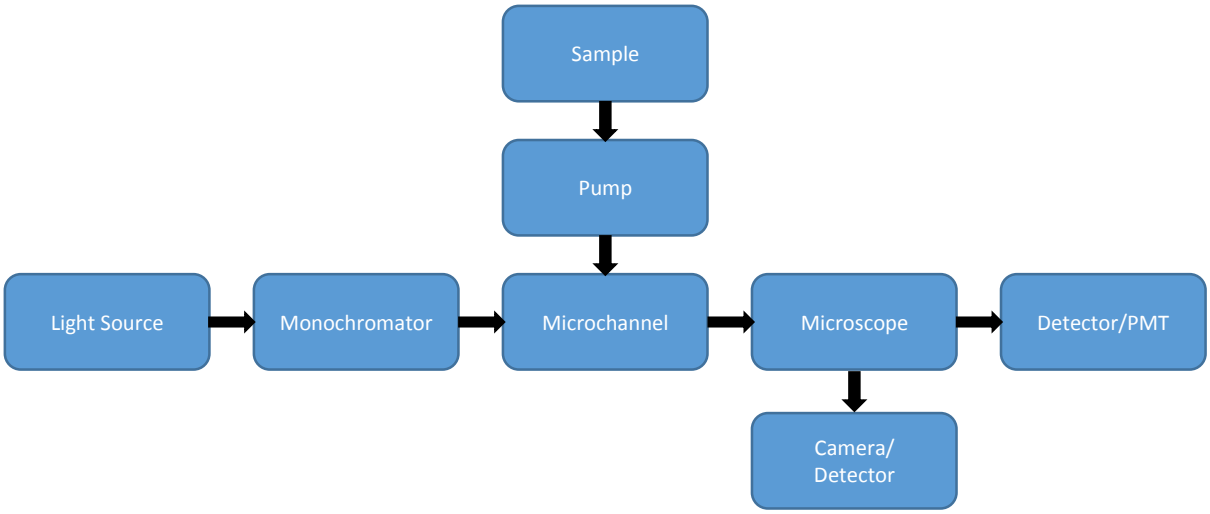

Figure 3.16- shows the generic system layout of the luminescent microscope setup.

During this experiment, two states of luminescence are expected. The first is the 'off-state', which is when DBM isn't present and not sensitising the **$EuSi_2$** silica microparticles. The second state is the 'on-state' which is when the solutions of **$EuSi_2$** silica microparticles are mixed with the DBM analyte solution and sensitisation of europium occurs generating lanthanide luminescence. When using the photoluminescence microscope, two excitation wavelengths were used; 395 nm and 370 nm. The 395 nm wavelength was used to excite the europium directly to observe the emission signal under direct excitation of **$EuSi_2$** coated silica microparticles in order to validate the presence of the europium microparticles, and to verify the intensity of the proposed "off-state" (*figure 3.19*). This could be used to compare the luminescence intensity of the "on state" and the indication of the analyte presence (*figure 3.20)*. The 370 nm wavelength was used to excite the DBM directly (on-state) to see if energy transfer from the excited DBM to the **$EuSi_2$** was occurring whilst the two solutions where

mixing together and if any europium signal is present which would indicate ternary complex formation.

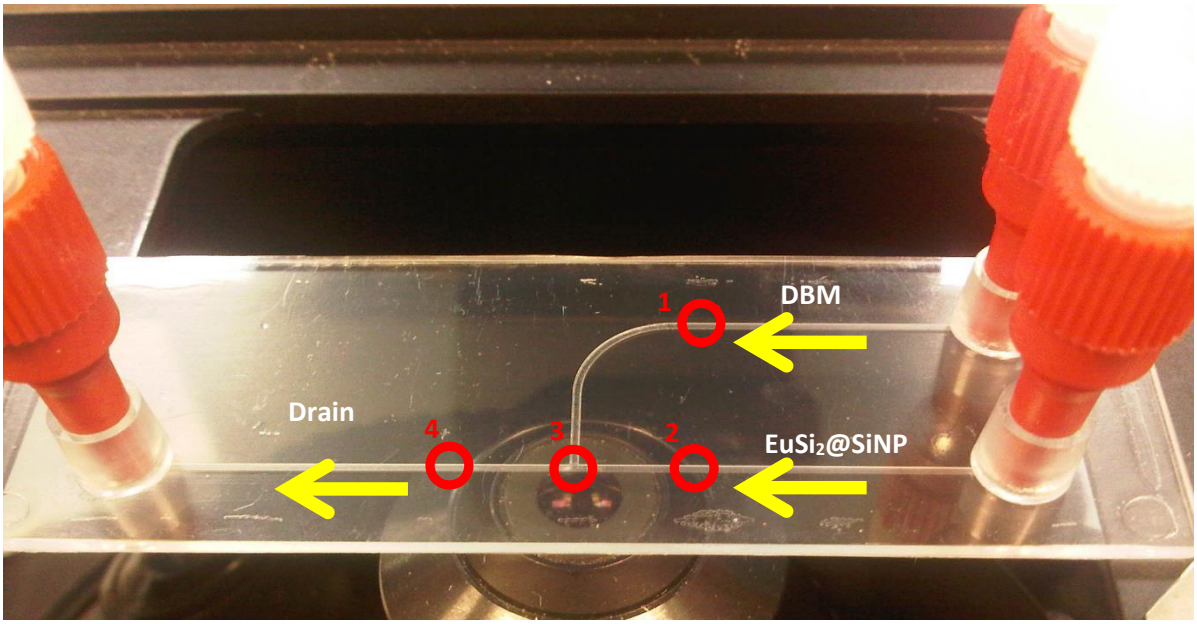

Figure 3.17- Photograph of the microfluidic channel used for the detection of DBM using luminescence microscopy

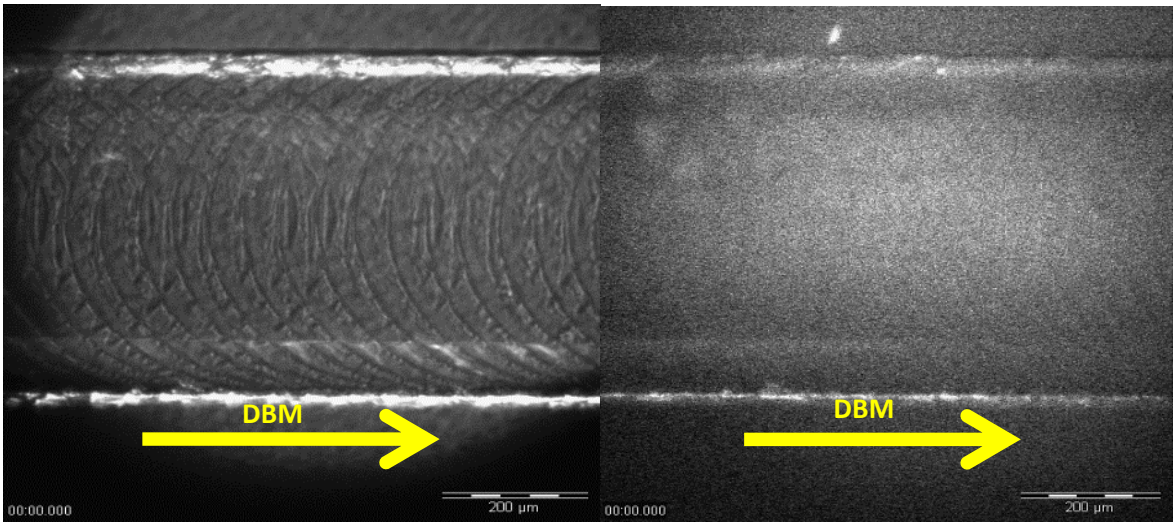

Figure 3.18 - Microscope images of the microfluidic device at position 1. (Left)- Bright field image. (Right) Epiluminescence image (>510 nm). The arrow indicates the direction of flow. NB-circular lines are a defect as a result of the manufacturing process.

Two images of the DBM ethanolic solution flowing from left to right are shown in *figure 3.18*. The bright field image shows a clear solution as one would expect. The epiluminescence image shows all luminescence signals arising from the channel with a wavelength of 510 nm or greater, due to the 510 nm dichroic filter in place in the microscope. The emission profile of DBM is a broad band from 400 nm to 500 nm. Thus no signal is expected to be found in the DBM channel, as the luminescence signal would be removed by the presence of the dichroic filter. This is important because when we view the channel under the luminescence mode, any luminescence is displayed by intensity and not by wavelength. Hence without the presence of the 510 nm dichroic filter, we would not be able to visually distinguish the fluorescence from the DBM molecules and the luminescence arising from the europium silica microparticles flowing in the channels. An emission scan was recorded over the range of 550-

750 nm, which provided that just background noise was observed and no europium signal was present.

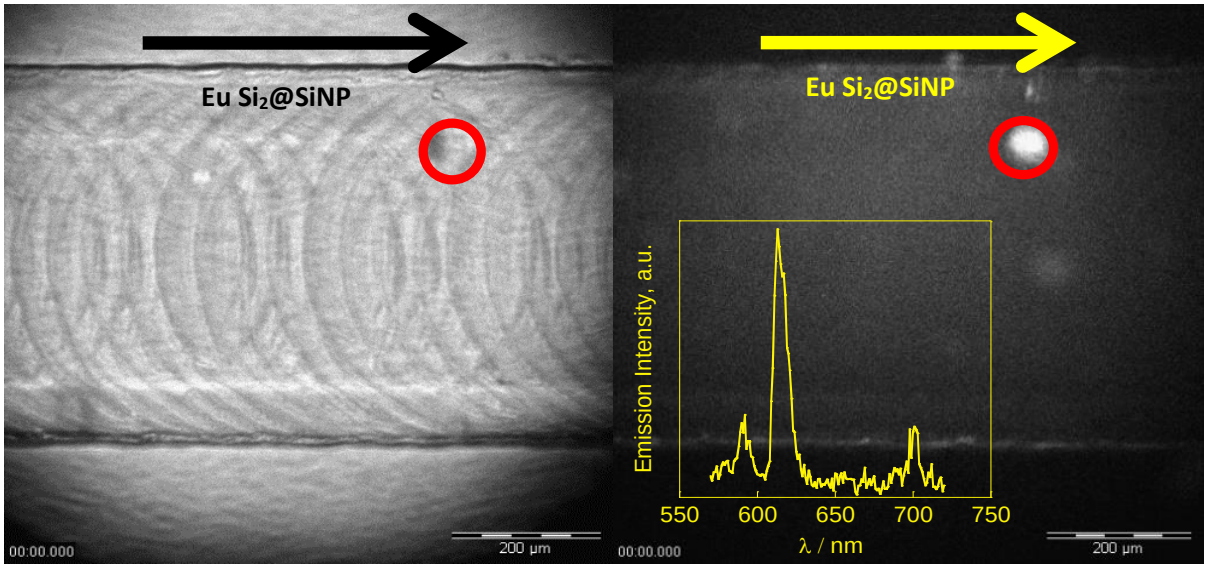

Figure 3.19 - Microscope images of the microfluidic device at position 2. (Left)- Bright field image. (Right) Epiluminescence image (>510 nm). The arrow indicates the direction of flow. λ_{exc}=395 nm, λ_{em}=614 nm

At position 2 on the microfluidic device, (*figure 3.19)*, we see from the bright field image that the microchannel is similar to the bright field image containing the ethanolic DBM solution, it is a colourless and clear solution. However we can also note an additional defect in the channel circled in red. Looking at the epiluminescence of the channel we can see an anomaly. The anomaly is bright compared to the rest of the channel, whilst observing this in flow we noticed that this concentrated spot did not move with the flowing current provided from the syringe pump and concluded that this must be a result of a build-up of microparticles in a defect within the microchannel. In this instant we used two wavelengths to investigate the channel. The first was the wavelength used to excite DBM, 370 nm, this resulted in no europium emission being detected. However using emission spectroscopy, exciting the europium directly, and in

conjunction with the nanoparticle build within the defect, we was able to confirm the presence of **$EuSi_2$** coated silica microparticles within the channel.

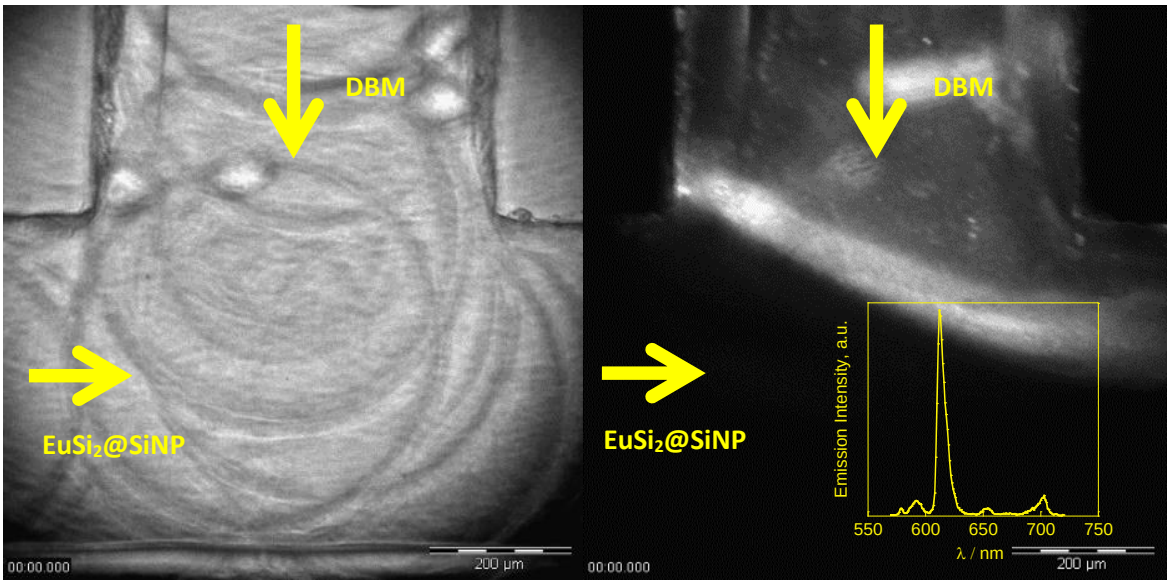

Figure 3.20- Microscopy images of the microfluidic device at position 3. (Left)- Bright field image. (Right) Epiluminescent image (>530 nm). The arrow indicates the direction of flow see previously figure 3.17. λ_{exc}= 370 nm,λ_{em}=614 nm

Position 3 is located at the T-Junction, the merging point of the two microchannels; the receptor solution **$EuSi_2$** and the analyte DBM. The T-Junction is clearly shown in *figure 3.20* where the ethanolic DBM solution is coming down from the top of the image, and the **$EuSi_2$@SiNP** aqueous solution flowing from left to right. Again the channels are clear and colourless. However whilst looking at the epiluminescence image we can see a clear activation of the receptor solution evident by strong luminescence across the merging gradient of the two solutions.

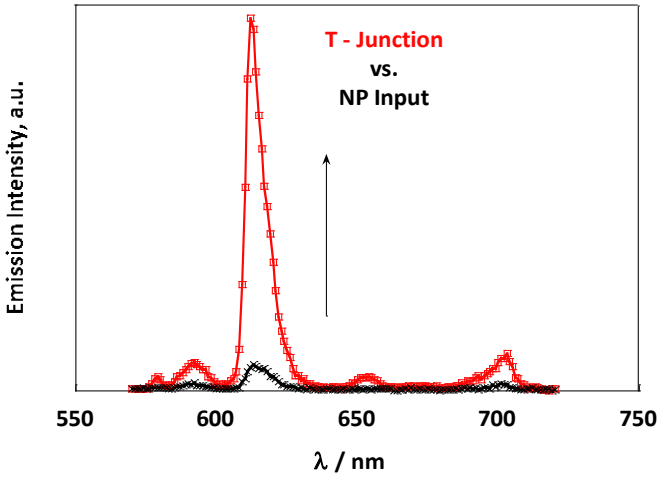

Figure 3.21 - Emission spectra comparing the emission profiles of (X) $EuSi_2$@SiNP and (□) EuSi2@SiNP-DBM at positions 2 and 3 on the microfluidic device respectively.

The 'on-state' shows 760 % increase in the luminescent intensity from the off state (*figure 3.21*). This is an eight- fold increase in luminescence intensity, which is greater than the two-fold luminescent intensity increase in solution. This shows that **$EuSi_2$** is better sensitised by DBM on an anchored surface than in solution.

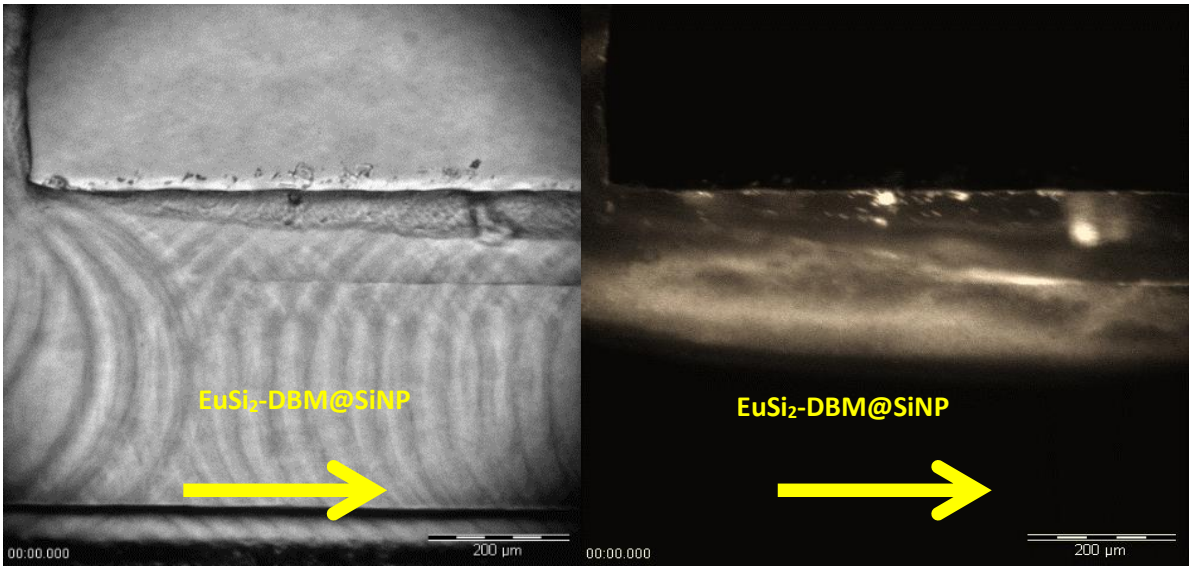

Figure 3.22-Both images are of the microfluidic device at position 4. (Left)- Bright field image. (Right) Epiluminescent image (>530 nm). The arrow indicates the direction of flow.

Position 4 is at the drain in the device, where waste solution is collected (*figure 3.22*). Whilst looking at the epiluminescence of the drain microchannel we can see the activated luminescence of the europium coated silica microparticles, but also a dark shadow on the lower portion of the microchannel. Though speculation we can say that this is due to the different flow currents involved in the microchannel, where the force of the incoming flow of **$EuSi_2$@SiNPs** is greater than that of the DBM solution. Even though the flow rate for both channels were set to the same flow rate, the laminar flow from the DBM channel is reduced because of the bend in the microchannel reducing the overall force arriving at the T-Junction. The greater laminar flow arriving from europium coated silica microparticles channel prevents uniform mixing of the solutions at the T-junction and the drain, where the current is too strong for DBM to mix uniformly and form a ternary complex with **$EuSi_2$** throughout the channel. This leaves europium sensitisation to occur only where the two solution current fronts collide, and

an absence of activation where the DBM isn't present. The luminescence was again measured by emission spectroscopy to give a characteristic europium profile of similar intensity to the T-Junction. This experiment gives us an insight to mixing dynamics of two fluids across a T-Junction which could be used to study fluid dynamics in laminar flow systems or developed further into protein recognition within tissues to localise protein concentrations points.

3.4.6 - Dye Encapsulated Bimodal Silica Microparticles - $LnSi_2@Si_{500} \subset Ru(Phen)_3$

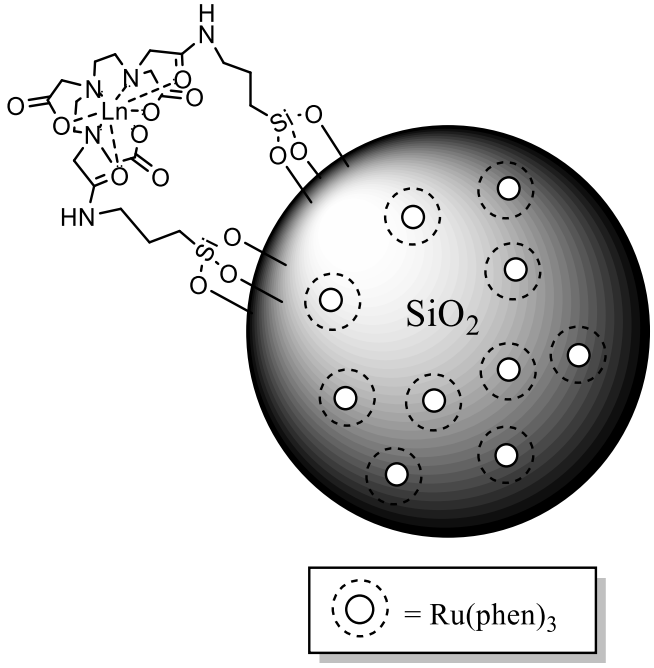

Figure 3.23 - Schematic representing $LnSi_2@Si_{500} \subset Ru(Phen)_3$

The design of **H_3LSi_2** was used for development of bimodal microparticles (*figure 3.23*). Bimodal microparticles can be prepared with MRI active compounds, fluorescent organic dye, luminescent lanthanide complexes and fluorescent transition metal complexes depending on their desired functionality. Bimodal probes that combine the use of lanthanides and transition

metals would allow emission signals from both the lanthanide attached and the dye in the interior of the nanoparticle to be collected. Thus bringing the brightness of $[Ru(Phen)_3]Cl_2$ and the time gated characteristic lanthanide emission profiles and large stokes shift into one probe. In this part of the chapter we will discuss the use of lanthanide coated silica microparticles in combination with encapsulation of ruthenium trisphenathroline in the silica nanoparticle's core. We also will show the functionalization of silica microparticles with **EuQuinSi**, with and without transition metal cores. The synthesis and characterisation of the microparticles, and dye encapsulated microparticles has been previously carried out within the Pikramenou group by Mark Goodwin and Dr. David Lewis.[167]

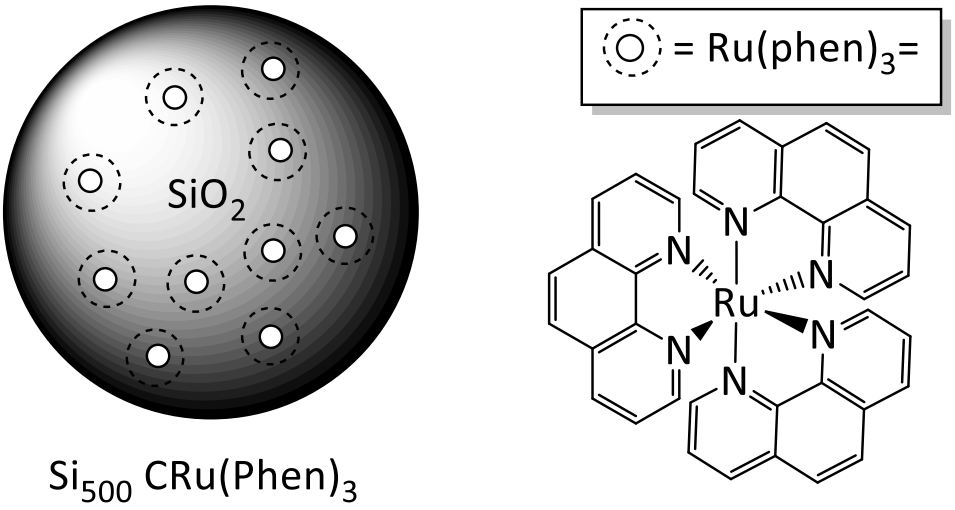

Figure 3.24 - Schematic representing $Si_{500} \subset Ru(Phen)_3$

Before studying the effect of on **$LnSi_2$** on the surface of silica microparticles with encapsulated $[Ru(Phen)_3]Cl_2$ inside the core of the silica microparticles, the effect of encapsulating $[Ru(Phen)_3]Cl_2$ inside of silica microparticles was studied (*figure 3.24*). $[Ru(Phen)_3]Cl_2$ encapsulated silcia microparticles ($Ru(Phen)_3 \subset$SiNP) were characterised by emission and

excitation spectroscopy, luminescence lifetime measurements, quantum yield and UV-Vis spectroscopy. A standard solution was also made to compare the effect of dye encapulation against the photophysical properties of the complex. A UV-Vis spectra of the standard solution and of the dye encapsulated microparticles were taken and when compared the absorbance spectra of the microparticles, the absorbance bands of the dye were not observed; due to the scattering of the silica microparticles. The $[Ru(bpy)_3].Cl_2$ measurements were taken as control, a 100% loading standard. This was needed in order to quantify the concentration of encapsulated dye emission and excitation spectroscopy was used.

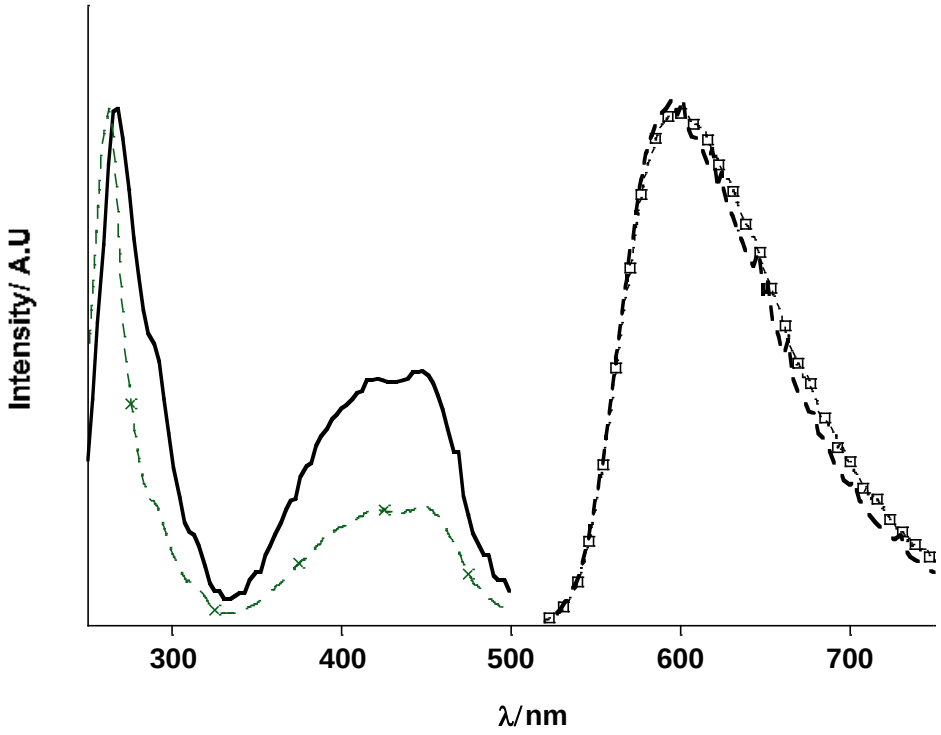

Figure 3.25 - (- - -) Normalised emission spectrum of Si_{500} ⊂$Ru(Phen)_3$ and (-□-) Normalised emission spectrum of $[Ru(Phen)_3]Cl_2$ ethanonlic solution. (-X-) Normalised excitation spectra of Si_{500} ⊂$Ru(Phen)_3$ stained particles and (—) excitation spectrum of $[Ru(Phen)_3]Cl_2$ ethanolic solution. λ_{exc}=450 nm, λ_{em}=600 nm

The $[Ru(Phen)_3]Cl_2$ emission and excitation spectra from the dye encapsulated microparticles (*figure 3.25*) are quite conclusive that the dye is present in the microparticles with good absorption of the ^{1}MLCT and $\pi-\pi^*$ transitions at 450 nm and 280 nm respectively in the excitation spectra. The emission from the ruthenium ^{3}MLCT is seen for both the $[Ru(Phen)_3]Cl_2$ and the **Si_{500}⊂Ru(Phen)$_3$** microparticles.

Table 3.1-Shows the lifetimes of the ruthenium species, in oxygenated atmosphere and inert atmosphere compared to encapsulate conditions.

Species	**Lifetime / ns**
$Ru(phen)_3$ stained Si_{500} Microparticles	1260
$[Ru(Phen)_3]Cl_2$ H_2O	420
$[Ru(Phen)_3]Cl_2$ EtOH aerated	190
$[Ru(Phen)_3]Cl_2$ EtOH degassed	370

The lifetime *(table 3.1)* of the dye in the interior of the nanoparticle are much higher than the 'free' dye complexes in the standard solutions in EtOH and water. This is due to the protective matrix of the silica microparticles preventing quenching from the oxygen triplet state. [168]

In order to compare the $[Ru(Phen)_3]Cl_2$ encapsulated microparticles as a luminescent probe, the concentration of the encapsulated dye was calculated by using emission spectroscopy. An estimate for dye loading of both microparticles was found by measuring the emission difference between the first supernatant collected from centrifugation-redispersion

methodology used in the purification process against a standard composed of a solution that would represent maximum concentration. The standard was made by using the same quantity of solvents and $[Ru(Phen)_3]Cl_2$ as in the nanoparticle synthesis, but omitting the TEOS and replacing it with water to stop the formation of microparticles.

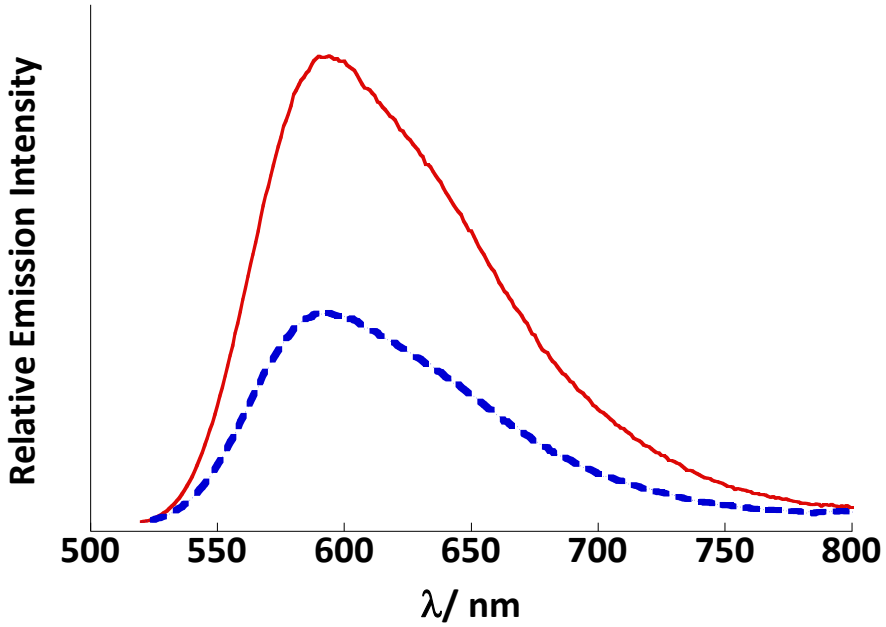

Figure 3.26 - (—) Emission spectra of the standard $[Ru(Phen)_3]Cl_2$. (- - -) Emission spectrum of $[Ru(Phen)_3]Cl_2$ supernatant. Emission spectrum displaying how much $[Ru(Phen)_3]Cl_2$ was not absorbed into silica microparticles. λ_{ex}=450 nm

Table 3.2- The table shows the result of the estimation of dye loading

SiNPs	**Peak area**	**$[Ru(Phen)_3]Cl_2$ % Loading**	**$[Ru(Phen)_3]Cl_2$ / mmol mL^{-1}**	**$[Ru(Phen)_3]Cl_2$ in SiNP / mmol mL^{-1}**
500 Standard	8.3×10^7	-	4.7×10^{-3}	-
Si_{500} $\subset Ru(Phen)_3$	4.5×10^7	**46%**	-	2.2×10^{-3}

The concentration of $[Ru(Phen)_3]Cl_2$ that has been loaded into the silica microparticles is shown in table 3.2. Integration of the emission spectrum (*figure 3.26*) for both the standard and the supernatant can give us a percentage of loading and from this work out an approximate concentration of dye in the microparticles of 2.2 mM which is 46% of the dosing concentration. Once the concentration of $[Ru(Phen)_3]Cl_2$ encapsulated on the inside of silica microparticles had been established we attached **$EuSi_2$** and **$NdSi_2$** to the outside surface of the silica microparticles.

$EuSi_2$ and **$NdSi_2$** were attached to the surface of **Si_{500}⊂Ru(Phen)$_3$** (*figure 3.27)* in attempt to produce microparticles with dual functionality. The lanthanide complexes were formed in situ and added to a collidal suspension of preformed **Ru(Phen)$_3$⊂SiNP**.

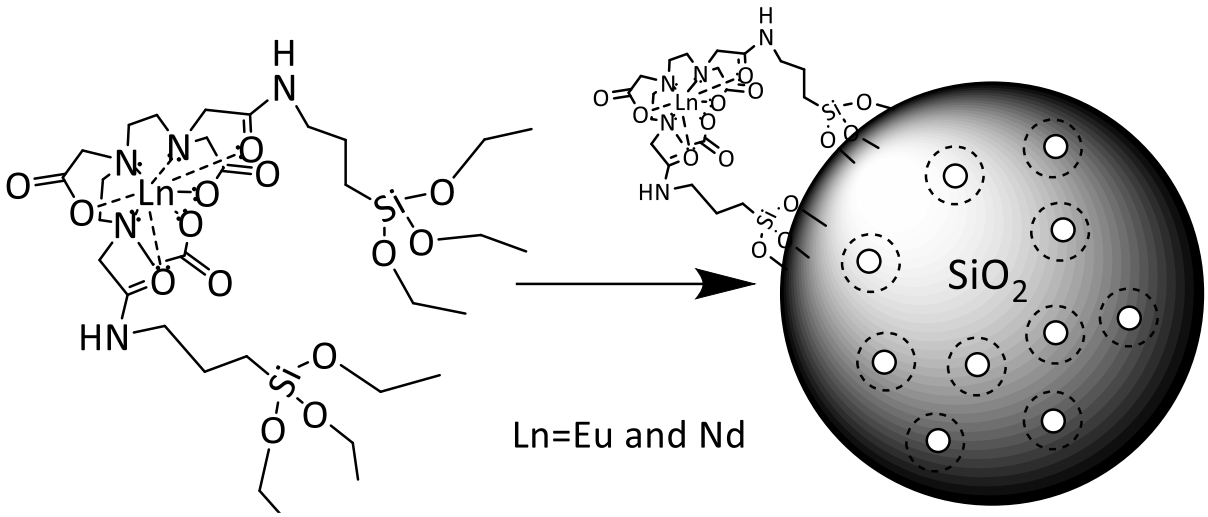

Figure 3.27-Schematic diagram showing the attachment of $LnSi_2$ to the surface of Si_{500}⊂Ru(Phen)$_3$

These complexes attach to surface of the silica microparticles to give **$LnSi_2$@ Si_{500}⊂Ru(Phen)$_3$** and following purification, gave silica microparticles with dual funtionality.

$EuSi_2$@Si_{500}⊂Ru(Phen)$_3$ and **$NdSi_2$@Si_{500}⊂Ru(Phen)$_3$** were tested for visible and NIR emission respectively. We examined the microparticles to observe if there was any energy transfer between the encapsulated $[Ru(Phen)_3]Cl_2$ and the surface bound **$LnSi_2$**. Unfortunately no lanthanide emission was obtained for either microparticles, this indicates that no energy transfer processes occurs to the lanthanide complex from the $[Ru(Phen)_3]Cl_2$. Naturally the *f*-

f absorption transition is forbidden and would give a very weak signal, negligible in this case, and without sensitisation lanthanide emission is not expected to be seen under these conditions. The only possible way that lanthanide emission would be observed is if there was an energy transfer process from the $[Ru(Phen)_3]Cl_2$ to the lanthanides, however due to significant distance between the TMs and lanthanides, no lanthanide emission was observed.

Non-$[Ru(Phen)_3]Cl_2$ encapsulated microparticles with the same lanthanide complexes attached on the surface were synthesised as a control and gave no emission from the lanthanide ions as expected. This indicates that the $[Ru(Phen)_3]Cl_2$ emission was not overwelming any weak europium emission that would occur through direct excitation of the lanthanide, but reinforces the fact that there is no sensitisation from the $[Ru(Phen)_3]Cl_2$ to the lanthanide. To obtain the combinatory properties of these to probes, the lanthanide system needs to modified to work independently of the $[Ru(Phen)_3]Cl_2$.

$EuSi_2@Si_{500}\subset Ru(Phen)_3$ and **$NdSi_2@Si_{500}\subset Ru(Phen)_3$** showed no lanthanide emission properties. We believe this to be lack of sensitisation from the $[Ru(Phen)_3]Cl_2$ through the silica wall. Thus through modification of the $LnSi_2$ ligand architecture we aim to obtain lanthanide emission.

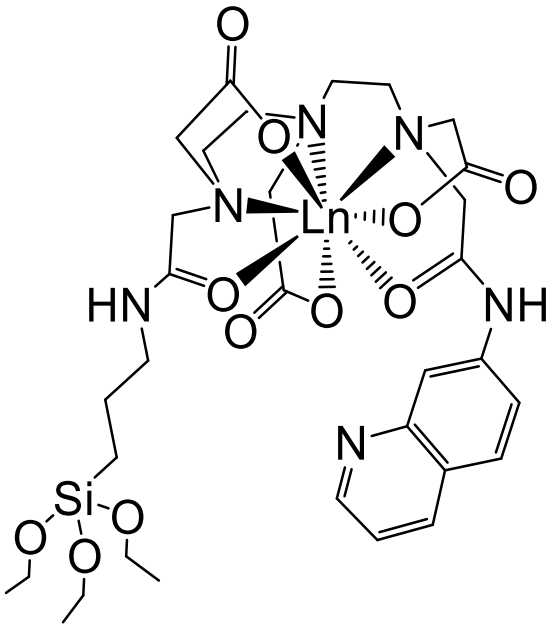

Figure 3.28 -The chemical structure of the redesigned lanthanide complex, incorporating quinoline.

The surface silica attachment here has been redesigned to incorporate a sensitiser quinoline, into the mother ligand (*figure 3.28*). The quinoline sensitiser group is added to populate, via energy transfer from its triplet state, the emissive state of lanthanide metal ions bound in the ligand to give a long-lived luminescence signal. The sensitiser has an energy level at 21000 cm^{-1} which is found to populate a range of lanthanide triplet states for luminescence signals.[169] Previously the symmetric ligand has been made to give emission from lanthanide with good success. By incorporating the quinoline directly into the system it allows for dual-luminescence detection, thus increasing the usefulness of the probe. Also the new ligand will be less restrictive in nature than **H_3Si_2** as the **H_3LQuinSi** ligand would allow greater water

exchange for use with gadolinium giving it greater potential for use as an MRI contrast agent, but also open potential to sense for larger molecules binding to europium or neodymium. The shape of the ligand with the open DTPA backbone has been predicted to make it possible for two water molecules to be coordinated to the lanthanide, hence increasing the number of water molecules undergoing exchange and the efficiency of the contrast agent.[17,31]

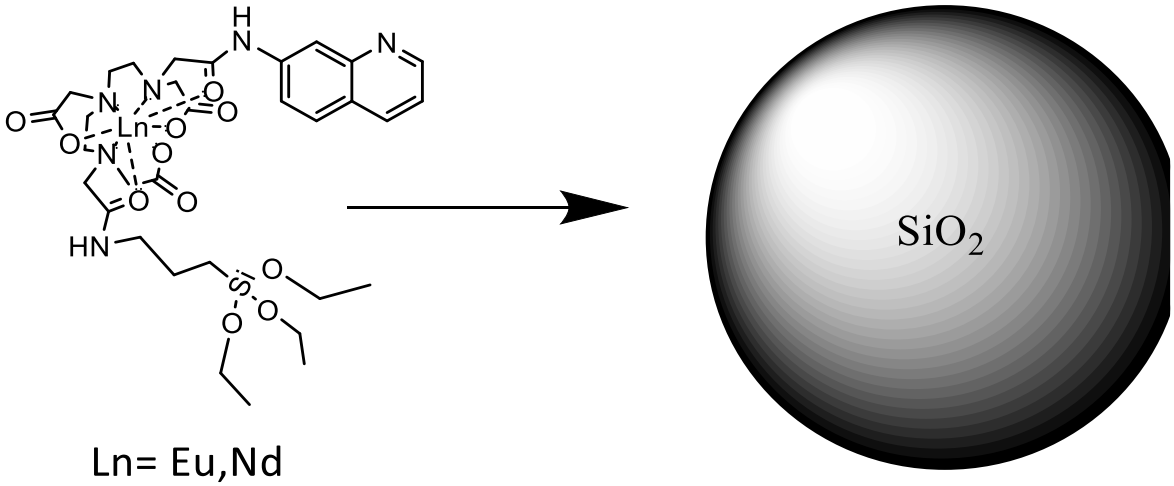

Figure 3.29 - A representation of chemical structure of LnQuinSi binding to the surface of a 500nm sized silica nanoparticle.

EuQuinSi@Si$_{500}$ has no $[Ru(Phen)_3]Cl_2$ in the core of the silica nanoparticle and only the asymmetric lanthanide complex attached to the outside surface (*figure 3.29*). The microparticles gave a clear europium emission signal upon excitation at 320 nm *(figure 3.29*). This indicates the successful sensitisation of the europium emission signal by energy transfer from the quinoline. The excited triplet state transfers energy to the emissive $^5D_0$ state of europium which gives a luminescence signal when relaxing to the ground state vibrational levels of $^7F_{4\text{-}0}$. The peaks observed are characteristic sharp transitions expected of the

lanthanide ion indicating the europium complex is present in the silica matrix of the nanoparticle.

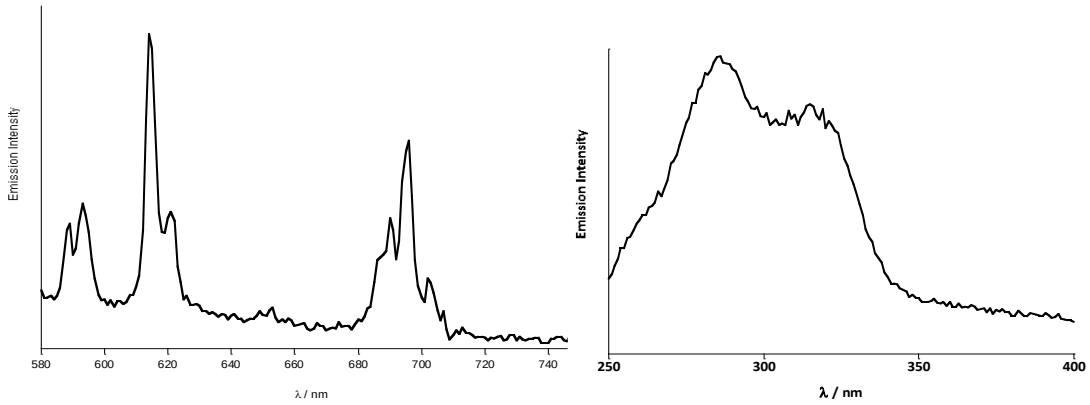

Figure 3.30- (Left) Emission spectrum of EuQuinSi@Si$_{500}$, (Right)- Excitation spectrum of EuQuinSi@Si$_{500}$ microparticles in water, (0.1% wt), λ_{ex}=320nm, λ_{em} = 618 nm.

The excitation spectrum (*figure 3.30, right)* of the particles shows the presence of the quinoline ligand from the band 300-350 nm for the S_0 to S_1 internal conversion transition. The lower band at ~290 nm, is the shoulder peak of quinoline from the complex attributed to the $\pi-\pi^*$ transition within the quinoline fused ring system. The lifetime was measured for these microparticles, and was found to be 520 μs, providing further evidence of complex attachment to the silica microparticles.

NdQuinSi@Si$_{500}$ was also synthesised in order to use the infrared emissive properties of neodymium. No near-infrared emission was measured from the microparticles with the asymmetric ligand complex. This is probably due weak loading of the lanthanide coated microparticles, resulting in a poor emission intensity. Deuterated methanol and deuterated

water were used as solvents to try and reduce quenching of any neodymium emission and enhance signal, this however did not result in any detection of neodymium emission.

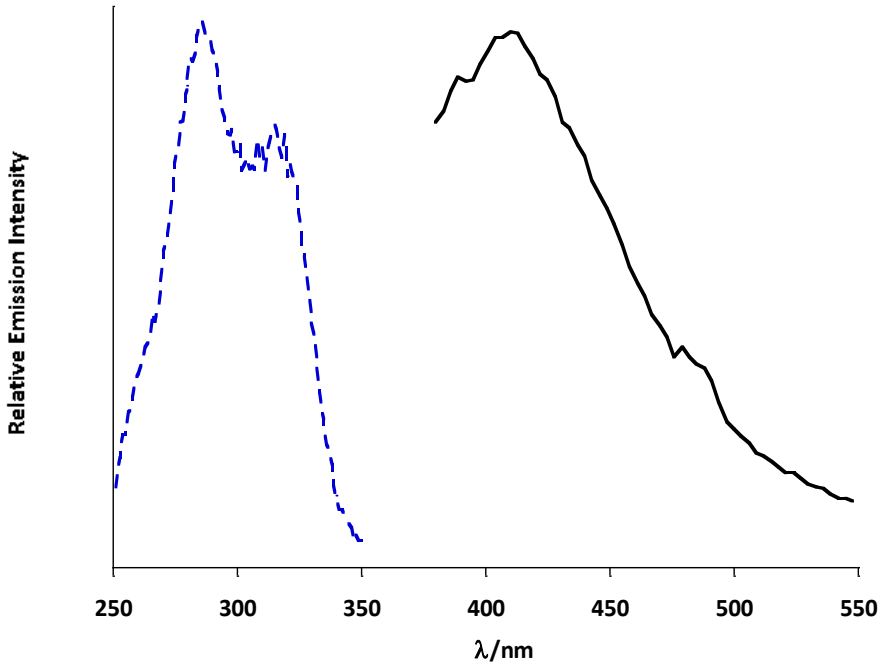

Figure 3.31 - Emission and excitation spectrum showing the ligand fluorescence of NdQuinSi@Si$_{500}$. Normalised (---) Excitation spectrum of NdQuinSi@Si$_{500}$ and (—) Emission spectrum of NdQuinSi@Si$_{500}$, λ_{exc}=320 nm, λ_{em}=420 nm coating in water, (0.1% wt).

The ligand emission and absorbance was measured to see if despite the lanthanide not emitting, the ligand had been attached to the microparticles. This led to the conclusion that the ligand is present on the microparticles. The emissive energy levels of the neodymium do match up to receive intramolecular energy transfer from the triplet state of quinoline, resulting in the fact that the neodymium may not have been chelated by the complex. *Figure 3.31* only shows the fluorescence from the excited singlet state to the ground state of the ligand. If there was energy transfer to the lanthanide then we would expect the emission from

the ligand to be reduced, however this was not the case, this was tested by binding the ligand to the surface of the microparticles and titrating in neodymium ions. The excitation spectra confirmed the presence of the ligand. Ytterbium was also attempted under the same conditions as neodymium, resulting in the same conclusion. Unfortunately no NIR emission was detected for neodymium or ytterbium, only europium emission was detected on the surface of the silica microparticles, thus we then attached **EuQuinSi** to the surface of **Si_{500}⊂Ru(Phen)$_3$** silica microparticles (*figure 3.32*) and tested them for dual functionality.

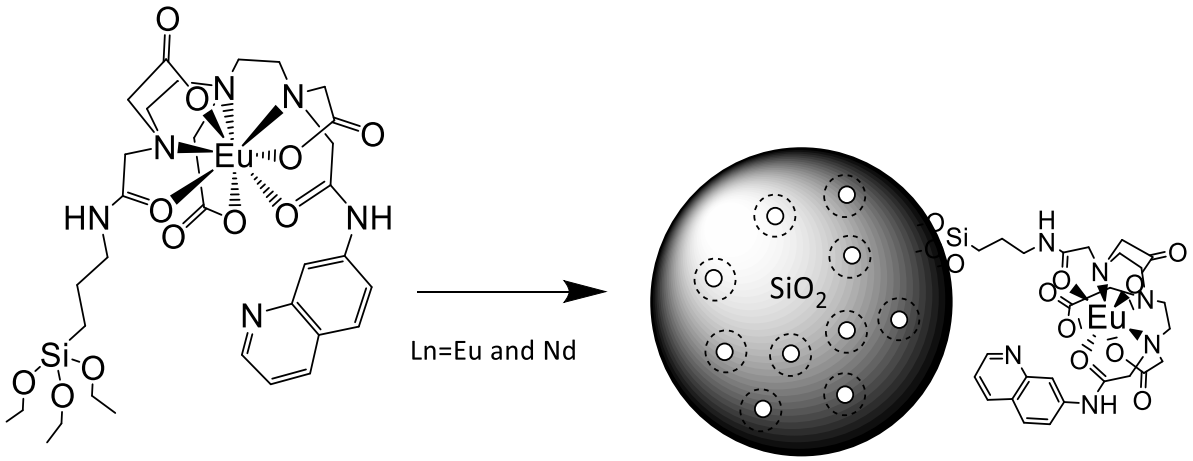

Figure 3.32 - Diagram showing the attachment of EuQuinSi to the surface of encasulation {Ru(Phen)$_3$]Cl$_2$ silica microparticles.

The emission spectrum of the **EuQuinSi@Si_{500}⊂Ru(Phen)$_3$** is shown in *figure 3.33*. The spectrum successfully shows that whilst exciting the quinoline at 320 nm we can observe the unique europium emission profile from the surface of the microparticles. The spectrum does show peaks of both emitting complexes, the europium and ruthenium due to the absorption overlap of quinoline and ruthenium (III) trisphenanthroline.

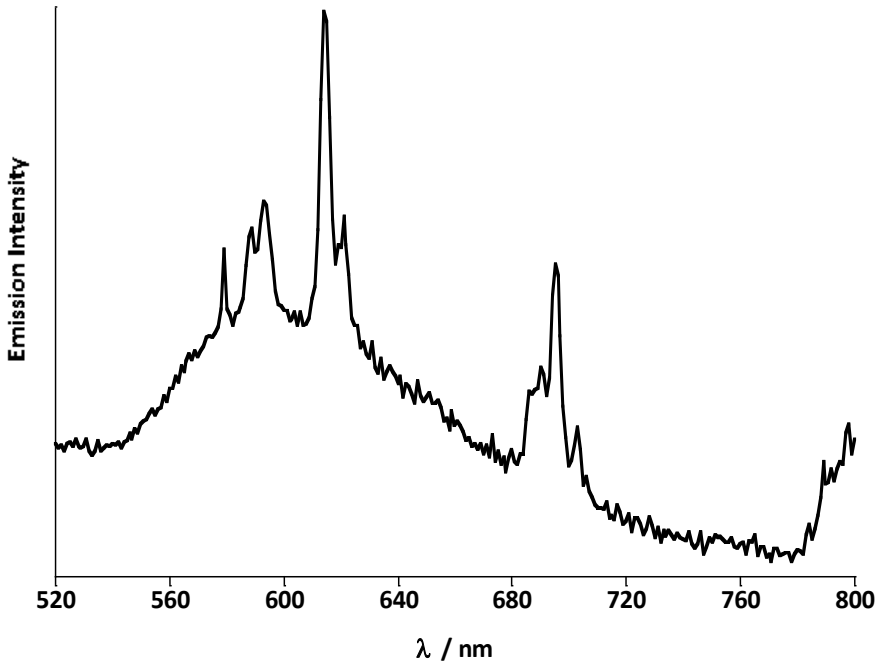

Figure 3.33 - Emission spectra EuQuinSi@Si_{500} ⊂Ru(Phen)$_3$ in water, (0.1% wt) λ_{ex}=320 nm, λ_{em} =618 nm.

The broad peak at 530 - 720 nm shows the ruthenium emission (*figure 3.33*) from the $[Ru(Phen)_3]Cl_2$, and the four peaks at ca. 580, 590, 620 and 700 nm show the $^5D_0 > ^7F_{J=0-3}$ show quinoline sensitised europium transitions emitting from the silica microparticles. We tested the bimodal microparticles for long lifetimes associated with lanthanides, and found a lifetime of 556 μs, attributing to the presence of europium. In contrast we tested the biomodal particles for just ruthenium emission.

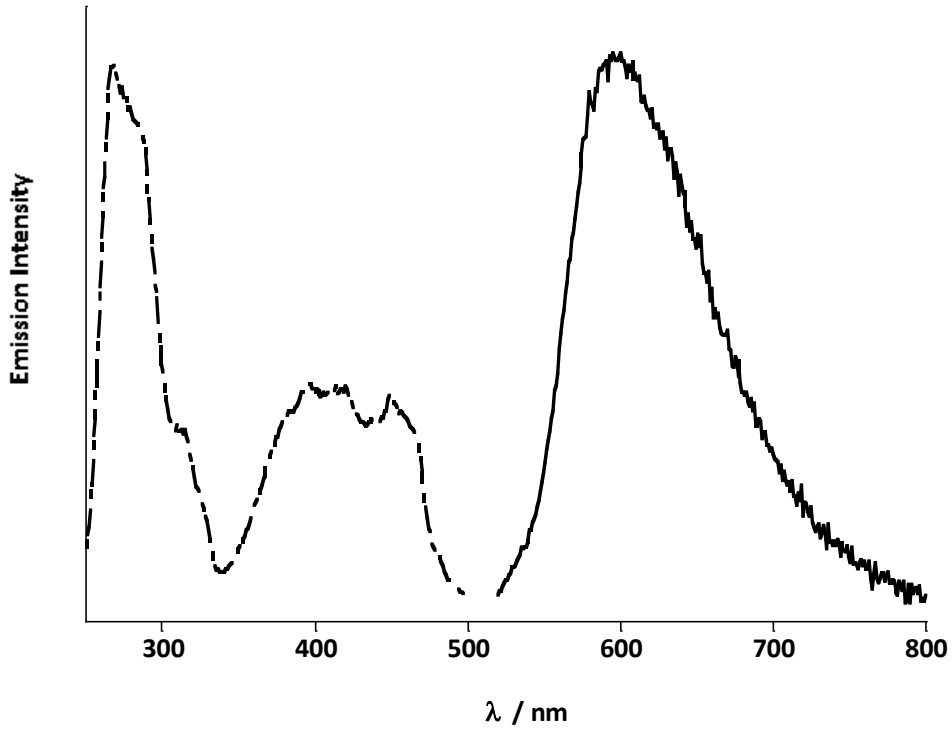

Figure 3.34 - Emission (—) and excitation (- - -) spectra of EuQuinSi@Si$_{500}$ ⊂Ru(Phen)$_3$, (10 µM). λ_{exc}= 450 nm, λ_{em}=618 nm.

The excitation and emission spectra of the encapsulated dye (*figure 3.34*), show that **[Ru(Phen)$_3$]Cl$_2$** still remains in the silica matrix after lanthanide complex attachment with a strong emission signal. The excitation spectrum of the **[Ru(Phen)$_3$]Cl$_2$** dye indicates its presence within the microparticles from the $\pi-\pi^*$ (260 nm) and the ^{1}MLCT (450 nm) transitions. From the emission spectrum of both the ruthenium and europium we can also say that the probe can be tuned for the emission desired. If strong red emission is desired then we can excite the probe at 450 nm to obtain stronger ruthenium emission and also excite in the visible part of the electromagnetic spectrum which is less damaging than UV to cells and

tissues. If the long lifetime and distinctive emission bands of the europium are required then we can excite the quinoline at 320 nm.

Table 3.5-The lifetimes of the lanthanide coated microparticles.

Microparticles	Lifetimes / µs	
	Lanthanide emission	**$[Ru(Phen)_3]Cl_2$ emission**
Si_{500} ⊂Ru(Phen)$_3$	-	1.3
EuQuinSi@Si_{500}	522	-
EuQuinSi@Si_{500} ⊂Ru(Phen)$_3$	556	1.6
NdQuinSi@Si_{500} ⊂Ru(Phen)$_3$	-	1.3
YbQuinSi@Si_{500} ⊂Ru(Phen)$_3$	-	1.7

The lifetime of $[Ru(Phen)_3]Cl_2$ emission from within the microparticles silica matrix was measured using a 445 nm diode laser, and the europium luminescence sensitised by quinoline was excited using a microsecond flashlamp at 320 nm. Table 3.5 shows the summary of the comparative lifetimes. Europium's lifetime remains relatively unchanged if the $[Ru(Phen)_3]Cl_2$ is encapsulated or not, this would largely be due to the fact the lanthanide complex is exposed to same external environments in both case with no effect arising from the presence of the $[Ru(Phen)_3]Cl_2$.[168] The life times in table 3.5 are also evidential that **EuQuinSi@Si_{500} ⊂Ru(Phen)$_3$** can be used selectively for europium or ruthenium.

$NdSi_2@Si_{500} \subset Ru(Phen)_3$ and **$YbSi_2@Si_{500} \subset Ru(Phen)_3$** were prepared to couple the properties of a lanthanide near-infrared emitter with the transition metal visible light emitter within the same nanostructure. However, no near infra-red emission was observed during initial studies. Increasing the concentration of the particles by a factor of 10 did not change the lack of emission signal from the NIR lanthanides hence confirming they were not sensitised sufficiently. Emission spectra with excitation wavelength at 450 nm indicates the $[Ru(Phen)_3]Cl_2$ dye is still present in each of these samples. With excitation at 320 nm, the emission of the asymmetric ligand was measured to see if it is present on the particles, despite not being able to sensitise the lanthanide emission. The peak between 280 nm and 330 nm indicate that the ligand is in the sample and therefore it is likely that the inefficient energy transfer of the ligand is the cause of the lack of lanthanide emission and the synthesis of ligand attachment may have been successful.

3.4.7 - Detection of DBM Using $EuSi_2$ SAM

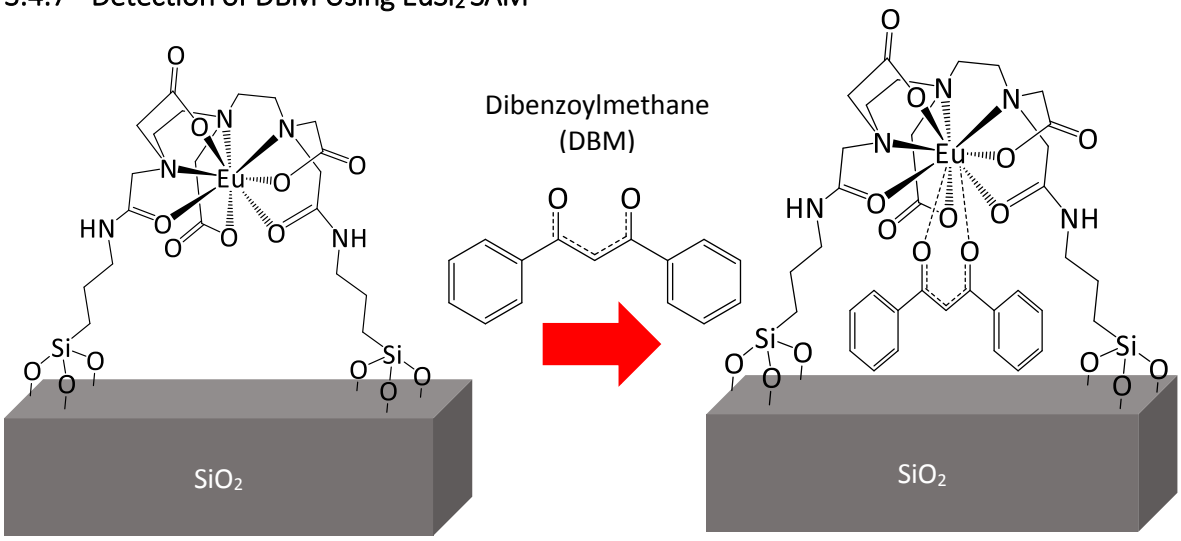

Figure 3.35- Representing the detection of DBM on a $EuSi_2$ SAM

A **$EuSi_2$** SAM was formed as described in chapter 6 and tested for its luminescence properties. The emission spectrum of **$EuSi_2$** SAM is far weaker than the solution of **$EuSi_2$**. This is not surprising as the concentration used previously was 0.15 mM in solution and compared to a surface that is theoretically 0.19 nmol cm^{-2}. The poor surface emission is ideal for use as an "off-state", and concluding this we now demonstrate the SAM's ability to coordinate DBM to europium within the self-assembled monolayer of **$EuSi_2$** (*figure 3.35*) on silica to dramatically enhance the surface luminescence, and how this technique can be used to screen for small analytes.

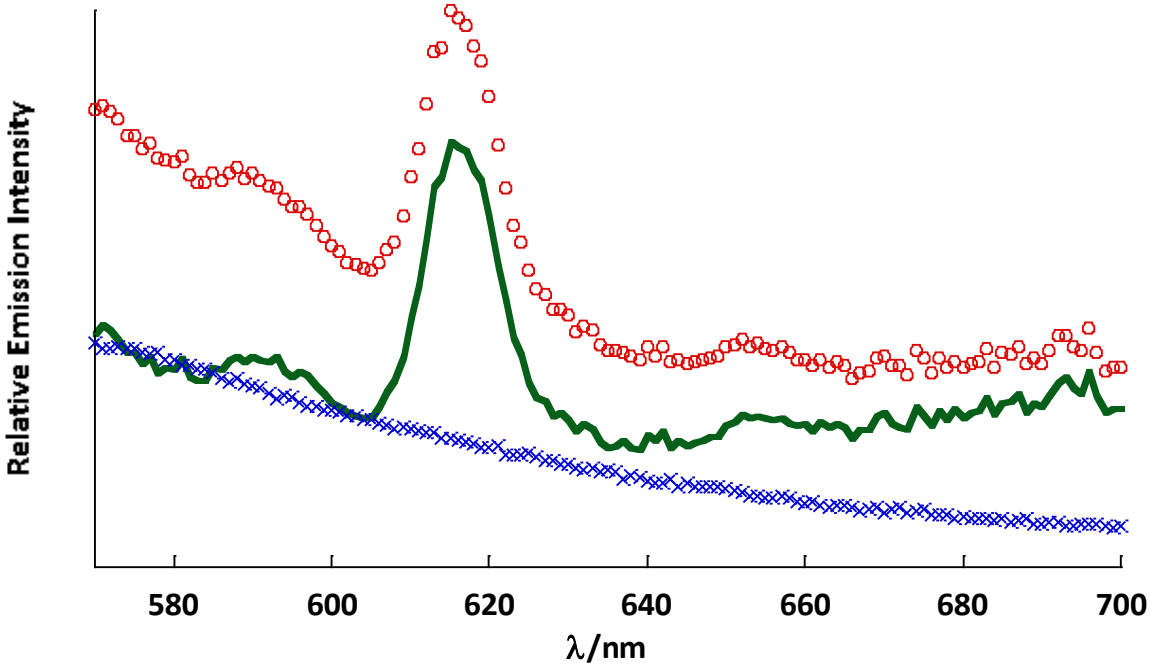

Figure 3.36 - Surface emission from a SAM of $EuSi_2$ on a silica slide before and after DBM coordination (1mM, ethanolic). (X)-Emission spectrum of $EuSi_2$ SAM λ_{exc} = 370 nm. (O)-Emission spectrum of $EuSi_2$ in the presence of DBM ($EuSi_2$-DBM), λ_{exc} = 370 nm. (—) Emission spectrum difference between O-X spectra.

We first tested the **$EuSi_2$** SAM surface for emission at two different excitation wavelengths, 370 nm, where we would excite DBM, this was done to represent the emission from the surface as a baseline (*figure 3.36*). The second excitation was at 395 nm in order to excite the europium directly. Exciting the europium directly or at 370 nm gave no europium emission due to the low concentration of **$EuSi_2$** on the surface indicating an "off-state". The **$EuSi_2$** coated silica surface was taken and submerged into a 1 mM ethanolic solution of DBM with one molar equivalent of triethylamine solution for 24 hrs. After this time the SAM was rinsed with copious amounts of ethanol, and dried with a nitrogen stream to give **$EuSi_2$-DBM**.

The emission spectra of **$EuSi_2$-DBM** is shown in *figure 3.36*, indicating that **$EuSi_2$** is being sensitised by the presence of DBM, the "on-state". When DBM is not present, there is no luminescence and we observe no emission due to the lack of direct sensitisation of the europium emissive states. This information indicates that it is possible to use this SAM to screen for analytes, with the "on-off" luminescence from europium indicating sensitisation and analyte binding to the europium in the **$EuSi_2$** SAM.

As mentioned before these analytes will need to meet certain criteria in order to sensitise europium in solution; small enough to fit in the cavity, coordination sites and containing a chromophore, with appropriate triplet energy levels. However when we are screening for analytes and using SAMs, the surface cavity size becomes more restricted as the **$EuSi_2$** and the silicon dioxide surface forms a pseudo macrocycle through covalent bonds between complex's two terminal silylether legs and the silicon dioxide surface forming Leg-Si-$(O\text{-}Si\text{-}O)_x$-Si-Leg. The pseudo macrocycle acts as steric barrier for larger analytes that could bind to the free complex. Forming the pseudo macrocycle makes the system more selective as the access to the coordination site is more restricted whilst **$EuSi_2$** is anchored to the surface. The aforementioned emission caused by the coordination of DBM to **$EuSi_2$**, and ellipsometric studies (see chapter 5) show evidence that there is space in the pseudo macrocycle cavity for analyte binding. Also appropriate substrates needs to be chosen to screen small aromatics acids accordingly; the absorption edge of silica substrates provides difficulty when dealing with analytes that absorb below 350 nm. The absorption edge of glass can be negated by using

quartz, which lowers the absorbtion edge below 250 nm or by using gold as shown in **Chapter 2.**

3.4.8 - Surface Europium Emission- Comparison of Quartz and Silica Materials

Here we complex **$EuSi_2$** SAM with DBM on silica and quartz to illustrate the limitations of using glass substrates and exciting simple aromatics that absorb inside the absorption edge of glass (*figure 3.37*). As with all silica based devices, there is an absorption edge at 350 nm. All of the simple aromatic acids tried previously absorb in the region of 350 nm or less except for DBM. We use SAM's of **$EuSi_2$** complexes to DBM, and excite at the absorption edge to demonstrate the photo physical boundaries associated with glass when using glass in development of silica based devices. We attempted to observe europium emission by recording the emission over 550-750 nm and directly exciting the europium at 395nm. The spectra of $EuSi_2$ on silica showed dominate scattering profile from the silica and consequently no europium signal.

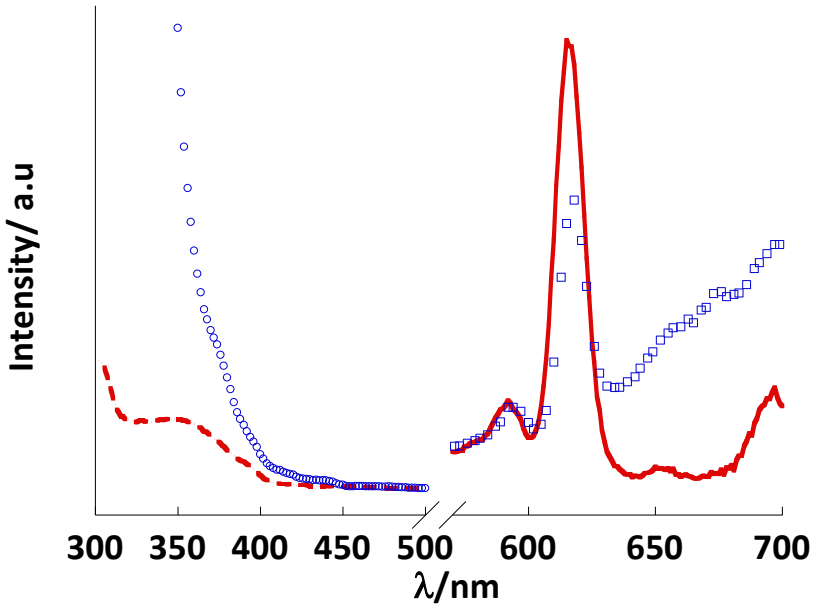

Figure 3.37 - (O)-Silica excitation spectrum. (- - -) Quartz excitation spectrum. (□) silica emission spectrum. (—) Quartz emission spectrum. - Excitation and emission spectra comparing the photophysical properties of $EuSi_2$ complexed to DBM on quartz and on silica, λ_{em} = 618 nm, and λ_{exc} = 350nm.

The spectra above (*figure 3.37*) shows the excitation and emission comparison of **$EuSi_2$** on the surface of quartz and silica material, post submerging in an 1 mM ethanolic DBM solution, then washing with copiuous amounts of ethanol and dried under a nitrogen stream. The excitation spectrum in *figure 3.37* shows that the most absorptive band of **$EuSi_2$-DBM** on silica arises at 350 nm, which is true due to the presence of DBM, however the true excitation band is masked by the presence of silica, causing the excitation spectrum to give a false positive result. If we compare the results of using quartz material treated in parallel, excitation spectrum of **$EuSi_2$-DBM** shows the true excitation band, and matches the solution absorbtion band of DBM. Exciting at 350 nm will still cause absorption at the silica surface, which in turn will cause the silica to scatter the absorbed light across the spectrum. This can include the area in which we would expect to see europium emission, resulting in a false positive result at

the detector for europium signal. The false europium signal was examined by recording lifetimes of the surfaces whilst exciting at 350 nm. The results indicated pecosecond lifetimes which is not indicative of a europium luminescent lifetime, and indicative of scattered light from the silica. Another absorption band of the DBM can be seen at 370nm, which can be observed as a small shoulder in the excitation spectrum of EuSi-DBM on silica. Excitation at this wavelength gives rise to a characteristic europium emission spectrum and a lifetime was collected whilst exciting the surface at 370 nm of 700 μs.

The emission spectra of **EuSi$_2$-DBM** (*figure 3.37*) on silica and quartz both show the $^5D_0$>$^7F_{1,2}$ transitions, however the $^5D_0$>$^7F_{0,3}$, transitions are too weak to be observed on silica. Furthermore the $^5D_0$>$^7F_4$ europium emission band on the silica surface can be observed emerging from the residual scattering peak at 700nm on the emission spectrum, whereas quartz appears to be unaffected by residual scattering unlike the silica material. The **EuSi$_2$-DBM** SAM on quartz shows superiority when looking at the whole europium spectrum, observing a more distingusable $^5D_0$>$^7F_3$and the $^5D_0$>$^7F_4$ transitions. Overall the quartz as predicted provides more desirable properties over traditional silica material. In both cases we can observe the absorption band arising from the DBM in the excitation spectra; although it is more clearly defined and separated out from the silica's absorption edge in the excitation spectrum than from the quartz material. Comparison of the relative intensity of the two surfaces showed very little difference, but quartz showed a more characteristic europium emission profile, due less scattering and more resolved europium transition bands.

Luminescence microscopy was used to analyse the surface of the silica surfaces, and analyse SAM coverage. As we know for gold surfaces, complexes tend to form islands of compacted compounds, due to the "hopping nature" of the gold sulphur bond.[170] However since the SAMs on silica is formed through polymerisation of the hydroxysilyl and the silica surface there is no hopping nature involved as the silyl compounds are anchored to the surface. Using luminescence microscopy we examined the surface of **EuSi$_2$-DBM**, and investigated the activated surface coverage.

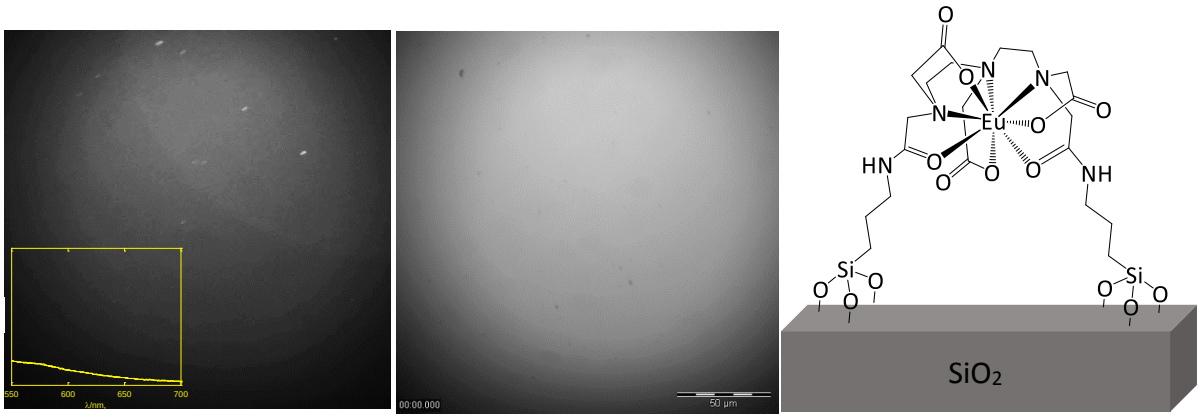

Figure 3.38- Luminescence microscopy images at 40x objective. (Left) Luminescent intensity image of EuSi$_2$ complex on a silica surface. (Right) Bright field image.

A luminescence microscopy image of the **EuSi$_2$** SAM on silica is shown in *figure 3.38*. We observe that there is no surface luminescence and there is formation of concentrated emissive spots randomly distributed across the surface of the silica slide. If we look at the bright field image in parallel which was taken at the exact same position as the luminescent intensity image, we can conclude that a few spots arise due to defects in the silica. These defects will cause scattering of the monochromatic light source which show up as emission at the

detector, acting as a false positive result. However looking comparatively there is a high frequency of islands that are not co-localised with visible imperfections which would indicate some surface imperfections that we cannot observe through the 40x objective. These may allow for seeded growth on the surface giving rise to higher concentration of compounds in localised areas. This would need to be investigated further to conclude a definite answer, using techniques like atomic force microscopy (AFM) to compare the roughness of the surface and if there is SAM formation on the indicated areas.

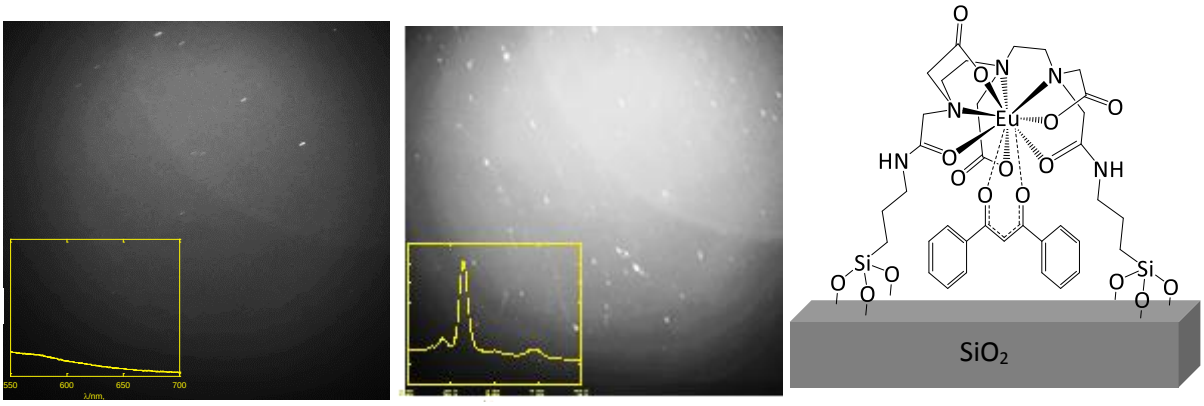

Figure *3.39*- Luminescence microscopy image of $EuSi_2$ on silica (Left) and $EuSi_2$-DBM on silica, with insets displaying the emission profile for the respective areas.λ_{em} = 618 nm, and λ_{exc} = 370nm

A comparison is shown in *figure 3.39* of the before and after ternary complex formation of **$EuSi_2$** and DBM on the surface of silica using the luminescent microscope. Inset figures show the emission spectra representing the emission intensity arising from the focused area of the SAM.

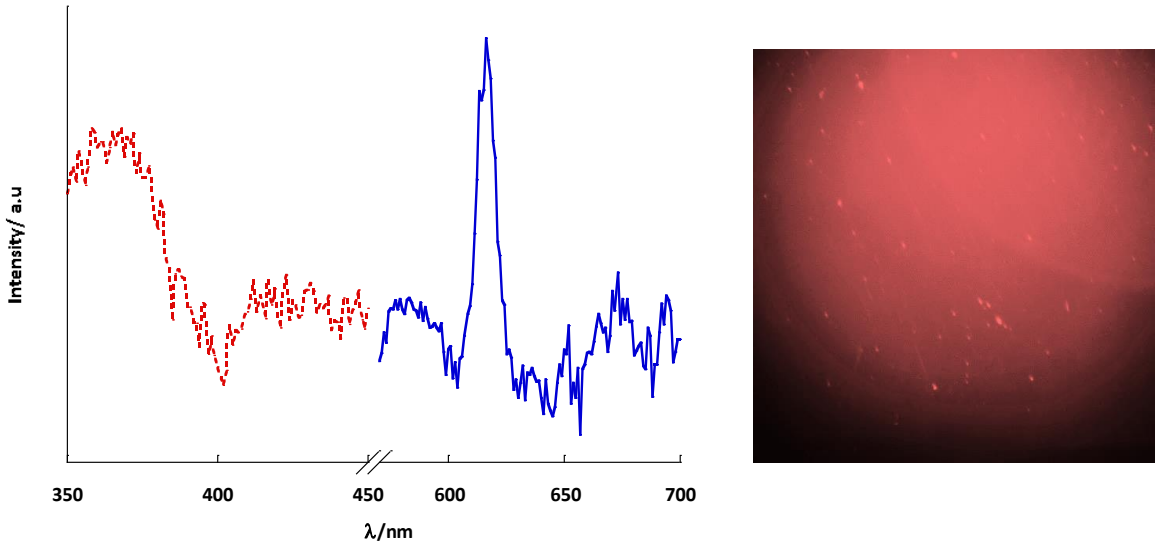

Figure 3.40 - Left is (- - -) Excitation and (—) emission spectra comparing the photophysical properties of $EuSi_2$ complexed to DBM on silica under the luminescent microscope, right- Luminescence microscopy image of $EuSi_2$-DBM on silica, λ_{em} = 618 nm, and λ_{exc} = 370nm.

Through analysis of the surface luminescence we can instantly see that the intensity of the emission is significantly lower using the luminescence microscope setup (*figure 3.40*). This is because the luminescence intensity of the surface is relative to the intensity of the excitation source. Due to the microscope setup, a fraction of the excitation light is retained upon surface excitation. Thus resulting in a far weaker signal whilst using the microscope setup. In the excitation spectra of the SAM we observe strong evidence to suggest the presence of DBM, with increased energy transfer to the europium over the range of 350- 390 nm, which has a strong overlap with DBM's absorption band.

$EuSi_2$ SAM's on silica were studied by luminescence spectroscopy. The surface coverage expected to be on the surface of a 1 cm^2 silica slide is less than that of a densely packed SAM of organic thiols due to the complex having a larger molecular footprint than that of short

alkane thiols such as hexane thiol. Computational modelling can approximate the complex's radius in an ideal system. Using Chem3D we can calculate the distance between sulphur binding groups and thus work out the radius and molecular footprint. From this we can calculate the theoretical surface concentration from 100% coverage, although this is only an estimation.

Theoretical calculation of surface concentration of a **$EuSi_2$** SAM bound to a 1 cm^2 surface:

$$Molecular\ Footprint\ =\ \pi r^2 =\ \pi 0.55\ nm^2 = 0.93\ nm^2$$

$$Number\ of\ molecules\ per\ surface = \frac{1.00\ cm^2\ per\ surface}{0.93\ nm^2}$$
$$= 1.16\ x10^{14}\ molecules\ per\ surface$$

$$Surface\ concentration = \frac{1.16\ x10^{14}\ molecules\ per\ surface}{6.02\ x\ 10^{23}\ molecules\ per\ mole}$$
$$= 1.92\ x\ 10^{-10}\ moles\ per\ surface = 0.19\ nmols\ cm^{-2}$$

The above calculation deduces that the theoretical concentration on the surface of 1 cm^2 piece of silica is 0.19 nmols cm^{-2}, which compared to the solution concentration 0.15 mM is a relatively very low concentration. There are no reports of 100% coverage of transition metal complexes.[91] The central charged ion, hydrophobic backbone and carbonyl groups exposed to the outside of the complex all contribute to steric and electrostatic interactions generating a large molecular footprint, unlike organic thiols which have hydrophobic alignment, and minimal steric interactions that assist in close packing and formation of highly dense SAMs. There is also no physical or chemical interaction that could help induce close packing of the

compound, thus making lanthanide complex form less dense SAMs which in turn would make a surface less luminescent.

3.4.9 - Ternary Complex formation of $EuSi_2$- Solution Luminescence studies

The complex **$EuSi_2$** was tested with regards to its binding capabilities, with several simple aromatic salts: benzoate (BZA), phthalate (PTA), isophthalate acid (IsoPTA), picolinate (PA) and dipicolinate (DPA) in solution (figure 3.41). These acids are simple in terms of complexity and have either one or two carboxylic acids present, and/or contain a heteroatom in the aromatic ring facilitating mono, bi, and tridentate coordination. These variants all have different binding affinities to **$EuSi_2$** because of the chemical composition, thus leading to different photophysical responses upon coordinating to **$EuSi_2$**, whilst containing a chromophore.

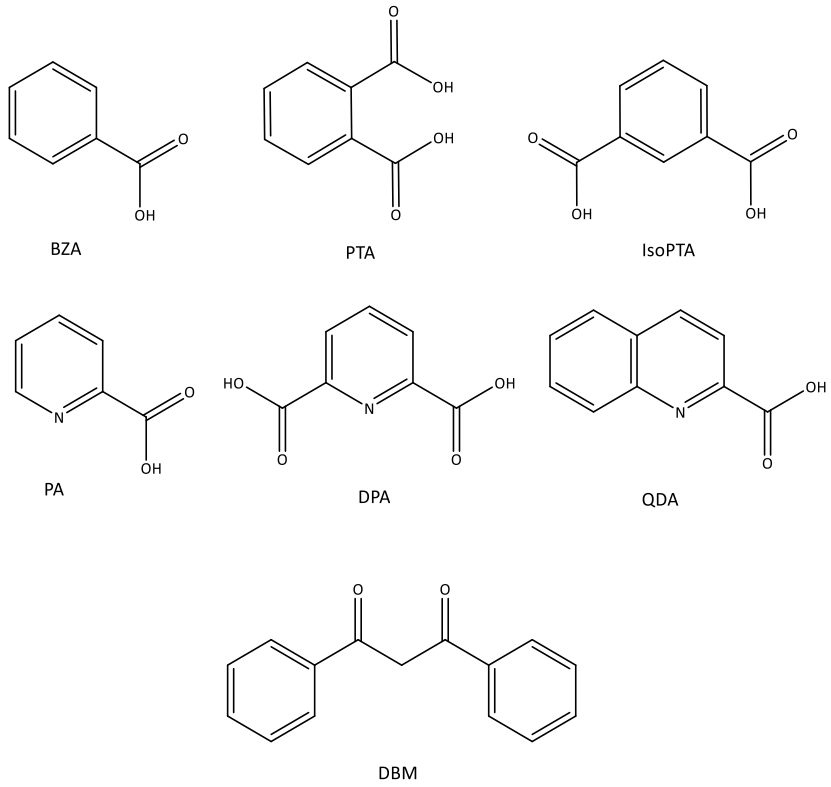

Figure 3.41 - Chemical structure of the simple aromatics screen with $EuSi_2$. Benzoic acid (BZA), phthalate acid (PTA), isophthalate (IsoPTA), picolinic acid (PA), dipicolinic acid (DPA), Quinaldic Acid (QDA) and Dibenzolymethane (DBM).

The controlled ternary complex formation of **$EuSi_2$** with these simple aromatic acids was carried out in ethanolic solution and was investigated by luminescence spectroscopy. Through titration of the deprotonated aromatic acid moieties and excitation at 280 nm, the evolution of the signature europium emission was monitored over the range of 550-750 nm. Emission spectra were obtained for each ternary complex formation and then integration of the peaks allowed for the stoichiometry of the system to be obtained.

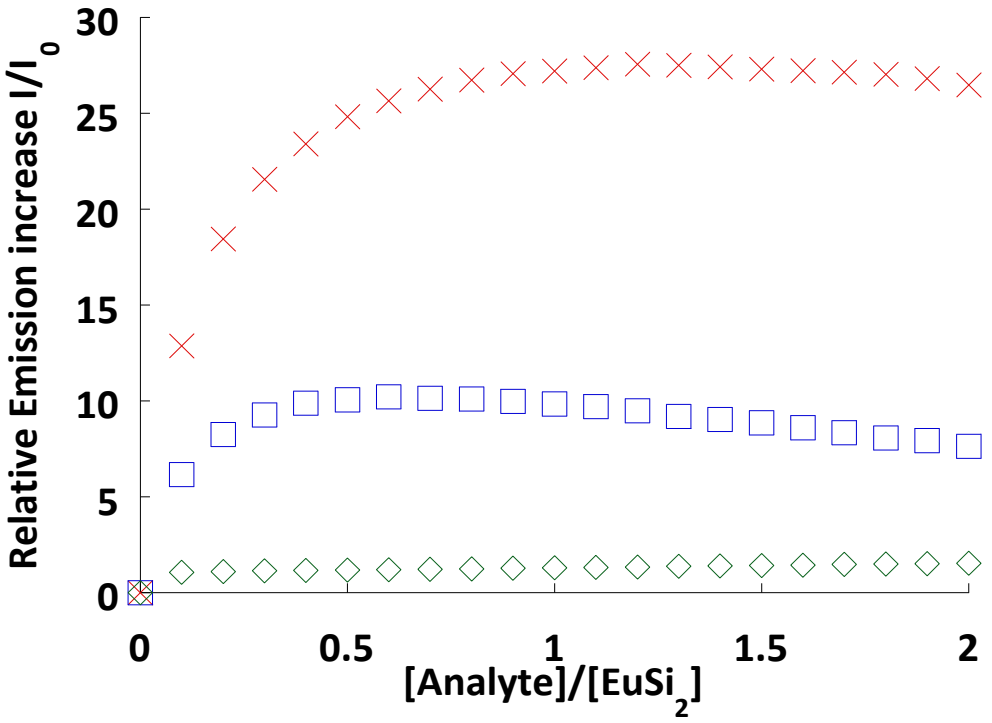

Figure 3.42 - Integrated emission intensity plot against the molar equivalents of titrant added. (λ_{ex} =280 nm) for titration of analyte (0-100 μL, 9 mM, 3 eq of NEt_3) into an ethanolic solution of EuSi2 (0.12 mM). (X) - Isophthalate, (□) -Phthalate, (◊) – Benzoate.

Three simple aromatic acids are shown to sensitise $EuSi_2$ in solution; Benzoate (◊) Phthalate (□) and Isophthalate (X), (*see figure 3.42*). Benzoate was chosen as the simplest aromatic acid, with only one coordination site through the carboxylate group. Looking at the integrated plot, it shows that benzoate is a relatively weak sensitiser and that there is no clear indication of a saturation point or of strong binding events taking place. The emission intensity increase almost looks linear by nature after two equivalents of benzoate has been added. It is known that benzoate is a poor lanthanide sensitiser,[64] thus europium's emission isn't expected to increase significantly. The lack of saturation could also be due to high triplet state of benzoic acid.

The emission intensity increase for the ternary complex formation of phthalate with **$EuSi_2$** was a 10 fold increase. The emission intensity increase was significantly higher than that of Benzoate. This would indicate clear coordination of the acid directly coordinated to the lanthanide. Phthalate has two strong oxygen donors that can coordinate to the lanthanide in a bidentate motif, making the coordination capabilities greater than that of benzoate. However after one equivalent of phthalate, the emission starts to decrease quite dramatically due small amounts of precipitate forming in solution, thus lowering the concentration of **$EuSi_2$**. However the binding interaction between isopthalate and **$EuSi_2$** clearly shows a distinct 1:1 stoichiometric binding event. Isophthalate has two possible coordination sites as it contains two carboxylates. Only one of them is being used to coordinate to the lanthanide, saturating the coordination sphere of the europium ion. Analysis of *figure 3.41*, it is clear to say that the emission intensity has saturated at one molar equivalent. Unlike phthalate, Isopthalate's emission plateaus off cleanly, thus indicating no additional binding interactions from excess isopthalate to **$EuSi_2$**, and Isophthalate remains soluble in the solution mixture. (For more detailed plots of the three analytes see appendix). When comparing the results of these small aromatic acid binding to **$EuSi_2$** with the work of Ruston *et al.*[64] whom also demonstrated the sensitisation of europium DTPA-bisamide ligands with these simple aromatic acids, we found the results to be quite similar. Ruston's complex with benzoate showed only a two-fold increase in sensitisation, the phthalate acid showed an eight fold increase where **$EuSi_2$** shows a 1.5 fold and 10 fold at 1 equivalent respectively.[64] showing no selective advantage of using **$EuSi_2$** in solution over the compound Ruston had used.

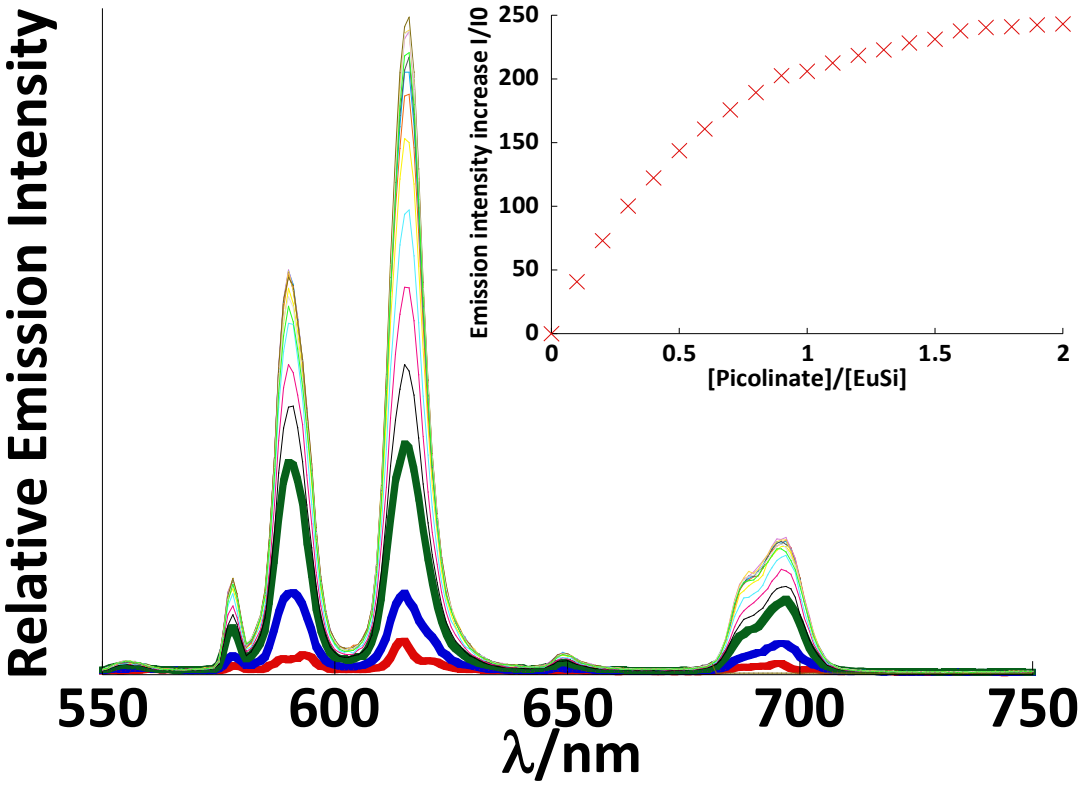

Figure 3.43 - (Left) Corrected emission spectra (λ ex =280 nm) for titration of picolinate (0-100 μL, 9 mM, 3 eq of NEt_3) into an ethanolic solution of EuSi2 (0.12 mM), (inset) integrated emission intensity plot against the molar equivalents of titrant added.

The ternary complex formation between **$EuSi_2$** and picolinate was demonstrated to show the bidentate nature with two different functional groups. Picolinate has a heteroatom in the pyridine ring and contains a carboxylic acid functional group. Picolinate is capable of bidentate coordination to **$EuSi_2$** and demonstrated the strongest sensitisation of **$EuSi_2$**. In theory, the major cavity should only have enough space to accommodate one picolinate molecule leading to a 1:1 stiochiometric ratio. The excitation scan shows intramolecular energy transfer from the picolinate to europium further indicating that picolinate is coordinated to and sensitising the europium. The integration plot shows a massive increase in europium signal and saturates

around one equivalent of picolinate to **EuSi$_2$**, thus further indicating a 1:1 binding, and formation of a luminescent ternary complex. The graph still shows further increase after one equivalent of picolinate is added, this is most likely due to slow coordination of the picolinate to **EuSi$_2$** in solution competing for the remaining free coordination sites.

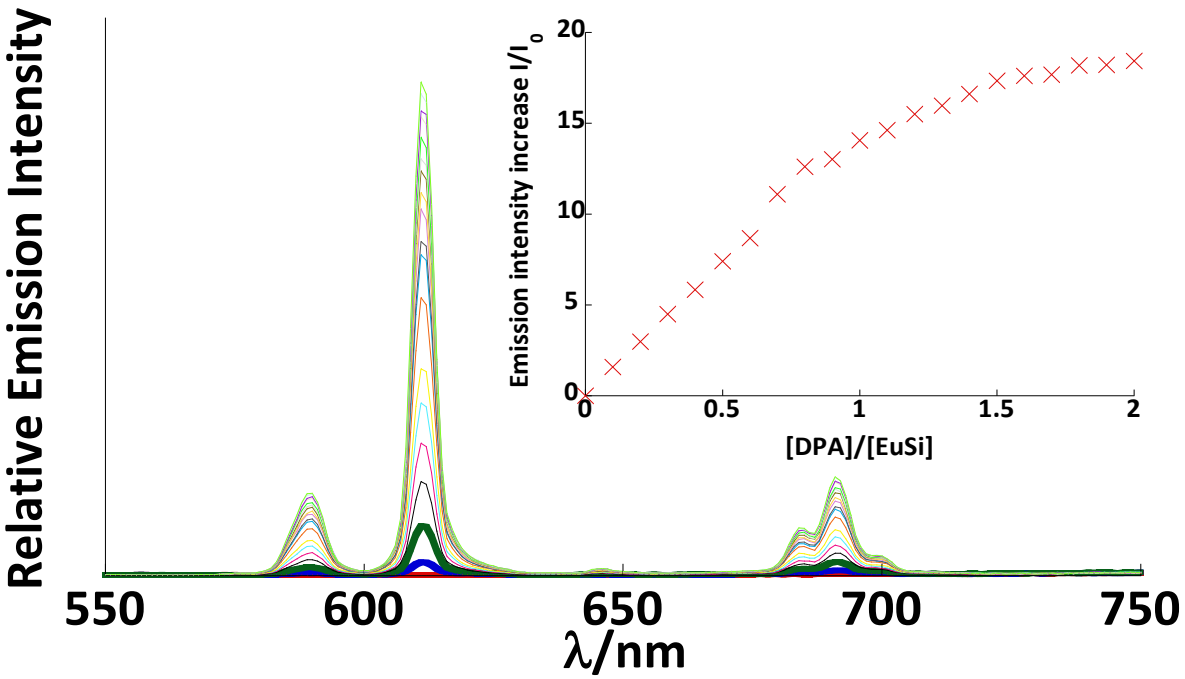

Figure 3.44 -(Left) Corrected emission spectra (λ_{ex} =280 nm) for titration of dipicolinate (0-100 μL, 9 mM, 3 eq of NEt$_3$) into an ethanolic solution of EuSi$_2$ (0.12 mM), (Right) integrated emission intensity plot against the molar equivalents of titrant added.

Dipicolinate gave another example of lanthanide sensitisation through energy transfer from the chromophore to the europium emissive states (*figure 3.44*). Dipicolinate like picolinate has both a heteroatom in the benzene ring and carboxylic acid groups, with an additional carboxylic acid group in the *meta*-position. Having two carboxylic acid groups and a pyridyl group would suggest a sensitiser that would have tridentate binding nature. As mentioned

previously lanthanides have a coordination number of 8-10, eight of which would be occupied by the silyl-DTPA ligand. Thus when dipicolinate binds to the **EuSi$_2$** it should only bind in a bidentate or monodentate motif. From analysis of the photophysical data there is an emission intensity increase from zero equivalents of dipicolinate to one equivalents, and thus saturating out at two equivalents. It is not possible that two dipicolinate molecules are coordinated to the europium complex in a tridentate or bidentate motif. Thus it would suggest that dipicolinate in this case is binding through a monodentate motif, stabilised through π–π stacking of the two molecules. Ruston *et al*.[64] also compared picolinic acid and dipicolinic acid to lanthanide DTPA bis-amide complexes. **EuSi$_2$** showed greater sensitisation for picolinic acid then Ruston's compound with **EuSi$_2$** luminescence increasing by 200 fold and Rustons' complex increasing by only 30 fold. However dipicolinic acid sensitised Ruston's complex more than **EuSi$_2$**, 1000 fold increase against 14 fold increase. It is important to note however that Ruston reported the significant increase of europium emission to 14000 fold increase at five equivalents of dipicolinic acid, and theorised competition for the europium ion. In the case of **EuSi$_2$** the dipicolinic acid binding reaches a plateau, indicative of the europium not leaching out of the ligand. Thus if **EuSi$_2$** was anchored to a surface in a device, any bound dipicolinic acid would remain bound to the europium complex at the surface when the device surface is washed.

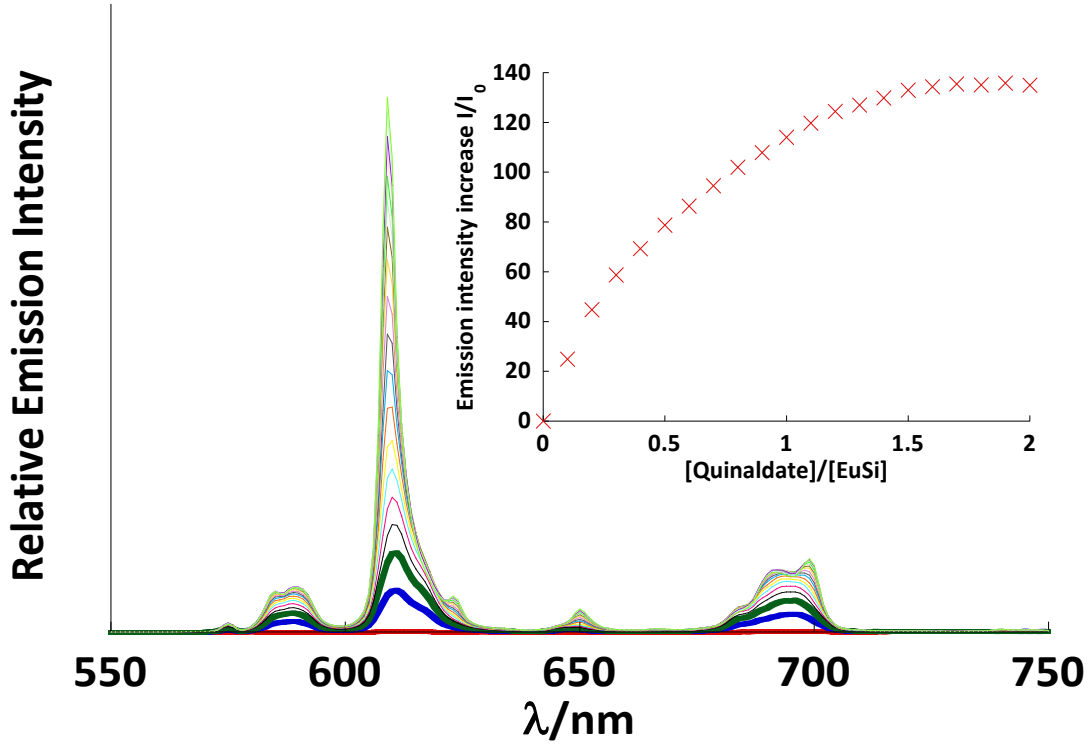

Figure 3.45-(Left) Corrected emission spectra (λ ex =280 nm) for titration of quinaldate (0-100 μL, 9 mM, 3 eq of NEt_3) into an ethanolic solution of $EuSi_2$ (0.12 mM), (Right) integrated emission intensity plot against the molar equivalents of titrant added.

Quinaldate was also chosen because it contains the same coordinating functional groups as picolinate, one carboxylic acid group in the *meta*-position and heteroatom in the pyridine ring. The only variation is that quinaldate is a fused ring system, the combined nature of a benzene ring and picolinate. The variation of the acid takes into consideration a more conjugated π-system and greater steric hinderance than picolinate. Quinaldate does show sensitisation of the europium (*figure 3.45*), meaning that there is coordination to the europium and that **$EuSi_2$** can accommodate slightly larger aromatic acids. Again π–π stacking of the quinoline could attribute for the small increase in emission after one equivalent.

We have shown that simple aromatic acids have coordinated to **$EuSi_2$** successfully but have varying amounts of sensitisation with picolinate giving just under 250 fold increase in the luminescent intensity, and benzoate barely giving a 2 fold increase. With a system like **$EuSi_2$** it is possible to differentiate between these aromatic acids with limited selectivity in a mixed solution, either by measuring the difference in luminescent intensity, or by using variable excitation sources, as molecules like QDA and DBM can absorb visible radiation and excite europium, whereas benzoate and phthalate only absorb UV radiation.

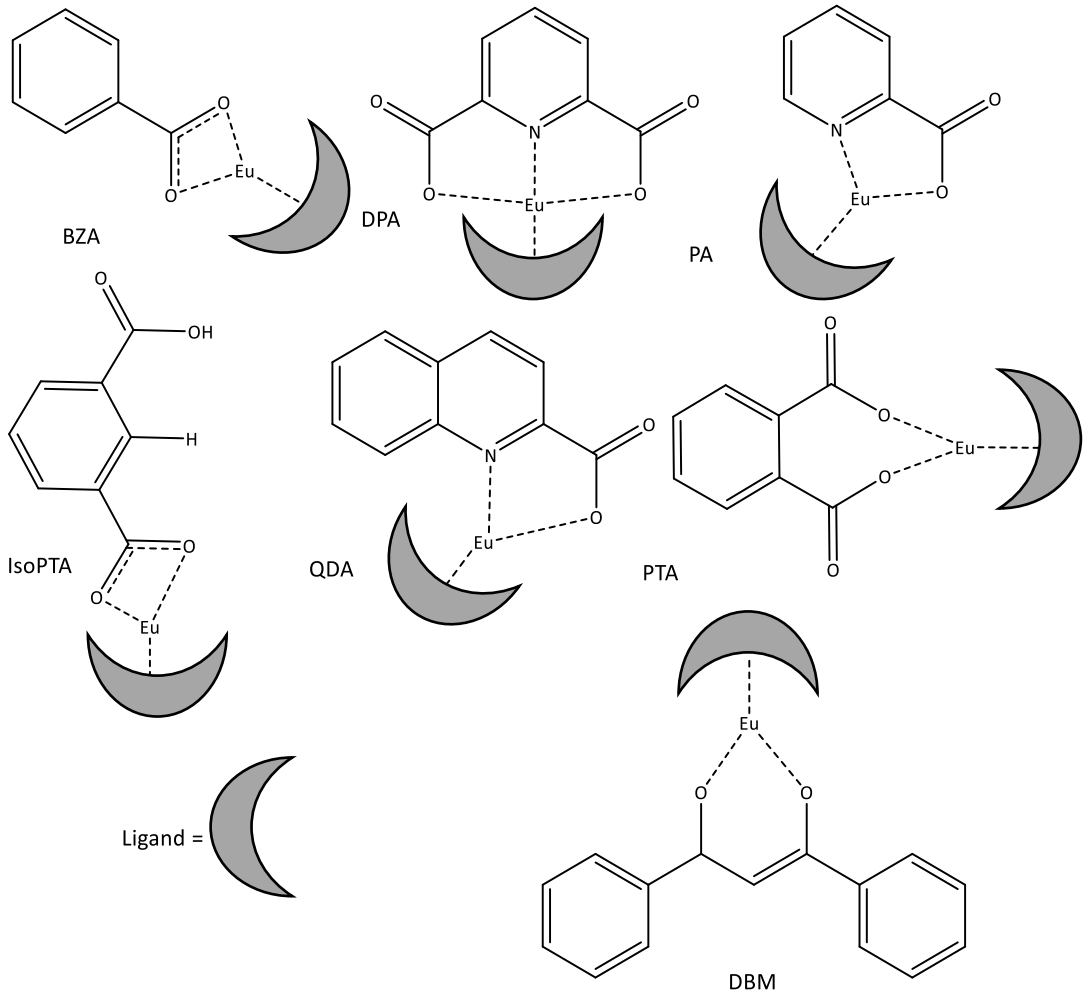

Figure 3.46 - Representing the binding motifs of simple aromatic acids to $EuSi_2$.

While the relative emission intensity increase would indicate the effective sensitisation of the simple aromatic acids to the **$EuSi_2$**, it gives us no information about the coordination of the simple aromatic acids, therefore the coordination of these molecules can only be speculated. The theoretical coordination of DTPA-bisamides is eight and since lanthanides have a coordination number of 8-10, this essentially leaves a coordination site of either two monodentate molecules or one bidentate molecule.

Benzoate shows essentially negligible sensitisation of **$EuSi_2$**. Benzoate is known to poorly sensitise europium, however since only one binding site is available on the acid, it would expected that the saturation point in the emission spectra to indicate the number benzoate molecules bound to **$EuSi_2$** in a bidentate binding motif (*figure 4.46*). This should in turn give information on how many coordination sites are present in **$EuSi_2$**.

When working with analytical detection methods, the limit of detection (LOD) is always an attractive attribute of the system that is being used. We also determine the limit of detection for **$EuSi_2$** in ethanolic solution with simple aromatic acids and compare this with molar absorption coefficients and relate this to relative sensitisation. For spectral information of the LOD experiments please see the appendix.

Table 3.6- Comparison of coordination properties of simple aromatic acids[171-177]

Name	Coordination sites	Acid/**$EuSi_2$** @saturation	Molar absorption coeffcient (ε) @λ_{exc} / $M^{-1}cm^{-1}$	Limit of Detection/ M	Triplet Energy Level/ cm^{-1}
BZA	2	-	730	1×10^{-3}	27000
PTA	2	1	730	1×10^{-5}	26000
IsoPTA	2	1	1200	1×10^{-6}	26000
PA	2	1	3900	1×10^{-6}	25000
DPA	3	1	4000	1×10^{-6}	25000
QDA	2	1	5200	1×10^{-8}	23000
DBM	2	1	12400	1×10^{-8}M	22000

The LOD is shown in Table 3.6 for all the analytes tested, showing various degrees of europium sensitisation, thus elucidating information on sensitivity to the simple aromatic acids. The LOD was determined by monitoring a >10% increase in europium emission over an increasing concentration gradient. Quinaldate showed the greatest sensitivity with **$EuSi_2$**, whereas benzoate showed relatively poor detection limits. Benzoate's weak LOD is related to its ability to sensitise the europium and absorb light, with a molar absorptivity coefficient of 730 $M^{-1}cm^{-1}$. The emission intensity increase at equimolar concentrations showed an intensity increase of only 1.5 fold, from which we can conclude that we would expect benzoate to have a weak LOD. On the other hand, quinaldate had an intensity increase of 140 fold increase at equimolar concentration and exhibits far better sensitisation of the europium ion. Quinaldate has a higher molar absorptivity coefficient of 5200 $M^{-1}cm^{-1}$, thus would relate to its greater

sensitivity, and stronger LOD. Quinaldate also has the lowest triplet state expect for DBM thus most likely indicating that quinaldate has the most optimal triplet state to energy transfer to europiums emissive states.

We have shown the sensing capabilities of **$EuSi_2$** with simple aromatics however predicting the sensitisation seems to be a fine line between binding affinities of the analytes and the possible binding modalities of the simple aromatic acid, molar absorption coefficients and also the triplet states of the analytes.

3.4.10 - Photophysics: Ternary Complex Formation of $YbSi_2$ and Curcumin

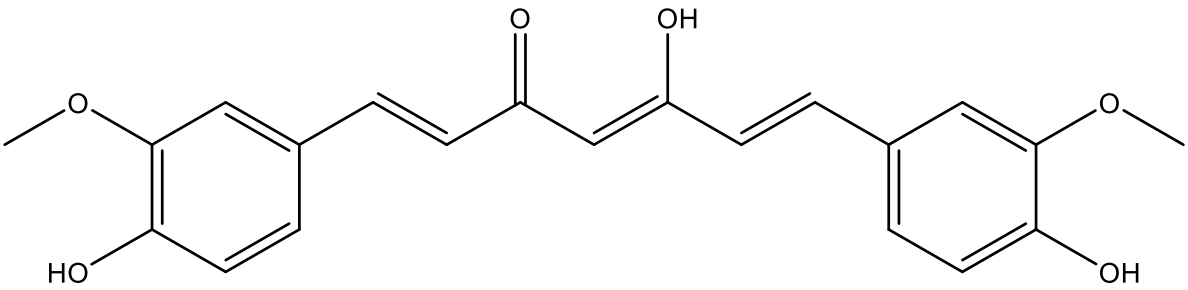

Figure 3.47 - The chemical structure of Curcumin

Curcumin is a diarylheptanoid (*figure 3.47)*, and β-dikentonate curcuminoid that is purified and extracted from the spice turmeric. The diarylheptanoid is part of the ginger family and contains antioxidant properties greater than that of vitamin E.[178] R. N. Bui and co-workers[179] show the non-phenolic derivative of a curcuminoid chelating to NIR lanthanide-phenanthroline complexes. Other researchers have shown curcuminoid based-lanthanide complexation.[180,181] Here we demonstrate that $YbSi_2$ is sensitised in solution by the addition of Curcumin, and shown NIR-sensitisation.

The chelation of the principal compound curcuminoid found in turmeric has been demonstrated in *figure 3.48*, chelating to **$YbSi_2$** ligand in an ethanolic solution which was monitored by luminescence emission spectroscopy.

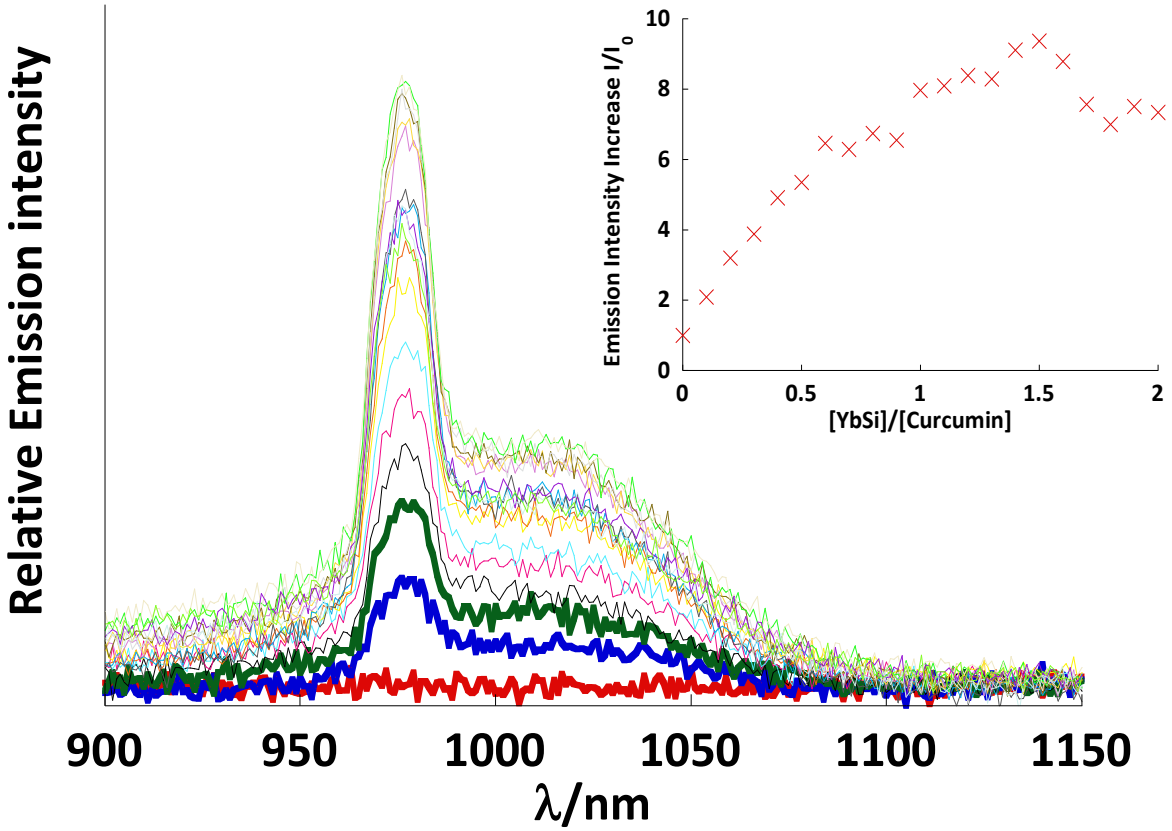

Figure 3.48-(Left) Emission spectra (λ ex = 380 nm) for titration of curcumin (0-100 μL, 0.9 mM) into an ethanolic solution of $YbSi_2$ (150 μM), (inset) integrated emission intensity plot against the molar equivalents of titrant added.

The emission spectrum clearly shows the evolution of the ytterbium emission profile, showing the most intense band at 982 nm, and a broad shoulder at 990-1180 nm. Through integration of the emission spectra we can see that the emission saturates after one equivalent of curcumin has been added. At saturation, the emission intensity has increased eight-fold compared to the absence of curcumin. Excitation scan of the Yb emission at 1162 nm revealed that the sensitisation was due to the binding of min.

3.5 - Experimental

3.5.1 - Synthesis of H_3LSi_2

DTPA bisanhydride (5.00 g, 14.0 mmol) was dissolved in 100 mL of anhydrous pyridine under nitrogen. 3-aminopropyl triethoxysilane (6.85 g, 31.0 mmol) was added and the resultant reaction mixture and was stirred under nitrogen for 24 hours. The product was then precipitated with copious amounts of hexane (400 mL), isolated via Büchner filtration, then washed with hexane (5 x 100 mL). The residue was then left to air dry for five minutes, then dried under high vacuum to yield 10.5 g (yield = 93 %) of the desired compound. MS (ESI negative ion): *m/z* 631.3, $[M-H]^-$ for the silanetriol from a basic solution. ^{1}H-NMR (300 MHz, DMSO-d_6) δ_H ppm: 0.51 (t, 4H), 1.13 (t, 18H), 1.44(p, 4H), 2.81 (t, 4H), 2.94 (t, 4H), 3.04 (q, 4H), 3.22 (s, 6H), 3.34 (s, 4H), 3.73 (q, 12H), 8.06 (t, 2H).^{13}C-NMR (100 MHz, DMSO-d6): δ 18.7, 19.0, 23.1, 41.5, 51.0, 51.4, 52.6, 55.7, 56.4, 58.3, 170.7, 173.4.[99]

3.5.2 - Synthesis of $LnSi_2$ (Ln =Eu, Gd, Yb)

100 mg (0.18 mmol) of H_3LSi_2 was dissolved in tetrabutylammonium hydroxide (5 ml, 40 % aqueous), stirred for 30 minutes, then one equivalent of the lanthanide solution (1 mL, 0.18 mmol) in water was pipetted into the stirring solution, stirred further for 30 minutes. MS (ESI negative ion): $[EuSi_2]$ m/z 951 $[M-H]^-$, $[GdSi_2]$ m/z, 959 $[M+H]^+$.

3.5.3 - $EuSi_2$ Attachment to $Si_{500/800}$ Microparticles

DTPA (100 mg, 0.28 mmol), DIPEA (97 µL, 0.56 mmol), DMAP (ca. 0.5 mg) and APTES (131 µL, 0.56 mmol) were dissolved in pyridine (ca. 2 mL), and stirred for 3.5 hrs. $EuCl_3.H_2O$ (100.8 mg, 0.28 mmol) was added and stirred for 1 hrs. The solution was then added to a solution of $Si_{800/500}$ microparticles (1 mg/ mL, 20 mL) and stirred for 24 hrs. The microparticles were obtained by centrifugation-redispersion (4400 rpm, 30 min per wash) into water (3 x 30 mL), then ethanol (1 x 30 mL) and dried in a desiccator. The silica microparticles was previously developed and characterised by Rossi et al.[166] and formed with good agreement with dye encapsulated silica microparticless form by Pikramenou et al.[167] giving an average nanoparticle size of 752 ± 50 nm by light scattering measurements, a zeta potential of -59 mV for 800 nm silica microparticless and for 500 nm sized particles; 460 ± 65 nm by light scattering measurements and a zeta potential of -48 mV.

3.5.6 - Synthesis of Asymmetric H_3QuinSi

DTPA (0.5 g) was dissolved in DMSO (3 mL) under a steady flow of nitrogen. Over 24 h (0.4417 mL / minute) 6-aminoquinoline (0.20 g) in DMSO (10 mL) was added to the solution under nitrogen. APTES (0.156 mL) was added and the reaction mixture was stirred for 48 h. ^{1}H NMR (300 MHz, d_6- DMSO) ∂_H ppm: 0.52 (t, 4H), 1.14 (t, 18H), 1.46 (p, 4H), 2.83 (t, 4H), 2.97 (t, 4H), 3.04 (q, 4H), 3.23 (s, 6H), 3.34 (s, 4H), 3.73 (q, 12H), 8.10 (t, 2H). 8.47 (1H, d, J = 5.2, = 1.3, H_{19}), 8.14 (1H, d, ^{3}J = 8.3, H_{17}), 7.74 (1H, s, H_{16}), 7.50 (1H, dd, J = 9.2, J = 2.3, H_{21}), 7.43 (1H, dd, J = 8.3, 5.2, H_{18}), 7.28 (1H, d, J = 9.2, H_{20}), 3.98 (6H, q, J = 7.0, H_2), 1.66 (2H, m, H_4), 1.09 (9H, t, J =

7.0, H_1), 0.57 (2H, m, H_3). ^{13}C NMR (400 MHz, d_6- DMSO) ∂_c ppm: 40.9, 52.4, 52.9, 55.6, 58.9, 115.5, 122.1, 124.0, 124.2, 128.7, 129.8, 135.9, 137.2, 145.2, 149.4, 170.3, 173.0, 173.4, 173.5, 222.0. MS (ESI positive ion): m/z (of the asymmetric ligand) 361.0 $[M/2]^+$, 520.2 [M-quinoline]$^+$.

3.6 - Nanoparticle Preparation

3.6.1 - Synthesis of Si_{500}⊂Ru(phen)$_3$

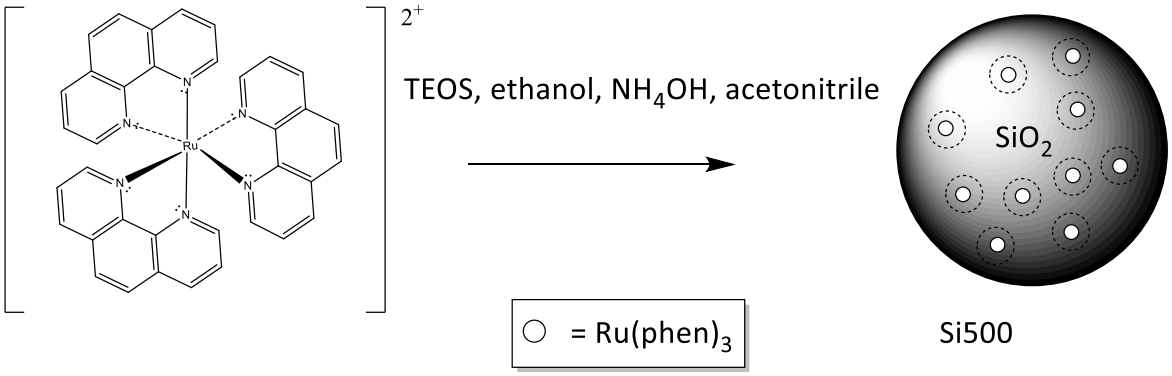

Figure 3.49-A schematic showing [Ru(Phen)$_3$]Cl$_2$ stained silica microparticles:

A solution of tetraethyl*ortho*silicate (1.3 mL) in ethanol (5 mL) was stirred under nitrogen. Aqueous ammonia solution (30 % w/w, 7 mL) in ethanol (18.7 mL) and [Ru(Phen)$_3$]Cl$_2$ (0.5 mg mL^{-1}) in acetonitrile (3 mL) was added. The solution was stirred for 1 h and the microparticles were obtained by centrifugation-redispersion (4 x 10^3 rpm, 30 min per wash) into water (3 x 30 mL), then ethanol (1 x 30 mL) and dried to give a pale orange solid (0.39 g).

Blank silica microparticles were produced as a control. A solution of tetraethyl*ortho*silicate (6.3 mL) in ethanol (5 mL) was stirred under nitrogen and a solution of aqueous ammonia solution (30 % w/w, 7 mL) in ethanol (18.7 mL) and acetonitrile (3 mL) was added. The solution was stirred for 1 h and the microparticles were obtained by centrifugation-redispersion (4 x 10^3 rpm 30 min per wash) into water (3 x 30 mL), then ethanol (1 x 30 mL) and dried to give a white solid (0.34 g). L. M. Rossi et al. Quantities of reactants used for varying the diameter of silica microparticles.[166]

3.6.2 - Synthesis of Si_{800}

A solution of tetraethylorthosilicate (6.3 mL), aqueous ammonia solution (30 % w/w, 3 mL), ethanol (22.7 mL) and acetonitrile (3 mL) was stirred under nitrogen for 1 h. The microparticles were obtained by centrifugation-redispersion (13.7 x 103 rpm 1h per wash) into water (3 x 30 mL), then ethanol (1 x 30 mL) and dried to give a bright orange solid (0.0788 g). L. M. Rossi et al. Quantities of reactants used for varying the diameter of silica microparticles.[168]

3.6.3 - $EuSi_2$ – SAM procedure.

H_3Si_2 was formed through route 2, chelated with europium through titration experiment monitoring by emission spectroscopy, then scaled up to make a 1 mM solution of **$EuSi_2$**. Clean silica slides were immersed into the 1 mM **$EuSi_2$** solution and left sealed and isolated from light for 24hrs. After this time the slides was washed with copious amounts of to remove any unbound material. The SAMs on silica were then dried via a nitrogen stream and placed under nitrogen in a vial and then sealed until use.

3.6.4 - SAM Cleaning Procedure

Silica cover slips were submerged in piranha solution (3:1, sulphuric acid: hydrogen peroxide) for 45 minutes. The clean silica slides were then washed with copious amounts UHQ water, followed by copious amounts of ethanol. The slides were then dried by a nitrogen stream and then immediately submerged into the SAM solution.

4 - Sensing with Sulphur Active UV Absorbing Lanthanide Complexes on Gold Surfaces

4.1 - Introduction

Sensing with an absorbing lanthanide complex ligand has its advantages and disadvantages over the systems mentioned in Chapters 2 and 3. Through incorporation of chromophores into the ligand design it allows the system to operate without the need of additional sensitisation. Thus the analyte does not need to contain a chromophore to have a measurable change on lanthanide emission. One of the most common uses of these systems is a luminescent pH sensor. Parker et al[104,182] has developed lanthanide pH sensors, based on 1,4,7,10-tetraazacyclododecane derivatives to encapsulate the lanthanides and attach various chromophores to the system (*figure 4.0*).

In one example Parker *et al*. attaches a phenanthridinium chromophore as a sensitiser to the lanthanide chelating system, it created a UV absorbing lanthanide complex which showed robust pH sensing capabilities that are stable up to 6 months, and have a stable pH range from 5 to 8. The system works by the protonation on the phenanthridinium chromophore's nitrogen atom, which supresses photoinduced electron transfer, allowing for the population of the phenanthridinium's singlet excited stated and then leading to sensitisation of the europium, increasing europium emission.

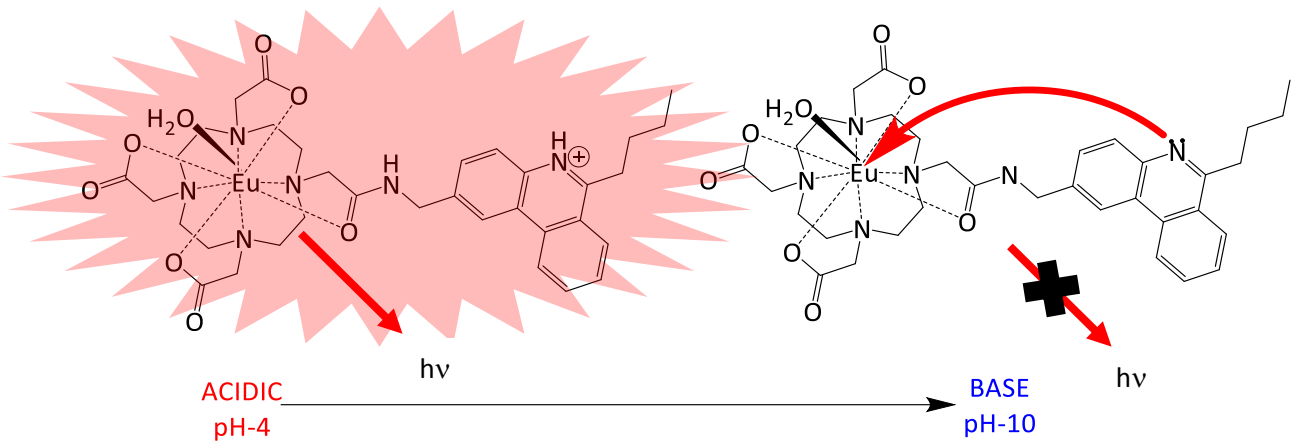

Figure 4.0- Representation of the sensing process of the chromophore containing lanthanide complex designed by Parker et al[183] as a pH sensor

Parker's system relies on the change of luminescence from the europium, but that requires the europium to already be sensitised, thus the presence of the phenanthridinium chromophore. Looking at the system results we can tell that the luminescence decreasees, as the basicity of the solution increases, however the luminescence is never completely quenched, so that the europium's luminescence isn't completely switched off. Which can be used as another detection tool in sensing systems.

An example of a luminescent system that is completely switched off is shown by C. Weder et al's[107] (*figure 4.1*), where they have used a highly fluorescent 2,6-bis(1'-methylbenzimidazolyl) pyridine (Mebip) ligands to act as "antenna" for Eu^{3+} ions. They show that it was possible to quench or enhance the fluorescence and luminescence of organic fluorophores and lanthanide complexes respectively through the detection of organophosphates as chemical warfare agent mimics.[184] Organophosphates are toxic species commonly found in both pesticides and chemical-warfare agents whose rapid and severe effects on human and animal

health lay in their ability to block the action of acetylcholinesterase, a critical central nervous-system enzyme.[185]

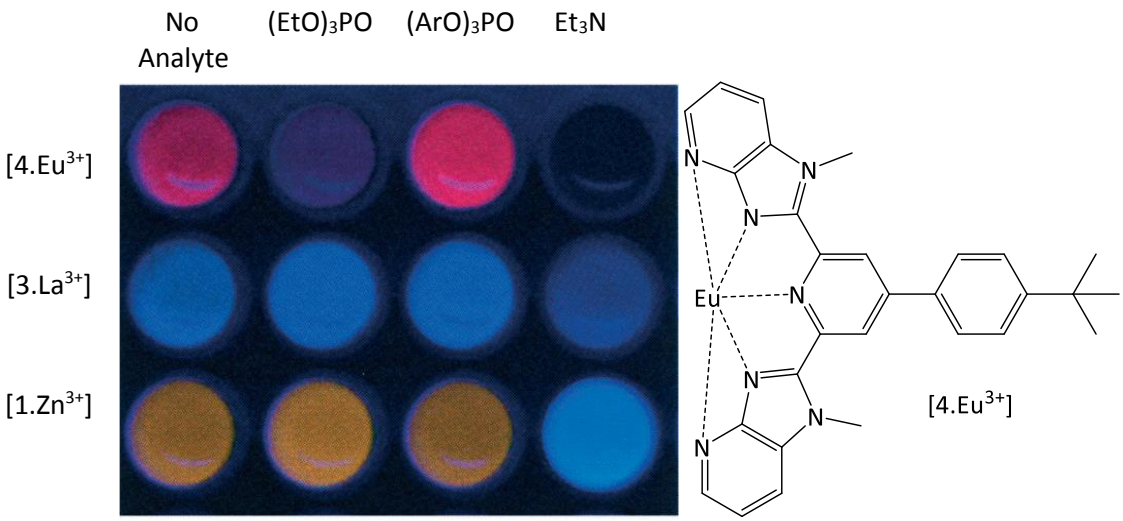

Figure 4.1 - Colour assay demonstrating the effect of coordinating organophosphates and chromophore containing lanthanide chelate.[107]

Weder's system relies on competitive binding, where the sensitised ligand gets displaced by the organophosphates, and the change in luminescence is measured, most of which can be seen by eye at an analyte concentration range of 2.5 mM. Though displacement of the sensitising ligand, the lanthanide luminescence is switched off in the presence of alkyl phosphates, but enhanced in the presence or aromatic phosphates, most likely do to sensitisation of the europium through the presence of aromatic groups in the aromatic phosphates. Other systems where used to compare and contrast behaviours, lanthanium and zinc as well as various sensistisers. The results showed that the system had selectivity and limits of detection down to 20 μM.

The ability to selectively sense for fluoride ions over other halides using lanthanide complexes is reported by Tripier et al[186] .The group demonstrated that the ligand "L" (*figure 4.2*) complexed with lanthanides; Eu, Tb and La showed to be highly selective for fluoride ions in aqueous solution.

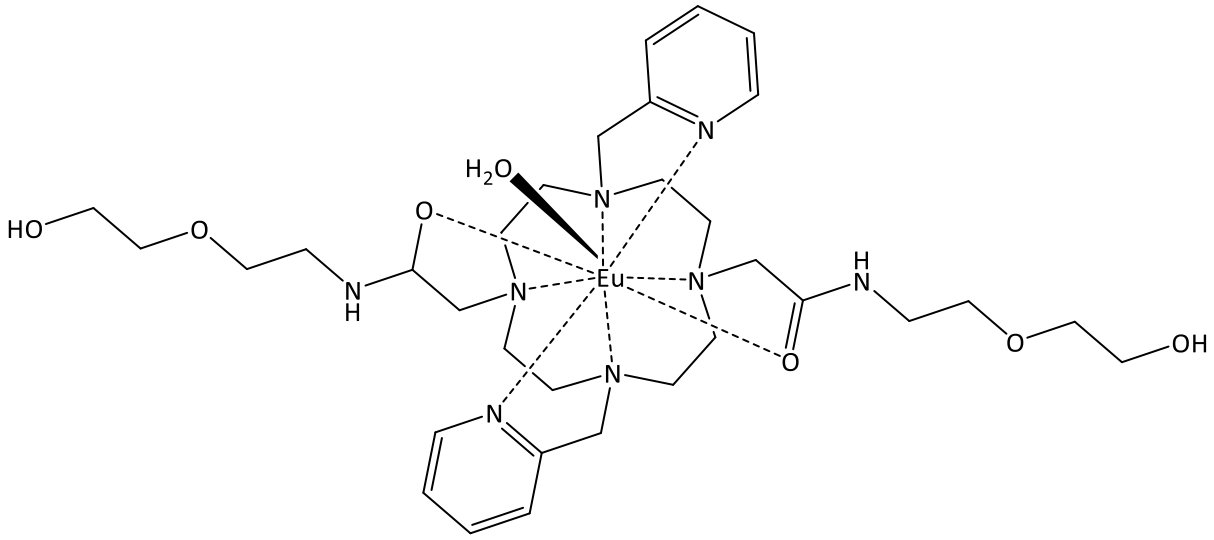

Figure 4.2 - The chemical structure of ligand 'L'

The interaction of fluoride ions and [LnL(H_2O)], was monitored by luminescence spectroscopy. The emission spectra showed an increase in the signal intensity from the lanthanide when fluoride ions were bound to the complex as well as an increase in quantum yield. The increase in lanthanide emission was due to the displacement of the coordinated water molecule, a high vibrational molecule which quenches lanthanide emission with the fluoride ion. This selectivity may be attributed over the other halide ions (bromide and chloride) due to the hard nature of the fluoride ion, which results in a stronger interaction with hard Lewis acids such as the Ln^{3+} ions.[187] However, the size of the anion (1.33, 1.81, and 1.96 Å for F^-, Cl^-, and Br^-,

respectively) could also play an important role in the observed selectivity as well as the increase in electronegativity as you go up the group on the periodic table, implying that the high charge density of the fluoride ion is the dominating factor in the lanthanide complex's selectivity.

SAMs are well studied, and in the case of organic simple alkane chain thiols, forming compact, dense monolayers on the surface in the case of Morgner et al.[188] These are supported by the nature of the hydrophobic alkyl chains pointing away from the surface, and the strong sulphur-gold bond formed at the surface. In the case of lanthanide complexes, they can be modified to incorporate surface attachment groups, which allow the complex to form a whole host of materials MOF, NP, thin films, and can also form SAMs.

Here we show a SAM developed by J. Davis et al.[24] (*figure 4.3*) The SAM contained a binuclear lanthanide complex chelated onto pre-formed catechol SAM, showing reversible chelation on the surface and switch off and on of europium and terbium emission. More importantly to note was their study into how varying the bonding length between the gold surface and lanthanide ion effects the lanthanide emission with respect to quenching.

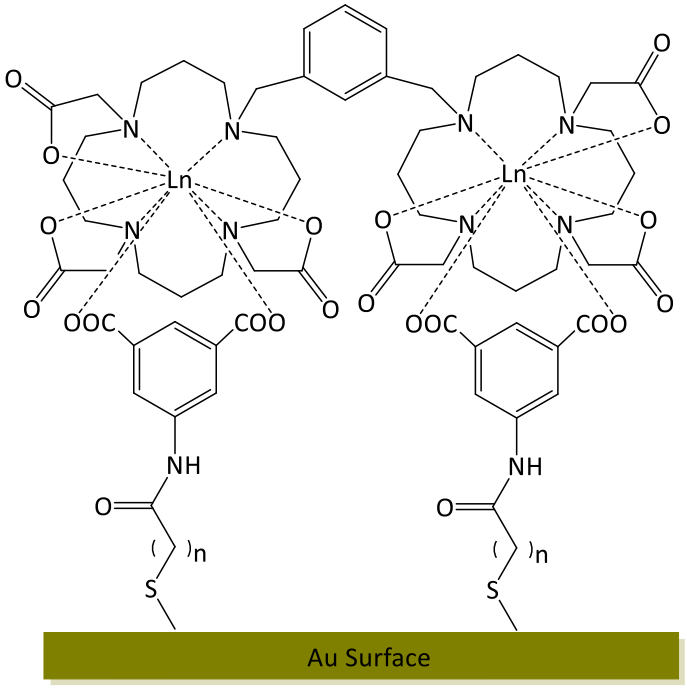

Figure 4.3 - Reversible Binuclear DOTA complex SAM recognition produced by Davis et al[24]

The group modified the catechol chain length from 5, 10 and 15 carbons long and demonstrated that the luminescent intensity increased approximately ten fold by increasing the chain length from 5 to 15 carbons. These findings are in agreement when we compare the results of these monolayers with previously published report in our group involving transition metal based ruthenium tris-bipyridine complex containing two thiols but no aliphatic legs as spacers,[189] which revealed that the spacer has a significant role in decreasing the quenching process.

4.1.1 - Lanthanide UV Absorbing Ligands

Previously in Chapter 2 we have explained the reason for using DTPA-Bisamide derivatives; greater binding affinity for lanthanides, eight coordinate, high hydrophobicity. However addition research in the group has shown that the effect of the most desirable systems did not just require the bisamide arms and the analyte to be bulky and hydrophobic, but also the presence of electronegative groups in the analyte system and that two fused ring system provided greater sensitisation to the core lanthanide than a singular aromatic system. The presence of electron withdrawing functional groups can also help to enhance emission by removing any quenching caused by electron transfer. To improve luminescence, derivatives of quinoline and hydroxyquinoline molecules were investigated, which have a lower triplet state than simple aromatic molecules like benzoate allowing for better energy transfer and sensitisation of europium centre, as the respective energy levels are more compatible for energy transfer. The quinoline and hydroxy-quinoline molecules had very significant effect on the emission intensity, with up to a 500 fold increase in relative signal intensity.

4.1.2 - The Design of UV Absorbing Ligands

The complexes that have been developed here use lanthanide enhanced or reduced sensitisation via recognition. It is composed of three major components. The first component is that the **EuL** has a chromophores in its ligand architecture (*figure 4.4*). For example quinoline which has the capacity to effectively absorb UV radiation and transfer the absorbed energy to the lanthanides emissive state, creating a lanthanide absorbing ligand (LnAL), resulting in a luminescent lanthanide complex. The second component of the system is the analyte, the component in which the system is designed to detect for. In this system, it has been designed to only detect for analytes which have chromophoric units which have the correct excited triplet state to undergo energy transfer, to the lanthanide emissive state enhancing the compounds already existing lanthanide emission. The analyte also needs to be small enough to fit into the cavity of **EuL** and have a coordinating functional group to directly bind to the lanthanide. The third component is a surface active functional group. In the case of **EuL** it contains two thiolacetate groups which can hydrolyse onto gold surfaces in the form of thiols.

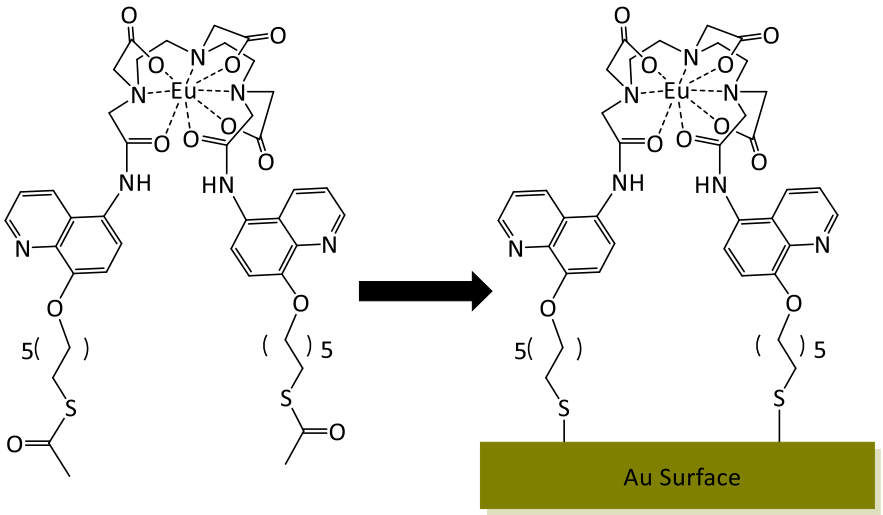

Figure 4.4 - Chemical Structure of EuL

Many surface active moieties for gold surfaces have been reported and mainly utilise sulphur as a 'soft' ligand to bind to the gold surface. Sulphur is able to form bonds with the gold surface that are more covalent in character than 'hard' ligands, such as oxygen and nitrogen; which are used for binding ligands to lanthanides. Soft metals, such as gold, form stable bonds to sulphur (~100 kJ mol^{-1}).[29,190] This stability means that sulphur containing moieties are stable on the surface over a wide array of temperatures[15] and potentials[191] and allow for highly organised SAMs to form on the surface of well-defined thickness, composition and structure.[28] SAMs that use sulphur to bind to surfaces include disulphides and thiols,[48,49] thioacetates,[4] thioctic acid,[192] with thiols being the most widely reported. Thiols are generally used for surface attachment, as they are the most understood moiety for this purpose. They also provide an easy method for attachment, as a surface can simply be left in the thiol solution for a period of time for self-assembly to occur. Thioacetates prove to be more difficult to chemisorb to the surface, however they are still able to bind but exhibit a slower binding mechanism, as the acetate needs to be cleaved prior to chemisorption.[40] To speed up the cleavage of the thioacetate bond they can be either deprotected to the free thiol prior to gold adsorption or deprotected in situ using an additive such as ammonium hydroxide[40], or deprotected as an additional reaction step.

Similarly to the design of **$EuSi_2$**, **EuQuinSi** and **EuBDS** (Chapter 1 and 2), placing complexes on a surface forms a scaffold, allowing for a more controlled system to be created. Having a planar surface and surface attachment allows for SAMs to be created. In the development of devices, SAM based systems are similar to lab-on chip systems and gives advantages such as

regenerative abilities of the device, saving in costs. Also, by making a device regenerative, it allows for the sampling solution to wash of the device, whilst keeping the host system still attached to the device, making the device reusable. When **EuL** is bound to a surface there is a pseudo macrocycle between the surface and **EuL**. The lanthanide complex does contain 6 carbon spacers between the binding sulphur groups and the lanthanide's core chelating group, this still only allow relatively small molecules to bind into the cavity similarly to **$EuSi_2$** which has a spacer of 4 units, preventing larger molecules from entering and binding, this restriction makes the system more specific.

4.2 - Results and Discussion

4.2.1 - Characterisation of Compound 2

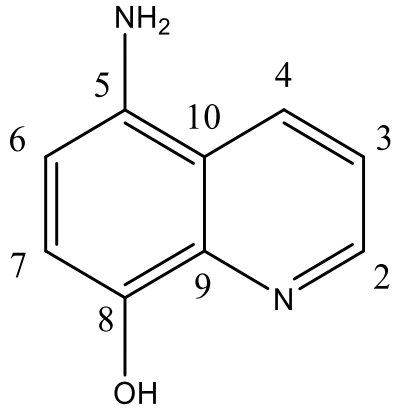

Figure 4.5- Chemical structure of Compound 2

Compound **2** (*figure 4.5*) has been characterised by ^{1}H-NMR spectroscopy, ^{13}C-NMR spectroscopy and mass spectrometry. The reaction was purified by washing with base to remove the dichloride salt. The amine being protonated in the dihydrochloride salt prevented successful mono protection of the amine, necessary for higher chemoselectivity at the hydroxyl group during the subsequent ether synthesis step. The reaction was monitored by ^{1}H-NMR spectroscopy. The ^{1}H-NMR spectra correctly displays the expected seven peaks excluding the solvent peak; 5 peaks from the quinoline in the aromatic region, plus the hydroxyl group in the same region. The remaining peak is in the aliphatic region, further down field than amines usually appear due to its attachment to the aromatic quinoline.

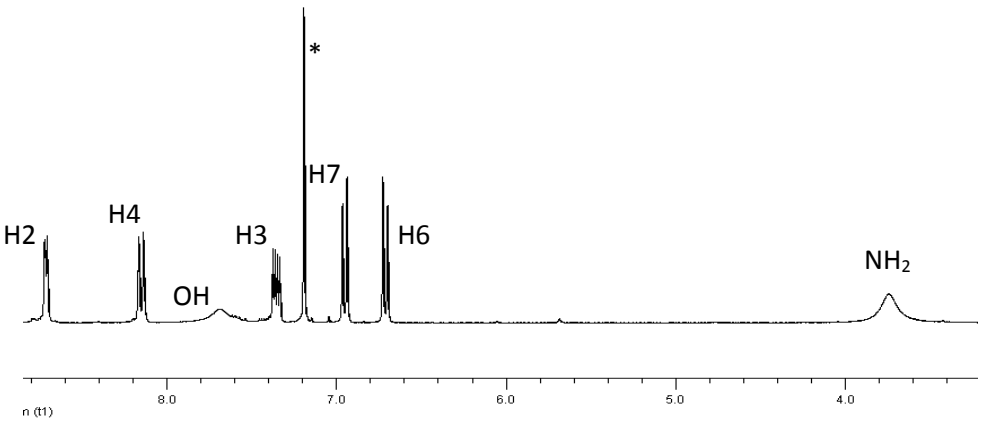

Figure 4.6-The ^{1}H-NMR spectrum of compound 2 -*indicates resonance peak from the solvent chloroform.

Following the ^{1}H-NMR spectra (*figure 4.6*), there is a disappearance of a broad peak at 11 ppm, previously integrated for 4H, representing the combined integration value of the protonated N on the pyridine ring of the quinoline and the protonated amine from **Compound 1**. Upon removal of the hydrochloride salt, the protonated amine peak shifted up field to 3.9 ppm, with an integration of 2H. Also the absence of the pyridine protonation indicates the starting material has been purified.

4.2.2 - Characterisation of Compound 3

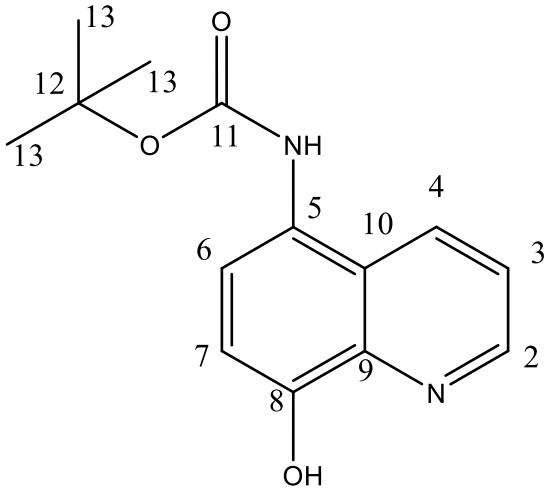

Figure 4.7 - Chemical structure of Compound 3

Compound 3 (*figure 4.7*) has been characterised by ^{1}H-NMR spectroscopy (*figure 4.8*), ^{13}C-NMR spectroscopy, electrospray mass spectrometry, and elemental analysis. The reaction was followed by TLC on neutral alumina plates. The reaction has proved to have gone to completion by ^{1}H-NMR spectroscopy as shown in *figure 4.8*. The ^{1}H-NMR spectra correctly presents eight resonance peaks; seven aromatic and one in the aliphatic region. Primarily the appearance of the methyl group at 1.5 ppm, and an integration of nine hydrogens shows the binding of the boc protecting group. The progression of the reaction is further evident by the resonance shift of H-6 from 6.9 ppm downfield to 7.4 ppm, this shows that the hydrogen is further de-shielded due to the presence of the boc protecting group, and thus must be relatively close via the sigma framework or through relative space, it is indeed possible that there could be some hydrogen bond interaction between either oxygen with a pseudo six member ring formation. The third evidence noticeable by ^{1}H-NMR spectroscopy is the down field shift of N*H* from 3.8 ppm to 6.4 ppm (a change from aliphatic region to aromatic spectral

regions) and the integration value decreasing from one hydrogen to two hydrogens indicates the formation of a carbamate bond. The final evidence is a downfield shift of peaks as opposed to upfield shift of peaks indicates that the bond formed contains electron withdrawing groups, causing hydrogens to become more de-shielded; the boc group is indeed an electron withdrawing protecting group capable of causing the downfield shift. Alternative routes for amine protection have been tried, varying the concentration of reagents and alternative reaction solvents have been used, all of which presented an undesired bis protected quinoline, having the boc protecting group present at the amine and the hydroxyl functional groups, this was characterised by ^{1}H-NMR spectroscopy and mass spectrometry. The final solution was to adjust the molar equivalent of boc protecting agent, to 1.05, and add to a cooled solution, dropwise over 45 minutes, producing a mono-protected species at the desired amine.

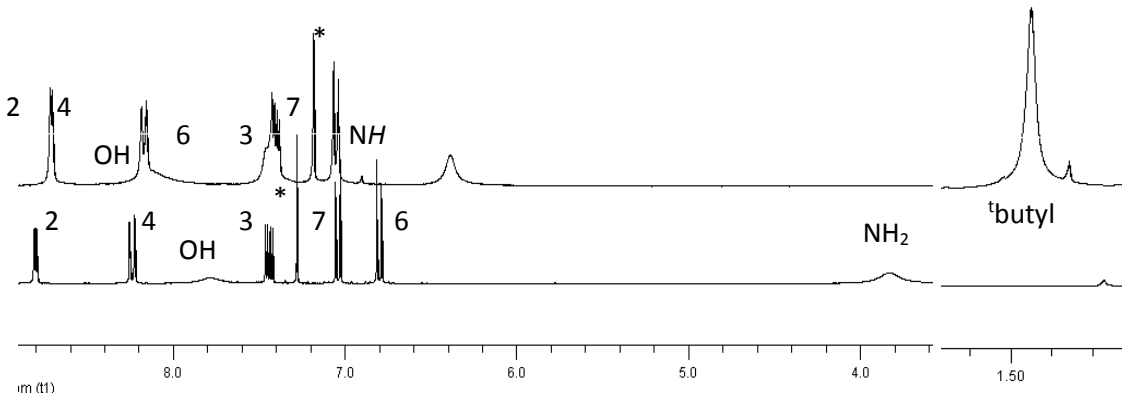

Figure 4.8 - The top ^{1}H-NMR spectrum shows Compound 3, and the bottom spectrum is of Compound 2 .*indicates resonance peak from the solvent chloroform.

4.2.3 - Characterisation of Compound 5

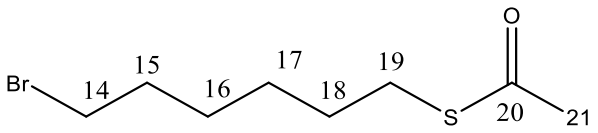

Figure 4.9-Chemical structure of Compound 5

The synthesis of **Compound 5** (*figure 4.9*) was confirmed by ^{1}H-NMR spectroscopy. The ^{1}H-NMR (*figure 4.10*) spectrum shows a shift of the triplet signal from H-19 upon binding to the thioacetic acid and the multiplet from the alkene H-18 shift upfield to where an alkane chain is expected.

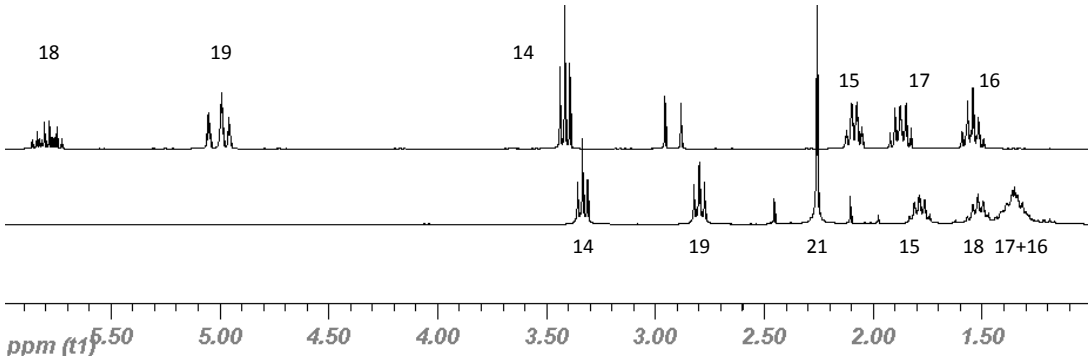

Figure 4.10 - The top structure is of Compound 5 and the bottom shows ^{1}H-NMR spectrum showing 6-bromo-1-hexene at the top, and Compound 5 at the bottom.

4.2.4 - Characterisation of Compound 6

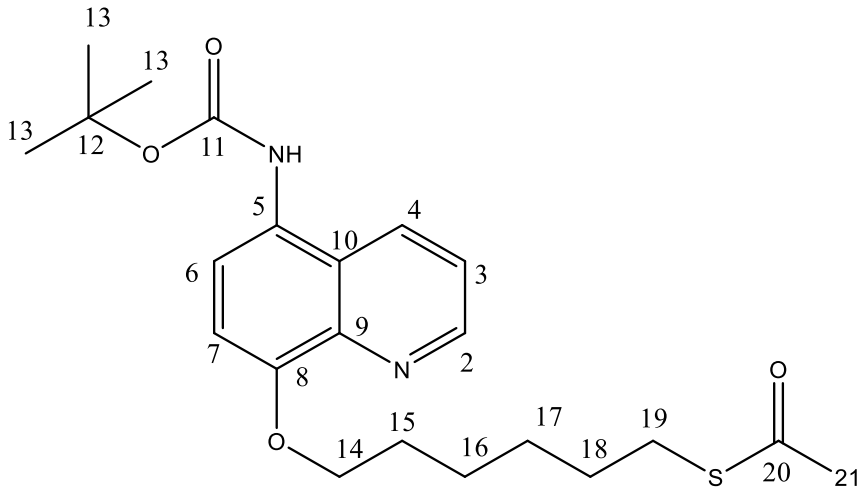

Figure 4.11 - Chemical structure of Compound 6

Synthesis of **Compound 6** was characterised and followed by ^{1}H-NMR spectroscopy, ^{13}C-NMR spectroscopy and mass spectrometry. As shown by *fig 4.12*, the ^{1}H-NMR spectrum correctly displays the predicted thirteen hydrogen environments; six from the aromatic; five from quinoline, one from the amide and seven in the aliphatic region; six from hexane carbon chain, and one signal from the boc protecting group. The appearance of the aliphatic hydrocarbon chain from **Compound 5** is now present in **Compound 6**. The hydrogens corresponding to positions 15, 16, 17 have been incorporated to the integration of the boc protecting group, at 1.5 ppm. As expected the hydrogens adjacent to the bromine atom in **Compound 5** are deshielded upon binding to a more electronegative element such as oxygen in **Compound 3**, this is shown by a shift in H-14 down field from 3.4 ppm to 4.3 ppm. The OH signal given at 8.2 ppm has also disappeared in the ^{1}H-NMR spectrum for **Compound 7** indicates binding at this point. The electrospray (positive) mass spectrometry revealed the parent ion at m/z 419.2, and two more peaks corresponding to the sodium and hydrogen adducts of the parent ion.

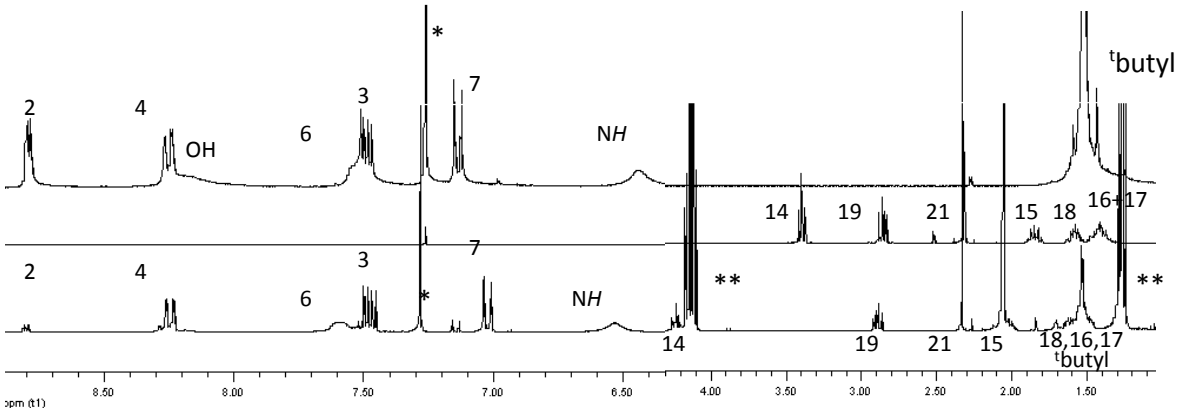

Figure 4.12 - The top structure shows compound 6, and below shows the ^{1}H-NMR spectrum of compound 3 at the top, compound 5 is shown by the middle spectrum and the bottom spectrum is compound 6. *Indicates resonance peak from the solvent chloroform, and **ethyl acetate.

4.2.5 - Characterisation of Compound 7

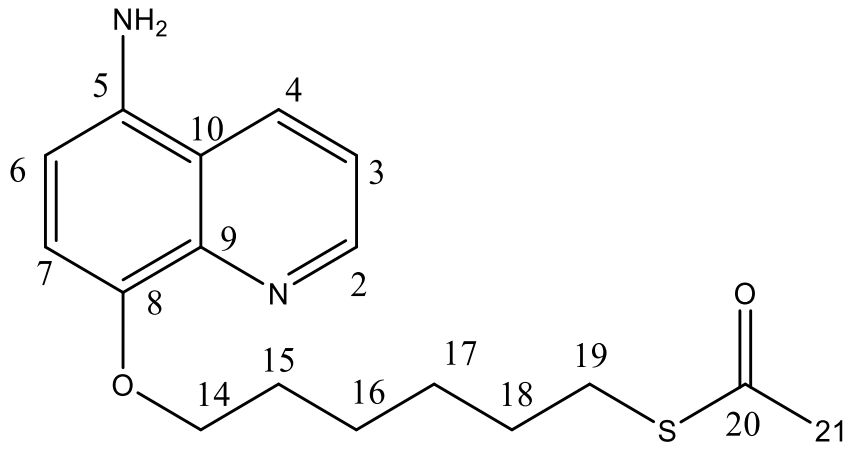

Figure 4.13 - Chemical structure of Compound 7

The boc deprotection step was characterised and followed by ^{1}H-NMR spectroscopy, ^{13}C-NMR spectroscopy and ES MS. The ^{1}H-NMR spectrum (*figure 4.14*) correctly displays the predicted twelve hydrogen environments; five from the aromatic region; all from quinoline, and seven in the aliphatic region; six from the hexane carbon chain and one signal from the amine. The expected disappearance of the boc signal at 1.5 ppm indicates cleavage of the carbamate bond and the shift of H-6 from 7.6 ppm upfield to 3.8 ppm its original signal location prior to Williamson either step, and the boc protection step, plus a correct indication of the re-protonation of the amine to give an integration of two hydrogens. The remaining signals are similar to the protected species, except for a slightly larger shift of H-7 this could be accounted for the larger *+I* inductive effect from the hexane chain. Mass spectrometry (electrospray positive) shows parent peaks at m/z 319.1, and the sodium adduct at m/z 341.1.

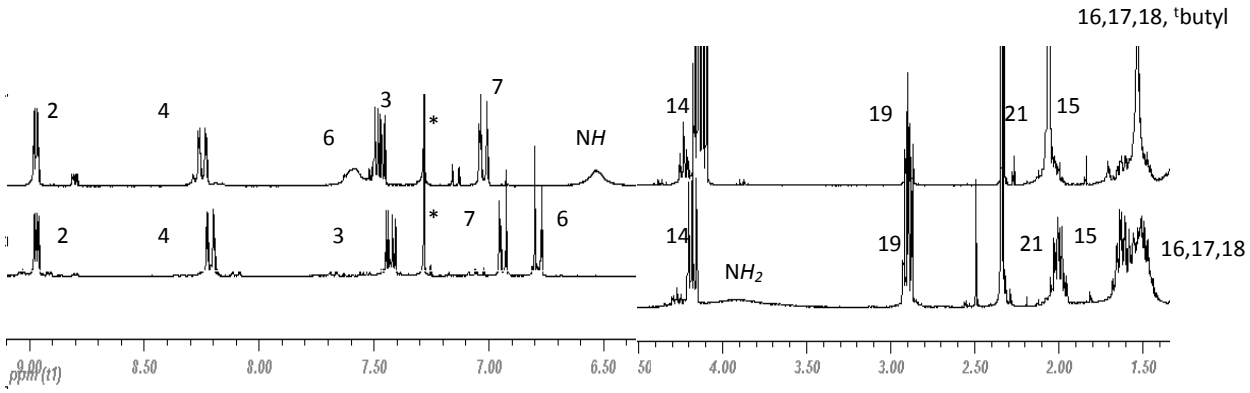

Figure 4.14 - A ^{1}H-NMR spectrum showing signals from Compound 6 at the top and the bottom spectrum shows signals from Compound 7. *Indicates resonance peak from the solvent chloroform.

4.2.6 - Characterisation of H_3L

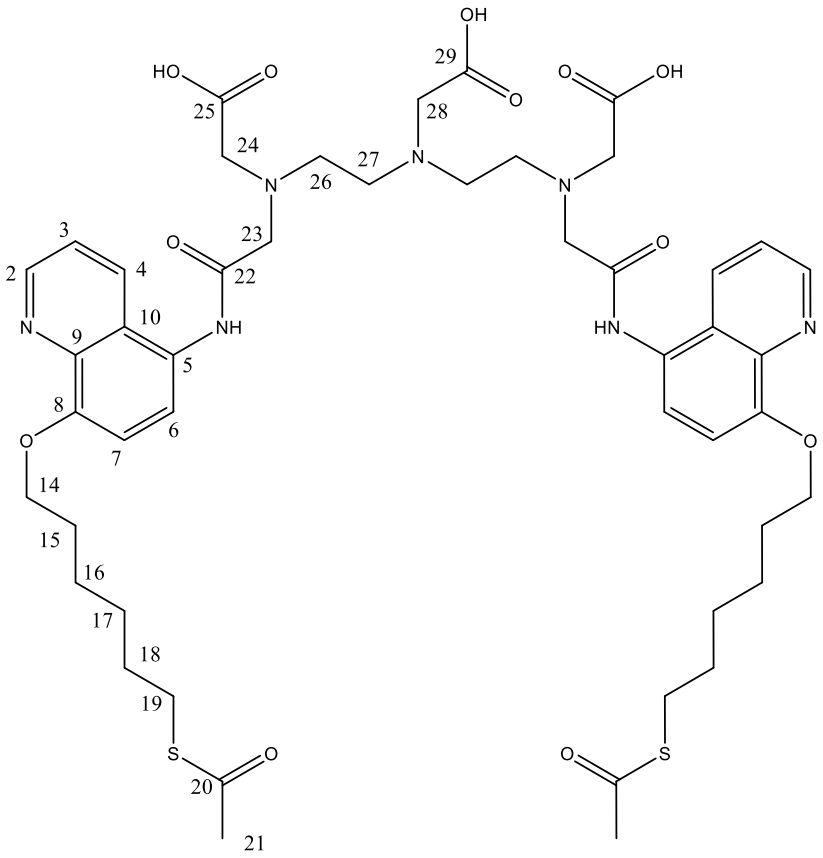

Figure 4.15 - Chemical structure of H_3L

H_3L (*figure 4.15*) was characterised by ^{1}H-NMR spectroscropy, ^{13}C-NMR spectroscopy, electrospray mass spectrometry and elemental analysis. The ^{1}H-NMR spectrum (*figure 4.16*) shows 16 environments; 6 in the aromatic region; 5 from quinoline, 1 from the amide bond, 10 signals in the aliphatic region; three from DTPA, and six from the hexane chain, and one from the thioacetate. Similar behaviour of the H-6 signal has been seen previously when protecting the amine group, which is also observed here too; the H-6 signal shifts due to amide formation, from 6.8 ppm to 7.6 ppm. The disappearance of the amine group signal and the appearance of the amide signal at 10.1 ppm shows binding, and a downfield shift shows nucleophilic attack of the amine from the quinoline to the carbonyl of the anhydride in DTPA

bis-anhydride. There is also an upfield shift of the ethylene hydrogen signals at 3.4 ppm and 3.1 ppm to 3.1 ppm and 2.9 ppm respectively. Opening the anhydride of DTPA bis-anhydride causes H-24 and H-23 signals undergo an upfield shift from 3.9 ppm to 3.5 ppm joining the other asymmetric ethylene proton signal adjacent to a carboxylic acid group (H-25). The carbon NMR spectra shows 25 environments and a needed 24, C-25 and C-29 have been assigned the same signal. Mass spectrometry shows the parent peak 994.2 and the base peak at 1016.2 representing the sodium adduct minus a hydrogen. Two more peaks; m/z 1018.2 is the parent ion plus sodium.

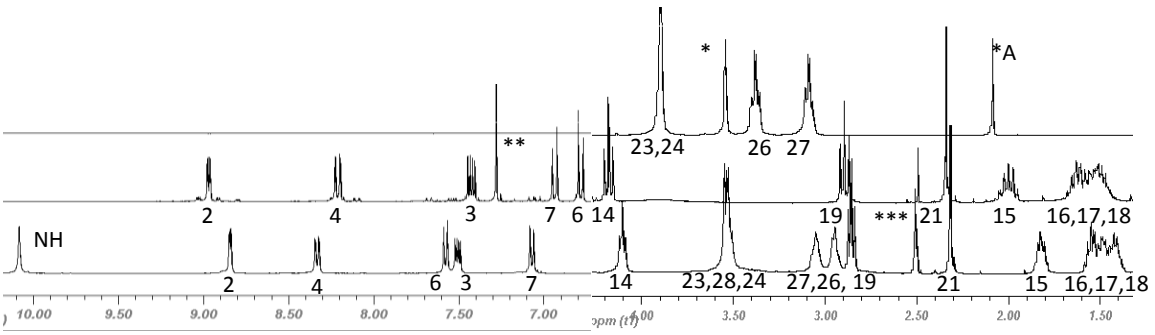

Figure 4.16 - The top structure is of H_3L and below is the ^1H-NMR spectrum is of DTPA Bis-anhydride. The middle spectrum is of compound 7. The bottom spectrum is of H_3L. *Indicates resonance peak from the solvent D_2O, and **Chloroform, the bottom spectrum was run in ***DMSO. *A-residual acetone.

4.2.7 - Characterisation of EuL and YL

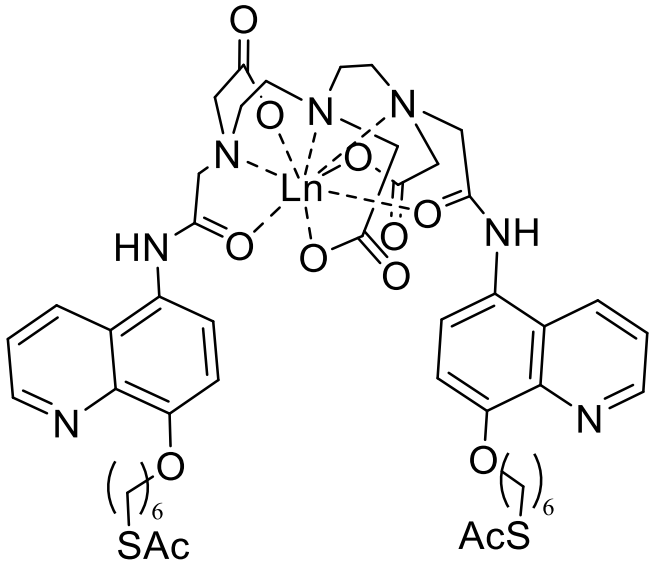

Figure 4.17 - The LnL lanthanide complex, Ln = Eu or Y

EuL (*figure 4.17*) has been characterised by electrospray time of flight mass spectrometry and photophysical studies. The first mass spectrum showed that the base peak was indicative of NH_4OH which was washed out after stirring in acetonitrile and filtration. The parent peak displayed the signature isotope pattern of europium, at m/z 1166.79. A peak at 1168.81 is the sodium adducts and peaks at m/z 1182.79 is the potassium adduct. At higher m/z there is an indication of doubly charged peaks of both the sodium adduct and the parent ion. Due to europium being highly paramagnetic, the ^{1}H-NMR spectrum will show a very broad singlet peak. Thus, to give more information about the proton environments present, the same procedure was performed but europium was replaced with yttrium, a diamagnetic transition metal of similar chemical properties as lanthanides, a diamagnetic analogue[193] giving the complex YL.

4.2.8 - Characterisation of YL

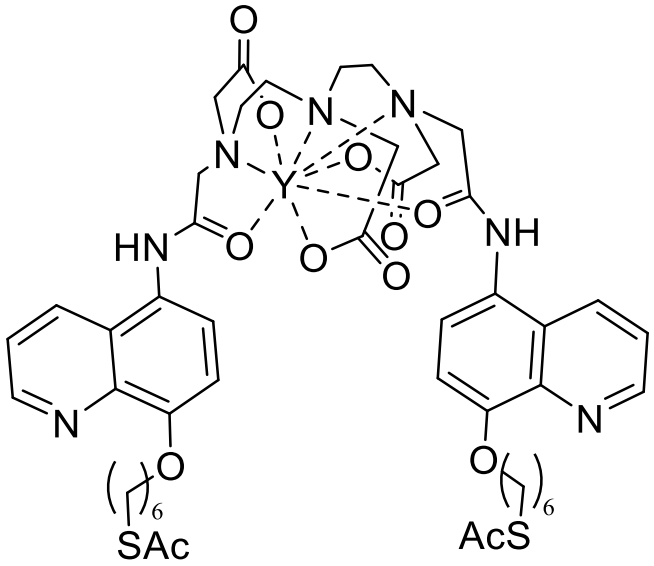

Figure 4.18 - The YL lanthanide complex

YL (*figure 4.18*) was characterised by ^{1}H-NMR spectroscopy. The ^{1}H-NMR signals are broad due the existence of a series of interchanging isomers giving rise to many different rotamers, each with slightly different chemical shifts, thus causing the signal to broaden.[56] The integration was still possible and the aliphatic region gives 52H and 48H was expected, and the aromatic gives an expected integration of 10 hydrogens.

4.3 - Photophysical studies of H_3L and EuL

4.3.1 - UV-Vis Spectroscopy

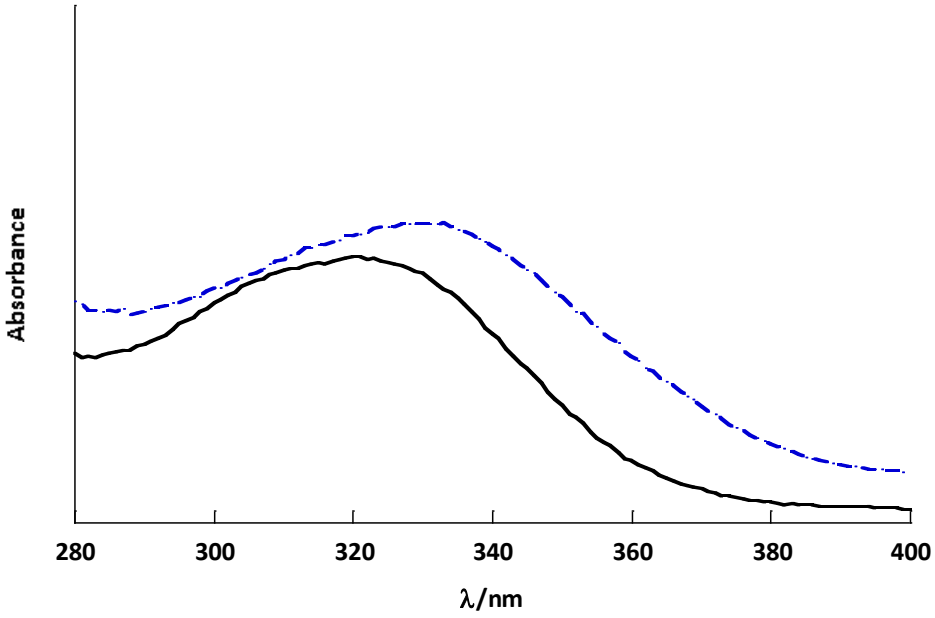

Figure 4.19 -Uv-Vis spectrum for H_3L (—) at 39μM in DMSO and EuL (---) at 32 μM in methanol

The absorbance spectrum of **H_3L** (*figure 4.19*), showed an intense broad band with λ_{max} = 330 nm, (ε=7991 $dm^3cm^{-1}mol^{-1}$). This is attributed to the singlet-singlet $\pi \rightarrow \pi^*$ absorption band and is characteristic of the quinoline. The spectrum is in agreement with a similar quinoline based compound, previously reported literature of λ_{max} = 330 nm by Kim *et al*.[194] The absorbance spectrum of **EuL** showed an intense broad band with λ_{max} = 315nm, (ε = 7711 $dm^3cm^{-1}mol^{-1}$). This is attributed to the singlet-singlet $\pi \rightarrow \pi^*$ absorption band and is characteristic of the quinoline, indicating that the ligand is still present, after binding with the lanthanide.

There is a blue shift in the λ_{max} of the absorption band from the ligand in DMSO to the complex in methanol after the europium is bound and this can be attributed to the change in solvent environment. UV-Vis spectroscopy of **H_3L** shows the absorption band where **H_3L** absorbs at and the λ_{max} indicates the most effective wavelength that will excite the ligand. Upon excitation, the ligand then under goes photon-induced energy transfer process, transferring energy to the europium, increasing the amount of lanthanide emission.

4.3.2 - Emission and Excitation spectroscopy of H_3L

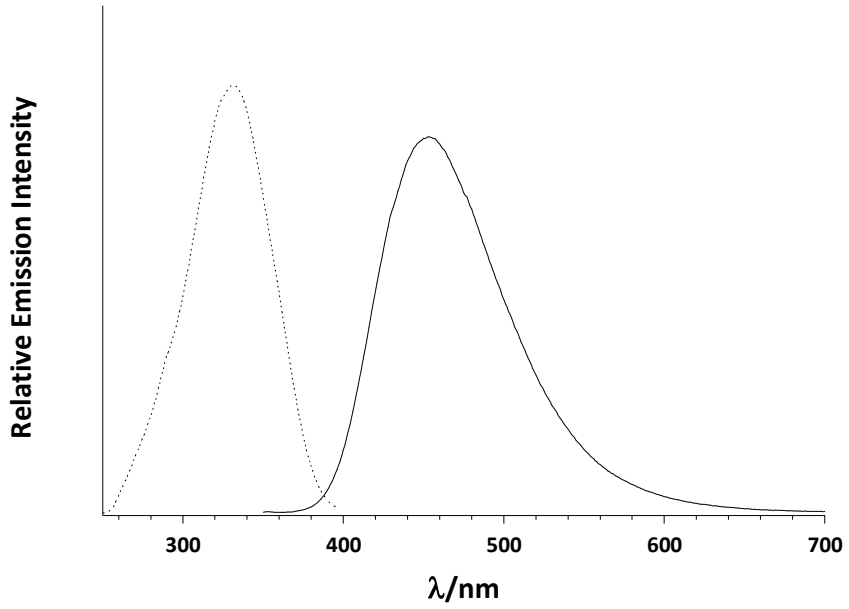

Figure 4.20 - Emission (---) and excitation (—) spectrum of H_3L in HPLC DMSO 39 μM, λ_{exc}=331 nm, λ_{em}=450 nm.

The emission spectrum of **H_3L** (*figure 4.20*) shows λ_{max}=450nm, this is characteristic of the fluorescent decay of the π^* triplet excited state of the quinoline sensitiser in **H_3L**. By exciting the quinoline at 331nm, and detecting the energy of the photons emitted upon fluorescent decay of the quinoline triplet excited state, the emission spectrum was recorded.

The emission band arising from the decay of the triplet excited state is important because the band is expected to decrease with the presence of europium due to energy transfer from the triplet excited state, to the ^5D_J bands of europium. To ensure the triplet excited state band

arises from excitation at 330 nm and not another wavelength, an excitation spectrum was recorded. Excitation spectroscopy detects the most efficient wavelength responsible for a specific emission wavelength. Thus with **H_3L** the most intense emission was at 450 nm, and by detecting the emission signal at 450 nm, and varying through a range of excitation wavelengths the most efficient wavelength responsible for 450 nm emission can be known. The results showed the most intense emission was obtained at λ_{exc} =330 nm. The excitation profile matched the profile of the Uv-Vis spectrum, as expected.

4.3.3 - Emission and Excitation Spectroscopy – EuL

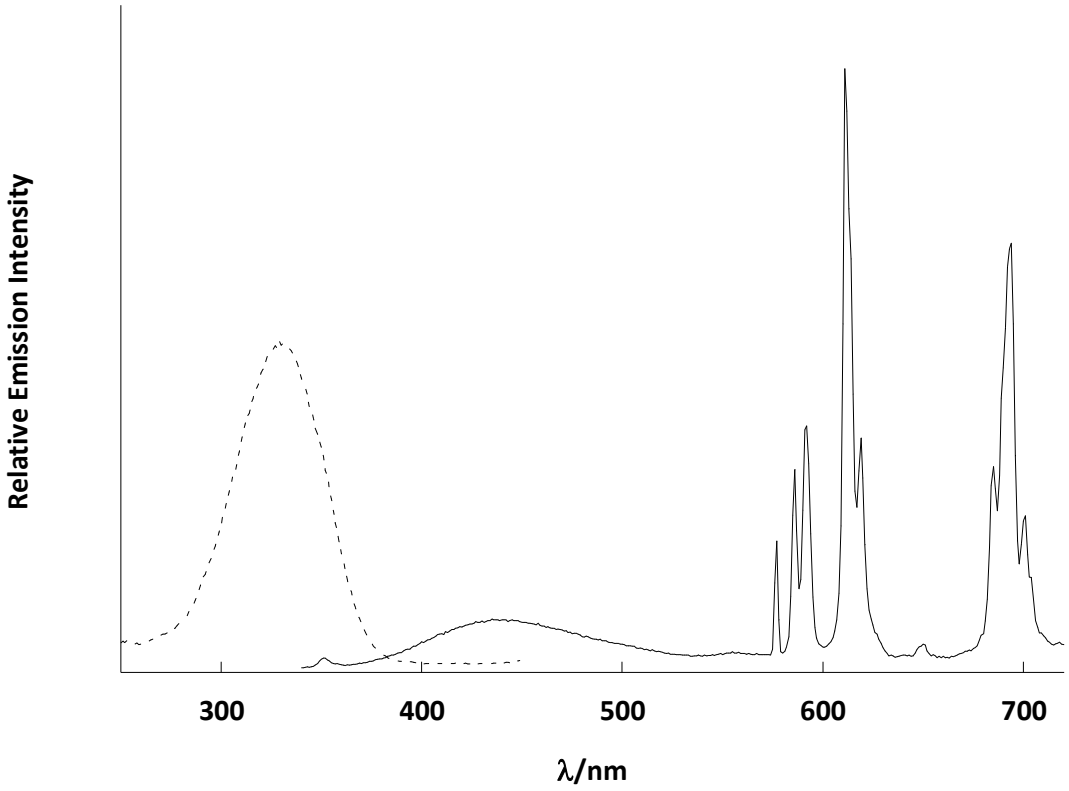

Figure 4.21- Excitation (---) and Emission (—) spectrum of EuL in Methanol 34.9 μM, λ_{exc}=320 nm, λ_{em}=612 nm

The emission spectrum for **EuL** (*figure 4.*21) showed characteristic red emission bands after excitation at 320 nm with $^5D_0 \rightarrow {}^7F_J$ (J= 0, 1, 2, 3, 4, 5) *f-f* transitions observed at 579, 594, 615, 652, 696 and 749 nm, with the most intense emission band at λ_{em}=615 nm. The emission spectrum showed that energy transfer to the europium had occurred. This was indicated by the decrease of the triplet excited $\pi^* \rightarrow \pi$ band at 450 nm, and the relatively intense europium *f-f* transitions bands.

For further studies of analyte and sensor binding studies, the evolution of europium emission bands needs to be monitored, thus it is important to ensure that the correct excitation

wavelength is chosen in order to promote energy transfer to the lanthanide, increasing the emission signal. Thus, like with H_3L, an excitation scan of **EuL** was recorded and showed the λ_{max} =330 nm by only detecting the wavelength of 615 nm emitted from **EuL**, and varying the excitation wavelength, the most efficient wavelength at exciting the quinoline can be known. The profile matched the profile of the UV-Vis spectrum, which is expected as only one absorption band is expected, the $\pi \rightarrow \pi*$ band between 250 and 400 nm.

4.3.4 - Lifetimes of EuL

The lifetime of the luminescent excited state in **EuL** (*figure 4.22*) is of great importance for its application as a sensor. If the lifetime of the sensor is longer than the detected analyte then observing the change in photophysical profile of the sensor becomes easily differentiated between the photophysical properties of the analyte and the sensor if any. Gated measurements may be introduced which cuts out any background organic fluorescence, from the analyte or any other biological organic molecules, typically in the nanosecond timescale, whereas europium emission extends to the millisecond range, having a longer life time than organic dyes.

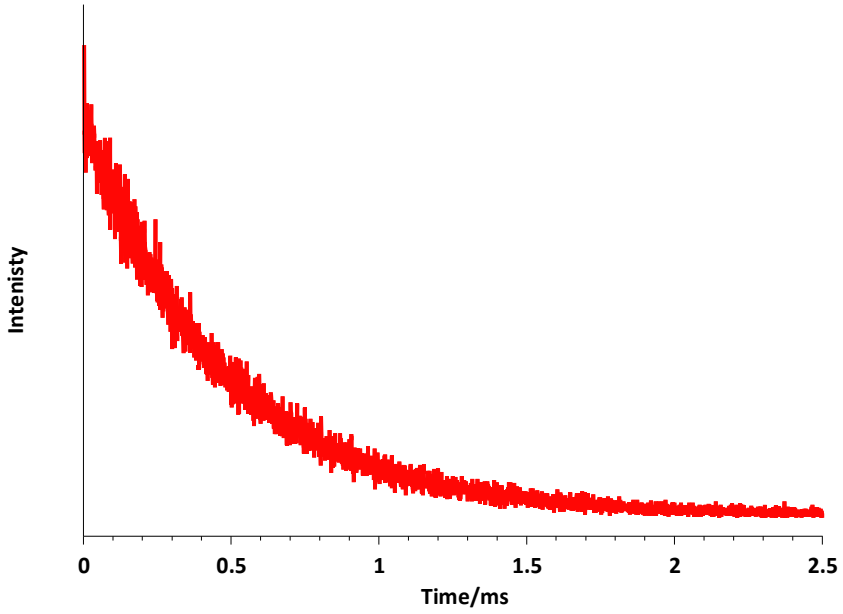

Figure 4.22- Luminescence lifetime decay of EuL at a concentration 34.9 μM, λ_{exc}=615 nm, methonol.

The observed life time of the luminescent excited state in **EuL** was 0.5 ms which is of comparable value to the europium lifetime in **EuQuinSi** (0.6 ms).

4.3.5 - NdL-NIR sensitisation

Near infrared (NIR) lanthanide, neodymium was used as the central lanthanide ion in H_3L to utilise the additional properties lanthanides, much like chapter 2 and the utilisation of curcumin with $YbSi_2$, where the advantages of NIR emitters has been explained in more detail. In short NIR emitters, like neodymium, have certain key benefits over shorter wavelength emitters in the field of bioanalytical and bioimaging. These benefits allows the user to more effectively distinguish lanthanide signal from autofluorescence emitting from biological matter, as the stokes shift is significantly larger using the neodymium based systems, ~740 nm as opposed to that of autofluorescence ~100 nm. Having a larger stokes shift implies that excitation source may have a broader excitation resolution, making the system cheaper, and potentially still have quality emission data from the NIR lanthanide system. The other properties of visible light emitting lanthanides still apply to NIR emitting lanthanides, thus sharp band structure and time gated approaches are still expected and can be taken respectively.

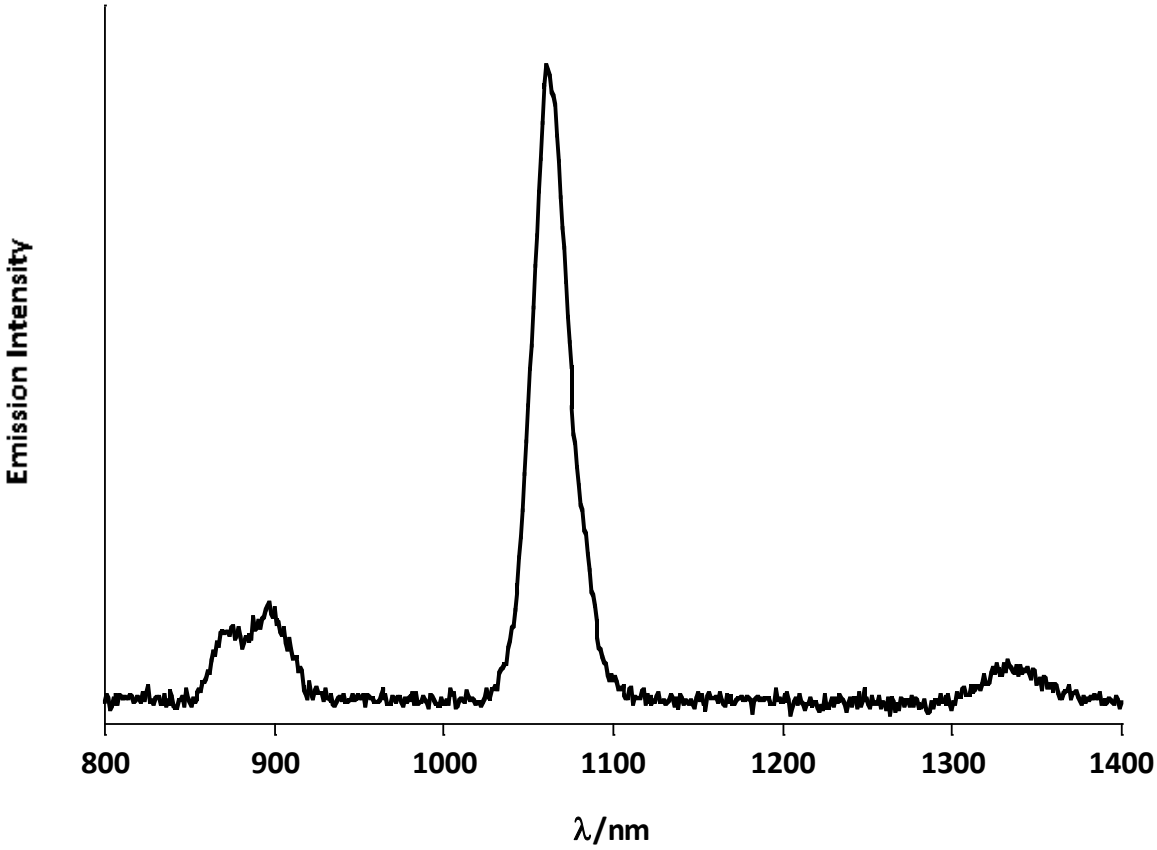

Figure 4.23 - Emission Spectrum of NdL (—) λ_{ex}= 320 nm, methanolic solution.

The emission spectrum for **NdL** (*figure 4.23*) showed characteristic near infrared emission bands after excitation at 320 nm yields characteristic near infra-red emission at 890, 1065 and 1350 nm assigned to the $^4F_{3/2}$ to ^4I_J (J = 9/2, 11/2, 13/2) transition of Nd(III). The emission spectrum showed that energy transfer from the quinoline to the neodymium had occurred. This coordination of **H_3L** to neodymium was also indicated by the decrease of the triplet excited $\pi* \rightarrow \pi$ band at 450 nm.

4.3.6 - EuL-Enhanced Lanthanide Emission - Sensing in Solution

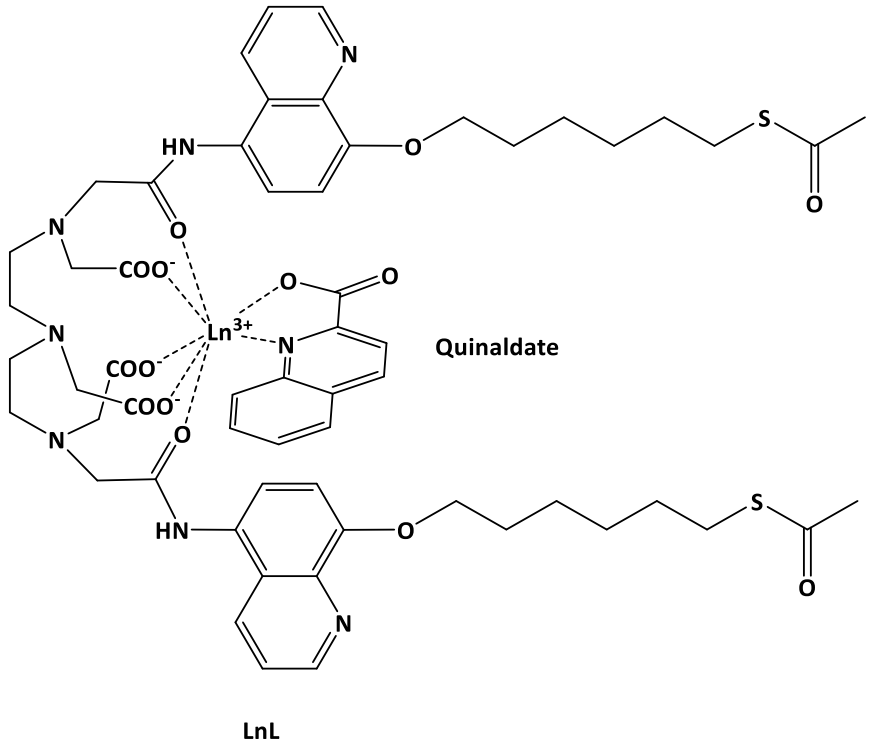

Figure 4.24 - Chemical structure of LnL with the potential binding of quinaldate.

Much like the cases with **EuBDS**, **EuSi$_2$**, and **EuUDS**, we investigated the use of **EuL** as a small analyte sensor (*figure 4.24*), with the like of quinaldate, DBM, dipicolinate and picolinate. Similarly with **EuL** the lanthanide system has chromophores built into the architecture of the complex. Which indicates that lanthanide emission is expected to be seen without the analyte that we are screening for having been bound to the lanthanide ion; thus we are not looking for the appearance of luminescence but a change in signal intensity. We have already shown that the **EuL** complex is highly emissive and that the energy originates from the excitation of the quinoline sensitisers. By using this system we expect enhanced lanthanide emission to occur, due to the addition of chromophoric small molecules binding to the lanthanide, and

this then increase in lanthanide emission becoming the detectable measure, to indicate, or even quantify the presence of our analyte.

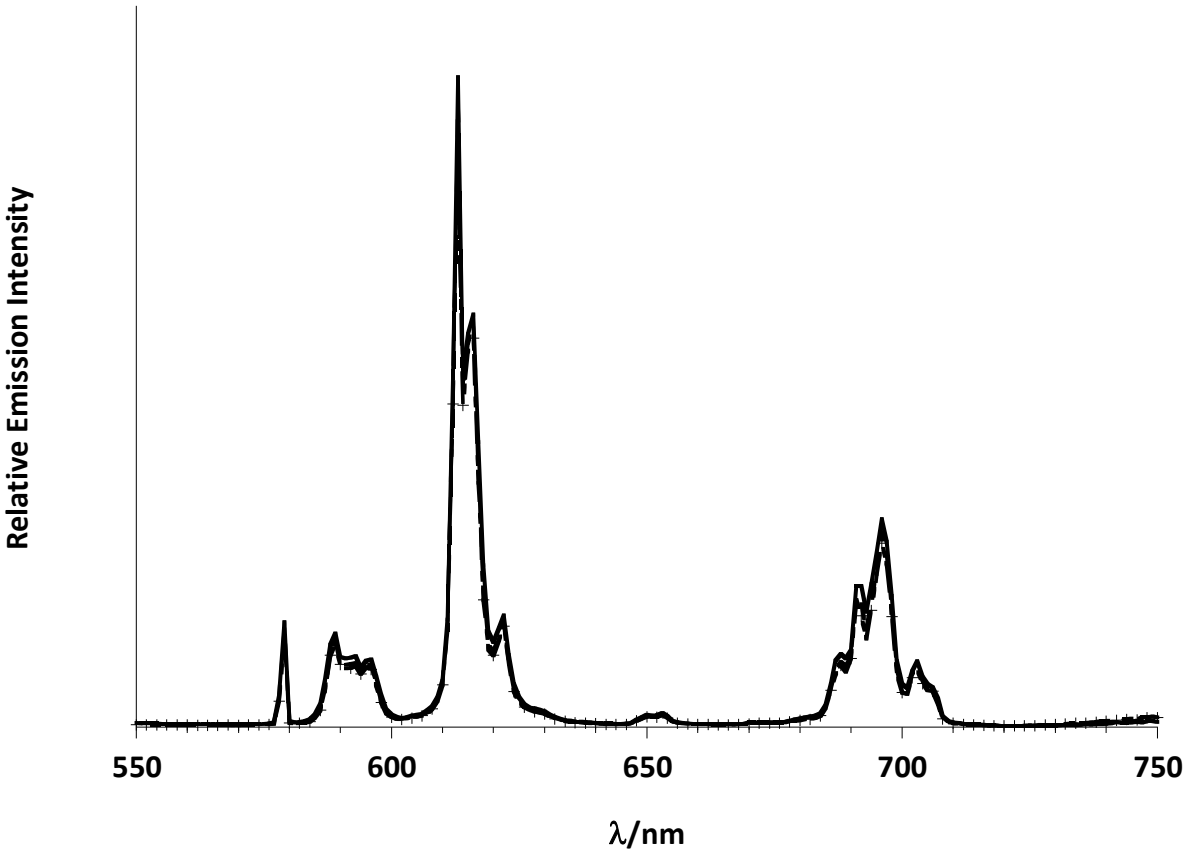

Figure 4.25 - Emission Spectrum of EuL (—), EuL + 1 molar equivalant of quinaldic acid (---), EuL + 4 molar equivalant of quinaldic acid (-+-), in THF/Water (1:1). λ_{ex}= 320 nm.

Quinaldic acid is a prime candidate to test **EuL** for its binding potential for small analytes, as the molecule it's self contains a carboxylate funtional group capable of binding to lanthanide. Also the absorbtion bands of the quinaldic acid and the **EuL**'s quinoline sensitisers overlap by UV-Vis spectroscopy, thus when exciting the **EuL**, the quinaldic acid would also be excited, and

if bound to **EuL** should undergo a similar energy transfer process that the incorporated quinolines undergo, sensitising europium further and enchancing the lanthanides emission. The triplet energy state of quinladic acid is very similar triplet energy level to that of the quinoline in EuL and cannot be excited independantly of one another as the absorption bands strongly overlap.

The europium emission coming from the EuL is shown in *figure 4.25*, upon addition of quinaldic acid we excepted to observe the relative emission intensity to increase. However this was not the case. Upon addition of the quinaldic acid there was no change in the relative emission intensity. We checked the pH of the solution was pH 7, this should indicate a deprotonated state of quinaldic acid, thus having a negative charge on the quinolate, and thus have binding potential to the lanthanide's positively charged centre. After serval repeats the outcome remained the same. We investigated the system further by addition of bases, buffer, isolating a potassium derivative and changing the analyte. Naturally the quinaldic acid was checked for purity, by ^{1}H-NMR and Mass spectrometry.

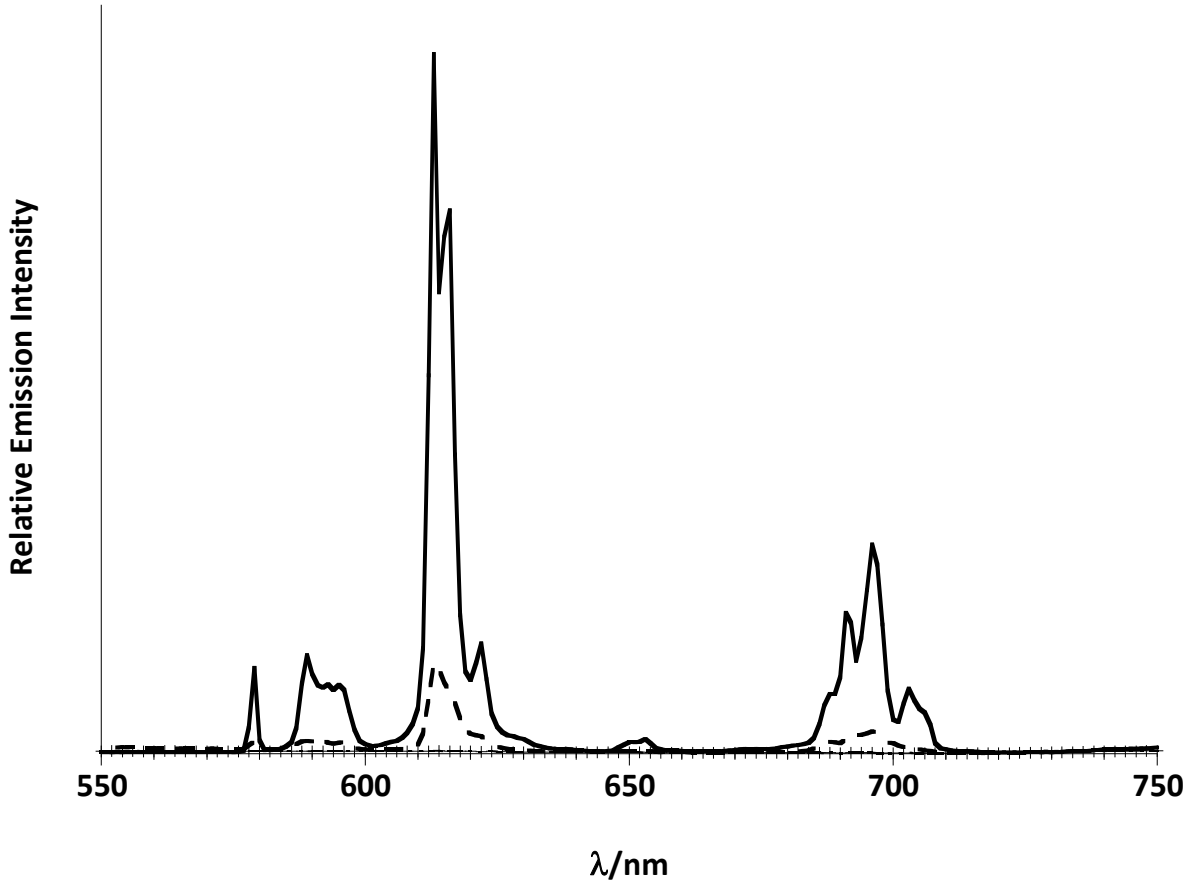

Figure 4.26 - Emission Spectrum of EuL (—), EuL + 1 molar equivalant of quinaldic acid and TBAH (---), EuL + 4 molar equivalant of quinaldic acid and TBAH (-+-), in THF/Water (38μM, 1:1). λ_{ex}= 320 nm.

To try and understand why quinaldic acid didn't sensitise **EuL**, we added an organic base, tetrabutyl ammonium hydroxide (TBAH) to the system. We chose TBAH as we didn't want any metal ions to effect the system, and with hydroxide ions present, this should ensure that quinaldate was definitely deprotonated. *Figure 4.25* depicts the **EuL** emission, and when the addition of a deprotanated solution of quinaldic acid is added, the relative emission intensity is dramatically reduced in nature, thus having a negative impact on the system. This was

assigned to hydroxide groups binding directly to the lanthanide ion and quenching its luminescence. To validate this hypothesis, NaOH was used, and triethylamine was also used.

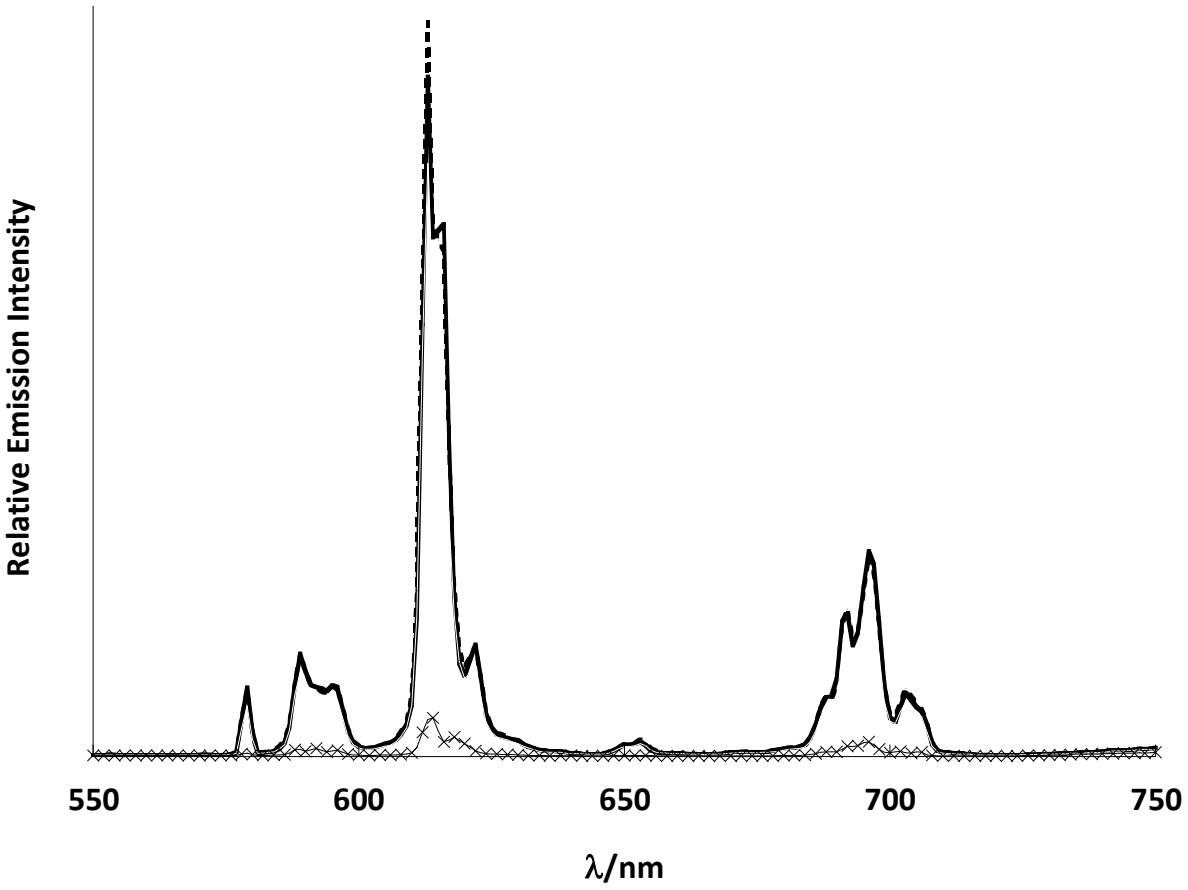

Figure 4.27 - Emission Spectrum of EuL (—), EuL + 1 molar equivalant of quinaldic acid and NaOH (---), EuL + 4 molar equivalant of quinaldic acid and NaOH (-x-), in THF/Water (38μM, 1:1). λ_{ex}= 320 nm.

The effect of using NaOH as a base in the **EuL** analyte binding system is shown by *figure 4.27*. The **EuL** emission is shown as expected, however with the addition of one molar equivalent of deprotonated quinaldic acid via sodium hydroxide, the emission remained unaffected, although further addition of quinaldate and sodium hydroxide proved as detrimental as the addition of TBAH. Proving that hydroxide ions quench the emission and could potentially be

blocking any analyte binding interaction. The addition of more quinaldic acid presents an issue of absorbing excitation energy, thus reducing excitation energy reaching the **EuL** complex, reducing the overall relative emission intensity.

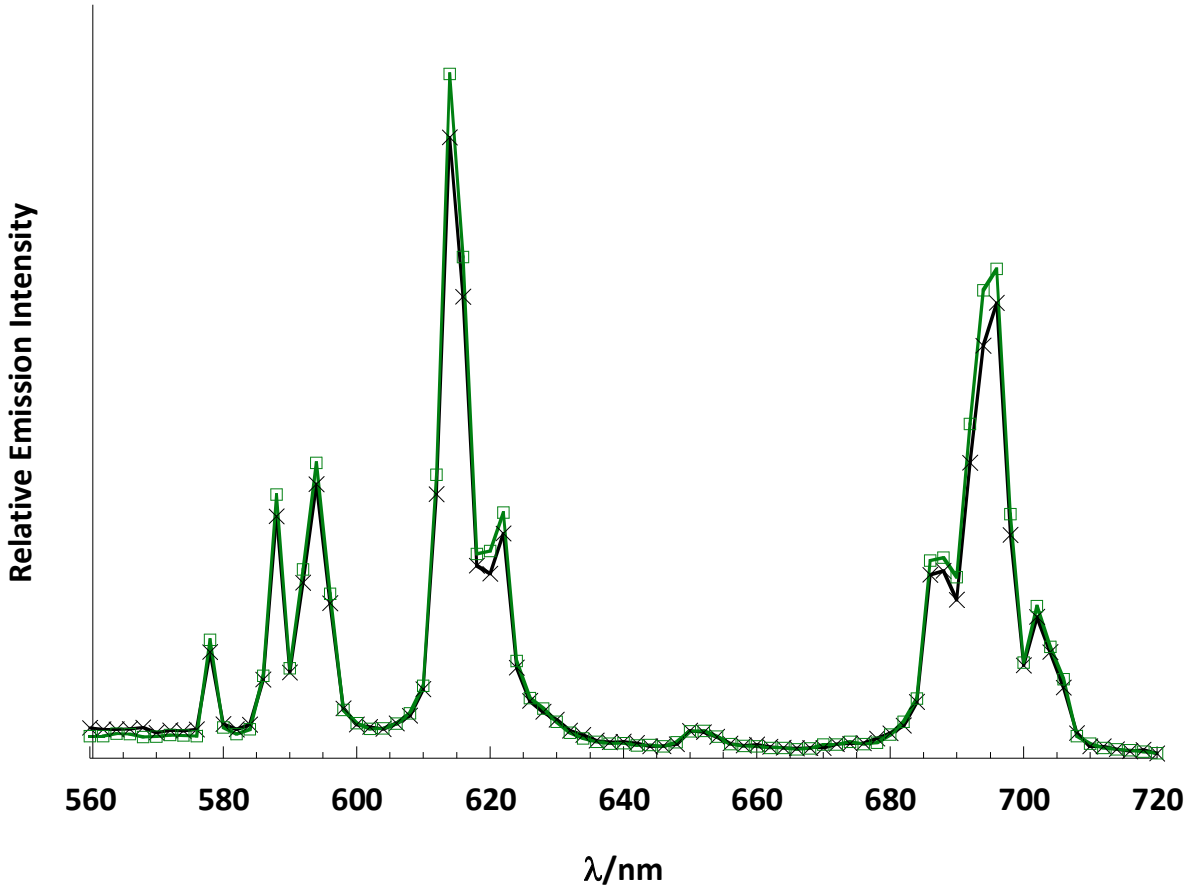

Figure 4.28 - Emission Spectrum of EuL (-x-) and 0.6 % PBS (v/v), EuL + 1 molar equivalant of potassium quinaldate and 0.6 % PBS (v/v (-□-), in THF/Water (38μM, 1:1). λ_{ex}= 320 nm.

One attempt to enable the use of a deprotonated quinaldate (*figure 4.28*), and avoid using hydroxide ions, was to isolate a potassium quinaldate salt. The isolation was performed by dissolving the quinaldic acid in 2M potassium hydroxide solution, and precipitation via ethyl acetate. The potassium adduct was found as a parent ion in Mass spectrometry and ^{1}H-NMR.

Figure 4.29 represents the effect of potassium quinaldate on **EuL**. The europium's emission can distinctively be seen. Upon addiction of the quinaldate salt the relative emission intensity stayed the same. The quinaldate salt again showed neglibale effect on the **EuL** system, indicative of a non-binding interaction.

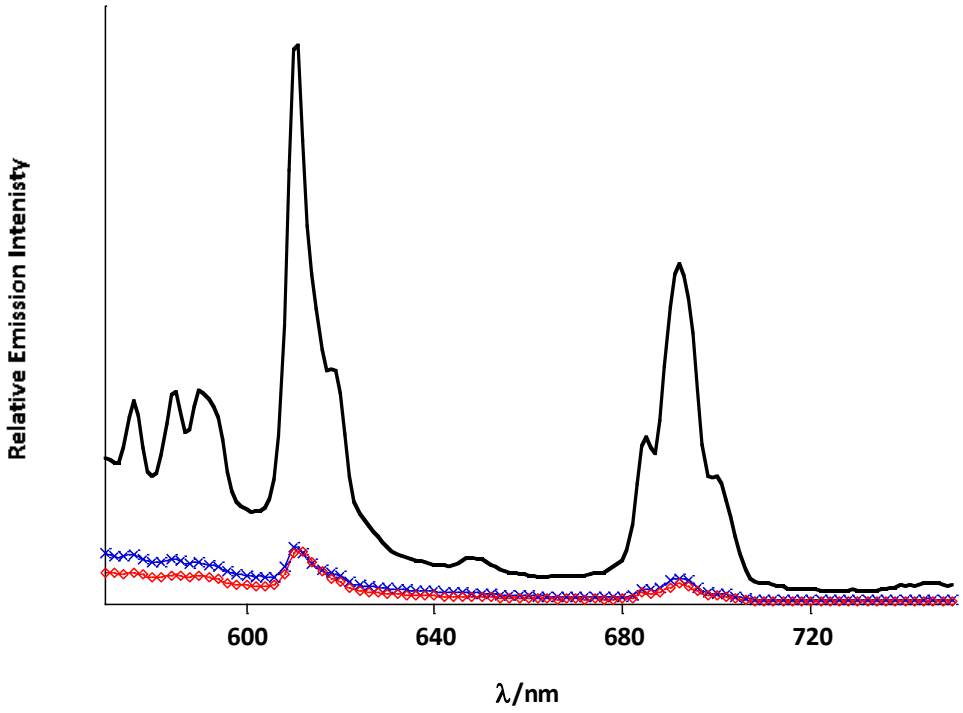

Figure 4.29 - Emission Spectrum of EuL (—) λ_{ex}= 320 nm, EuL (-X-) λ_{ex}= 380 nm, EuL+ 1 molar equivalant of DBM and 3 molar equivalents of Et_3N (-◊-), λ_{ex}= 370 nm in THF/Water (38μM, 1:1).

After attempting to bind quinaldate, a different analyte was tried, one with a stronger binding potential than quinaldate, DBM. DBM has two ketone functional groups, which causes the central hydrogens to become very acidic, and once deprotonated, the negative charge can be delocalised, thus stabilised. DBM has the potential to be bidentate in nature. Thus DBM is a stronger binding analyte than quinaldate. DBM also has different absorption band than **EuL**

unlike quinaldic acid, thus allowing independent excitation of binding analyte. *Figure 4.29* shows the emission spectra of **EuL**, and its addition of DBM deprotonated with the addition of three molar equivalents of triethyl amine. The **EuL** emission spectrum is as expected. As DBM has a broader absorption band than **EuL**, thus it is possible to just excite the DBM analyte, without exciting the quinoline to see if the DBM has any effect on the europium emission. Thus exciting **EuL** at 370 nm would remove any quinoline excitation. The small europium bands still present in the spectra are due to direct excitation of the europium ion. Upon addition of the deprotonated DBM ion, and excitation at 370 nm we would expect to see enhancement of the europium emission, but as evident by *figure 4.29*, there is no sensitisation from the DBM. The after additional condition changes to the try and find binding conditions, it was also evident that DBM did not bind to **EuL**. Thus analysing the system we theorised that the **EuL** binding cavity is too small to support additional binding analytes such as DBM and quinaldate. Smaller analytes, such as dipicolinate and picolinate were also tried concluding that **EuL** could not support any additional binding of chromophoric analytes.

4.3.7 - NdL-Analyte Sensing

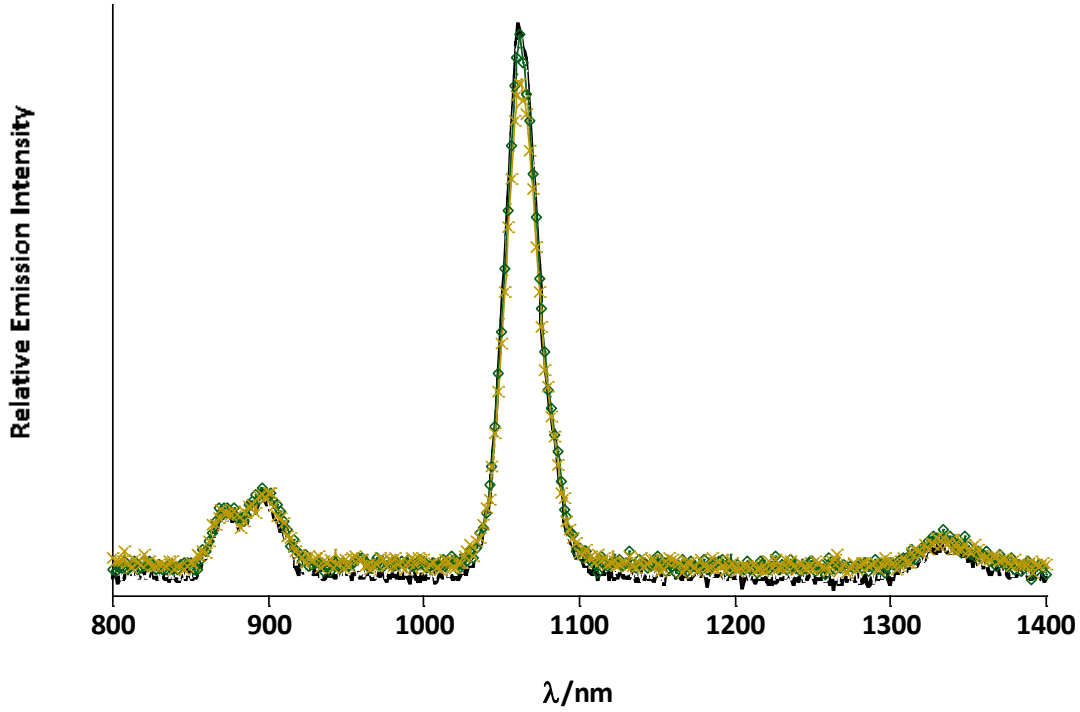

Figure 4.30 - Emission Spectrum of NdL (—), NdL + 1 molar equivalant of potassium quinaldate and 4 molar equivalents of TBAH (-◊-), EuL+ 5 molar equivalant of potassium quinaldate and 20 molar equivalents of TBAH (-X-), λ_{ex}= 320 nm in methanolic solution.

NdL was also chelated with potassium quinaldate in order to compare the observations that have been made with **EuL**. With **NdL** we would still theoretically expect enhanced sensitisation of the Neodymium emission, as the **NdL** system is identical in ligand design. Thus we still expect dual sensitisation from both quinolines built into the ligand, and the additional sensitisations arriving form any coordinated quinaldate molecules bound directly to the neodymium. Alas there was no additional sensitisation observed from the addition of potassium quinaldate to a solution of **NdL**, where the relative emission intensity remained the same when one molar equivalent of potassium quinaldate to **NdL** was added to the solution. Upon addition of 4 molar equivalents, the relative emission intensity showed a small decrease, attributed to the unbound potassium quinaldate absorbing excitation energy from the source.

This indicates that there is no sensitisation, and thus no binding associated with either system, leading to the conclusion that the lanthanide coupound's **NdL** and **EuL** are too sterically hindered to observe and ternary complex formation with small analytes.

4.3.8 - Surface Attachment of EuL to Gold

EuL was attached to the surface of gold to form Self-Assembled Monolayers (SAMs). The SAM was developed though submerging a clean gold surface into a 0.1 mM methanolic solution of **EuL**. It has been suggested that the removal of acetyl group from prior to SAM formation provides greater SAM coverage by Tour et al[4]. The removal of acetyl protecting group was done through the addition of ammonium hydroxide. The removal of acetyl group was checked via ^{1}H-NMR and ES MS of **Compound 5**. The effect of surface coverage is later shown by SPR in Chapter 5.

4.3.9 - Photophysics of Lanthanide complex on gold surfaces

Despite the lack of analyte recognition in solution, **EuL** was tested on the surface of gold for its luminescent properties. As discussed in the ligand design, the binding functional groups is through the thioacetyl groups, which become thiols once bound to the surface of the gold. It has been noted that systems using ammonium hydroxide in situ before SAM formation to deprotect the thiol groups were compared against systems in which no ammonium hydroxide was used. The comparison showed now difference in luminescent intensity.

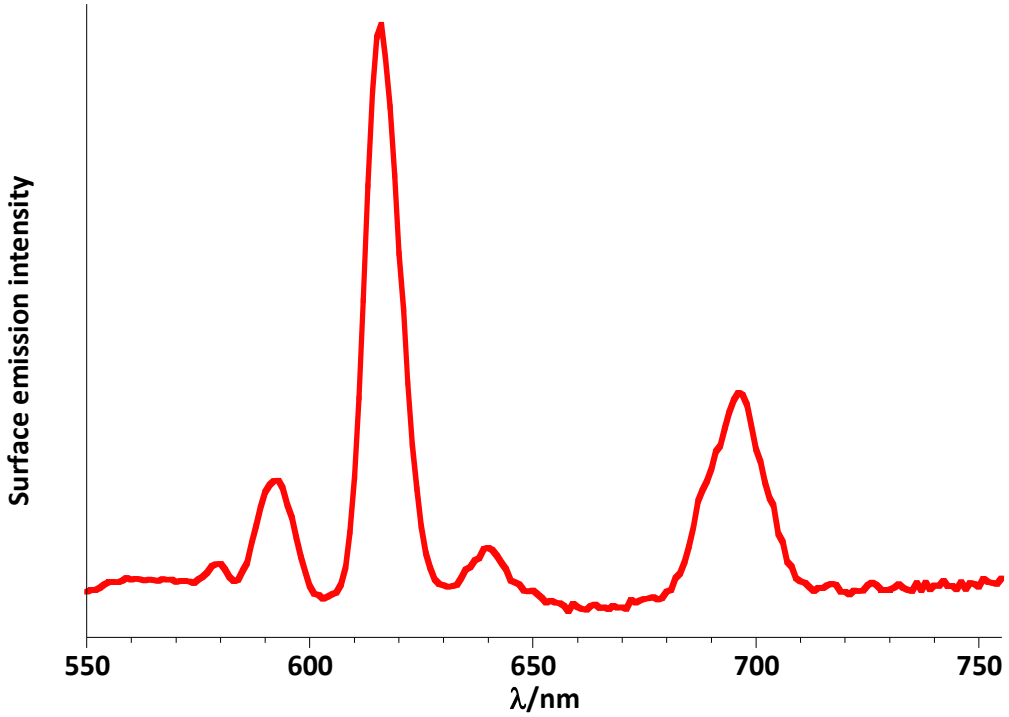

Figure 4.31- Emission Spectrum of EuL (—) λ_{ex}= 320 nm on the surface gold.

The emission spectrum for **EuL** attached the gold surface (*figure 4.31*) still showed characteristic red emission bands after excitation at 320 nm with $^5D_0 \rightarrow {}^7F_J$ (J= 0-4,) *f-f* transitions observed at 579, 594, 615, 642, and 696, with the most intense emission band at λ_{em} = 615 nm. The emission spectrum showed that energy transfer to the europium had occurred on the gold surface and that whilst attached to the gold surface there was significant lanthanide signal to be collected. The emission also indicates that the 6 carbon spaced legs on the systems shows that the lanthanide signal isn't quenched as it is supported at a significant distance away from the surface to prevent significant quenching to happen. The low concentration at the surface, has resulted in a loss of resolution in the emission spectrum,

when compared to the solution which is at a much higher concentration. The SAM was also submerged in a solution of deprotonated DBM and DPA, which resulting in no coordination.

4.3.9.1 - Surface lifetime of EuL

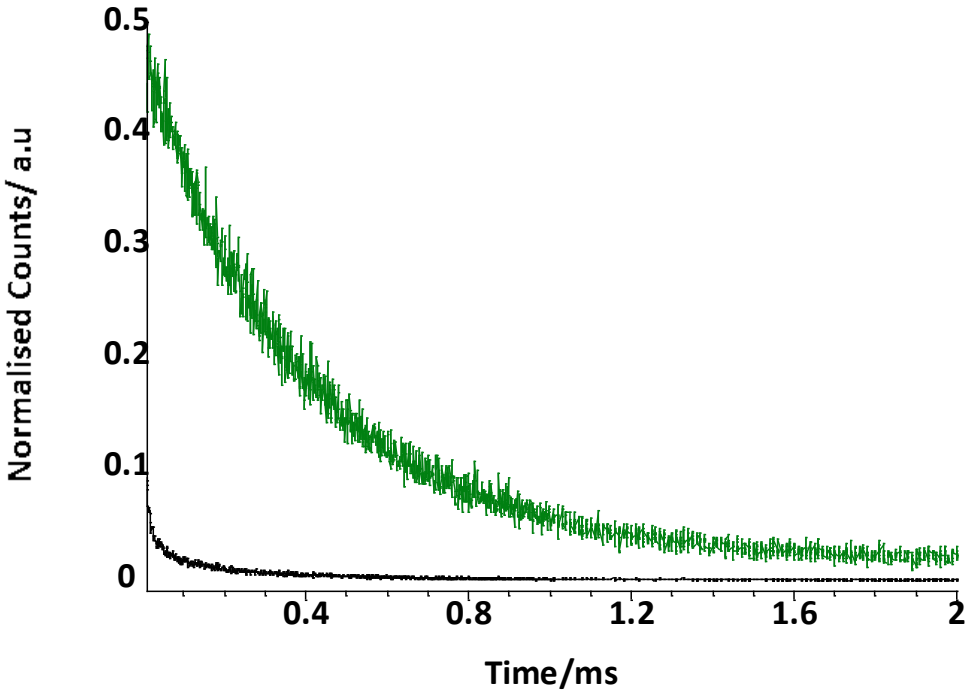

Figure 4.32 - Luminecent lifetime decay of EuL in methanolic solution (48 μM, top) and EuL bound to a gold surface.

The solution lifetime of **EuL** has been reduced when placed on the surface from 470 μs to 120 μs (*figure 4.31*). This indicates that the having a six carbon spacer is not long enough to omit any energy transfer process occurring between the complex and the gold surface.

4.4 - Surface Analysis of EuL

4.4.1 - XPS

X-ray photoelectron spectroscopy is a surface technique used to characterise SAMs. The information obtained from XPS gives information about the surface composition and binding interactions present on the surface. The observed binding energies in the XPS spectrum depend on a two factors; firstly is the electron density of a specific atom, and secondly the adjacent or surrounding environment of the atom, taking into consideration the electronegativity of said atoms.[195] With XPS, qualitative analyses of SAMs are routinely possible, but quantitative analyses proves to be difficult because of experimental uncertainties such as inhomogeneous SAMs, the matter-dependent attenuation length of photoelectrons is typically not known with certainty.[196]

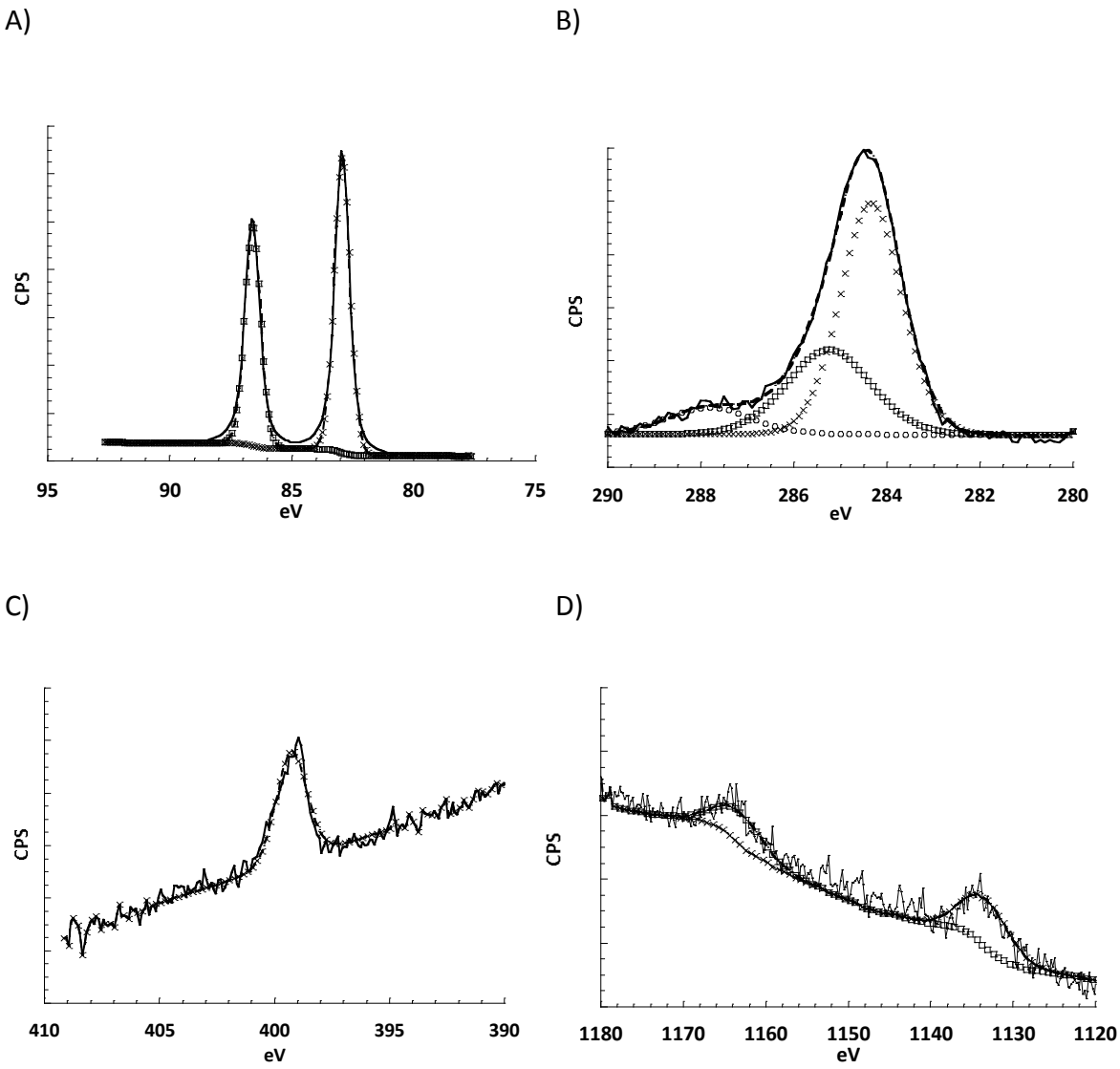

Figure 4.33 - XPS spectrum of A) Au-reference region (—)-Raw data, (---) fitted envelope, (□) – fitting for $4f_{5/2}$,(X) fitting for $4f_{7/2}$ B) C 1s region, (—)-Raw data, (---) fitted envelope, (□) – fitting for C 1s- C-C, (X)-fitting for C 1s-CNO environment (O)-fitting for C 1s – COO environment C) N 1s region, (—)-Raw data, (---) fitted envelope, (-x-)- baseline – fitting for and D) Eu 3d region (—)-Raw data, (---) fitted envelope, (□) – $Eu3d_{5/2}$ (X) – fitting for $Eu3d_{3/2}$.

The XPS spectrum of **EuL** on gold (*figure 4.33*) exhibits the characteristic C 1s and N 1s peaks at 284 and 400 eV which was referenced to referenced to Au $4f_{7/2}$ at 83.9 eV full widths at half-

maximum (fwhm) of 4.1 eV. Finally the C: N: S: Eu peak area ratios (after peak-fitting and adjustment with the atomic sensitivity factors) were 81:8:6:1 with the theoretical ratio being 81:13:4:2 gave poor agreement but evidence that all elements found in the complex were found on the surface.

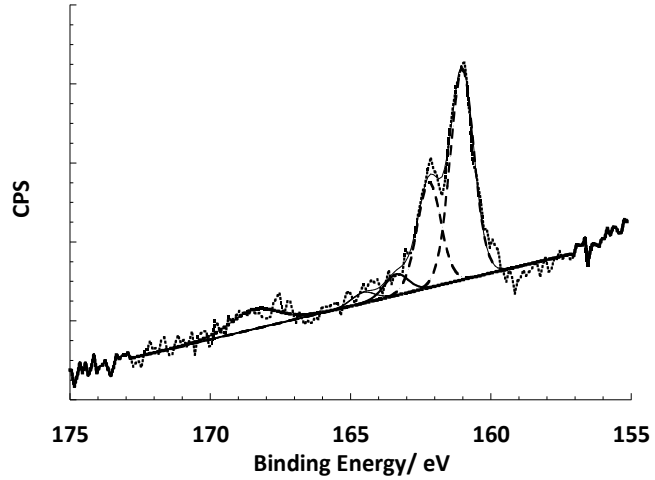

Figure 4.34 - XPS spectrum of S 2p region of EuL monolayer of gold

XPS can also provide information about the oxidation states of surface bound material, this is useful in understanding if the sulphur bonds in our system are chemical bound to the gold surface or physically absorbed to the surface. To do this we need to take a closer look at the S 2p region (*figure 4.34*). We assigned the photoelectron peaks with binding energies of around 161 and 162 eV to the doublet S $2p_{3/2}$ -S $2p_{1/2}$, respectively, for sulphur bound to gold. The unbound sulphur can be confirmed by the observation of a corresponding signal at around 163-164 eV of the S $2p_{3/2}$ – S $2p_{1/2}$.[197-199] The oxidation of sulphurs can also be seen in the XPS spectrum by a broad peak at around 168 eV.

It has previously been found that acetyl protected thiols provide an excellent method to avoid problems of isolating and using the oxidatively unstable thiols, stopping disulphide bond formation.[199] Acetyl protected thiols can be deacylated completely within 10 min using aqueous NH_4OH.[4] Experiments have also been carried out showing that SAM formation is possible without deprotection by base (in this case thioacetate will be eliminated in the process of monolayer formation, to form the gold thiolate). However higher concentrations of thioacetyl-containing adsorbates, relative to thiols, do required base deprotection to achieve monolayer coverage.[199] It was also reported that, in the cases of direct adsorption or base-promoted adsorptions of the thioacetyl-terminated systems, the XPS results confirmed that the SAMs were similar in their composition to the SAMs generated from the free thiols, [199] which suggests that acetyl protecting group is removed and has no further interactions with the gold surface. This is in agreement with the observations we have made.

EuL monolayers were formed by using the thioacetates with deprotection of the base, with NH_4OH. Looking at the S 2p region of the monolayers, indicates that 80% of the sulphur atoms are bound to the surface of gold. It is suggested that the thioacetate has been removed when considering the elemental composition of S:C:O ratio better match the theoretical absence of the acetyl protecting group. During the formation of the monolayers, when base (NH_4OH) was used to deprotect the thioacetate group, peaks for unbound sulphurs can be still be seen, which shows that using base does not provide a completely bound SAM. However it should also be noted that using base will cause the sulphur to oxidise which can be evaluated by relatively large peaks at around 168 eV.

4.4.2 - Surface UV-Vis Spectroscopy- Using Gold on Silica and Borofloat 33 substrates

Surface UV-Vis spectroscopy was used to characterise EuL's quinoline band on the surface gold. Upon first attempts, the transparency of the gold chips was an issue. The chips that were used were 100 nm of electron vapour deposited gold. The UV-Vis spectra showed only the absorbance of as a result of scattering and of the silica layer. Thus we used 30 nm gold chips deposited on a material named borofloat 33, a type of glass that has a lower absorption edge that that of glass, at 280 nm, thus having the potential to indicate the absorption band of quinolines on the surface of gold. Even with the adjustments to the surface gold, no absorption spectrum was obtained that was representative of the quinoline presence on the surface.

Here we have shown that XPS shows sulphur gold bond formation and in Chapter 5 we show that EuL is bound to surface through ellipsometry and SPR. SAM formation is done over time by exposing the clean surface to SAM solution. After which strong sulphur-gold bonds are formed, 188 kJ mol^{-1},[129] followed by cleaning the surface by washing the surface with copious amounts of **EuL** soluble solvent, followed by drying under a nitrogen stream. The washing process removes any unbound material. The bound material is left bound to the surface as evidence by an increase in surface thickness from ellipsometry and by a maintained refractive angle change from SPR after washing the surface.

4.5 - Experimental Overview

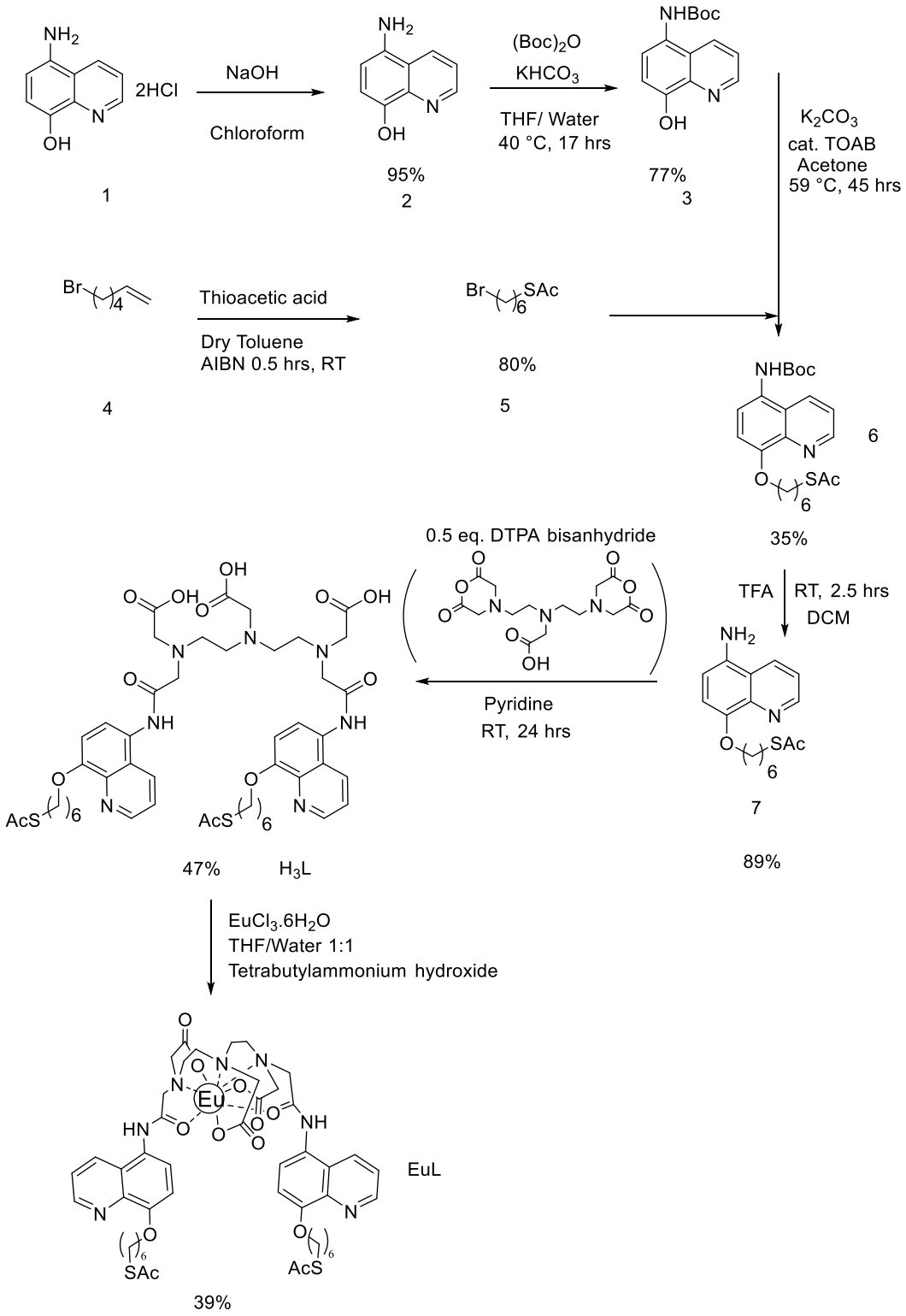

Schematic 3- Synthesis route of EuL

The synthesis of **EuL** is outlined in Schematic 3. **Compound 1** was neutralised in aqueous solution with NaOH to give the free amine and then isolated by extraction with chloroform to give **Compound 2**. The amine group was then protected with di-tertiary butyl bicarbonate, a boc protecting agent under basic conditions[200] leading to the boc protected **Compound 3**. This was necessary to facilitate nucleophilic attack from the hydroxyl group and not the amine of **Compound 3** to the sp^3 hybridised alpha C in **Compound 5**. **Compound 5** had to be first synthesised from **Compound 4**,[201] before Williamson ether synthesis could take place to afford **Compound 6**.[42] **Compound 7** was formed under strong acidic conditions causing removal of the boc protecting group.[41] Reforming the amide was necessary in order to attack the anhydride carbonyl of DTPA bis-anhydride, ensuring binding at the termini of the DTPA bis-anhydride molecule, and not the middle carboxylic acid group of DTPA bis-anhydride, leading to the formation of ligand **H_3L**, via a simple condensation reaction.[55] The ligand **H_3L** was then complexed to Eu^{3+} to form the final product **EuL** using known synthetic routes.[43]

The synthetic route was attempted several times. Alternative conditions for the protection of amine have been tried[202,203] without much success. A successful route has been achieved and reported in the experimental section.

4.5.1 - Synthesis of EuL

4.5.2 - Synthesis of Compound 2

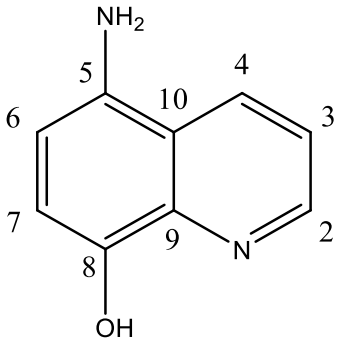

Figure 4.35 - Chemical structure of Compound 2

A solution of 5-amino-8-hydroxyquinoline dihydrochloride (2.00 g, 12.5 mmol, 100 mL) was adjusted to pH 8 using NaOH (20 mL, 1 M). The aqueous layer was then extracted using chloroform (400 mL x1, 200 mL x 1), the organic extracts were combined and dried using sodium sulphate (10 g) and reduced *in vacuo* at 40°C, to leave dark brown solids, yield 95%, (1.51 g, 9.44 mmol). ^{1}H-NMR (300 MHz, $CDCl_3$) δ_H ppm: 3.5-4.0 (2H, br, N*H*$_2$), 6.7-6.8 (1H, d, *J* = 8.1, H-6), 6.9-7.0 (1H, d *J* = 8.1,H-7), 7.3-7.4 (1H, dd, *J* = 8.6 *J'* = 4.2, H-3), 7.6-8.0 (1H, br, O*H*), 8.1-8.2 (1H, dd, *J* = 8.6, *J* = 1.1, H-4), 8.7-8.8 (1H, dd, *J* = 4.2, *J'* = 1.1, H-2). ^{13}C-NMR (400 MHz, $CDCl_3$) δ_C ppm: 147.7, 145.5, 138.8, 133.7, 130.4, 120.4, 119.1, 111.6, 110.0. M/z (ES+): 183.09 $[M+Na]^+$, 181.06 $[M+Na-2H]^+$,100%.

4.5.3 - Synthesis of Compound 3

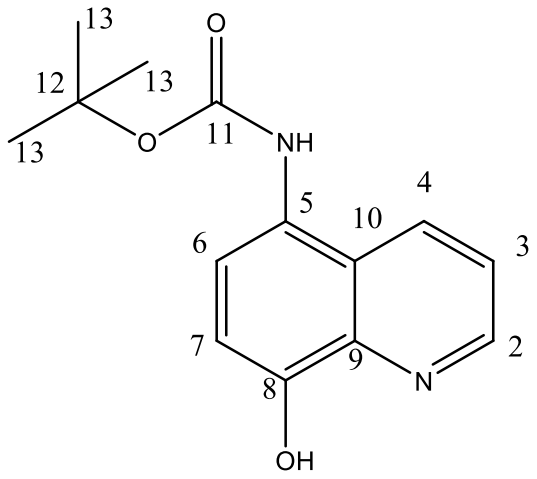

Figure 4.36- Chemical structure of Compound 3

Compound 2 (1.51 g, 9.44 mmol, 1 eq.) was dissolved in THF /water (100 mL 30:70). While stirring the mixture, potassium bicarbonate (3.77 g, 3.7 mmol, 4 eq.) was added and cooled to 0-5 °C under nitrogen. Di-tertiary butyl bicarbonate (2.16 g, 9.91 mmol, 1.05 eq.) was dissolved in THF (40 mL). The di-tertiary butyl bicarbonate solution was added to the reaction vessel dropwise over 45 minutes using a pressure equalised dropping funnel. After the solution and then left to stir for a further 30 minutes while maintaining 0-5 °C, after which the reaction was heated to 35-40°C and stirred for 18-hrs. The THF was then reduced *in vacuo*, followed by addition of water (50 mL). The aqueous layer was then transferred to a separating funnel, and the organic material was extracted with the addition of chloroform (1 x 300 mL, 3 x 100 mL), and allowed to settle for 20 mins. The organic layers was separated, and the organic extracts were combined and dried over 20 mins using sodium sulphate (10 g). The solvent was then reduced *in vacuo* at 40°C, and dried under high vacuum leaving a brick red powder, yield 77% (1.88 g, 7.23 mmol). R_f (alumina F_{254} running 60:40 ethyl acetate/hexane) 0.3. ^{1}H-NMR (300

MHz, $CDCl_3$) δ_H ppm: 1.4.-1.6 (9H, s, *^{t}butyl*), 6.3-6.5 (1H, br, N*H*), 7.0-7.1 (1H, d, *J* = 8.1, H-7), 7.3-7.4 (1H, dd, *J* = 8.4, *J'* = 4.2, H-3), 7.4-7.5 (1H, d, *J* = 11.0, H-6), 7.7-8.1 (1H, br, O*H*), 8.1-8.2 (1H, dd, *J* = 8.4, *J'* = 1.5, H-4), 8.5-8.7 (1H, dd, *J* = 4.2, *J'* = 1.5, H-2). ^{13}C-NMR (400 MHz, $CDCl_3$) δ_C ppm: 28.3, 109.3, 121.7, 123.9, 124.1, 131.4, 138.2, 147.8, 150.5, 156.0. M/z (ES+), 283 ($[M+Na]^+$), 261 ($[M+H]^+$), 205.0 ($[M-^t butyl+H]^+$, 100%); Calculated Elemental Analysis for $C_{14}H_{16}N_2O_3.(H_2O)_{0.2}$: C 63.7%, H 6.3%, N 10.6% Found: C 63.8 %, H 6.0%, N 10.3%.

4.5.4 - Synthesis of Compound 5

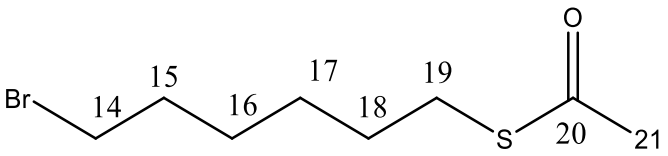

Figure 4.37 - Chemical strucutre of Compound 5

Thioacetic acid (1.86 g, 24.6 mmol, 2 eq.) with catalytic amounts of AIBN (0.025 g) was added to a solution of **Compound 4** (2.00 g, 12. 3 mmol, 1eq.) in dry toluene (15 mL). The solution was heated to reflux (125-130°C) under N_2 for 30 minutes. The reaction was then allowed to cool to room temperature where the reaction was quenched by the addition sodium bicarbonate (60 mL, 1 M). The organic layer was then extracted with ethyl acetate (120 mL) and washed with more sodium bicarbonate (60 mL, 1 M). After extraction the organic layer was dried over sodium sulphate, filtered and the solvent removed *in vacuo* at 40°C, and dried under high vacuum, leaving a yellow oil, yield 89.8% (2.64 g, 11.04 mmol). ^{1}H-NMR (300 MHz, $CDCl_3$) δ_H ppm: 1.2-1.5 (4H, m, H-17, H-16), 1.5-1.6 (2H, m, *J* = 7.2, *J'* = 6.8 H-18), 1.7-1.8 (2H, p, *J* = 7.2, *J'* = 6.8, H-15), 2.2-2.3 (3H, s, H-21) 2.7-2.9 (2H, t, *J'* = 7.2, H-19), 3.3-3.4 (2H, t, J 6.8, H-14); ^{13}C-NMR (400 MHz, $CDCl_3$) δ_C ppm: 27.6, 27.8, 28.9, 29.3, 30.6, 32.5, 33.7, 195.8. M/z (TOF MS EI^+): 240 $[M+H]^+$.

4.5.5 - Synthesis of Compound 6

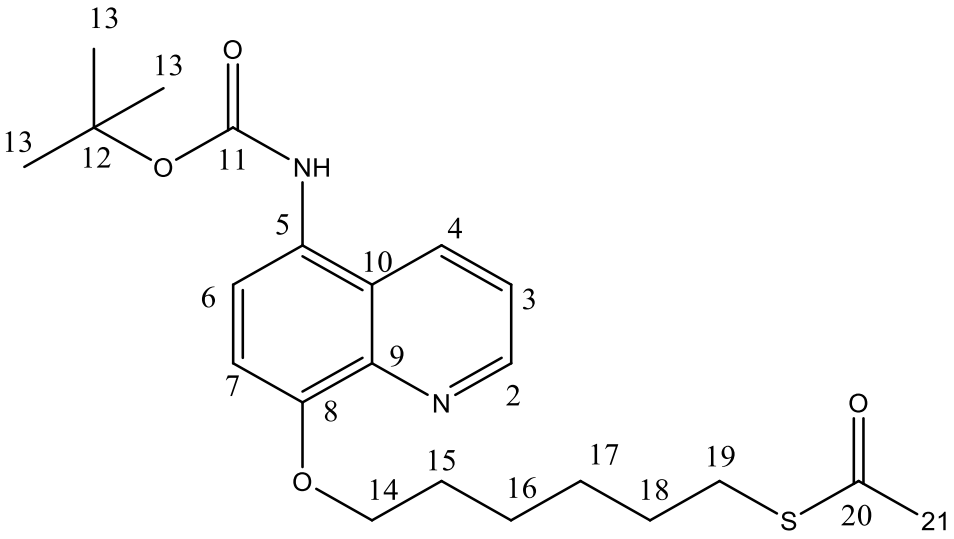

Figure 4.38 - Chemical structure of Compound 6

Compound 3 (1.88 g, 7.23 mmol, 1 eq.) was dissolved in acetone (30 mL) in the presence of potassium bicarbonate (8.00 g, 57.8 mmol, 8 eq.) and a catalytic amount of tetraoctyl ammonium bromide. The reaction was heated to 55-59 °C under nitrogen and held at this temperature for 30 minutes. Aside a solution of compound **5** (2.07 g, 8.68 mmol, 1.2 eq.) in acetone (5 mL) was prepared, and then added dropwise to reaction vessel using a pressure equalised dropping funnel over an hour, while maintaining the specific temperature range under nitrogen. Upon completion the reaction mixture was stirred under reflux at 59°C for 28 hrs. At which a TLC was taken indicating the presence of **Compound 3** R_f (silica F_{254} running 60:40 ethyl acetate/hexane): 0.2 and a product spot at 0.43. Additional compound **5** (0.35 g, 1.45 mmol, 0.2 eq.) in acetone (5 mL) was added. The reaction was left to stir for a further 17 hours. The reaction was then cooled to room temperature and filtered to remove salts. The filtrate was reduced in vacuo and the brown residue was cast between DCM (70 mL) and water

(40 mL) and stirred vigorously for 20 minutes and transferred into a separating funnel where the mixture was allowed to settle. The organic layer was separated and washed with brine (50 mL) and the organic layer was dried of sodium sulphate (11 g) and filtered. The filter cake was washed with DCM (2 x 5 mL). The filtrate was then reduced in vacuum at 40°C, leaving a black tar (3.22 g) which was purified on silica (150 g) eluting 30:70 ethyl acetate/hexane to give final product as a yellow oil, yield 31% (0.93 g, 2.22 mmol). R_f (silica F_{254} running 60:40 ethyl acetate/hexane) [glows yellow under short wavelength]: 0.46. ^{1}H-NMR (300 MHz, $CDCl_3$) δ_H ppm: 1.4-1.7 (16H, m, H-16, H-17, H-18, *t-butyl*), 1.9-2.0 (2H, m, *J* = 7.2, *J'* = 6.8, H-15), 2.3-2.4 (3H, s, H-21), 2.7-2.9 (2H, t, J 7.2, H-19) 4.2-4.3 (2H, t, J 6.8, H-15), 6.3-6.5 (1H, br, N*H*), 7.0-7.1 (1H, d, J 8.6, H-7), 7.4-7.5 (1H, dd, *J* = 8.6, *J'* = 4.0, H-3) 7.5-7.6 (1H, d, J 6.6, H-6), 8.2-8.3 (1H, dd, *J* = 8.6, *J'* = 1.7 H-4) 8.9-9.0 (1H, dd, *J* = 4.0, *J'* = 1.7 H-2). ^{13}C-NMR (400 MHz, $CDCl_3$) δ_C ppm: 25.6, 28.3, 28.5, 28.8, 29.0, 29.4, 30.6, 68.9, 80.6, 108.2, 121.4, 121.4, 122.6, 12.1, 130.6, 140.3, 149.1, 152.9, 154.4, 196.0. M/z (ES+) 441.2 $[M+Na]^+$, 420.2 $[M+H]^+$.

4.5.6 - Synthesis of Compound 7

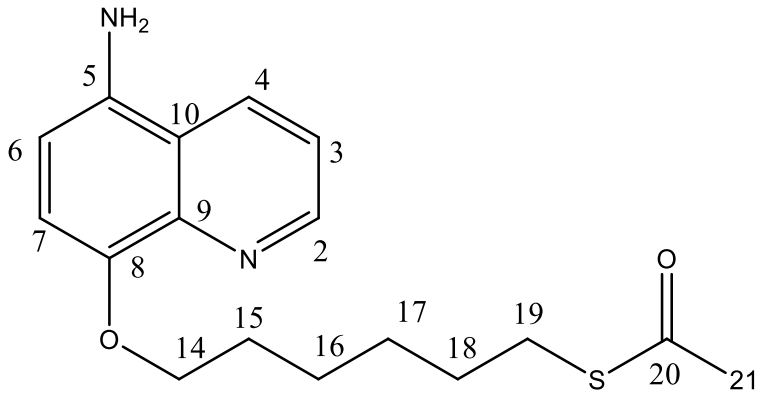

Figure 4.39 - Chemical structure of Compound 7

Compound 6 (0.93 g, 2.22 mmol, 1 eq.), was dissolved in anhydrous DCM (5 mL) under nitrogen. Trifluoroacetic acid (5 mL, 5.7 g, 50.1 mmol, 23 eq.) was added in three instalments via glass pipette to the stirring mixture over 5 minutes. The mixture was then continuously stirred for 2.5 hours under nitrogen at 20-25°C. The DCM was then reduced *in vacuo* and saturated aqueous sodium bicarbonate (30 mL) was added to the residue along with DCM (50 mL). The mixture was stirred vigorously for 10 minutes under nitrogen. The mixture was then allowed to settle and the layers separated. The organic layer was extracted, and the aqueous layer was washed with DCM (2 x 25 mL), and the organic extracts were combined and dried over sodium sulphate (11 g) for 30 minutes. The solution was then filtered and the solvent was removed under reduced pressure at 40°C leaving the product as a yellow oil, yield= 95% (0.67, 2.1 mmol). ^{1}H-NMR (300 MHz, $CDCl_3$) δ_H ppm: 1.4-1.7 (8H, m, H-17, H-18, H-19,), 1.9-2.0 (2H, m, *J* = 7.2, *J'* = 6.8, H-15), 2.3-2.4 (3H, s, H-21), 2.8-3.0 (2H, t, *J* = 7.2, H-19), 3.5-4.3 (2H, br, N*H*) 4.1-4.2 (2H, t, *J* = 6.8, H-15), 6.7-6.8 (1H, d, *J* = 8.3 H-6), 6.9-7.0 (1H, d, J 8.3, H-7), 7.4-7.5 (1H, dd, *J* = 8.6, *J'* = 4.0, H-3), 8.2-8.3 (1H, dd, *J* = 8.6, *J'* = 1.7, H-3) 8.9-9.0 (1H, dd, *J* =

4.0, *J'* = 1.7, H2). ^{13}C-NMR (400 MHz, $CDCl_3$) δ_C ppm: 25.7, 28.6, 29.0, 29.1, 29.4, 30.6, 69.3, 110.1, 110.4, 120.2, 120.6, 129.6, 130.0, 134.9, 149.1, 150.3, 196.0. M/z (ES+): 341.2 $[M+Na]^+$, 419.2 $[M]^+$.

4.5.7 - Synthesis of H_3L

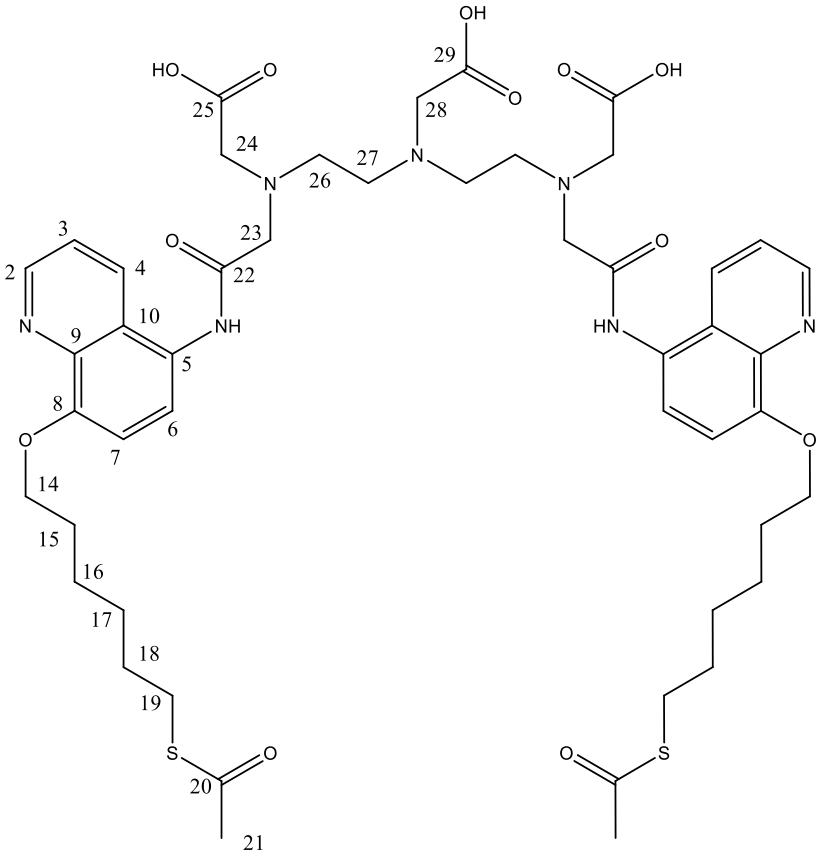

Figure 4.40 - Chemical structure of H_3L

H_3L (0.35 g, 0.99 mmol) was dissolved in a stirring solution of **Compound 7** (0.63 g, 1.98 mmol) in anhydrous pyridine (30 mL). The mixture was stirred at ambient temperature under nitrogen for 24 hours, and then the solvent was removed under vacuum at 40°C, leaving a deep red crystal. Water (30 mL) was added to give a dark red solution. The pH of the solution was adjusted to 3, where a gummy precipitate was formed. The water was decanted from the flask. The gummy precipitate was triturated in acetonitrile (50 mL) for 3 hours, after which a

light orange powder had formed, after which it was filtered and the cake was washed with acetonitrile (2 x 10 mL) and diethyl ether (10 mL) after which a beige powder was formed after drying, yield = 64% (0.45 g, 4.57 mmol). ^{1}H-NMR (300 MHz, d_6-DMSO) δ_H ppm: 1.3-1.7 (12H, m, H-16, H-17, H-18), 1.8-1.9 (4H, m, *J* = 7.3, *J'* = 6.8, H-15), 2.2-2.4 (6H, s, H-21), 2.8-2.9 (4H, t, *J* = 7.3, H-19), 2.9-3.2 (8H, m, H-27, H-26), 3.3-3.7 (10H, m br, H-23, H-28, H-24), 4.0-4.2 (4H, t, *J* = 6.5, H-14), 7.0-7.1 (2H, d, *J* = 8.5, H-7), 7.4-7.5 (2H, dd, *J* = 8.5, *J'* = 4.0, H-3), 7.5-7.6 (2H, d, *J* = 8.5, H-6), 8.3-8.4 (2H, dd, *J* = 8.5, *J'* = 1.5, H-4), 8.7-8.8 (2H, dd, *J* = 4.2, *J'* = 1.3, H-2), 10.0-10.1 (2H, s, N*H*). ^{13}C-NMR (400 MHz, d_6-DMSO) δ_c ppm: 25.1, 27.9, 28.3, 28.6, 29.1, 30.5, 51.6, 52.2, 55.0 , 55.5, 58.2, 68.3, 108.7, 121.3, 122.2, 124.2, 125.5, 131.2, 139.6, 148.7, 152.3, 170.2, 172.9, 195.3. M/z (ES+): 1018.2 $[M+Na+H]^+$ 1017.2 $[M+Na]^+$, 994.2 $[M]^+$. Elemental analysis for $(C_{48}H_{63}N_7O_{12}S_2).(H_2O)_{1.8}$, expected: N=9.6, C=56.2 H=6.5, found: N= 9.4, C =55.9, H= 6.2.

4.5.8 - Synthesis of LnL

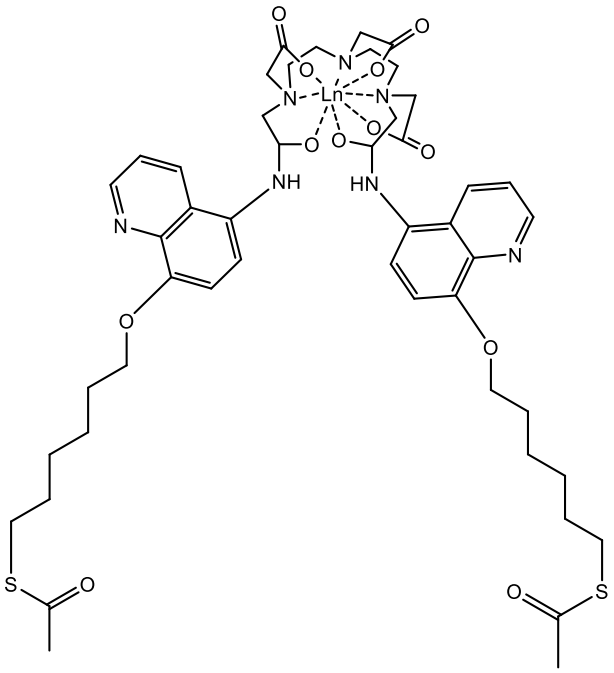

Figure 4.41 - Chemical structure of LnL

H_3L (1.0 eq.) was dissolved in a mixture of 1:1 THF/water (5 mL) and the pH of the solution raised by the dropwise addition of tetrabutylammonum hydroxide. At the same time a solution of $LnCl_3.6H_2O$ (1.0 eq.) was prepared in water (1 mL), which was then added to the ligand solution and more water (1 mL) was used to rinse the vial and added to the reaction vessel. THF was then removed *in vacuo* and the pH was raised to 5 by the addition of tetrabutylammonium hydroxide leading to the precipitation of a solid. The water was decanted off, and the solid was triturated in acetone (35 mL) at 0-5°C for one hour, after which a fawn powder was produced. The powder was isolated by filtration, and the cake washed with acetone (5 mL) and dried under N_2 (10 minutes) then dried under high vacuum to yield the title complexes.

4.5.9 - Synthesis of EuL

Following synthesis of LnL; H_3L (70 mg, 70.4 μmol, 1 eq.), $EuCl_3.6H_2O$ (25.8 mg, 70.4 μmol, 1 eq.). Yield= 39% (31.7 mg, 27.7 μmol). m/z (ES+): 1166.8 ($[M]^+$).

4.5.10 - Synthesis of YL

Following synthesis of **LnL**; **H_3L** (60 mg, 60.4 μmol, 1 eq.), $YCl_3.6H_2O$ (18.3 mg, 60.4 μmol, 1 eq.). Yield= 64% (42 mg, 38.8 μmol). ^{1}H-NMR (300 MHz, d_6-DMSO) δ_H ppm: 1.3-1.7 (m), 1.9-2.1 (m), 2.2-2.4 (m), 2.1-2.4 (m), 2.5-3.0 (m), 3.0-3.7 (m), 3.6-4.0 (m) 4.1-4.3 (br m), 4.5-4.7 (br d) aliphatic region integrates for 52H (theory: 48H), 6.8-7.0 (m), 7.1-7.3 (br s), 7.3-7.4 (d), 7.4-7.7 (m), 8.3-8.4 (br d), 8.5-8.6 (br s), 8.7-8.8 (m). Aromatic region integrates for 10H (theory: 10H).

5 - Surface Binding of Lanthanide Complexes to Gold and Silica Surfaces

5.1 - Introduction

We have previously shown the development of luminescent lanthanide complexes with gold and silica surface functionality to form SAM (Chapters 2-4), and their capacity for sensing applications. SAM characterisation can be done in numerous ways; XPS, infrared spectrometry and emission spectrometry. In this chapter we look at SAM formation over time through the use of Surface Plasmon Resonance (SPR) and characterise the SAM thickness by ellipsometry.

SPR is a relatively new technique in the fields of nanotechnology and biosensing.[204] SPR allows for investigation of surface binding interactions under flow conditions.[36,204] In the field of biology this can be related to the interaction of cells and with its surroundings[205,206] from static environments to switchable environments by Mendes *et al*.[191,207] The Mendes group have shown selective surface binding of NeutrVadin through interaction of surface bound biotin (vitamin H). The Group achieved this by synthesising a biotin receptor molecule, composing of biotin, four lysine molecules, and a thiol terminated cysteine molecule. The theory was based on the biotin's lysine chain, which is expected to collapse on its self when a negative potential was applied across the SAM surface, due to the electrostatics occurring between the positive charges lying on the lysine chain and the surface potential. Previous research in the group had shown that in order for effective collapsing to occur, the biotin SAM would need to be doped with shorted oligothiol chains.

This would allow for a less sterically restraining environment, and more efficient collapsing of the biotin chain. With efficient collapsing on the biotin chain, the biotin's head was no longer exposed limiting any NeutrVadin binding. They showed the effect of applying a change in potential across the surface in situ with SPR comparing neutral, negative and positive potential across the surface. The experiment was carried out by using a pre-formed SAM of a mixed biotin monolayer, and the NeutrVadin was introduced by flowing a solution over the surface. The surface was exposed to three electro potentials; without any surface potential applied across the surface as a control, when there was a positive and negative potential, and the change in resonance angle was monitored in each scenario. The results supported the theory and showed that the SAM surface showed the greatest SPR response when a positive potential was applied and next to negligible surface response under negative potential. This type of approach can be particularly useful in diverse biological and medical applications such as heavy metal detection,[208] drug delivery,[209] and surfaces that includes the release of trapped biological entities such as; DNA,[210] proteins,[211,212] and enzymes.[213]

SPR has been used by Whitesides et al to compare surface active esters[214] and thiols-protein adsorption. Whitesides created mixed SAM from oligothiol and oligo thiol-ester chains, and activated the surface of these mixed monolayers with EDC-NHS peptide coupling techniques (*figure 5.0*).

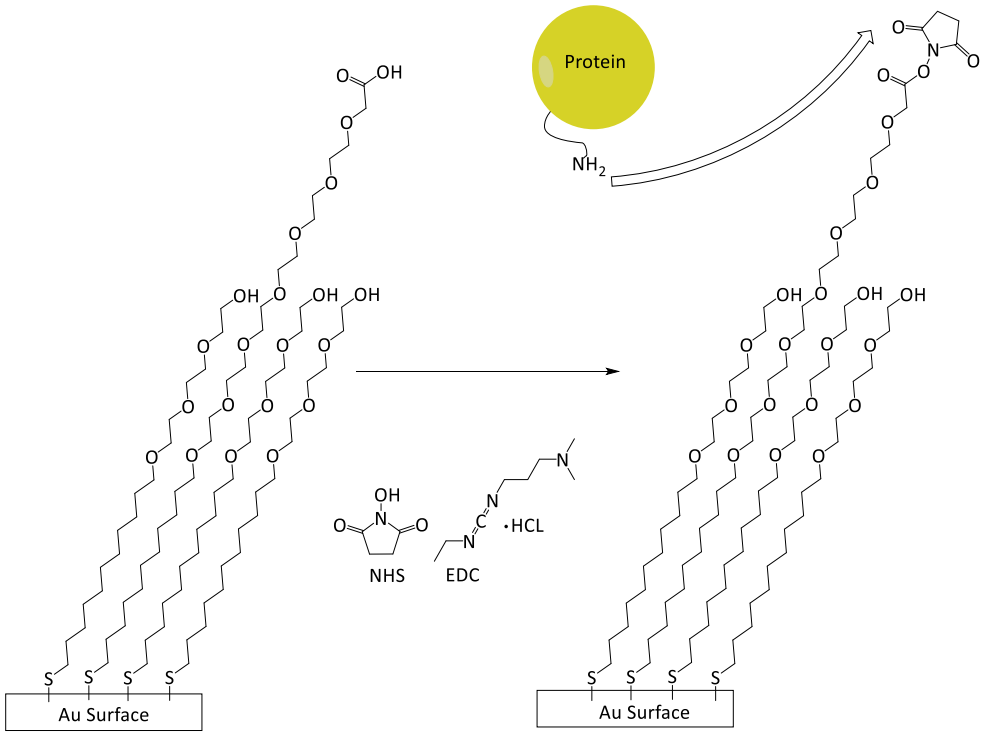

Figure 5.0 - Schematic representation of Whitesides et al SPR study with binding peptides[214]

Whitesides *et al.* showed that in conjunction with previous ellipsometric results[215] the surface binding of four different proteins; RNase A**,** lysozyme, fibrinogen, and pyruvate kinase. The added value of SPR showed that the proteins actually bound irreversible to the surface of the thiol-esters, where it was shown that during ellipsometry it was unsure if any weakly bound protein had been removed during the washing process.[216]

Pikramenou *et al*. also showed the detection of protein through luminescence.[212] Here the group had developed novel luminescent ruthenium and iridium complexes for gold surface attachment (*figure 5.1*) and detection of Bovine Serum Albumin (BSA). They showed detection of BSA through SPR and luminescence spectroscopy.

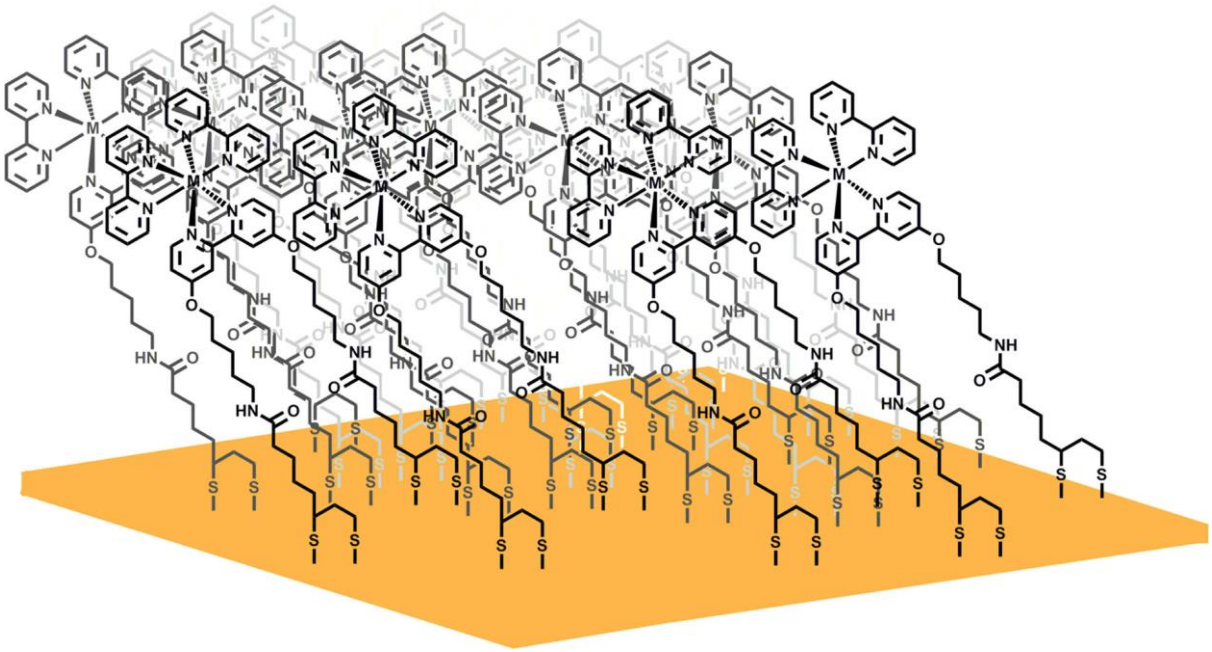

Figure 5.1 - Reproduced from Pikramenou et al paper, showing the SAM of luminescent transition metal complex.[212]

Using SPR Pikramenou *et al*. showed the change in refractive index over time. This was done by using a preformed SAM of the luminescent transition metal complex, and injecting over a solution BSA. The sensorgram showed a change in resonance angle of 0.4° for the luminescent ruthenium compound and 0.3° for the iridium analogue, indicating clear adsorption of the BSA to the SAM. The surface interaction of BSA to the SAM was conclusion and remained bound to the SAM even after washing the surface at a flow rate of 1500 $\mu l min^{-1}$.

As the SAM was of a luminescent nature, the luminescent properties of the surface was also investigate in the presence and absence of BSA. The lifetime of SAMs in the presence of BSA changed from 210 ns to 283 ns for ruthenium complex and a biexponential lifetime of 12 ns (17 %), 130 ns (83 %) to 15 ns (30%) 170 ns (70%) for iridium. These results were in agreement with the solution lifetimes found in the presence of 10 molar equivalents of BSA. The lifetime

of the ruthenium complex increased from 210 ns to 84 ns (4%), 250 ns (96%) and the iridium complex increased from 15 ns to 37 ns (8%), 283 ns (92%). The luminescent intensity also increased 80 fold in solution in the presence of BSA. For the case of ruthenium complexes, these shifts are attributed to the lack of solvent influence in the stabilization of the charge transfer states and possible the lack of free movement in the complexes.

5.2 - Project Aims

In this chapter we aim to characterise the surface attachment of lanthanide DTPA bis-amide complex on gold and silica substrates using SPR and ellipsometry. We will use SPR to show SAM formation over time, under flow conditions, and compare these surface interactions relative to the presence of sulphur containing functional groups. The SPR results will then be compared with that of the kinetic studies performed using ellipsometry. With the potential of intermolecular polymerisation forming at the substrate surface, it is essential that we characterise the SAM thickness in order to determine if the lanthanide complex forms a monolayer at the surface or a multilayer. This Chapter starts with an introduction to what SPR and ellipsometry is and how the techniques works, followed by an analysis of various lanthanide complexes injected through the system SPR system and ellipsometric results showing how SAM thickness of the surface active complexes in Chapter 2-4 changes over 24 hrs.

5.3 - SPR-The Technique

The technique of SPR works through using polarised light through a prism at the total internal reflection angle (*figure 5.2*). This results in no light to be refracted out or back but still allows for an electromagnetic field to be cause by the photons. The presence of the electromagnetic field causes the electrons of any adhered metal surface coating to become excited. Thus the electron density of the metal surface become excited, and has both magnitude and direction much like an electron density wave. The electron density wave or plasmon extends and is restricted to surface plane of the adhered metal. The plasmon travels though the metal surface and extend both below and above the metal surface.

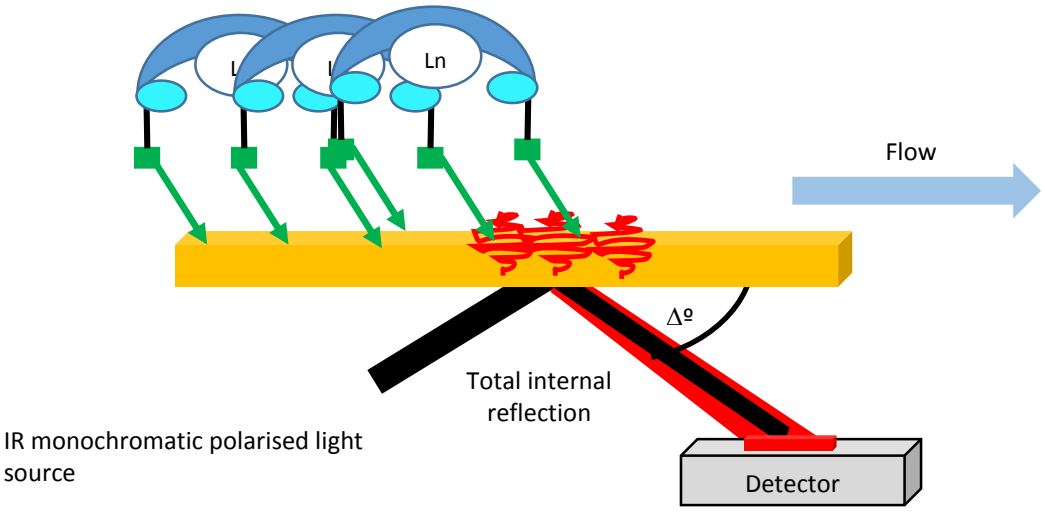

Figure 5.2 - Representing how SPR works

This plasmon that is exposed to the media, the opposite side that is receiving the IR monochromatic light source, is referred to as the evanescence wave, and is highly susceptible to change in the environment, this includes any binding molecules and changes in solvent conditions. With a change in environment above the metal surface, the resulting effect

changes the surface plasmon resonance angle. As well as the environment, the surface plasmon resonance angle mainly depends on the properties of the metal film and the wavelength of the incident light. The adhered metal has to have a conductive band capable of resonating with a reasonable wavelength of incident light, this limits the metals to silver, gold, copper, aluminium, sodium and indium. For practicality reasons the metals must be free from oxides, sulphides and be unreactive to atmosphere and liquid exposure, thus the best choice for SPR experiments is usual gold.

5.4 - Ellipsometry – The technique

Ellipsometry is an optical technique used in the field of SAMs and thin films to characterise the thickness of a particular material. The technique probes the surfaces dielectric properties by using polarised radiation, and by quantifying the change in the incident polarised radiation from the reflected polarised radiation, the thickness of a surface can be calculated with the aid of computer modelling. The technique is non-destructive and contactless since it is an optical technique meaning the same surface can be studied for analyte recognition and luminescent properties.

5.5 - Results and Discussion

5.5.1 - SPR of Surface Active and Non-active DTPA-bisamide Lanthanide Complexes

SPR works by detecting a change in refractive index. This change in refractive index at the surface is due to adsorbates coming into proximity with the surface of the sensor chip. For larger adsorbates such as proteins, this change is generally higher (ca. 0.4° or 4000 µRIU where RIU = refractive index unit),[191,211,214] then with smaller adsorbates expected to have lower responses, as molecular weight can contribute to the response.[217] Here we show the formation of SAMs using lanthanide complex's attachment to gold in real time and compare the relative association of a range of europium DTPA-bisamide derivatives, consisting of disulphides, thiol acetates, thiols, and non-gold binding variants (*figure 5.3*). As discussed previously the thiols bind to gold, and using SPR we demonstrate the interaction of lanthanide complexes both containing thiol groups and complexes without thiols.

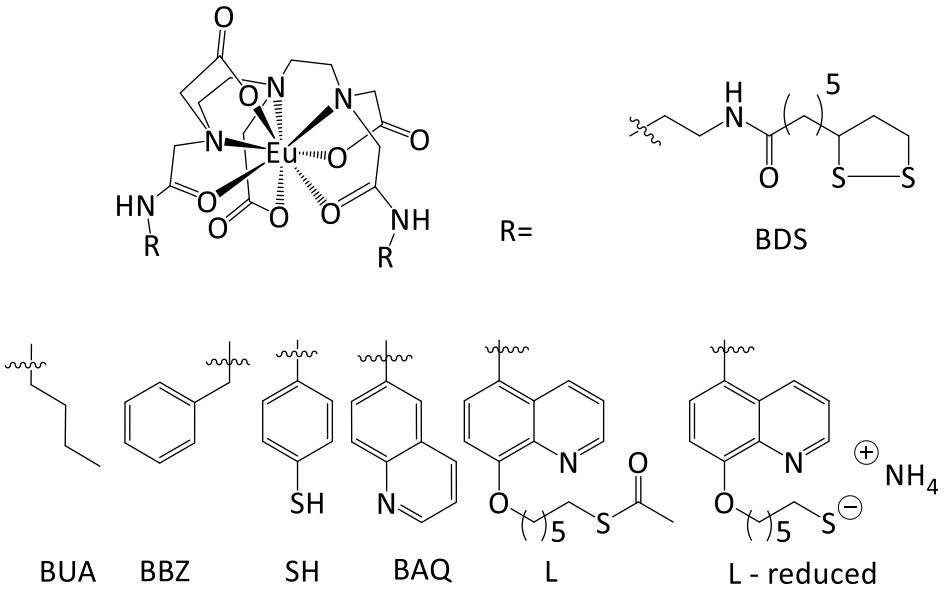

Figure 5.3 - Chemical structure of the lanthanide complexes compared using SPR.

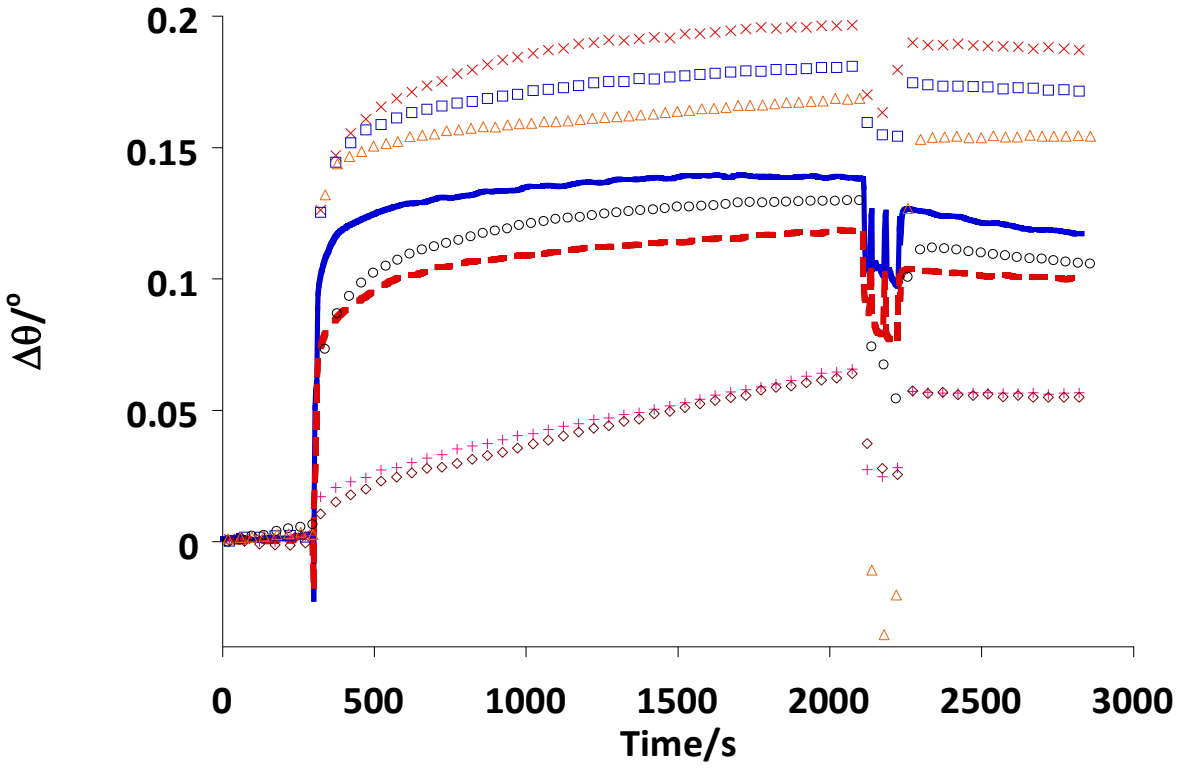

Figure 5.4 - Sensogram of various lanthanide DTPA-bisamide complexes injected (0.1mM, ethanolic or aqueous solutions*) over the surface of a gold substrate.(X) – EuL reduced, (□)- EuL,(Δ) – EuBDS*, Eu (—) – EuSH, (○) – EuUDS*, (---) – EuBAQ, (+) – EuBZZA, (◊) – EuBUA.

The sensogram (*figure 5.4*) demonstrates the kinetics of adsorption of a range of various 0.1 mM ethanolic lanthanide solutions (*complexes shown in figure 3*). For **EuL (**Chapter 4) reduced (deprotected prior to injection), we observe an increase in response units over 30 min from 0 to 0.20°, showing an association of the complex with the substrate. Subsequent washing in clean ethanol at a flow rate of 1500 µL min^{-1} followed by 10 min at a flow rate of 50 µL min^{-1} shows that some complex is specifically adsorbed to the surface, with an average

response of 0.19° even after solvent wash, which we expect for smaller adsorbates.[218] A similar trend is observed for EuL. The EuL complex wasn't deprotected prior to injection, and the SPR with the response increasing over 30 min from 0 to 0.18°. Following the wash step, the signal drops to 0.17°, also indicative of specific binding to the gold substrate. Through deprotecting the thioacetyl of **EuL** showed a greater response then direct thiol adsorption, indicating that the reduced form showed greater substrate coverage, even after washing the substrate.

Comparative studies using various DTPA-bisamide complex were used in order to compare the effects of having sulphur groups, the effect of having disulphides (**EuUDS –** Chapter 2) and bisdisulphides (**EuBDS-** Chapter 2) against lanthanide complexes that have aliphatic functional groups (**EuBUA**), non-thiol containing quinoline groups (**EuBAQ**) or benzyl amine groups (**EuBZZA**) whilst using SPR to show SAM adsorption over time. The binding interactions of all thiol containing complexes show a refractive angle change between 1.0-2.0°. Those without thiol functional groups gave substantially less angle change between 0-0.5°, with the exception of **EuBAQ**, indicating that necessity of sulphur-gold interaction for functionalising a gold surface (*figure 5.4*). **EuBAQ** showed the highest refractive angle change amongst the non-thiol containing lanthanide complexes, this is down to the affinity of nitrogen interactions with the gold surface with the two quinoline functional groups present in **EuBAQ** bisamide arms containing two nitrogen atoms with the potential of surface interactions.[219,220] **EuBAQ** remain associated to the surface even after washing the gold surface with clean ethanol under a high rate of flow for (1500 μL min^{-1}) for 300 seconds followed by ten minutes of a normal flow rate (50 μL min^{-1}) indicated by a refractive angle change of 0.9°.

EuUDS has a relatively low refractive angle change compared to the other thiol containing lanthanide complexes. This can be attributed to the positive charge on the complex, and the positive charge of a clean gold surface causing electrostatic repulsion, thus limiting the surface interaction between **EuUDS** and the gold substrate. The effect of using disulphides and thioacetates can be compared by analysing **EuL** and **EuBDS** respectively. These two complexes showed the highest refractive index change of 1.7° and 1.5° without the addition of deprotection agents. This result shows that using a disulphide and a thioacetate gave relatively similar surface coverage assuming that both complexes have similar refractive indexes. In all case SPR results were baselined to a $\Delta 0.001^{o}$ with the solvent prior to injection, and the surfaces

Comparatively all complexes have formed monolayers within the first minute after injection of the SAM solution, all monolayers reach saturated coverage after half an hour. These results agree with ellipsometric results with monolayers binding to the surface within the first half an hour. However, unlike ellipsometry, no surface structural information can be obtained from SPR, as the refractive angle change in SPR is only due to the presence and proximity of surface binding molecules to the gold surface. Whereas ellipsometry showed that the surface height changes over 24 hrs indicating surface reorganisation of SAMs.

5.42 Ellisometry of Surface Active Lanthanide DTPA- Bisamide complexes

All four of the lanthanide complexes studied throughout **Chapters 1-3** are surface active, and to confirm that the compounds form monolayers as predicted, ellipsometry was performed on all four SAMs. Ellipsometry was used to investigate the formation of the surface monolayer of the **EuBDS** (**Chapter 2**) complexes on planar gold surface as a function of time (*figure 5.5*). A kinetic study was performed at various intervals over and including 24 hours. Leaving the surface for 24 hours was necessary to achieve maximum loading while still maintaining a monolayer. The comparison with the SAM thickness after 24 hours and by Chem3D calculations, it was possible to deduce that the SAM formed was a monolayer and not a bilayer or multilayer. After 24 hours the total thickness of the surface was 1.96 ± 0.08 nm which is very close to the estimated length (~ 2.00 nm) of the molecule from Chem3D modelling. The Au-S (~ 2.36 Å) bond is also considered in this estimation.

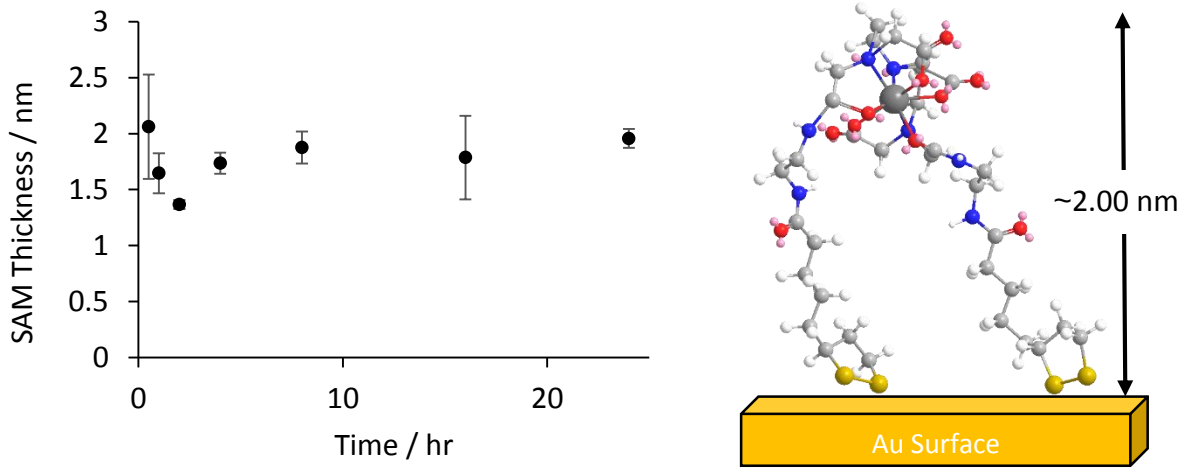

Figure 5.5-Kinetic study of EuBDS on the surface of gold, observing SAM formation over time via ellipsometry formed from a 1mM methanolic solution (left). Chem3D model of EuBDS with theoretical height (right).

The same experiment has been carried out on **EuUDS** (**Chapter 2**), to investigate the formation of the surface monolayer on planar gold surface as a function of time (*figure 5.6*). **EuUDS** has the disadvantage of only have two sulphurs to bind to the gold surface from one leg. This means that the complex has less structural constraints, and with the complexes -1 charge, results in a collapsible structure, producing a thin monolayer. From the Chem3D model it was estimated that the SAM thickness would be ~0.95 nm. The thickness after 24 hours deposition time was measured to be 0.86 ± 0.09 nm thus showing good agreement that **EuUDS** does form a collapsed monolayer.

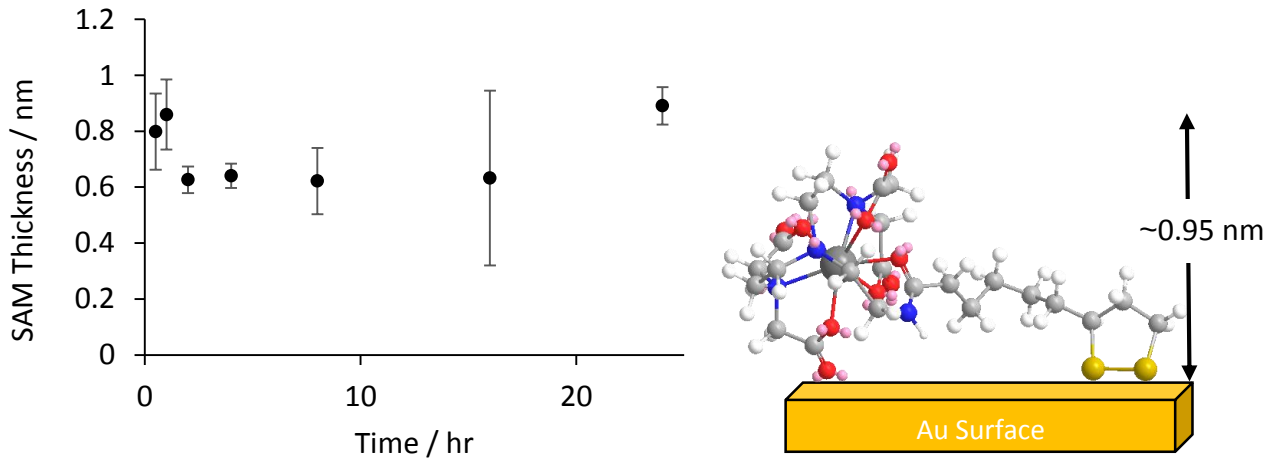

Figure 5.6- Kinetic study of EuUDS on the surface of gold, observing SAM formation over time via ellipsometry formed from a 1mM aqueous solution. Chem3D model of EuUDS with theoretical height (right).

In comparison to the disulphide based lanthanide complexes above, the bis thio-actyl lanthanide complex **EuL** (**Chapter 4**) was also tested for SAM thickness (*figure 5.7*). It was theorised to hold a similar structure to **EuBDS**, with an increase in rigidity arising from the presence of the quinoline rings, and planar nature of aromatic rings. We predicted using Chem3D that the SAM thickness of **EuL** would be ~ 1.73 nm. After 24hrs the **EuL** SAM was

tested for a final thickness value of 1.64 ± 0.10 nm. Ellipsometry data corresponding to the monolayer thickness of **EuL** is very close to the calculated length of the monolayer from Chem3D modelling.

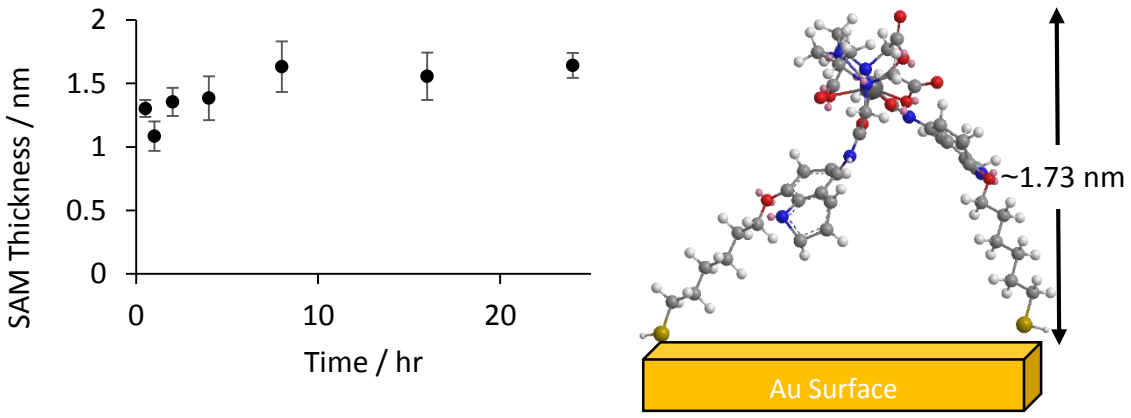

Figure 5.7 - Kinetic study of EuL on the surface of gold, observing SAM formation over time via ellipsometry, formed from a 1mM methanolic solution. Chem3D model of EuUDS with theoretical height (right).

As a comparison experiment, a planar gold surface was deposited in a solution of 1 mM **Na_3L** and **H_3L** (*figure 5.8*) for 24 hours. The surface thickness has been measured under the same conditions, resulting in a surface thickness of 1.13 ± 0.21 nm and 0.70 ± 0.32 nm. The SAM thickness for both **Na_3L** and **H_3L** are significantly less than **EuL**. This experiment helps prove the presence of europium ions in the SAM and how the chelating ligand moulds around the lanthanide ion, generating structure and rigidity to the complex, overall increasing the SAM thickness.

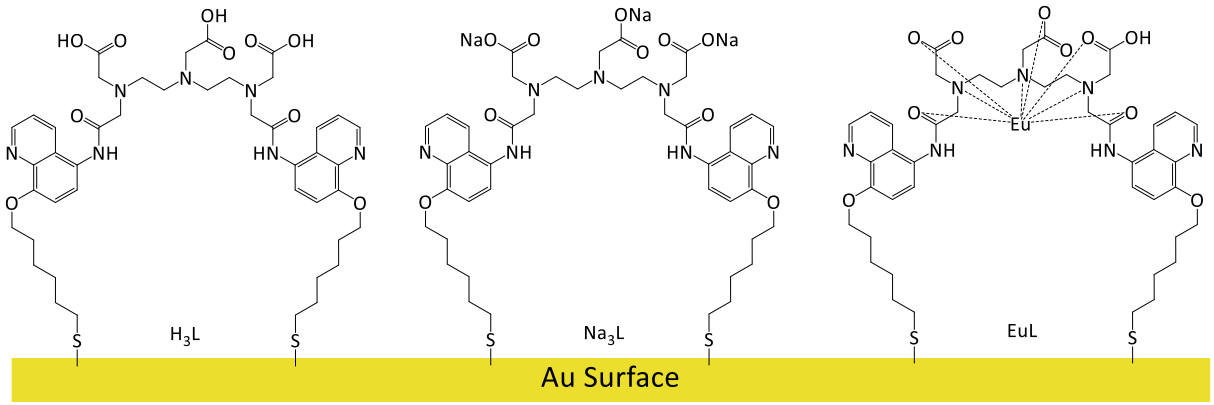

Figure 5.8 - Schematic representation of the H_3L Ligand and encapsulation of sodium and europium analogues.

In contrast, the thiolated lanthanide complex, **$EuSi_2$** (**Chapter 3**) was also compared to ensure that it too formed a monolayer, especially due to silyl nature to readily hydrolyse (*figure 5.9*). The kinetic study was carried out on silicon and not silica as ellipsometry is reflective optical technique and silica would provide experimental difficulty due to its optical transparency, thus SAM formation was performed on silicon as analogues counterpart. We predicted using Chem3D that the SAM thickness of **$EuSi_2$** would be ~ 1.53 nm. After 24hrs the **$EuSi_2$** SAM was tested for a final thickness value of 1.60 ± 0.08 nm. The found and theoretical SAM thickness agree with in error.

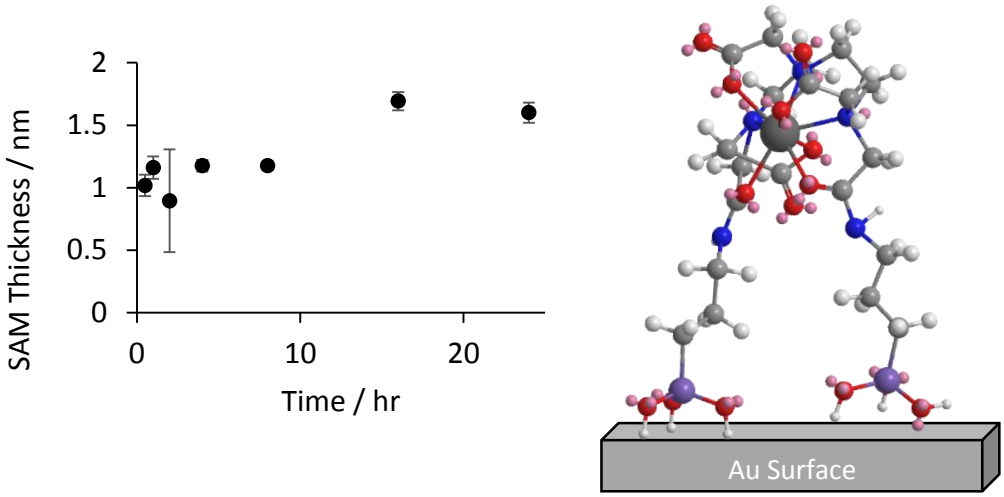

Figure 5.9 - Kinetic study of $EuSi_2$ on the surface of gold, observing SAM formation over time via ellipsometry formed from a 1mM ethanolic solution. Chem3D model of $EuSi_2$ with theoretical height (right).

Metal complex/ligand	~ Estimated length (nm)	Measured length (nm)
EuBDS	2.02	1.96 ± 0.08
EuUDS	0.95	0.86 ± 0.09
EuL	1.73	1.64 ± 0.10
Na_3L	-	1.13 ± 0.21
H_3L	-	0.70 ± 0.32
$EuSi_2$	1.53	1.60 ± 0.08

Table 4.1 - Ellipsometric summary of Lanthanide complexes and Ligands SAM thickness on gold and silica surfaces.

Ellipsometry data corresponding to the monolayer thickness of all complexes are very close to the calculated length of the monolayer of such molecules from Chem3D modelling (*table 5*).

In conclusion, we show surface coverage of lanthanide DTPA-bisamide complexes on silicon and gold surface, where SAMs are formed and stabilised over 12 hrs, with SPR all SAMs are formed after the first 500 seconds. SPR shows that faster surface binding with the presence of sulphur binding groups, and isn't necessarily enhanced by the presence of disulphide groups. There are limited surface interactions associated by the presence of terminal quinoline groups which increases the change in SPR resonance angle. XPS is shown in Chapter 3 showing sulphur-gold bond presence for **EuL** at the surface.

6 - General Experimental

Materials and Methods

All chemicals were purchased from Sigma-Aldrich, Fluka, Fisher Scientific, or Acros and used without further purification unless otherwise stated. Solvents were purchased from Sigma Aldrich and Fisher. Dimethylformamide (DMF) was obtained from AGTC Bioproducts Ltd. and dried with 3 or 4 Å molecular sieves for 24-48 hrs before use. HPLC grade solvents were used in photophysical studies. Water was deionised using an Elga Option 3 water purifier. Gold slides (30 nm on silicon with 5 nm Ti priming layer) were purchased from Georg Albert PVD, Germany. Diethylenetriaminepentaacetic bisanhydride was synthesised by Dr. Alison Savage through literature procedure. [120]

Equipment

NMR and Mass spectrometry

^{1}H and ^{13}C NMR were recorded on Brüker AVIII 300 and AVIII 400 spectrometers. $SiMe_4$ was used for an external reference of the ^{1}H and ^{13}C shifts. Deuterated solvents were obtained from Goss Scientific and used as supplied.

Matrix assisted laser desorption ionisation – time of flight (MALDI-TOF) mass spectrometry was carried out on a Brüker Biflex IV mass spectrometer, using Gentisic acid in CH_3CN with 0.1% TFA as the matrix. Electrospray mass spectrometry was carried out on a Micromass LC-TOF.

UV-Vis Spectroscopy

UV-Vis absorption spectra were carried out on Varian Cary 50 or Varian Cary 5000 spectrometers with 300 nm/min UV-Vis spectra were taken using 1 cm path length quartz cuvettes.

Luminescence Spectroscopy

Luminescence studies were carried out on a PTI fluorescence system, using a PTI L-201M with a 75 W xenon arc lamp as the illumination source. The detection system was a Shimadzu R928 PMT in a PTI model 814 analogue/photon counting photomultiplier. The emission monochromator is equipped with two interchangeable blazed gratings at 500 nm and 750 nm. PTI Felix fluorescence analysis software was used to record the data. Luminescence experiments were carried out using 1 x 1cm path length quartz cuvettes with four transparent polished faces.

Luminescence studies for the SAM developed on gold and silica surfaces were carried out using an Edinburgh instruments fluorescence system, FLSPM920. The illumination source uses a 450 W xenon arc lamp. The detection system used was a Hamamatsu R928 PMT. The emission monochromator is fitted with two interchangeable gratings blazed at 500 nm and 1200 nm. F900 spectrometer analysis software was used to record the data. Lifetimes were measured using a 100 W µF920H lamp. Lifetime data were fitted to monoexponential decays using Edinburgh Instruments F900 PC software using the exponential tail fit option.

Lifetimes were alternatively measured using a Continuum Surelite I SSP class 4 pulsed Nd-YAG laser (10 Hz) as the excitation source using the 355 nm harmonic. The signal was collected as a direct output from the PMT to minimise the response time of the apparatus. Data were recorded on a LeCroy 9350AM 500 MHz oscilloscope which was triggered by the laser, with an average of 500 shots. The lifetime data was analysed using Kaleidagraph software (Kaleidagraph 3.51, Synergy Software, 2000) for the PC and fitted using a non-linear least-squares iterative technique (Marquardt-Levenberg algorithm).

Luminescence Microscopy

Surfaces were imaged by luminescence microscopy using an Olympus IX71 inverted fluorescent microscope with a LUCPLFLN 40 × 0.60 NA objective coupled to an Edinburgh Instruments FLS920 spectrophotometer. Excitation was achieved with the use of a 450 W Xe lamp and europium emission (>510 nm) was detected by a Hamamatsu EMCCD C9100-13. Excitation and emission wavelengths were controlled using Edinburgh Instruments v6.8 PC software. Images were acquired using Cell^M 3.2 (Olympus Soft Imaging Solutions GmBH) and post-imaging analysis was performed using ImageJ 1.44c. Emission spectra were acquired using Edinburgh Instruments F900 v6.8 PC software.

SAM formation

This is the procedure for europium complexes on gold, unless stipulated otherwise. Gold substrates were cleaned using a UVO cleaner (1 h) and immersed in ethanol for at least 10 min before use, and submerging into 1mM solution Complex solution where 3-5mL of NH_4OH was added to the solution prior to gold submersion where applicable.

Particle Sizing

Particle sizing measurements were made using a Nanosight LM10 system controlled by NTA 2.2 software. Dynamic light scattering measurements were acquired using a Beckman-Coulter DelsaNano C instrument.

XPS

X-ray photoelectron spectroscopy was carried out at the University of Leeds by Dr. Benjamin Johnson. The instrument is a VG ESCAlab 250 with a monochromated Al Kα source. Experiments were performed under UHV ($\sim 10^{-10}$ mbar). Survey scans were recorded at a pass energy of 150 eV, detailed scans at 20 eV. Offline analysis of the spectra was performed using Casa 2.3.15 XPS software.

SPR

Gold chips (50 nm on glass, Reichert) were cleaned in Piranha solution (CAUTION: Piranha solution reacts violently with organic material) for 10 min, washed with ultrahigh purity (UHQ 18 MΩ cm) water followed by ethanol, and stored in ethanol until used. During the

experiments, the chips were equilibrated in the solvent system used for each experiment for at least 10 min to ensure a steady baseline. The system was then injected with the appropriate solution at an initial flow rate of 1500 µL min−1 followed by a flow rate of 10 or 0 µL min^{-1}. The slides were then washed with the solvent system at a flow rate of 1500 µL min^{-1}.

Ellipsometry

Ellipsometry measurements were taken using a Jobin-Yvon UVISEL ellipsometer with a He-Ne laser light source at a controlled angle of incidence of 70 °C using a wavelength range of 280–800 nm. The ellipsometric parameters, Δ and ψ, were recorded for control experiments and sample surfaces. By using DeltaPsi software and a group computer model for 30 nm gold SAMs, the thickness of the SAM surface could be determined**.** All measurements were made under conditions of ambient temperature, pressure and humidity. SAM thicknesses are averages of a minimum of five measurements at five different points along the sample surface.

7 – Conclusions

We have shown the synthesis of four lanthanide complexes developed further from previously established group research in order to incorporate surface functionality, hydrophobicity and sensitisers. Using the unique photophysical properties of lanthanides, the complexes developed were used to detect for small analytes showing varying degrees of luminescent enhancement depending on the analyte and lanthanide complex used, both on a surface and in solution. In Chapter 2 a non-absorbing lanthanide complex is synthesised and tested for its binding in solution and on the surface, demonstrating an off-on approach to molecular sensing on a SAM surface consisting lanthanide formed SAMs. Chapter 2 also shows a different synthetic approach, produced a negatively charged non-absorbing complex, which was tested for simple aromatics in solution and surface, and also tested for its sensing capacity for positively charged species. In Chapter 3 an absorbing lanthanide complex has been synthesised in order to increase the amount of water exclusion, but failed to show any analyte binding, possible due to its small cavity size.

In Chapter 4 we show how SAM formation on silica differs from gold, how optical transparency of the substrate can hinder the lanthanide system and enhance it, as well as contrasting the surface behaviour with a microparticle system, in which we show that it is possible to sense in *situ* under flow conditions, using lanthanide silica nanoparticles. The silica microparticles was also developed further to show the benefits of lanthanide-transition metal bimodal microparticles. In the final Chapter 5 we analyse SAM formation of these compounds on gold through analysis of ellipsometry and SPR we can observe and compare various europium complex binding to the surface over time. Surface attachment has been shown by XPS, SPR

and ellipsometry. SPR has shown accurate SAM formation under flow conditions and how much gold surface coverage is dependent on the use of sulphur containing groups. Ellipsometry has indicated rapid surface attachment and the presence of monolayers for all four complexes attached to surfaces, closely matching theoretical values.

The overall results show that SAMs of lanthanide complexes can be used to screen for small analytes at a loss of spectral resolution and limit of detection. The lanthanide complexes have also shown the sensing of small analytes is not limited to emission in the visible spectrum but the near infra-red spectrum is also possible. A direct comparison of using silica and quartz material in device development has been carried out showing how silica impedes the detecting of UV absorbing analytes.

Whilst we have shown that SAMs consisting of lanthanide complexes can be used to detect for small analyte in a simple and cost effective manner, much research is needed to primarily improve the surfaces limit of detection and accuracy, making the system more robust. This can be done in a number of ways. Firstly the surface can be developed in a layer by layer approach, potential improving surface coverage, and reducing surface quenching; thus increasing the surface luminescence and limit of detection.

The surface could be developed using molecular printing techniques, and by doing so a mixture of lanthanide complexes could be bound the surface in a reproducible method. The result could lead to ratiometric lanthanide surface bound sensors, by doing so the surface

could display greater screening capabilities. Equally the dual coating microparticles could also lead to interesting results by using its excitation tunability and dual emission properties localisation of the particles is more probable i.e. in the body. Much like the aims of Chapter 3, **EuL** and the attempt at developing **H_3BQUDS** at the end of Chapter 2, in would advantageous to synthesis a surface active UV-absorbing lanthanide complexes that can detect for small analytes on a surface comparing how surface luminescent enhancement or reduction compares to detection with non-absorbing UV lanthanide complexes.

Experiments with SPR and ellipsometry can be developed further and investigating the change in SPR response and SAM thickness respectively whilst in the presence of small analytes. Also surface regeneration should be investigated.

8 - References

(1) Dittrich, P. S.; Manz, A. *Nature Reviews. Drug Discovery* **2006**, *5*, 210.
(2) Whitesides, G. M.; Laibinis, P. E. *Langmuir* **1990**, *6*, 87.
(3) Love, J. C.; Estroff, L. A.; Kriebel, J. K.; Nuzzo, R. G.; Whitesides, G. M. *Chemical Reviews* **2005**, *105*, 1103.
(4) Tour, J. M.; Jones, L.; Pearson, D. L.; Lamba, J. J. S.; Burgin, T. P.; Whitesides, G. M.; Allara, D. L.; Parikh, A. N.; Atre, S. V. *Journal of the American Chemical Society* **1995**, *117*, 9529.
(5) Skulason, H.; Frisbie, C. D. *Journal of the American Chemical Society* **2002**, *124*, 15125.
(6) Bethencourt, M. I.; Srisombat, L.-o.; Chinwangso, P.; Lee, T. R. *Langmuir* **2009**, *25*, 1265.
(7) Browne, K. P.; Grzybowski, B. A. *Langmuir* **2010**, *27*, 1246.
(8) Franz, A. W.; Stoycheva, S.; Himmelhaus, M.; Muller, T. J. J. *Beilstein Journal of Organic Chemistry* **2010**, *6*, 9.
(9) Singh, A.; Dahanayaka, D. H.; Biswas, A.; Bumm, L. A.; Halterman, R. L. *Langmuir* **2010**, *26*, 13221.
(10) Eker, B.; Yilmaz, M. D.; Schlautmann, S.; Gardeniers, J. G. E.; Huskens, J. *International Journal of Molecular Sciences* **2011**, *12*, 7335.
(11) Valkenier, H.; Huisman, E. H.; van Hal, P. A.; de Leeuw, D. M.; Chiechi, R. C.; Hummelen, J. C. *Journal of the American Chemical Society* **2011**, *133*, 4930.
(12) Cook, K. M.; Nissley, D. A.; Ferguson, G. S. *Langmuir* **2013**, *29*, 6779.
(13) Ivashenko, O.; van Herpt, J. T.; Feringa, B. L.; Rudolf, P.; Browne, W. R. *Langmuir* **2013**, *29*, 4290.
(14) Liu, F.; Pang, J.; Wang, C.; Wang, L. *Langmuir* **2013**, *29*, 13003.
(15) Bain, C. D.; Troughton, E. B.; Tao, Y. T.; Evall, J.; Whitesides, G. M.; Nuzzo, R. G. *Journal of the American Chemical Society* **1989**, *111*, 321.
(16) Folkers, J. P.; Laibinis, P. E.; Whitesides, G. M. *Langmuir* **1992**, *8*, 1330.
(17) Hsu, S. H.; Yilmaz, M. D.; Blum, C.; Subramaniam, V.; Reinhoudt, D. N.; Velders, A. H.; Huskens, J. *Journal of the American Chemical Society* **2009**, *131*, 12567.
(18) Yilmaz, M. D.; Hsu, S.-H.; Reinhoudt, D. N.; Velders, A. H.; Huskens, J. *Angewandte Chemie International Edition* **2010**, *49*, 5938.
(19) Liang, C.-K.; Dubacheva, G. V.; Buffeteau, T.; Cavagnat, D.; Hapiot, P.; Fabre, B.; Tucker, J. H. R.; Bassani, D. M. *Chemistry – A European Journal* **2013**, *19*, 12748.
(20) Bonnet, C. S.; Massue, J.; Quinn, S. J.; Gunnlaugsson, T. *Organic & Biomolecular Chemistry* **2009**, *7*, 3074.
(21) Mrksich, M.; Dike, L. E.; Tien, J.; Ingber, D. E.; Whitesides, G. M. *Experimental Cell Research* **1997**, *235*, 305.
(22) Castellana, E. T.; Gamez, R. C.; Russell, D. H. *Journal of the American Chemical Society* **2010**, *133*, 4182.
(23) Murray, N. S.; Jarvis, S. P.; Gunnlaugsson, T. *Chemical Communications* **2009**, 4959.
(24) Lehr, J.; Bennett, J.; Tropiano, M.; Sørensen, T. J.; Faulkner, S.; Beer, P. D.; Davis, J. J. *Langmuir* **2013**, *29*, 1475.
(25) Bünzli, J. C. G. *Accounts of Chemical Research* **2006**, *39*, 53.
(26) Fitzgerald, K. T.; Holladay, C. A.; McCarthy, C.; Power, K. A.; Pandit, A.; Gallagher, W. M. *Small* **2011**, *7*, 705.
(27) Szunerits, S.; Boukherroub, R. *Chemical Communications* **2012**, *48*, 8999.
(28) Porter, M. D.; Bright, T. B.; Allara, D. L.; Chidsey, C. E. D. *J. Am. Chem. Soc.* **1987**, *109*, 3559.
(29) Ulman, A. *Chem. Rev.* **1996**, *96*, 1533.

(30) Grönbeck, H.; Curioni, A.; Andreoni, W. *Journal of the American Chemical Society* **2000**, *122*, 3839.
(31) Molard, Y.; Bassani, D. M.; Desvergne, J.-P.; Horton, P. N.; Hursthouse, M. B.; Tucker, J. H. R. *Angewandte Chemie International Edition* **2005**, *44*, 1072.
(32) Ray, D.; Belin, C.; Hui, F.; Fabre, B.; Hapiot, P.; Bassani, D. M. *Chemical Communications* **2011**, *47*, 2547.
(33) Bünzli, J.-C. G. *Accounts of Chemical Research* **2005**, *39*, 53.
(34) Cable, M. L.; Kirby, J. P.; Gray, H. B.; Ponce, A. *Accounts of Chemical Research* **2013**, *46*, 2576.
(35) Beulen, M. W. J.; Bügler, J.; de Jong, M. R.; Lammerink, B.; Huskens, J.; Schönherr, H.; Vancso, G. J.; Boukamp, B. A.; Wieder, H.; Offenhäuser, A.; Knoll, W.; van Veggel, F. C. J. M.; Reinhoudt, D. N. *Chemistry – A European Journal* **2000**, *6*, 1176.
(36) Basabe-Desmonts, L.; Reinhoudt, D. N.; Crego-Calama, M. *Chemical Society Reviews* **2007**, *36*, 993.
(37) Wang, J.; Wu, J.; Chen, Y.; Wang, H.; Li, Y.; Liu, W.; Tian, H.; Zhang, T.; Xu, J.; Tang, Y. *Dalton Transactions* **2012**, *41*, 12936.
(38) Zhu, B. C.; Zhang, X. L.; Li, Y. M.; Wang, P. F.; Zhang, H. Y.; Zhuang, X. Q. *Chemical Communications* **2010**, *46*, 5710.
(39) Wood, Z. A.; Schröder, E.; Robin Harris, J.; Poole, L. B. *Trends in Biochemical Sciences* **2003**, *28*, 32.
(40) Wang, Y.; Li, B.; Zhang, L.; Zuo, Q.; Li, P.; Zhang, J.; Su, Z. *Chemphyschem* **2011**, *12*, 349.
(41) Tripier, R.; Platas-Iglesias, C.; Boos, A.; Morfin, J. F.; Charbonniere, L. *European Journal of Inorganic Chemistry* **2010**, 2735.
(42) De Silva, A. P.; Gunaratne, H. Q. N.; Rice, T. E. *Angewandte Chemie-International Edition* **1996**, *35*, 2116.
(43) De Silva, A. P.; Rupasinghe, R. *Journal of the Chemical Society-Chemical Communications* **1985**, 1669.
(44) Geißler, D.; Linden, S.; Liermann, K.; Wegner, K. D.; Charbonnière, L. J.; Hildebrandt, N. *Inorganic Chemistry* **2013**, *53*, 1824.
(45) Yu, J. A.; Lessard, R. B.; Bowman, L. E.; Nocera, D. G. *Chemical Physics Letters* **1991**, *187*, 263.
(46) Binnemans, K.; Görller-Walrand, C. *Chemical Physics Letters* **1995**, *235*, 163.
(47) Moore, E. G.; Samuel, A. P. S.; Raymond, K. N. *Accounts of Chemical Research* **2009**, *42*, 542.
(48) Sabbatini, N.; Guardigli, M.; Lehn, J.-M. *Coordination Chemistry Reviews* **1993**, *123*, 201.
(49) Law, G.-L.; Pham, T. A.; Xu, J.; Raymond, K. N. *Angewandte Chemie International Edition* **2012**, *51*, 2371.
(50) DeOliveira, E.; Neri, C. R.; Serra, O. A.; Prado, A. G. S. *Chemistry of Materials* **2007**, *19*, 5437.
(51) Sabbatini, N.; Guardigli, M.; Manet, I.; Ungaro, R.; Casnati, A.; Ziessel, R.; Ulrich, G.; Asfari, Z.; Lehn, J.-M. *Pure & Applied Chemistry* **1995**, *67*, 5.
(52) Yu, J.-A.; Lessard, R. B.; Bowman, L. E.; Nocera, D. G. *Chemical Physics Letters* **1991**, *187*, 263.
(53) Bushby, L. M., Durham University, 2001.
(54) Lehn, J.-M. *Angewandte Chemie International Edition in English* **1990**, *29*, 1304.
(55) Lewis, D. J.; Day, T. M.; MacPherson, J. V.; Pikramenou, Z. *Chemical Communications* **2006**, 1433.
(56) Beeby, A.; M. Clarkson, I.; S. Dickins, R.; Faulkner, S.; Parker, D.; Royle, L.; S. de Sousa, A.; A. Gareth Williams, J.; Woods, M. *Journal of the Chemical Society, Perkin Transactions 2* **1999**, 493.
(57) Alexander, V. *Chemical Reviews* **1995**, *95*, 273.
(58) Kim, H. J.; Eichinger, A.; Skerra, A. *Journal of the American Chemical Society* **2009**, *131*, 3565.
(59) Laurent, S.; Vander Elst, L.; Muller, R. N. *Quarterly Journal of Nuclear Medicine and Molecular Imaging* **2009**, *53*, 586.

(60) Tiwari, A. K.; Sinha, D.; Datta, A.; Kakkar, D.; Mishra, A. K. *Chemical Biology & Drug Design* **2011**, *77*, 388.
(61) Nash, K. L.; Brigham, D.; Shehee, T. C.; Martin, A. *Dalton Transactions* **2012**, *41*, 14547.
(62) Debroye, E.; Eliseeva, S. V.; Laurent, S.; Vander Elst, L.; Petoud, S.; Muller, R. N.; Parac-Vogt, T. N. *European Journal of Inorganic Chemistry* **2013**, *2013*, 2629.
(63) Magennis, S. W.; Craig, J.; Gardner, A.; Fucassi, F.; Cragg, P. J.; Robertson, N.; Parsons, S.; Pikramenou, Z. *Polyhedron* **2003**, *22*, 745.
(64) Ruston, L. L.; Robertson, G. M.; Pikramenou, Z. *Chemistry-an Asian Journal* **2010**, *5*, 571.
(65) Lewis, D. J.; Dore, V.; Rogers, N. J.; Mole, T. K.; Nash, G. B.; Angeli, P.; Pikramenou, Z. *Langmuir* **2013**, *29*, 14701.
(66) Pearson, R. G. *Journal of the American Chemical Society* **1963**, *85*, 3533.
(67) Hirano, S.; Suzuki, K. T. *Environ Health Perspect* **1996**, *104 Suppl 1*, 85.
(68) Liu, Y.; Wu, X.; He, C.; Jiao, Y.; Duan, C. *Chemical Communications* **2009**, 7554.
(69) Liu, Y.; Wu, X.; He, C.; Jiao, Y.; Duan, C. Y. *Chemical Communications* **2009**, 7554.
(70) Shunmugam, R.; Tew, G. N. *Chemistry – A European Journal* **2008**, *14*, 5409.
(71) Rathfon, J. M.; Al-Badri, Z. M.; Shunmugam, R.; Berry, S. M.; Pabba, S.; Keynton, R. S.; Cohn, R. W.; Tew, G. N. *Advanced Functional Materials* **2009**, *19*, 689.
(72) Ai, K.; Zhang, B.; Lu, L. *Angewandte Chemie-International Edition* **2009**, *48*, 304.
(73) Li, H. R.; Cheng, W. J.; Wang, Y.; Liu, B. Y.; Zhang, W. J.; Zhang, H. J. *Chemistry-a European Journal* **2010**, *16*, 2125.
(74) Oh, W.-K.; Jeong, Y. S.; Song, J.; Jang, J. *Biosensors and Bioelectronics* **2011**, *29*, 172.
(75) Cable, M. L.; Kirby, J. P.; Levine, D. J.; Manary, M. J.; Gray, H. B.; Ponce, A. *Journal of the American Chemical Society* **2009**, *131*, 9562.
(76) Yung, P. T.; Lester, E. D.; Bearman, G.; Ponce, A. *Biotechnology and Bioengineering* **2007**, *98*, 864.
(77) Kim, S.; Kwak, J.; Lee, S.-Y. *Colloids and Surfaces B: Biointerfaces* **2014**, *117*, 252.
(78) Andolina, C. M.; Morrow, J. R. *European Journal of Inorganic Chemistry* **2011**, 154.
(79) Forster, T. *Discussions of the Faraday Society* **1959**, *27*, 7.
(80) Armelao, L.; Bottaro, G.; Quici, S.; Cavazzini, M.; Raffo, M. C.; Barigelletti, F.; Accorsi, G. *Chemical Communications* **2007**, 2911.
(81) Armelao, L.; Bottaro, G.; Quici, S.; Scalera, C.; Cavazzini, M.; Accorsi, G.; Bolognesi, M. *Chemphyschem* **2010**, *11*, 2499.
(82) Minoofar, P. N.; Hernandez, R.; Chia, S.; Dunn, B.; Zink, J. I.; Franville, A. C. *Journal of the American Chemical Society* **2002**, *124*, 14388.
(83) Meng, Q. G.; Fu, L. S.; Wang, S. B.; Zhang, H. J.; Li, H. R.; Chuai, X. H.; Li, Y. H.; Zhang, S. Y. *Thin Solid Films* **2001**, *388*, 87.
(84) de Souza, J. M.; de Sa, G. F.; de Azevedo, W. M.; Alves, S.; de Farias, R. F. *Optical Materials* **2005**, *27*, 1187.
(85) Turel, M.; Čajlaković, M.; Austin, E.; Dakin, J. P.; Uray, G.; Lobnik, A. *Sensors and Actuators B: Chemical* **2008**, *131*, 247.
(86) Lobnik, A.; Majcen, N.; Niederreiter, K.; Uray, G. *Sensors and Actuators B: Chemical* **2001**, *74*, 200.
(87) Iqbal, P.; Rawson, F. J.; Ho, W. K. W.; Lee, S.-F.; Leung, K. C.-F.; Wang, X.; Beri, A.; Preece, J. A.; Ma, J.; Mendes, P. M. *ACS Applied Materials & Interfaces* **2014**, *6*, 6264.
(88) Acevedo, D.; Bretz, R. L.; Tirado, J. D.; Abruna, H. D. *Langmuir* **1994**, *10*, 1300.
(89) Buess-Herman, C. *Progress in Surface Science* **1994**, *46*, 335.
(90) Bretz, R. L.; Abruña, H. e. D. *Journal of Electroanalytical Chemistry* **1995**, *388*, 123.
(91) Bertoncello, P.; Kefalas, E. T.; Pikramenou, Z.; Unwin, P. R.; Forster, R. J. *The Journal of Physical Chemistry B* **2006**, *110*, 10063.
(92) Kalyanasundaram, K.; Grätzel, M. *Coordination Chemistry Reviews* **1998**, *177*, 347.

(93) Cardinaels, T.; Ramaekers, J.; Nockemann, P.; Driesen, K.; Van Hecke, K.; Van Meervelt, L.; Lei, S.; De Feyter, S.; Guillon, D.; Donnio, B.; Binnemans, K. *Chemistry of Materials* **2008**, *20*, 1278.
(94) Huang, Y.; Zhao, S.; Chen, Z.-F.; Shi, M.; Chen, J.; Liang, H. *Chemical Communications* **2012**, *48*, 11877.
(95) Comby, S.; Surender, E. M.; Kotova, O.; Truman, L. K.; Molloy, J. K.; Gunnlaugsson, T. *Inorganic Chemistry* **2013**, *53*, 1867.
(96) Liu, J.; Du, B.; Zhang, P.; Haleyurgirisetty, M.; Zhao, J.; Ragupathy, V.; Lee, S.; DeVoe, D. L.; Hewlett, I. K. *Biosensors and Bioelectronics* **2014**, *61*, 177.
(97) Deng, W.; Jin, D. Y.; Drozdowicz-Tomsia, K.; Yuan, J. L.; Goldys, E. M. *Langmuir* **2010**, *26*, 10036.
(98) Malba, C.; Bellotto, L.; Freris, I.; Enrichi, F.; Cristofori, D.; Riello, P.; Benedetti, A. *Journal of Luminescence* **2013**, *142*, 28.
(99) Taylor-Pashow, K. M. L.; Rocca, J. D.; Lin, W. *Nanomaterials* **2011**, *2*, 1.
(100) Savage, A. C.; Pikramenou, Z. *Chemical Communications* **2011**, *47*, 6431.
(101) Hammond, S. P., University of Birmingham, 2009.
(102) Davies, A.; Lewis, D. J.; Watson, S. P.; Thomas, S. G.; Pikramenou, Z. *Proceedings of the National Academy of Sciences* **2012**.
(103) Gulino, A.; Lupo, F.; Condorelli, G. G.; Motta, A.; Fragala, I. L. *Journal of Materials Chemistry* **2009**, *19*, 3507.
(104) Parker, D. *Coordination Chemistry Reviews* **2000**, *205*, 109.
(105) Lafleur, J. P.; Senkbeil, S.; Jensen, T. G.; Kutter, J. P. *Lab on a Chip* **2012**, *12*, 4651.
(106) Nguyen, T. D.; Tseng, H. R.; Celestre, P. C.; Flood, A. H.; Liu, Y.; Stoddart, J. F.; Zink, J. I. *Proc. Natl. Acad. Sci. U.S.A.* **2005**, *102*, 10029.
(107) Knapton, D.; Burnworth, M.; Rowan, S. J.; Weder, C. *Angewandte Chemie International Edition* **2006**, *45*, 5825.
(108) Borner, H. G.; Kuhnle, H.; Hentschel, J. *Journal of Polymer Science Part a-Polymer Chemistry* **2010**, *48*, 1.
(109) Cui, J.; Yan, Y.; Wang, Y.; Caruso, F. *Advanced Functional Materials* **2012**, *22*, 4718.
(110) Maity, D.; Manna, A. K.; Karthigeyan, D.; Kundu, T. K.; Pati, S. K.; Govindaraju, T. *Chemistry-a European Journal* **2011**, *17*, 11152.
(111) Kuhn, H. *The Journal of Chemical Physics* **1970**, *53*, 101.
(112) Prudêncio, M.; Rohovec, J.; Peters, J. A.; Tocheva, E.; Boulanger, M. J.; Murphy, M. E. P.; Hupkes, H.-J.; Kosters, W.; Impagliazzo, A.; Ubbink, M. *Chemistry – A European Journal* **2004**, *10*, 3252.
(113) Williams, M. A.; Rapoport, H. *The Journal of Organic Chemistry* **1993**, *58*, 1151.
(114) http://www.britglass.org.uk/history-of-glass; British Glass Manufacturers' Confederation: 9 Churchill Way, Chapeltown, Sheffield, South Yorkshire, S35 2PY. UK., 2013.
(115) Argyo, C.; Weiss, V.; Bräuchle, C.; Bein, T. *Chemistry of Materials* **2013**, *26*, 435.
(116) Carniato, F.; Tei, L.; Arrais, A.; Marchese, L.; Botta, M. *Chemistry – A European Journal* **2013**, *19*, 1421.
(117) Caruso, F.; Caruso, R. A.; Möhwald, H. *Science* **1998**, *282*, 1111.
(118) Duarte, A. P.; Mauline, L. Ã. l.; Gressier, M.; Dexpert-Ghys, J.; Roques, C.; Caiut, J. M. A.; Deffune, E.; Maia, D. C. G.; Carlos, I. Z.; Ferreira, A. A. P.; Ribeiro, S. J. L.; Menu, M.-J. l. *Langmuir* **2013**, *29*, 5878.
(119) Ehlert, N.; Mueller, P. P.; Stieve, M.; Lenarz, T.; Behrens, P. *Chemical Society Reviews* **2013**, *42*, 3847.
(120) Francis, B.; Raj, D. B. A.; Reddy, M. L. P. *Dalton Transactions* **2010**, *39*, 8084.
(121) Huang, X. G.; Wang, Q.; Yan, X. H.; Xu, J.; Liu, W. S.; Tang, Y. *Journal of Physical Chemistry C* **2011**, *115*, 2332.
(122) Jung, H.-y.; You, S.; Lee, C.; You, S.; Kim, Y. *Chemical Communications* **2013**, *49*, 7528.
(123) Klajn, R.; Stoddart, J. F.; Grzybowski, B. A. *Chemical Society Reviews* **2010**, *39*, 2203.

(124) Lee, J. E.; Lee, N.; Kim, T.; Kim, J.; Hyeon, T. *Accounts of Chemical Research* **2011**, *44*, 893.
(125) Lupo, F.; Fragala, M. E.; Gupta, T.; Mamo, A.; Aureliano, A.; Bettinelli, M.; Speghini, A.; Gulino, A. *Journal of Physical Chemistry C* **2010**, *114*, 13459.
(126) Mody, K. T.; Popat, A.; Mahony, D.; Cavallaro, A. S.; Yu, C.; Mitter, N. *Nanoscale* **2013**, *5*, 5167.
(127) Popat, A.; Hartono, S. B.; Stahr, F.; Liu, J.; Qiao, S. Z.; Qing Lu, G. *Nanoscale* **2011**, *3*, 2801.
(128) Reineck, P.; GÃ³mez, D.; Ng, S. H.; Karg, M.; Bell, T.; Mulvaney, P.; Bach, U. *ACS Nano* **2013**.
(129) Slowing, I. I.; Trewyn, B. G.; Giri, S.; Lin, V. S. Y. *Advanced Functional Materials* **2007**, *17*, 1225.
(130) Tang, F.; Li, L.; Chen, D. *Advanced Materials* **2012**, *24*, 1504.
(131) Vallee, A.; Humblot, V.; Pradier, C. M. *Accounts of Chemical Research* **2010**, *43*, 1297.
(132) Wu, W.; Sun, Z.; Zhang, Y.; Xu, J.; Yu, H.; Liu, X.; Wang, Q.; Liu, W.; Tang, Y. *Chemical Communications* **2012**, *48*, 11017.
(133) Zhang, K.; Zhou, H.; Mei, Q.; Wang, S.; Guan, G.; Liu, R.; Zhang, J.; Zhang, Z. *Journal of the American Chemical Society* **2011**, *133*, 8424.
(134) Vitale-Brovarone, C.; Verné, E.; Robiglio, L.; Martinasso, G.; Canuto, R.; Muzio, G. *Journal of Materials Science: Materials in Medicine* **2008**, *19*, 471.
(135) Salinas, A. J.; Esbrit, P.; Vallet-Regi, M. *Biomaterials Science* **2013**, *1*, 40.
(136) Fernandez-Moreira, V.; Song, B.; Sivagnanam, V.; Chauvin, A.-S.; Vandevyver, C. D. B.; Gijs, M.; Hemmila, I.; Lehr, H.-A.; Bünzli, J.-C. G. *Analyst* **2010**, *135*, 42.
(137) Chen, B.; Wang, L.; Zapata, F.; Qian, G.; Lobkovsky, E. B. *Journal of the American Chemical Society* **2008**, *130*, 6718.
(138) Comstock, M. J. In *Fluorescent Chemosensors for Ion and Molecule Recognition*; American Chemical Society: 1993; Vol. 538, p i.
(139) Hou, F.; Cheng, J.; Xi, P.; Chen, F.; Huang, L.; Xie, G.; Shi, Y.; Liu, H.; Bai, D.; Zeng, Z. *Dalton Transactions* **2012**, *41*, 5799.
(140) Escobedo, C. *Lab on a Chip* **2013**, *13*, 2445.
(141) Choi, C. J.; Wu, H.-Y.; George, S.; Weyhenmeyer, J.; Cunningham, B. T. *Lab on a Chip* **2011**, *12*, 574.
(142) Gruschke, O. G.; Baxan, N.; Clad, L.; Kratt, K.; von Elverfeldt, D.; Peter, A.; Hennig, J.; Badilita, V.; Wallrabe, U.; Korvink, J. G. *Lab Chip* **2012**, *12*, 495.
(143) Kagan, D.; Campuzano, S.; Balasubramanian, S.; Kuralay, F.; Flechsig, G. U.; Wang, J. *Nano Letters* **2011**, *11*, 2083.
(144) Unger, M. A.; Chou, H.-P.; Thorsen, T.; Scherer, A.; Quake, S. R. *Science* **2000**, *288*, 113.
(145) Haeberle, S.; Zengerle, R. *Lab on a Chip* **2007**, *7*, 1094.
(146) Brolo, A. G.; Gordon, R.; Leathem, B.; Kavanagh, K. L. *Langmuir* **2004**, *20*, 4813.
(147) Gordon, R.; Sinton, D.; Kavanagh, K. L.; Brolo, A. G. *Accounts of Chemical Research* **2008**, *41*, 1049.
(148) Binnemans, K. *Chemical Reviews* **2009**, *109*, 4283.
(149) Hsu, S.-H.; Yilmaz, M. D.; Blum, C.; Subramaniam, V.; Reinhoudt, D. N.; Velders, A. H.; Huskens, J. *Journal of the American Chemical Society* **2009**, *131*, 12567.
(150) Ludden, M. J. W.; Reinhoudt, D. N.; Huskens, J. *Chemical Society Reviews* **2006**, *35*, 1122.
(151) Lenaerts, P.; Görller-Walrand, C.; Binnemans, K. *Journal of Luminescence* **2006**, *117*, 163.
(152) Kolbe, G. *Das komplexchemische Verhalten der Kieselsäure* Jena, Germany, 1956.
(153) Stöber, W.; Fink, A.; Bohn, E. *Journal of Colloid and Interface Science* **1968**, *26*, 62.
(154) Wang, Y.; Yu, A.; Caruso, F. *Angewandte Chemie International Edition* **2005**, *44*, 2888.
(155) Nguyen, T. D.; Leung, K. C. F.; Liong, M.; Liu, Y.; Stoddart, J. F.; Zink, J. I. *Adv. Funct. Mater.* **2007**, *17*, 2101.
(156) Nguyen, T. D.; Leung, K. C. F.; Liong, M.; Pentecost, C. I. D.; Stoddart, J. F.; Zink, J. I. *Org. Lett.* **2006**, *8*, 3363.
(157) Nguyen, T. D.; Liu, Y.; Saha, S.; Leung, K. C. F.; Stoddart, J. F.; Zink, J. I. *J. Am. Chem. Soc.* **2007**, *129*, 626.

(158) Li, M.; Chen, Z.; Yam, V. W.; Yanbing, Z. *ACS Nano* **2008**, *2*, 905.
(159) Qian, L.; Yang, X. *Adv. Funct. Mater.* **2007**, *17*, 1353.
(160) Rossi, L. M.; Shi, L. F.; Quina, F. H.; Rosenzweig, Z. *Langmuir* **2005**, *21*, 4277.
(161) Zisman, W. A. *Product R&D* **1969**, *8*, 98.
(162) Condorelli, G. G.; Tudisco, C.; Motta, A.; Di Mauro, A.; Lupo, F.; Gulino, A.; Fragala, I. L. *European Journal of Inorganic Chemistry* **2010**, 4121.
(163) Moorthy, M. S.; Cho, H.-J.; Yu, E.-J.; Jung, Y.-S.; Ha, C.-S. *Chemical Communications* **2013**, *49*, 8758.
(164) Sun, C.-Y.; Wang, X.-L.; Qin, C.; Jin, J.-L.; Su, Z.-M.; Huang, P.; Shao, K.-Z. *Chemistry – A European Journal* **2013**, *19*, 3639.
(165) Asenath Smith, E.; Chen, W. *Langmuir* **2008**, *24*, 12405.
(166) Rossi, L. M.; Shi, L.; Quina, F. H.; Rosenzweig, Z. *Langmuir* **2005**, *21*, 4277.
(167) Lewis, D. J.; Dore, V. D.; Goodwin, M. J.; Savage, A. C.; Nash, G. B.; Angeli, P.; Pikramenou, Z. *Meas. Sci. Technol.* **2012**, *23*, 084004.
(168) Timpson, C. J.; Carter, C. C.; Olmsted, J. *The Journal of Physical Chemistry* **1989**, *93*, 4116.
(169) Lewis, D. J.; Moretta, F.; Holloway, A. T.; Pikramenou, Z. *Dalton Transactions* **2012**, *41*, 13138.
(170) Hakkinen, H. *Nat Chem* **2012**, *4*, 443.
(171) Ayranci, E.; Bayram, E. *Journal of Hazardous Materials* **2005**, *122*, 147.
(172) Rybakova, I. A.; Prilezhaeva, E. N.; Korotaeva, L. M.; Strel'tsova, E. D.; Litvinov, V. P. *Dokl Chem* **2005**, *400*, 3.
(173) Crans, D. C.; Trujillo, A. M.; Bonetti, S.; Rithner, C. D.; Baruah, B.; Levinger, N. E. *The Journal of Organic Chemistry* **2008**, *73*, 9633.
(174) Li, C.-W.; Benjamin, M. M.; Korshin, G. V. *Environmental Science & Technology* **2000**, *34*, 2570.
(175) Stephenson, H. P.; Sponer, H. *Journal of the American Chemical Society* **1957**, *79*, 2050.
(176) Chin, L.-F.; Kong, S.-M.; Seng, H.-L.; Tiong, Y.-L.; Neo, K.-E.; Maah, M.; Khoo, A.-B.; Ahmad, M.; Hor, T.-S.; Lee, H.-B.; San, S.-L.; Chye, S.-M.; Ng, C.-H. *J Biol Inorg Chem* **2012**, *17*, 1093.
(177) Steven L. Murov, I. C., Gordon L. Hug *Handbook of photochemistry*; Marcel Dekker, INC: New York, 1993; Vol. 420.
(178) Zhu, W.; Cromie, M. M.; Cai, Q.; Lv, T.; Singh, K.; Gao, W. *PLoS ONE* **2014**, *9*, e92992.
(179) Seltzer, M. D.; Fallis, S.; Hollins, R. A.; Prokopuk, N.; Bui, R. N. *Journal of Fluorescence* **2005**, *15*, 597.
(180) Hussain, A.; Somyajit, K.; Banik, B.; Banerjee, S.; Nagaraju, G.; Chakravarty, A. R. *Dalton Transactions* **2013**, *42*, 182.
(181) Priyadarsini, K. I. *Journal of Photochemistry and Photobiology C: Photochemistry Reviews* **2009**, *10*, 81.
(182) Blair, S.; Lowe, M. P.; Mathieu, C. E.; Parker, D.; Senanayake, P. K.; Kataky, R. *Inorganic Chemistry* **2001**, *40*, 5860.
(183) Parker, D.; Yu, J. *Chemical Communications* **2005**, 3141.
(184) Munro, N. *Environ Health Perspect* **1994**, *102*, 18.
(185) Orient, J. M. *JAMA* **1989**, *262*, 644.
(186) Tripier, R.; Platas-Iglesias, C.; Boos, A.; Morfin, J.-F.; Charbonniere, L. *European Journal of Inorganic Chemistry* **2010**, 2735.
(187) Pearson, R. G. *Inorganic Chemistry* **1988**, *27*, 734.
(188) Chenakin, S. P.; Heinz, B.; Morgner, H. *Surface Science* **1998**, *397*, 84.
(189) Bertoncello, P.; Kefalas, E. T.; Pikramenou, Z.; Unwin, P. R.; Forster, R. J. *J. Phys. Chem. B* **2006**, *110*, 10063.
(190) D'Aleo, A., Williams, R. M., Chriqui, Y., Iyer, V. M., Belser, P.,; Vergeer, F., Ruiz, V., Unwin, P. R., De Cola, L. *The Open Inorganic Chemistry Journal* **2007**, 26.
(191) Yeung, C. L.; Iqbal, P.; Allan, M.; Lashkor, M.; Preece, J. A.; Mendes, P. M. *Advanced Functional Materials* **2010**, *20*, 2657.

(192) Willey, T. M.; Vance, A. L.; Bostedt, C.; Van Buuren, T.; Meulenberg, R. W.; Terminello, L. J.; Fadley, C. S. *Langmuir* **2004**, *20*, 4939.
(193) Castano-Briones, M. M.; Bassett, A. P.; Meason, L. L.; Ashton, P. R.; Pikramenou, Z. *Chemical Communications* **2004**, 2832.
(194) Kim, S. H.; Ge, P.; Katzenellenbogen, J. A. *Chemical Communications* **2009**, 183.
(195) Be´thencourt, M. I.; Srisombat, L.-o.; Chinwangso, P.; Lee, T. R. *Langmuir* **2009**, *25*, 1265.
(196) Fadley, C. S.; Baird, R. J.; Siekhaus, W. J.; Novakov, T.; Bergstrom, S. A. *J. Electron Spectrosc. Relat. Phenom.* **1974**, *4*, 93.
(197) Gelius, U.; Heden, P. F.; Hedman, J.; Lindberg, B. J.; Bernt, J.; Manne, R.; Nordberg, R.; Nordling, C.; Siegbahn, K. *Phys. Scr.* **1970**, 70.
(198) Lu, H. B.; Campbell, C. T.; Castner, D. G. *Langmuir* **2000**, *16*, 1711.
(199) Tour, J. M.; Jones, L.; Pearson, D. L.; Lamba, J. J. S.; Burgin, T. P.; Whitesides, G. M.; AUara, D. L.; Parikh, A. N.; Atre, S. V. *J. Am. Chem. SOC.* **1995**, *117*, 9529.
(200) Shendage, D. M.; Frohlich, R.; Haufe, G. *Organic Letters* **2004**, *6*, 3675.
(201) Pearson, A. J.; Hwang, J.-J. *The Journal of Organic Chemistry* **2000**, *65*, 3466.
(202) Chankeshwara, S. V.; Chakraborti, A. K. *Organic Letters* **2006**, *8*, 3259.
(203) Perron, V.; Abbott, S.; Moreau, N.; Lee, D.; Penney, C.; Zacharie, B. *Synthesis-Stuttgart* **2009**, 283.
(204) Hoa, X. D.; Kirk, A. G.; Tabrizian, M. *Biosensors and Bioelectronics* **2007**, *23*, 151.
(205) Hung, A.; Mwenifumbo, S.; Mager, M.; Kuna, J. J.; Stellacci, F.; Yarovsky, I.; Stevens, M. M. *Journal of the American Chemical Society* **2011**, *133*, 1438.
(206) Hung, A.; Mager, M.; Hembury, M.; Stellacci, F.; Stevens, M. M.; Yarovsky, I. *Chemical Science* **2013**, *4*, 928.
(207) Mendes, F.; Paulo, A.; Santos, I. *Dalton Transactions* **2010**, *40*, 5377.
(208) Verma, R.; Gupta, B. D. *Food Chemistry* **2015**, *166*, 568.
(209) Jeon, S.; Moon, J.-M.; Lee, E. S.; Kim, Y. H.; Cho, Y. *Angewandte Chemie International Edition* **2014**, *53*, 4597.
(210) Mendes, P.; Lashkor, M.; Rawson, F. J.; Preece, J. *Analyst* **2014**.
(211) Stenberg, E.; Persson, B.; Roos, H.; Urbaniczky, C. *Journal of Colloid and Interface Science* **1991**, *143*, 513.
(212) Adams, S. J.; Lewis, D. J.; Preece, J. A.; Pikramenou, Z. *ACS Applied Materials & Interfaces* **2014**.
(213) Flatmark, T.; Stokka, A. J.; Berge, S. V. *Analytical Biochemistry* **2001**, *294*, 95.
(214) Lahiri, J.; Isaacs, L.; Tien, J.; Whitesides, G. M. *Analytical Chemistry* **1999**, *71*, 777.
(215) Prime, K. L.; Whitesides, G. M. *Journal of the American Chemical Society* **1993**, *115*, 10714.
(216) Mrksich, M.; Sigal, G. B.; Whitesides, G. M. *Langmuir* **1995**, *11*, 4383.
(217) Davis, T. M.; Wilson, W. D. *Analytical Biochemistry* **2000**, *284*, 348.
(218) Peterlinz, K. A.; Georgiadis, R. *Langmuir* **1996**, *12*, 4731.
(219) Abdou, H. E.; Mohamed, A. A.; Fackler, J. P. In *Gold Chemistry*; Wiley-VCH Verlag GmbH & Co. KGaA: 2009, p 1.
(220) Solomun, T.; Christmann, K.; Baumgaertel, H. *The Journal of Physical Chemistry* **1989**, *93*, 7199.

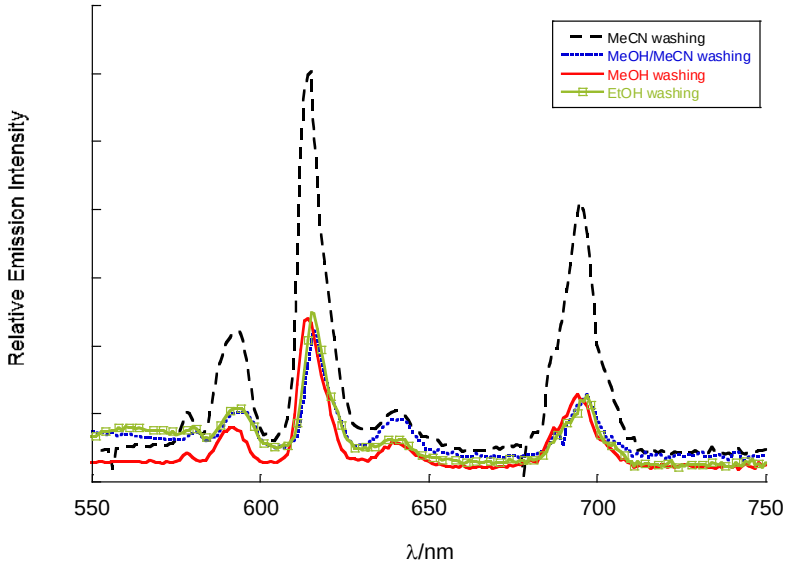

Figure 8.3- Displaying emission spectrum EuL SAM on gold exposed to different solvents in the washing procedure

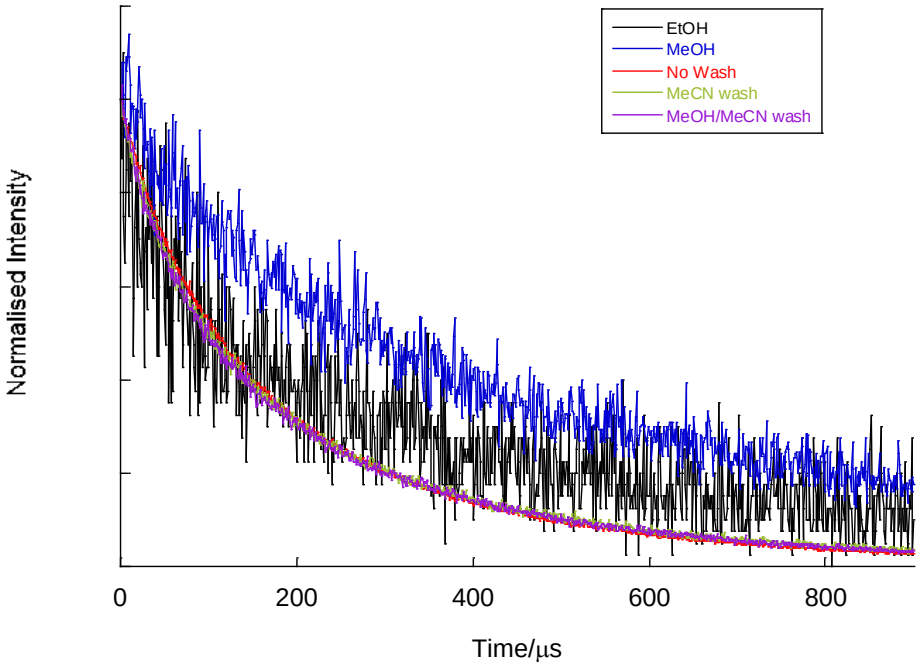

Figure 8.4 - Luminescent decay lifetime of EuL SAM on gold exposed to different solvents in the washing procedure and the absence of a washing procedure.

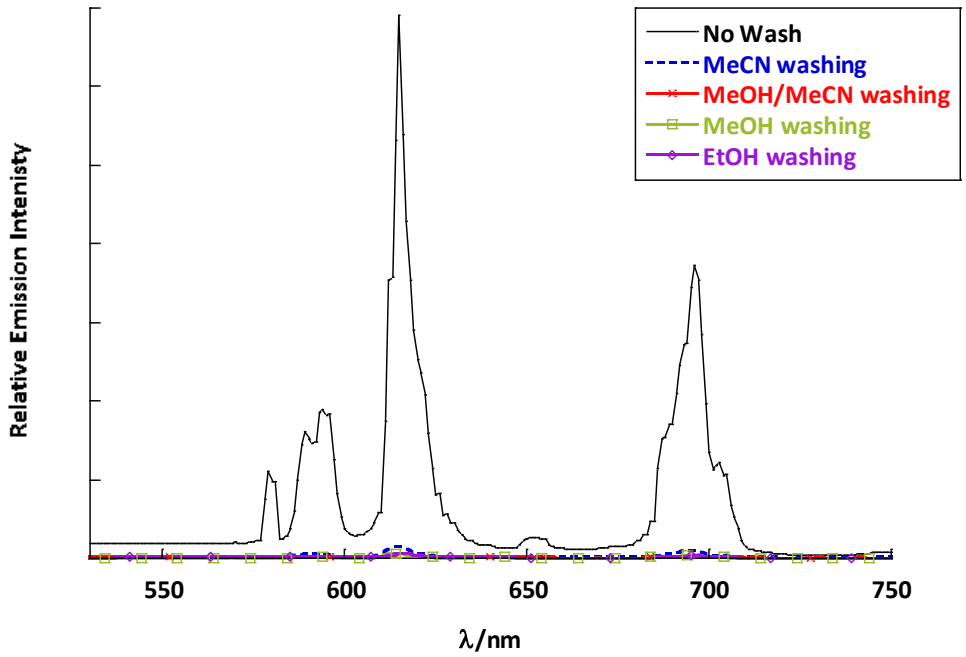

Figure 8.5- Displaying emission spectrum EuL SAM on gold exposed to different solvents in the washing procedure and the absence of a washing procedure

Figures used to determine the limit of detection.

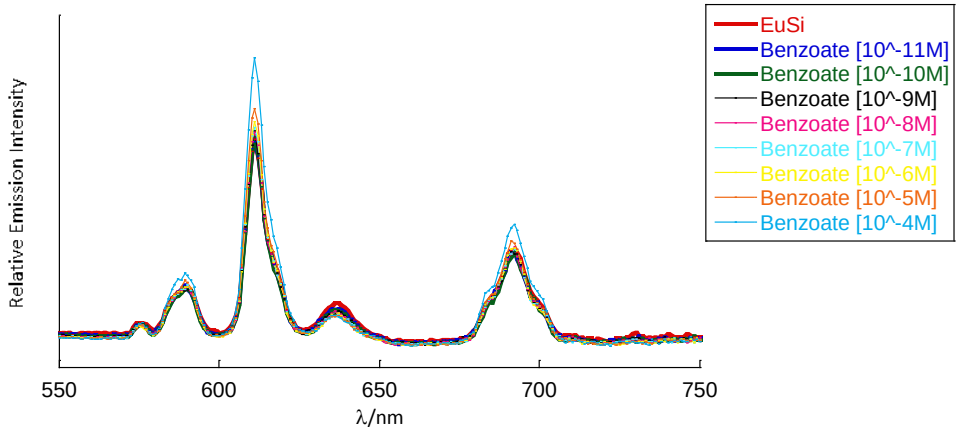

Figure 8.6- Emission spectra (λ_{ex} =280 nm) for the titration of Picolinate (10 fold increases in concentration) into a Ethanolic solution of $EuSi_2$ (0.15 mM)

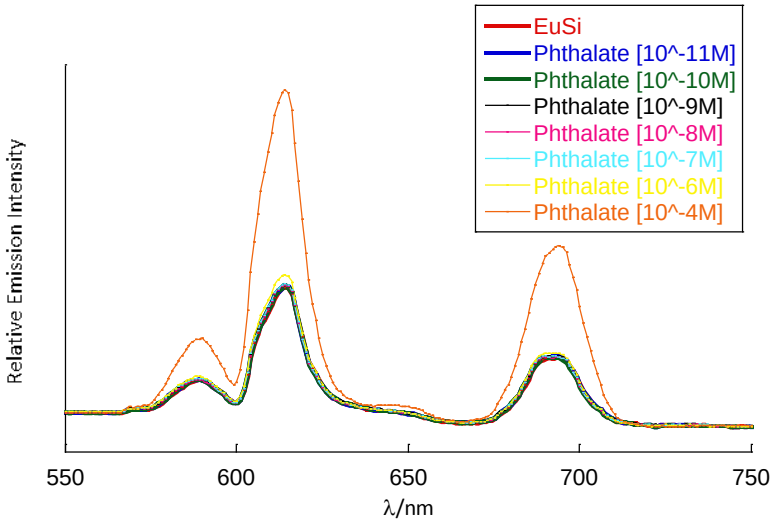

Figure 8.7 Emission spectra (λ_{ex} =280 nm) for the titration of Phthalate (10 fold increases in concentration) into a Ethanolic solution of $EuSi_2$ (0.15 mM)

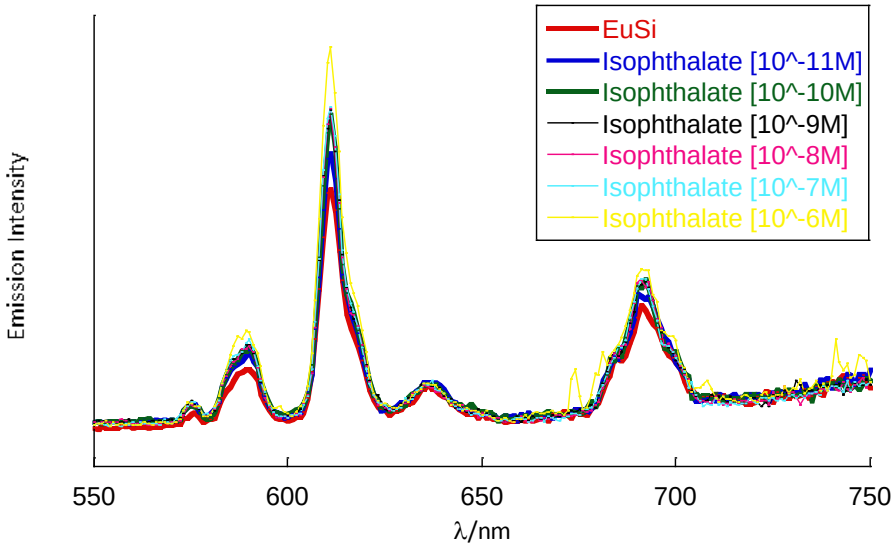

Figure 8.9- Emission spectra (λ_{ex} =280 nm) for the titration of Isophthalate (10 fold increases in concentration) into a Ethanolic solution of $EuSi_2$ (0.15 mM)

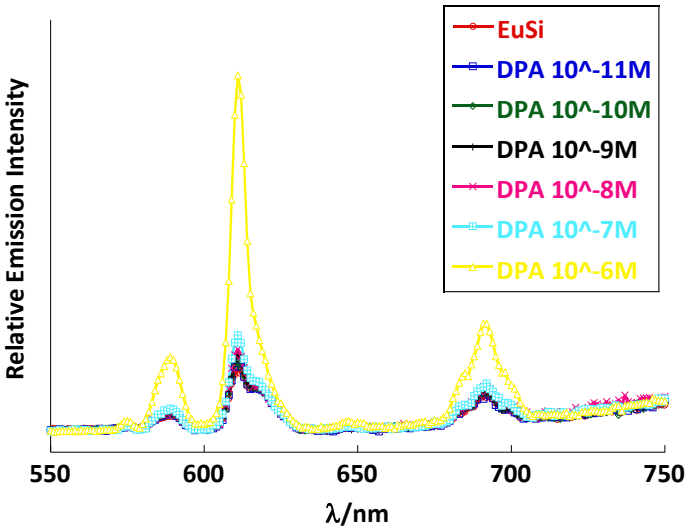

Figure 8.10 - ***Emission spectra (λ_{ex} =280 nm) for the titration of dipicolinate (10 fold increases in concentration) into a Ethanolic solution of $EuSi_2$ (0.15 mM)***

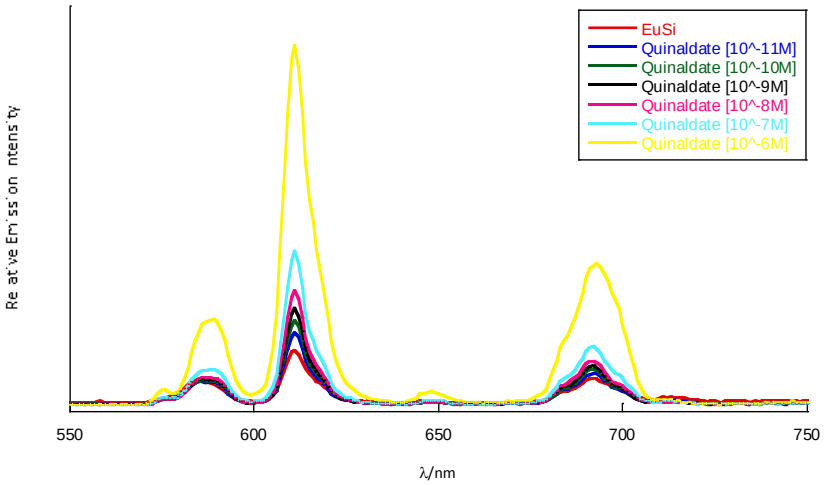

Figure 8.12 Emission spectra (λ_{ex} =280 nm) for the titration of quinaldate (10 fold increases in concentration) into a Ethanolic solution of $EuSi_2$ (0.15 mM)

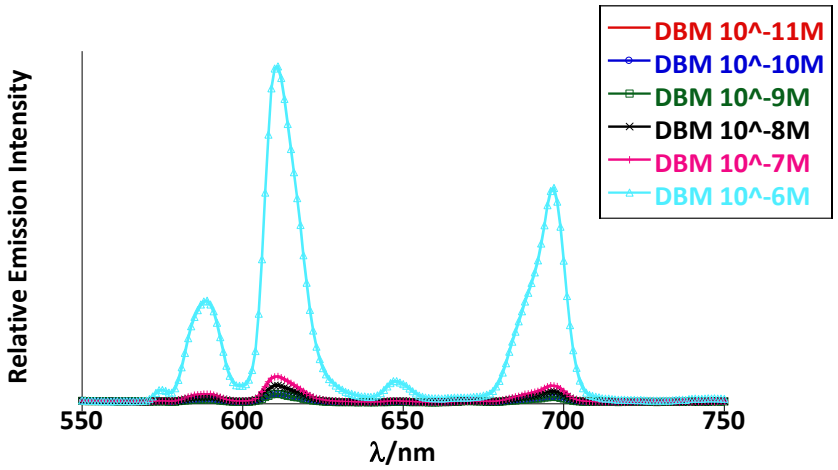

Figure 8.13 Emission spectra (λ_{ex} =280 nm) for the titration of dibenzoylmethane (10 fold increases in concentration) into a Ethanolic solution of $EuSi_2$ (0.15 mM)